IntechOpen

Topics in Radar Signal Processing

Edited by Graham Weinberg

TOPICS IN RADAR SIGNAL PROCESSING

Edited by **Graham Weinberg**

Topics in Radar Signal Processing
http://dx.doi.org/10.5772/intechopen.69785
Edited by Graham Weinberg

Contributors

Tamás Pető, Rudolf Seller, Moutaman Mirghani, Ahmed Awad, Alexander Totsky, Karen Egiazarian, Shobha Ram, Gaspare Galati, Gabriele Pavan, Jiwoong Yu, Min-Ho Ka, Sumin Kim, Guolong Cui, Xianxiang Yu, Lingjiang Kong, Stéphane Méric, Jean-Yves Baudais, Stefan Brueggenwirth, Simon Wagner, Tobias Müller, Pascal Marquardt, Christian Bräu, Marcel Warnke, Fernando Rial, Octavian Dumitru, Gottfried Schwarz, Daniela Espinoza-Molina, Mihai Datcu, Herman Hummel, Christiaan Hummel

Notice

First published in London, United Kingdom, 2018 by IntechOpen
eBook (PDF) Published by IntechOpen, 2019
IntechOpen is the global imprint of INTECHOPEN LIMITED, registered in England and Wales, registration number: 11086078, The Shard, 25th floor, 32 London Bridge Street
London, SE19SG – United Kingdom
Printed in Croatia

British Library Cataloguing-in-Publication Data
A catalogue record for this book is available from the British Library

Additional hard and PDF copies can be obtained from orders@intechopen.com

Topics in Radar Signal Processing
Edited by Graham Weinberg

p. cm.

Print ISBN 978-1-78923-120-5

Online ISBN 978-1-78923-121-2

eBook (PDF) ISBN 978-1-83881-419-9

Meet the editor

Graham Weinberg, PhD, was educated at the University of Melbourne, Australia, where he studied mathematical analysis and probability theory. Since 2002, he has been employed at Defence Science and Technology (DST) Group, where he has spent his entire time examining radar detection issues for X-band high-resolution maritime surveillance radar. He is a member of the IET and a senior member of the IEEE. In addition to this, he is an associate editor of IET Electronics Letters. In 2016, he wrote a book (*Radar Detection Theory of Sliding Window Processes, CRC Press, 2017*) documenting his extensive research in the area of noncoherent CFAR.

Contents

Preface

Since its inception during World War II, radar has continued to be a topic of significant importance in both military and civilian contexts. Although the reflectivity of electromagnetic waves was first investigated by the German physicist Heinrich Hertz around 1886, its value, in a military context, was not realised until experimentalists in the United Kingdom, the United States and Europe found that the presence of aircraft could be detected via remote sensing, providing a significant early warning advantage. This resulted in much research and development of radar technology and then applications of it to aircraft traffic control as well as weather surveillance.

Although radar began as an experimental science, it was found that its performance could be modelled by studying the environment in which it operated and also enhanced by designing its underlying algorithms on the basis of the theoretical developments. With improvements in electronics and technology, it was found that it was necessary to develop better algorithms to facilitate the extraction of radar information from processed radar returns.

Thus, there continues to be a lot of interest in the development of radar signal processing algorithms for modern radar applications. This book thus provides a sample of contributions to modern radar signal processing. This includes a series of chapters examining synthetic aperture radar (SAR), multiple-input multiple-output (MIMO) radar, micro-Doppler processing, as well as analysis of waveforms, radar detection, and clutter suppression issues. It is hoped that the chapters in this book would provide readers with future directions for research in these areas.

Graham Weinberg
Defence Science and Technology (DST) Group
Australia

Section 1

MIMO Applications

Chapter 1

Waveform Design and Related Processing for Multiple Target Detection and Resolution

Gaspare Galati and Gabriele Pavan

Additional information is available at the end of the chapter

http://dx.doi.org/10.5772/intechopen.71549

Abstract

The performance of modern radar systems mostly depends on the radiated waveforms, whose design is the basis of the entire system design. Today's coherent, solid-state radars (either of the phased array type or of the single-radiator type as air traffic control or marine radars) transmit a set of deterministic signals with relatively large duty cycles, an order of 10%, calling for pulse compression to get the required range resolution. Often, power budget calls for different pulse lengths (e.g., short, medium, and long waveforms with a rectangular envelope) to cover the whole radar range. The first part of the chapter includes the topic of mitigating the effect of unwanted side lobes, inherent to every pulse compression, which is achieved both by a careful and optimal design of the waveform and by a (possibly mismatched) suitable processing. The second part of the chapter deals with the novel noise radar technology, not yet used in commercial radar sets but promising: (1) to prevent radar interception and exploitation by an enemy part and (2) to limit the mutual interferences of nearby radars, as in the marine environment. In this case, the design includes a tailoring of a set of pseudo-random waveforms, generally by recursive processing, to comply with the system requirements.

Keywords: radar pulse compression, noise radar technology

1. Introduction

The main concern of radar signal processing is the extraction of useful information (generally referred to as "targets") from the background and disturbance of various kinds (noise, clutter, and jammer) [1, 2]. A typical processing input to a surveillance (or search) radar is the set of echoes from a point target at the generic reference position, which, for the two-dimension (2D) case, are naturally organized in *Range* (fast time) and in *Azimuth* (slow time), see **Figure 1**. **Figure 2** shows a real case of plan position indicator (PPI) acquisition.

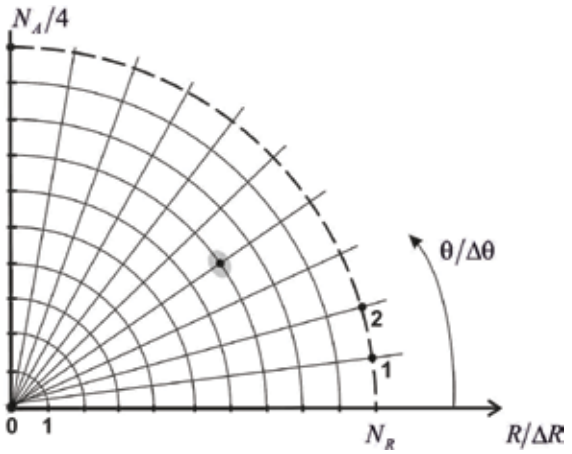

Figure 1. Range-Azimuth point target. $\Delta\theta$ = Azimuth resolution, ΔR = range resolution, N_A = number of azimuth cells, and N_R = number of range cells.

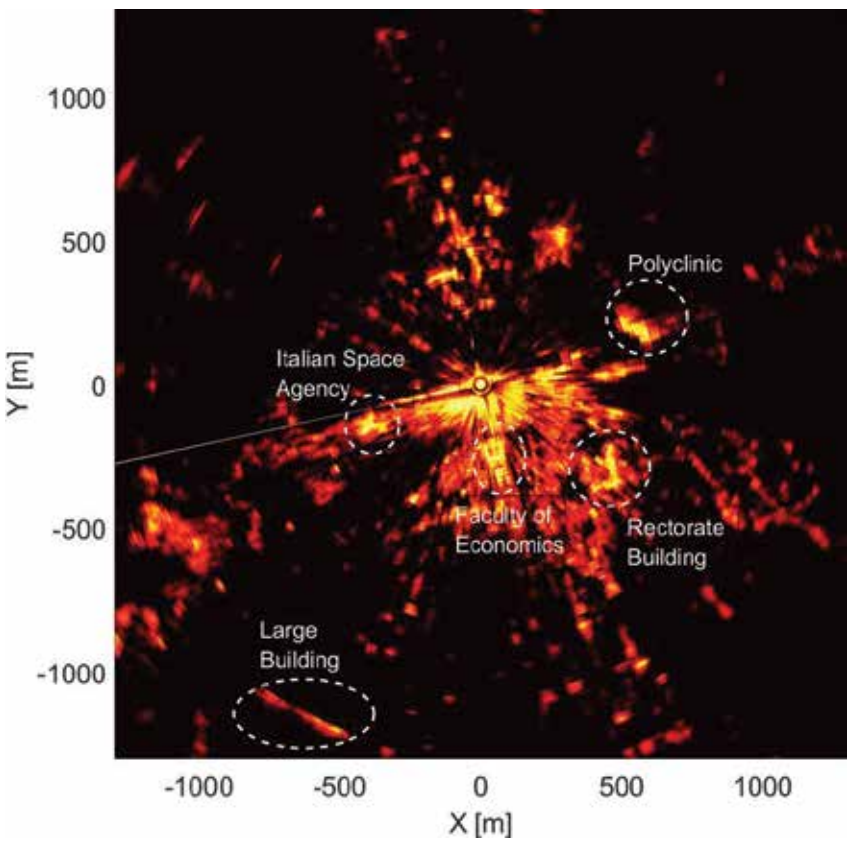

Figure 2. Real case of PPI acquisition (Tor Vergata University area).

The status of electronic technology of early radars of the World War II (WWII) period brought the designers to use simple waveforms, that is, rectangular pulses and sequences of them. Very soon, they understood that a receiver bandwidth *matched* to the transmitted pulse, that is, roughly equal to the reciprocal of the pulse duration, maximizes the output signal to noise ratio or *SNR* [3, 4]. The *Range* resolution, ΔR, is a function of the pulse duration τ, expressed in distance units, that is:

$$\Delta R = c\tau/2 \tag{1}$$

where $c = 2.99792 \times 10^8\ m \cdot s^{-1}$, which is the speed of light. In order to cope with the conflicting requirements of increasing the average power, proportional to the pulse duration, while maintaining a fair *Range* resolution, *Pulse Compression* techniques were devised and applied after WWII both in the USA and in the Soviet Union [5, 6]. These techniques use sophisticated waveforms in the place of the simple, rectangular pulse, with matched filtering (with sometimes a wanted mismatching). The early waveforms, still used today, were mostly based either on bi-phase coding, for example, Barker [7], or on the even most popular frequency modulation (FM or LFM in the linear case), also known as *chirp* signal [8, 9].

Historically, the design of the chirp radar in the Western world was made public in the 1960s [8] and, in the Eastern world, in the works (1950s) by Yakov Shirman[1] [11].

The radar signals synthesis problem was first examined by the ambiguity function (AF), introduced by Woodward in the 1950s [12]. Basically, the AF is a two-variable real function representing the modulus (sometimes the squared modulus) of the matched filter output when at the input there is a delayed and Doppler-shifted replica of the radar waveform. In the following, we assume the widely used correlation processor in radar reception, which is equivalent to the above-discussed matched filter (MF). The AF allows us to quantify the distribution in *Range* (i.e., delay) and in radial velocity (i.e., Doppler frequency) of the interference level due to point scatterers outside the reference delay-Doppler cell (i.e., the cell in which a target is to be detected and located). In the 1960s and 1970s, there were many attempts to use the AF to design radar waveforms with "good" characteristics, that is, "low enough" sidelobes in *Range* (and in radial velocity) and "well shaped" mainlobe (i.e., a narrow peak). Such specifications, referred to the envelope of the matched filter output, did not led to significant results in terms of practical waveforms design. Not only because the phase was ignored in them but, mainly, because a waveform designed according to a specific ambiguity function, for example, a *"thumbtack"* shaped one, might be hardly implementable in a real radar for various reasons, first of all the relevant need to transmit constant-modulus signals to maximize the energy radiated on the target and hence, the detection capability. In fact, dynamic range is another constraint to be carefully considered in addition to eclipsing losses, to coding accuracy, and so on. The interest in the AF has reoccurred in the 1990s and 2000s with the studies of multiple transmitters and multiple receivers' radar as a multiple input multiple output (MIMO) system [13–16], often named *netted*, *multistatic,* or *multisite*, as well as with studies of

[1]Y. Shirman received the IEEE Pioneer Award in 2009 "For the independent discovery of matched filtering, adaptive filtering, and high-resolution pulse compression for an entire generation of Russian and Ukrainian radars" [10].

integration of telecommunication capabilities in radars [17]. These systems call for waveforms designed and optimized in order to get a low Peak Side-Lobe Ratio (*PSLR*), good orthogonality properties, and a low degradation in the mainlobe, that is, low *SNR* loss (typically 1–2 *dB*, depending on the weighting function used). Considering that a single *dB* of additional *SNR* gained is nearly equivalent to a 25% increase in the transmitter power, for cost-effective solutions it is relevant to avoid these losses due to the weighting.

Concerning the waveforms selection and the related matched filter (MF), we can distinguish among: (1) rectangular pulse, (2) deterministic single code (Barker, Frank, Chirp,…), and (3) multiple codes, whose extent may theoretically reach an infinity number of signals (MIMO, noise radar).

In case (1), after a first analog (radio frequency (RF) or intermediate frequency (IF)) filtering before the analog-to-digital (A/D) conversion to limit the useful band and to suppress the thermal noise, an approximation of the rectangular MF is usually implemented using a Bessel filter, followed by sampling and A/D conversion (about two samples for a pulse).

In case (2), after sampling and A/D conversion of the sub-elements of the code (chips), a digital MF to the code is used: if $x[n]=x(nT)$ is the sequence of the samples of $x(t)$ obtained with a sampling period T, then the digital impulse response $h[k]$ of the digital filter is $x^*[N-n]$ where N is an integer equal or greater than the length of the numeric code.

In case (3), it is suitable to carry out directly the correlation between the received signal and the stored replica of the transmitted signal, which could vary each waveform repetition time (WRT) or each group of WRT. The fastest operation is in the frequency domain multiplying the spectrum of the signals (fast Fourier transform [FFT] and "zero padding") to obtain the aperiodic convolution/correlation. The algorithm is conceptually simple and compatible with the modern processing means also for high sample rates (in the order of hundreds of mega samples/second). It is based on the following steps: (1) computation, by FFT, of the Fourier transform of the received and reference signals, that is, $X(f)$ and $H(f)$, respectively; (2) after "zero padding" multiplication of $X(f)$ by the conjugate $H^*(f)$; and (3) inverse fast Fourier transform (IFFT) of the previous product.

In the following, we present the main characteristics of both deterministic and random signals and their comparison, including an analysis of the auto and cross-correlation functions and spectral properties, with recommendations for their practical use.

2. Waveform requirements

In the following, we will consider both *continuous-time* signals with duration T, that is, of the type $s(t)$ for $0<t<T$ with mean power $\frac{1}{T}\int_0^T |s(t)|^2 dt$, and *discrete-time* signals of the type s_k for $1\le k\le N$ with mean power $\frac{1}{N}\sum_{k=1}^{N} |s_k|^2$. We consider the main requirements of a set of M signals with complex envelope $s_i(t)$ for $i=1,\ldots,M$, pulsewidth T, same power, and band B. For each signal (we drop the index i in the following), they are defined by:

- $PSLR = \frac{\max_k(\tilde{s}_k)}{\max_k(m_k)}$ and Integrated Side-Lobe Ratio $(ISLR) = \frac{\sum_k |\tilde{s}_k|^2}{\sum_k |m_k|^2}$ where $\tilde{s}_k$ and m_k, are respectively the sidelobe and the mainlobe samples of the autocorrelation of $s(t)$.
- Crest factor C (or peak-to-average ratio, PAR): $C = PAR = \frac{max_k(|s_k|)}{\sqrt{\frac{1}{N}\sum_{k=1}^{N}|s_k|^2}}$ where N is the number of signal samples. C is the peak amplitude of the waveform divided by the *rms* value of the waveform.
- Mean envelope-to-peak power ratio $(MEPPR) = \frac{\frac{1}{N}\sum_{k=1}^{N}|s_k|^2}{max_k\left(|s_k|^2\right)}$, where $MEPPR = \frac{1}{C^2}$.

To evaluate the orthogonality between the signals $s_i(t)$ and $s_j(t)$, the normalized cross-correlation is defined as:

- $r_{ij}(t) = \frac{|R_{ij}(t)|}{|R_{i(j)}(0)|}$ where $R_{ij}(t) = \int s_i^*(\theta)s_j(t+\theta)d\theta, i \neq j$. The normalized cross-correlation is practically limited by the *compression ratio BT* (product between time duration T and bandwidth B) and, in most cases, the desired value is less (i.e., better) than $-30\ dB$.

In the frequency domain, the spectral band occupancy defines the frequency interval in which most of the spectrum of the waveform is allocated, generally taken as the equivalent noise band width, $NBW = \frac{1}{2\pi}\int_0^\infty \left|\frac{H(\omega)}{H_{max}}\right|^2 d\omega$, where $|H_{max}|$ is the maximum amplitude of the frequency response of the filter. Sometimes this item is overlooked, especially when noise-like waveforms are concerned, but it is of paramount importance in most real-world radars.

3. Deterministic waveforms

3.1. Linear frequency modulation (LFM)

Pulse Compression allows the radar designer to play with additional degrees of freedom since the signal duration is decoupled with the *Range resolution*: instead of expression (1), the following relationship holds:

$$\Delta R = c/2B \tag{2}$$

where B is the signal bandwidth. A straightforward, well-known way to generate a signal of duration T, with a carrier f_0, whose spectrum occupies a given band B (large enough to satisfy the resolution requirement, i.e. from $f_0 - \frac{B}{2}$ to $f_0 + \frac{B}{2}$), is the LFM of that carrier in a given time interval T, that is, with an instantaneous frequency:

$$f(t) = \frac{B}{T}t \qquad -\frac{T}{2} \leq t \leq +\frac{T}{2} \tag{3}$$

The resulting time-domain complex envelope signal $s(t)$ has a unit amplitude and, from Eq. (3), a quadratic instantaneous phase:

$$s(t) = \exp\left(j\frac{\pi B}{T}t^2 - j\alpha_0\right) \qquad -\frac{T}{2} \le t \le +\frac{T}{2}, \qquad \alpha_0 = \frac{\pi BT}{2} \tag{4}$$

According to the stationary phase principle [9, 18], for a large enough number of independent samples or product BT (compression ratio), the group delay of an LFM signal is proportional to the instantaneous frequency. The spectrum of $s(t)$ is mostly contained in the interval from $\frac{-B}{2}$ to $\frac{+B}{2}$, and it is *quasi rectangular* (see **Figure 3**) with constant amplitude and linear phase in the bandwidth B (and ideally, zero amplitude outside it).

The resulting output of the matched filter (autocorrelation function) has the shape shown in **Figure 4**. It has a time duration $1/B$ and a (unacceptable) *PSLR* of about 13.2 *dB* below the main

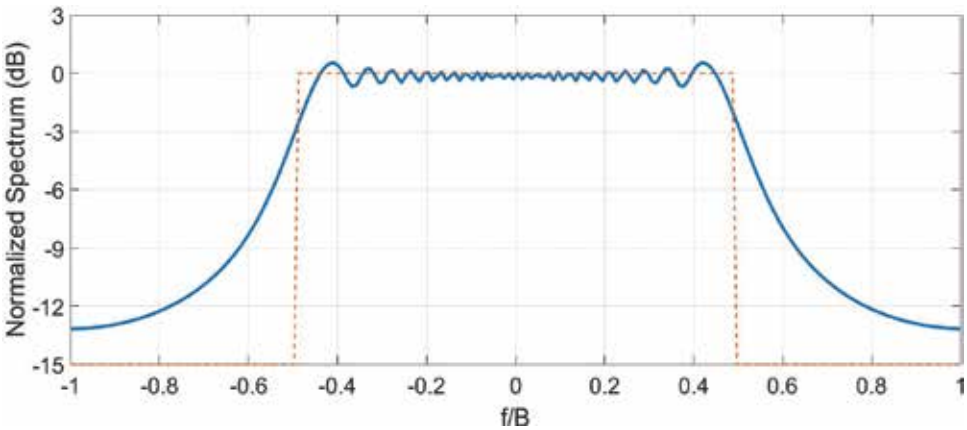

Figure 3. Normalized spectrum of a LFM signal for $BT = 100$. With BT increasing, the spectrum shape is closer and closer to a rectangle (dashed line).

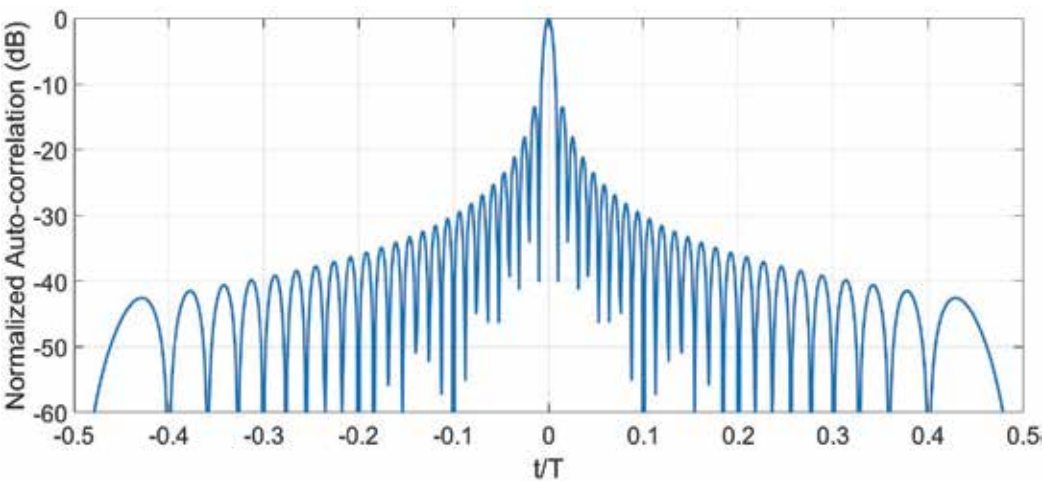

Figure 4. Normalized autocorrelation of a LFM signal with $BT = 100$.

peak. To mitigate the masking effect of nearby targets, the sidelobe level of the autocorrelation function of the transmitted pulse has to reach very low values (<-60 *dB* in some applications such as marine radars) comparable to the two-way antenna sidelobes in *Azimuth*, calling for a more sophisticated frequency modulation law, the non-linear frequency modulation (NLFM) [19].

3.2. Non-linear frequency modulation (NLFM)

In the past, accurate NLFM waveforms were difficult to design, produce, and process. However, the progress of technology now offers the possibility to produce and process high BT, sophisticated NLFM waveforms. The advent of high-speed and high dynamic range Digital-to-Analog-Convertors (DACs) and high-speed large-scale field programmable gate arrays (FPGAs) facilitates generating high-performance precision digital waveforms. Moreover, FPGAs and fast Analog-to-Digital-Convertors (ADCs) allow the direct sampling fairly wide bandwidth signals, and modern high-speed processors allow more sophisticated filtering and detection algorithms to be employed. Historically, the Millett waveform, that is, with a *"cosine squared on a pedestal"* weighting, is the oldest NLFM [19]. By means of the well-known *spectral windows* [9, 18–21], NLFM waveforms can be easily designed. However, this method, relying on the stationary phase principle, is effective in terms of *PSLR* values only when *BT* is large (in practice, greater than a few thousands; see **Figure 5**, where NLFN is obtained by Hamming weighting) and is less effective when a low *BT* is required, as it happens in various civil applications like air traffic control (ATC) radar and marine (or navigation) radar.

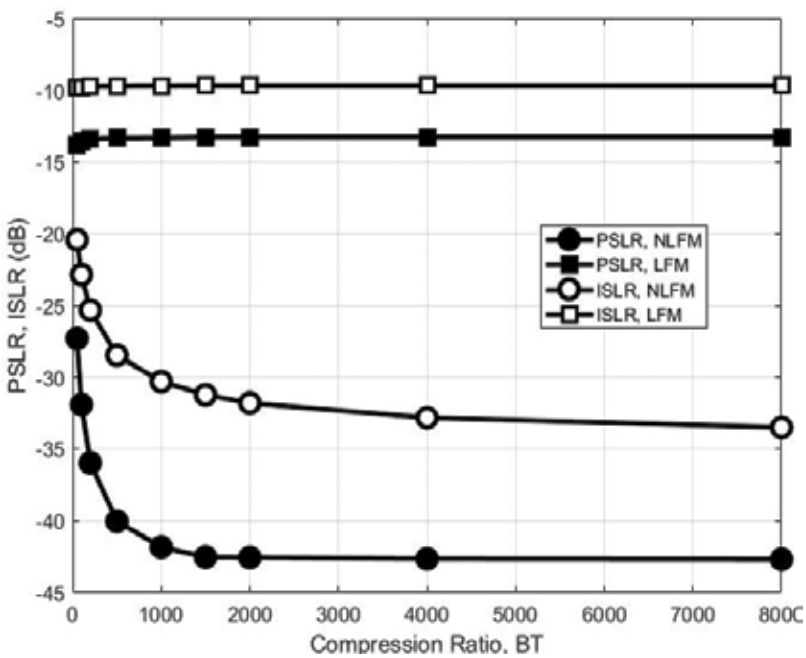

Figure 5. PSLR and ISLR versus the compression ratio (*BT*) for LFM and NLFM (Hamming weighting) signals.

The requirement for further reducing the sidelobe level of the autocorrelation function has been satisfied either by *"tailoring"* the NLFM law or by the use of some sidelobe suppression filter in reception. The latter is used at the expense of losses in the *SNR*, with the additional disadvantage of high complexity and high sensitivity to Doppler frequency that can only be compensated by a bank of filters with another increase of complexity and cost. The former requires a careful design. Let us remember that a waveform with duration T and bandwidth B has $2BT$ degrees of freedom that is completely described by $2BT$ values. Hence, it is clear that for relatively low (tens or hundreds) values of the compression ratio BT, the design is more difficult; see also the NLFM curves of **Figure 5**, with a significant performance degradation for $BT < 500$.

A new design method to cope with the *low compression ratio* problem has been presented in [22, 23], leading to a kind of *Hybrid*-NLFM (HNLFM), whose amplitude, however, is not constant during the duration T of the signal, thus creating implementation problems with the widely used saturated (C-class) power amplifiers. This family of waveforms is enhanced and analyzed in the following.

3.3. Hybrid non-linear frequency modulation (HNLFM)[2]

Let us consider a narrowband signal $x(t) = a(t)\cos[2\pi f_0 t + \phi(t)]$ with power spectrum centered at f_0 and both amplitude modulation (AM) and phase modulation (PM). Its complex envelope is $s(t) = a(t)e^{j\phi(t)}$ where $a(t)$ and $\phi(t)$ denote, respectively, the AM and PM. The Stationary Phase Principle establishes that the amplitude spectrum $|S(\omega_t)|^2$ of the signal $s(t)$ at the instantaneous angular frequency $\omega_t = 2\pi f_t$ can be approximated as:

$$|S(\omega_t)|^2 \cong 2\pi \frac{a^2(t)}{|\phi''(t)|} \tag{5}$$

where $\phi''(t)$ is the second derivative of $\phi(t)$. Hence, the energy spectral density at the frequency $\omega_t = \phi'(t)$ is larger when the rate of change of ω_t is smaller, that is, around the stationary phase point. From Eq. (5), the amplitude modulation function $a(t)$ can be derived for a given spectrum shape (often assumed *Gaussian* or *rectangular* from $-B/2$ to $-B/2$) and for a given instantaneous frequency law $\phi'(t)$:

$$a(t) \cong \sqrt{\frac{1}{2\pi}\left|S\left(\phi'(t)\right)\right|^2 |\phi''(t)|} \tag{6}$$

However, the applicability of the stationary phase approximation depends on the compression ratio BT. For any compression ratio, a suited frequency modulation function (in radians) can be obtained as a weighted sum of the *non-linear tangent* FM term and the LFM one, hence the name Hybrid-NLFM, [22, 23]:

[2]Part of the results on HNLFM have been funded by Selex-ES (now, Leonardo Company) under the research contract COLB/CTR/2013/20/A.

$$\phi'(t) = \pi B\left\{\alpha \frac{1}{tg(\gamma)}\, tg\left(\frac{2\gamma B}{T}\right) + (1-\alpha)\frac{2t}{T}\right\} \tag{7}$$

where $\alpha \in (0,1)$ is the weight, B the sweep frequency interval, γ the non-linear tangent FM rate, and $t \in \left[\frac{-T}{2}, +\frac{T}{2}\right]$ with T denoting the pulse-width. If $s(t)$ is a signal with a Gaussian spectrum $|S(\omega_t)|^2 = \exp\left(\frac{-\omega_t^2}{B^2}\right)$, we may use the optimized values of α and γ, that is, those values that reach the optimum *PSLR*, maximizing the transmission efficiency $\frac{1}{T}\int_{-T/2}^{+T/2} a^2(t)dt$. **Figure 6** shows the resulting normalized amplitude weighting whose loss (with respect to a rectangular pulse) results as low as 0.58 *dB* only. **Figure 7** shows a zoom around $a(t)=1$ of **Figure 6** evidentiating its amplitude ripples of the order of 10^{-3}. In **Figure 8**, the corresponding frequency modulation is shown. **Figure 9** shows the *PSLR* of the matched filter output for this optimized type of waveform (solid line circles). A dramatic improvement with respect to the Millet waveform is clearly seen.

As usual, with *BT* decreasing, the approximation due to the principle of the stationary phase becomes worse causing an increase in the *PSLR*. However, with $BT = 64$, the *PSLR* (-51 *dB*) is

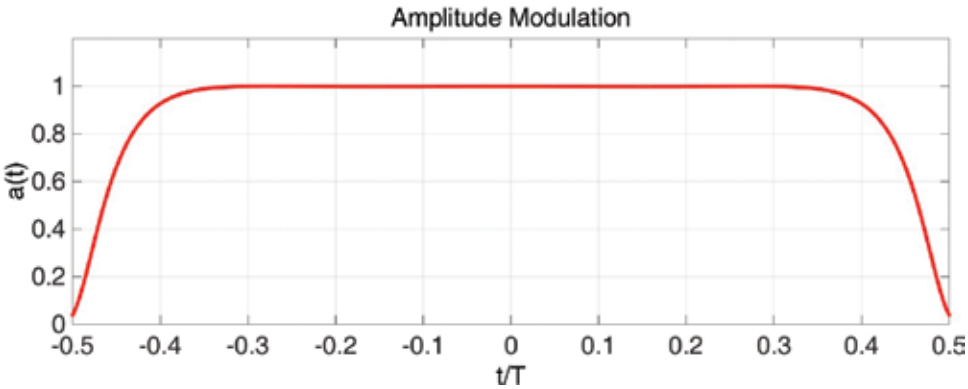

Figure 6. Optimum amplitude modulation for the HNLFM signal.

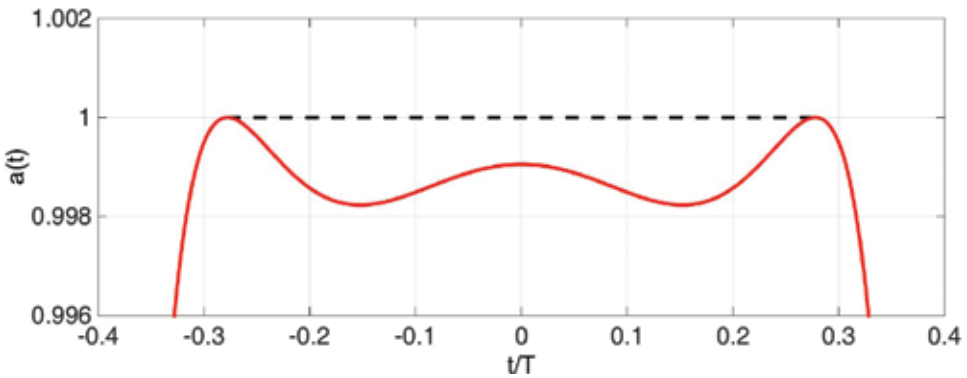

Figure 7. Optimum amplitude modulation for the HNLFM signal, zoom near the unit (solid line).

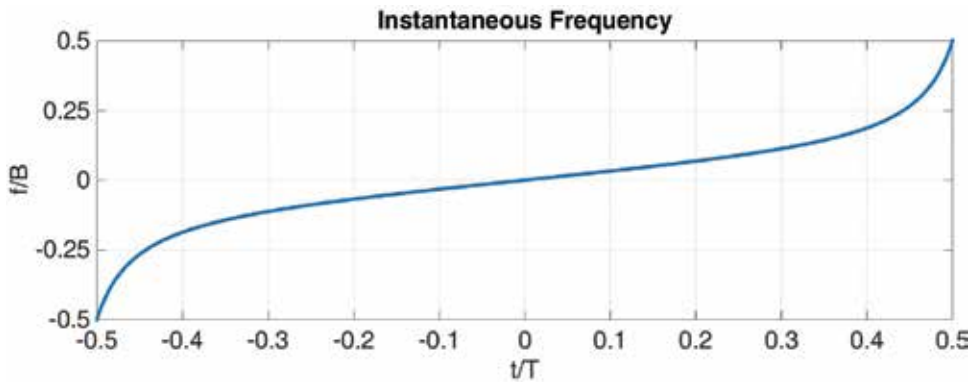

Figure 8. Instantaneous frequency of the HNLFM signal.

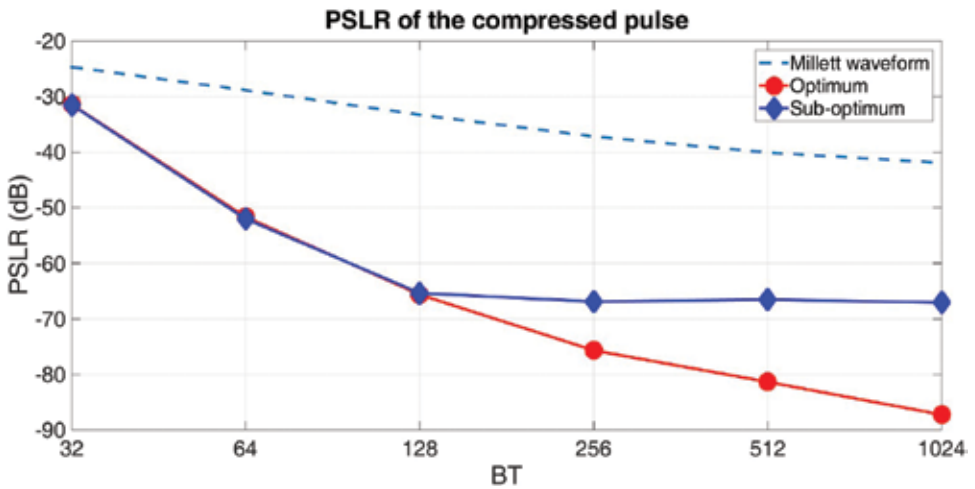

Figure 9. PSLR versus the compression ratio (BT) for HNLFM.

still compatible with many applications and for $BT = 256$ the PSL is -75 *dB*, suited to most applications. These excellent results (solid line circles in **Figure 9**) are possible *if and only if* the amplitude weighting is strictly the one shown in **Figure 7** (continuous line) and the frequency modulation is the one of **Figure 8**. In practice, it may be hard to practically implement these requirements on $a(t)$, with ripples of the order of 1 over 1000. It is preferable that the amplitude of the transmitted signal should be kept constant (with the power amplifier working in saturation at least in the central part of the pulse). However, this choice leads to increasing the *PSLR* by 25–30 *dB*. An improvement can be obtained using a sub-optimum waveform where the ripples shown in **Figure 7** are removed imposing a constant value (unit value), see the dashed line in **Figure 7**. The corresponding *PSLR* results in only 10–20 *dB* greater than the optimized signal when $BT \geq 256$ (diamonds in **Figure 9**).

To evaluate the effect due to the radial velocity v_r, supposing $v_r = 250$ *m/s* (900 *km/h*, i.e., 500 *knots*, reasonable limit reached by a civil aircraft) and a compression ratio of 256, in the L or S band, the effect due to Doppler on the output from the matched filter is very limited, particularly on the *PSLR*. Finally, to evaluate the effect of the analog-to-digital conversion, we considered as an input to the waveform generator a digital sequence coded with n bits. In reception, the coefficients of the matched filter are coded with the same number of bits. Varying n (8, 10, 12), as one could expect, a *PSLR* better than -60 *dB* calls for a 10 *bit* quantization, while with 12 bits it is possible to stay very close to the theoretical limit. Using commercial components, the matched filter coefficients are typically quantized at 16 bits, while for the data (I/Q after ADC), 12 bits seem appropriate. So, the quantization should not increase the sidelobes by a significant amount. The good performance of the HNLFM to get very low sidelobes of the compressed pulse, and also for low *BT*, is strictly dependent on the ability of the signal generation and amplification chain, including the RF power amplifier, to faithfully reproduce the amplitude modulation of **Figures 6** and **7**, calling for highly linear A-class amplifiers. Moreover, the available bandwidth is not fully exploited because of the particular frequency law of Eq. (7), which is the main law responsible for the low sidelobe level.

4. Orthogonal waveforms

In MIMO applications [13], M different waveforms (codes) are typically required, where M is the number of the transmit elements. In reception, the orthogonal property of the M transmitted waveforms permits their separation. Neglecting the polarization aspects, orthogonality may be imposed in the *time domain*, in *frequency domain,* or in *signal space*. In most radar applications, obtaining the orthogonality in the signal space is the best choice to avoid potential performance degradation due to the loss of coherence of the target response [24]. Good candidates to design deterministic signals that satisfy the orthogonality requirements are the well-known *"up"* and *"down"* chirp (LFM and NLFM) [14], but in this case, only one pair of signals can be defined. To obtain M pairs (with $M > 1$) of signals, the Costas codes represent a possible solution [25]. Alltop sequences [26] and OFDM signals [27] also can be considered. The main limitation of the OFDM approach is due to the non-constant envelope of the signals, that is, MEPPR <1, meaning that the transmitter does not work at its maximum power.

Another class of waveforms is the *non-deterministic* signals (*random* signal or *noisy waveforms*). Among these, the class of random *phase signals* (with constant amplitude [28], see paragraph 5.1) has two main advantages as compared to the signals introduced before. The former is the possibility to generate a large enough number of orthogonal signals, which is of great importance in MIMO radar systems. The latter is about the detectability; in fact, they are random signals so they place limitations on the detection, the identification, and the eventual spoofing of the signal, an element of great importance in many military applications which require low detectability of the radar system. Finally, the crest factor reaches unity. The random signals, such as the noise waveforms, will be described in Section 5.

4.1. Comparison among orthogonal waveforms

4.2. Up and down LFM and NLFM

For *up* and *down* LFM the amplitude of the cross-correlation has been evaluated in [29]:

$$|r_{12}(t)| = 2\left|\mathcal{F}\left(\sqrt{BT}\left(1-\frac{|t|}{T}\right)\right)\right| \qquad -T < t < +T \tag{8}$$

where $F(\cdot)$ is the *Fresnel Integral* in a complex form: $F(z) = \int_0^z \exp\left(j\frac{\pi}{2}y^2\right)dy$. For the *up* and *down* NLFM, the evaluation of the cross-correlation leads to very complicated expressions and its values are better derived by simulation. **Figure 10** reports the normalized cross-correlation versus the compression ratio BT for LFM and NLFM, the latter obtained supposing a Hamming weighting. The performance limitation due to the compression ratio is clearly shown.

4.3. Costas codes

A Costas code [25], see **Figure 11**, can be obtained dividing the time-frequency plane in M sub-elements (chips) of equal duration t_b and band $\Delta f = 1/t_b$.

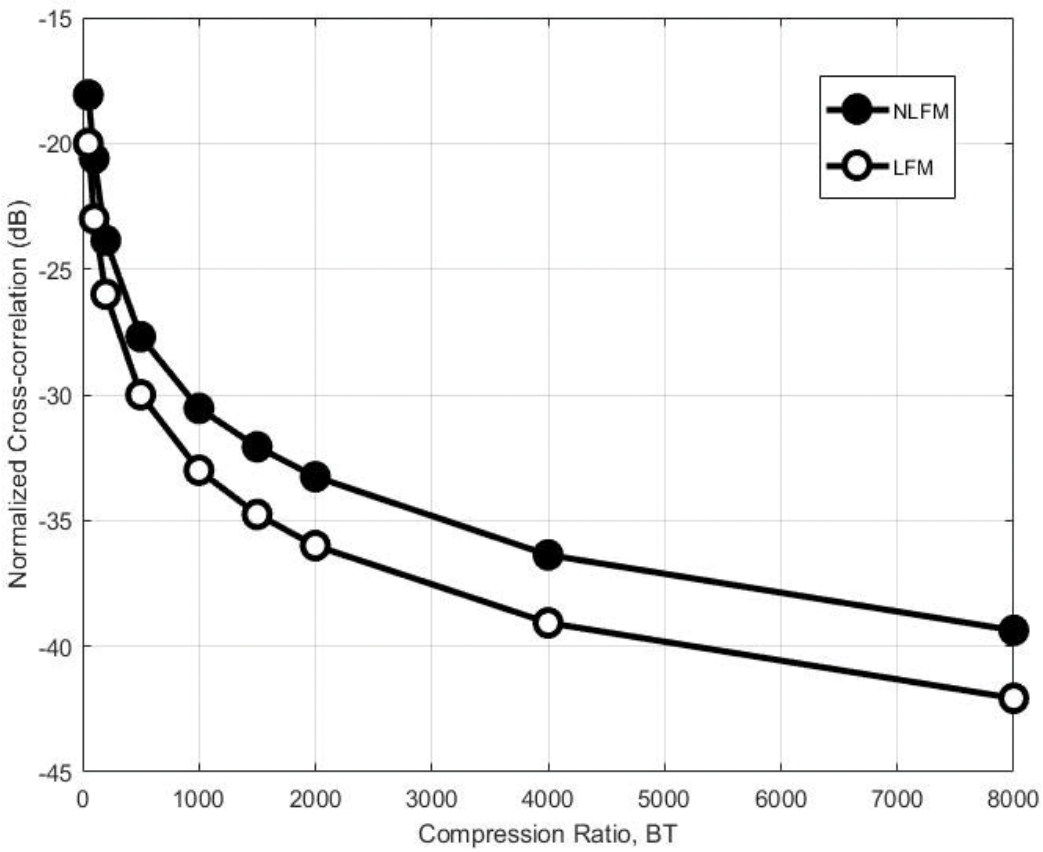

Figure 10. Cross-correlation versus the compression ratio (BT) for LFM and NLFM signals.

http://dx.doi.org/10.5772/intechopen.71549

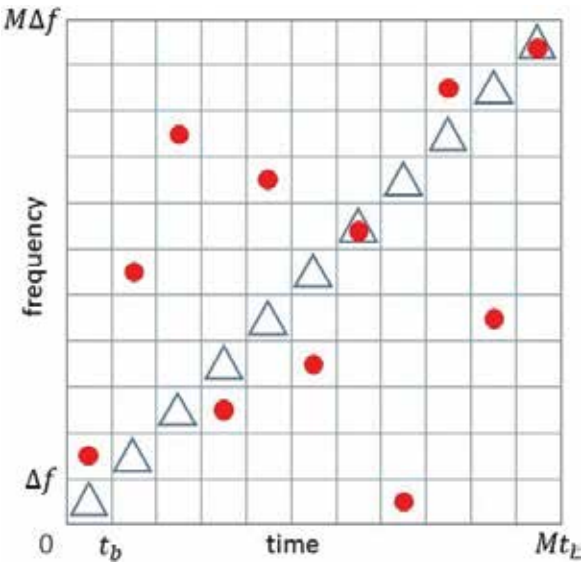

Figure 11. Circles show an example of Costas code with M = 11, hopping sequence: {2, 6, 9, 3, 8, 4, 7, 1, 10, 5, 11}. Triangles show the time-frequency relationship for a discretized Linear FM signal with the same duration and bandwidth.

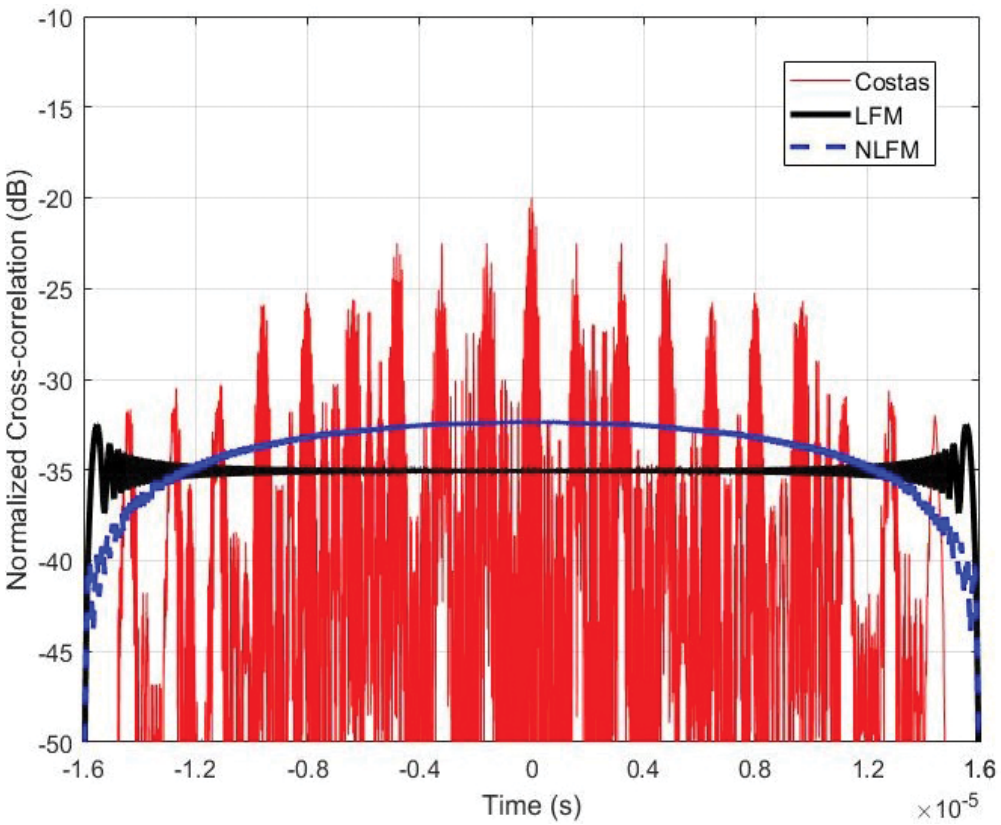

Figure 12. Normalized cross-correlation of a pair of Costas codes ($BT = 1600$) compared with the ones of LFM and NLFM *up* and *down* signals.

The complex envelope of a Costas signal of length $T = Mt_b$ (M integer) is:

$$s(t) = \frac{1}{\sqrt{M}t_b} \sum_{m=1}^{M} \exp\left(j2\pi f_m t\right) rect_b\left[t - (m-1)t_b + \frac{T}{2}\right] \tag{9}$$

where t_b is the chip time and $f_m = a_m \Delta f$, where $m = 1, 2, \ldots, M$ is the carrier frequency of the chip m, $a = [a_1, a_2, \ldots, a_M]$ is the sequence of distinct integers between 1 and M defining the particular code (*hopping sequence*) and $rect_b(t)$ is equal to 1 for $0 \le t < t_b$ and 0 elsewhere. The bandwidth is $B = M \cdot \Delta f$ and the resulting compression ratio is M^2. The typical *PSLR* is the same as a linear discrete chirp with the same number of elements M.

A modified Costas signal has been introduced to decrease the sidelobes of the AF at *zero* Doppler as reported in Ref. [30]. **Figure 12** shows the normalized cross-correlation for a pair of Costas codes compared with *up* and *down* LFM and NLFM with the same *BT*, that is, 1600.

5. Random waveforms: Noise radar technology

Noise radar technology (NRT) [15, 31–35] makes use of *pseudo-random* waveforms that are realizations of a Gaussian band-limited random process or transformations of it. These *"pure noise"* realizations, once generated and stored, are not strictly random anymore as they act as deterministic signals with known *PSLR*, *Range* resolution and ambiguity function. The number of different possible realizations to be used is theoretically unlimited (modern pseudo-random numbers generator can reach a period of 2^{1492} [36], as implemented in the MATLAB generator: practically infinity), so that each radar can operate with its own signal, possibly different from the others. For a pure noise waveform, the *PLSR* value does not strongly depend on the amplitude modulation but, rather, on the time-bandwidth product *BT*. The bandwidth being limited by the application context (e.g., about 50 and 200 *MHz* as a maximum, for a marine radar), *BT* may be increased at will by selecting a continuous wave (CW) architecture instead of the pulsed one, keeping unchanged the compression processing (computation of the correlation or of the ambiguity function) at the receiver side. The power can be significantly lowered with respect to an equal-performance pulse radar architecture. Considering a typical maximum *Range* of 150 *km* (80 *NM*) with a *Range* resolution of 150 *m*, a comparison between pulsed HNLFM and CW noise radar can be done while keeping the transmitted energy constant. For this purpose, let us consider the sub-optimal HNLFM (see **Figures 6** and **7**) since the power loss with respect to the optimal amplitude modulation is only 0.58 *dB*. In a CW architecture, the maximum delay due to *Range* is generally set as *one-fourth* of the wave repetition time (WRT), which corresponds to the signal time duration if we neglect the data processing time between consecutive sweeps. Then imposing $\frac{WRT}{4} = \frac{2 \cdot R_{max}}{c}$, for $R_{max} = 150$ *km*, it is required that $WRT = 4000$ μs. Knowing the time duration of the noise signal (WRT_{noise}) and the HNLFM pulse width (T_{HNLFM}), the relationship between the needed peak powers can be evaluated as: $P_{noise} = P_{HNLFM} \cdot \frac{T_{HNLFM}}{WRT_{noise}}$ where P_{noise} and P_{HNLFM} are, respectively, the peak power of CW noise and pulsed radar. With $WRT_{noise} = 4000$ μs and $T_{HNLFM} = 128$ μs, it results as: $P_{noise} = 0.032 \cdot$

P_{HNLFM}. Then, the required power for a CW noise radar is about 15 *dB* lower than the peak power required for a pulsed radar, keeping unchanged the maximum *Range*. Lowering the transmitted power means less solid-state modules and a straightforward RF power production/generation design.

5.1. Unimodular noisy signals

Theoretically a unimodular noisy signal shows a complex envelope with constant amplitude and with a phase $\phi(t)$ being a *zero-mean* Gaussian process with *root mean square (RMS)* σ and density spectrum within the band b. In [28], it has been shown that the normalized autocorrelation function of these signals can be written in a closed-form expression as:

$$R(\tau) = \exp\left\{-\sigma^2\left[1 - \rho(\tau)\right]\right\} \tag{10}$$

where $\rho(\tau)$ is the correlation coefficient of $\phi(t)$. $R(\tau)$ depends on the bandwidth b, on the pulse length T and on the phase fluctuation σ. The bandwidth b is related to the width of the main peak, that is, it determines the *Range* resolution. An increase of T, and consequently of the compression ratio, causes a reduction of the *Range* sidelobe level, whereas the mainlobe width remains fixed, being independent of T. Finally, σ has two different effects. The former is on the sidelobe level: an increase of σ causes a decrease of the sidelobe level and an improvement of the *PSLR*. The latter concerns the resolution. In fact, σ establishes a connection between the bandwidth of the modulated signal and the bandwidth of the modulating signal $\phi(t)$. In more detail, when σ increases, the final bandwidth increases too. As a consequence, a large value of σ gives an improved resolution. In [28], a simple relation between the *RMS* bandwidth of the phase modulated signal (B_{rms}) and the *RMS* bandwidth of the phase modulating noise (b_{rms}) has been found as $B_{rms} = \sigma \cdot b_{rms}$. For the sidelobe suppression, the expression of the autocorrelation function Eq. (10) would show a continuous improvement of the sidelobe suppression as σ increases. Unfortunately, this is not true: the periodic nature of the phase $\phi(t)$ with a folding in the $[-\pi, +\pi]$ interval has been neglected in [28], and in reality, the model can be used only for values of σ much smaller than π.

Considering realistic and correct simulations aimed at a potential application, the best approach generates the signal through a white Gaussian process with its *in-phase* and *quadrature* components (I, Q) that are band limited as desired. The procedure to generate M independent pure noise unimodular band-limited signals is shown in **Figure 13**. The (I, Q) samples, that have to be filtered by the frequency window $H(f)$, are $\{x_i\}_{i=1}^{N}$ where N is the number of generated samples and x_i is the i^{th} complex (I, Q) sample.

After the frequency domain windowing, the signal amplitude is saturated to the maximum value through a Zero-Memory-Non-Linear (ZMNL) transformation, while the phase is kept unchanged. Since the (I, Q) samples come from a random process, at each run the algorithm provides different realizations having the same average performances in terms of *PSLR* and cross-correlation level, while the *Range* resolution only depends on the used $H(f)$. Unimodular band-limited (with a rectangular window) pure noise shows a *Range* resolution similar to the

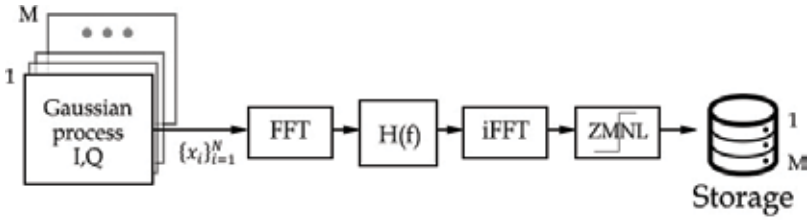

Figure 13. Scheme to generate M independent pure noise unimodular band-limited signals.

LFM with the same band, and the secondary lobes are slightly fluctuating (the *PSLR* is comparable to the LFM). For the far lobes, the *PSLR* is empirically related to the *BT* by:

$$PSLR_{dB} = -10 \cdot log_{10}(BT) + k \tag{11}$$

with k of the order of 10–13 *dB*, which corresponds to -23 *dB* for $BT = 4000$.

The cross-correlation level between two independently generated pure noise signals is of the same level as the autocorrelation sidelobes, excluding the central zone. This fact calls for sidelobe-suppression methods. Sidelobe suppression of both the autocorrelation and cross-correlation function of a set of M waveforms (with $M > 1$ and of the order of a few units or a few tens) is a relevant problem in a MIMO radar, whose receivers have to discriminate, after each matched filter, the *mth* signal among the others. So, M *"orthogonal"* waveforms are required [13] for MIMO radar and for space-time coding or *"colored"* transmission [16].

5.2. Range sidelobe suppression algorithms

Many approaches have been used in the past years to cope with the *Range* sidelobe problem, starting from the time (or frequency) weighting of the received signal. Algorithms are available to generate signals with suitable autocorrelation characteristics without the need for sidelobe suppression in reception. However, using the generation algorithms, significant complexity is demanded to the generation side in terms of computational burden to achieve a "useful" waveform. In any case, this issue can be trivially overcome by offline methods, generating a large enough set of noisy waveforms ready to be transmitted and stored in mass memory.

A first method to reduce the sidelobes of the unimodular noisy signals uses an iterative procedure based on alternative projections in the frequency and in time domain [15]. Using this approach, if the compression ratio is greater than 5000 the mean *PSLR* reaches -30 *dB*, however it remains limited to -36 *dB* for $BT = 30{,}000$. Regarding the cross-correlation of a pair of noise signals, it is comparable with the ones of the LFM and NLFM.

A second approach, starting from a random process realization (**Figure 13**), runs in order to minimize a certain objective function with defined constraints. In this case, the objective function is the *PSLR* and the constraints are the limited bandwidth and the unity amplitude needed to fully exploit the amplifier. Often, due to convergence considerations, the *ISLR* is

minimized instead of the *PSLR* because the former is an integrated value over all the sidelobes region while the latter is only a local value that can rapidly change point by point.

A powerful sidelobe suppression algorithm family, Cyclic Algorithm New (CAN), described in [17] provides several interesting ways to approach the suppression problem. To suit to particular needs, the *Radarlab* group in Tor Vergata University developed a new algorithm to generate noisy waveforms having a limited bandwidth and a unimodular amplitude, with the possibility to tune the suppressed zone length depending on the particular application [37].

The main idea is to minimize the difference between the obtained and the desired autocorrelation functions through a process that runs cyclically until a stop criterion is satisfied, for example, the difference between two consecutive steps is less than a given threshold. The constraints to be satisfied within this minimization lead to different algorithms belonging to the wide CAN family. These constraints can be the unit amplitude, the number of suppressed sidelobes, as well as the mainlobe width (i.e., the required bandwidth) or others.

For this purpose, the CAN family also provides a MIMO version for the algorithms in which the quantity to be minimized is the difference between the obtained and the desired covariance matrix. The main drawback of the CAN algorithms is their inability to manage the bandwidth increase, as the mainlobe of the signal generated by using the CAN algorithm is very narrow. In fact, these algorithms converge to a deep sidelobe suppression at the expense of a full-Nyquist occupied bandwidth, which unfortunately is not suitable for applications in which spectrum regulations must be met. Only one CAN algorithm (named SCAN, Stopband-CAN) is able to manage the spectrum constraint. If the SCAN is applied to generate noise unimodular signals with $BT = 4096$ and $B = 1\ MHz$, the related aperiodic autocorrelation is shown in **Figure 14**.

Keeping BT unchanged, the SCAN algorithm improves the *PSLR* by about 20 dB with respect to the unimodular noise from which the algorithm starts. The mainlobe is kept wide since the SCAN spectrum is well shaped within the required 1 MHz bandwidth. The drawback of the SCAN algorithm is that the sidelobes close to the mainlobe are still quite high. To overcome

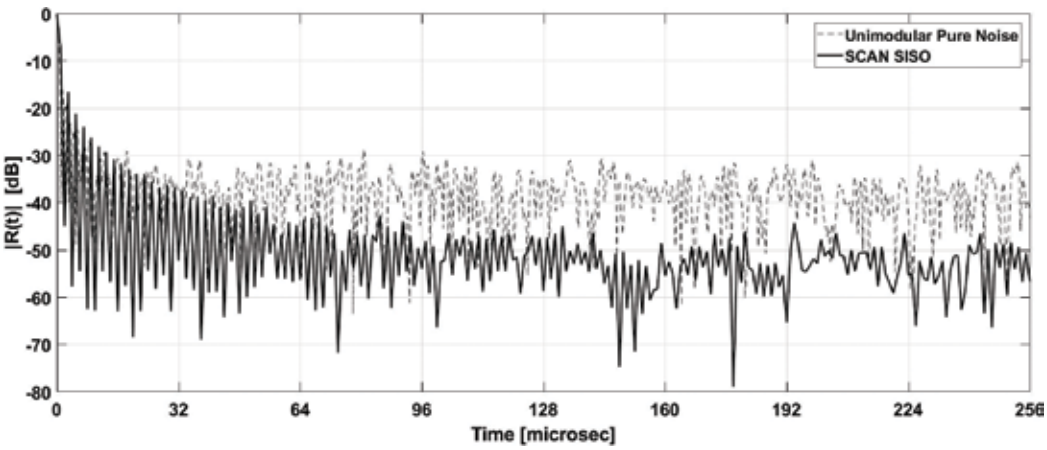

Figure 14. Unimodular noise compressed pulse: SCAN. $B = 1\ MHz$ and $T = 4096\ \mu s$.

the issue, our group has developed the Band Limited Algorithm for Sidelobes Attenuation (BLASA) algorithm [37] whose typical result is shown in **Figure 15**. It comes from the CAN idea and provides very low sidelobes even in the area close to the mainlobe. It is called Single Input, Single Output (SISO) because a single waveform is generated at each run. The BLASA SISO spectrum is still well shaped within the allowed 1 *MHz* bandwidth, providing a *Range* resolution of 150 *m*.

Being a SISO algorithm, BLASA does not lower the cross-correlation level between two independently generated waveforms. Hence, their cross-correlation is at the same level as the initial unimodular pure noise.

As in the CAN family, even for the BLASA SISO, a MIMO version exists [37] which is able to jointly generate a number *M* of waveforms at each run, that is, *M* signals belonging to the same set. The BLASA MIMO is developed to manage the suppression of both auto and cross-correlation functions, still keeping the bandwidth limited. Due to the limited number of samples that BLASA MIMO can manipulate, the joint suppression region in cross and auto-correlations cannot be as long as the whole length of the pulse. The length of the suppressed zone depends on the number *M* of waveforms in the generated set: the lower *M*, the longer the suppressed length. Moreover, the suppressed zone length depends on the amplitude constraint: it increases if amplitude modulation is allowed while it decreases if the unimodular constraint is applied. Hereafter, only the unimodular case will be considered. The limited length of the suppressed zone represents a valid tool to mitigate the clutter effect, especially near the mainlobe, that is, the target's closest *Range* cells. Because of the narrow -3 *dB* bandwidth, the mainlobe is four times wider than the expected 150 *m*, which corresponds to a 1 *MHz* bandwidth. Nevertheless, this behavior is deterministic and can be overcome by choosing properly the signals' occupied bandwidth. The big advantage of the BLASA MIMO pseudorandom signals with respect to the deterministic HNLFM is the possibility to average coherently the *Range* sidelobes in the *Azimuth*. In fact, if the transmitted waveform changes each Waveform Repetition Time within the dwell time, the averaged compressed pulse presents a sidelobe level reduced by the quantity: $\Delta SL = 10 \cdot log_{10}(L)$ where ΔSL is the lowering in

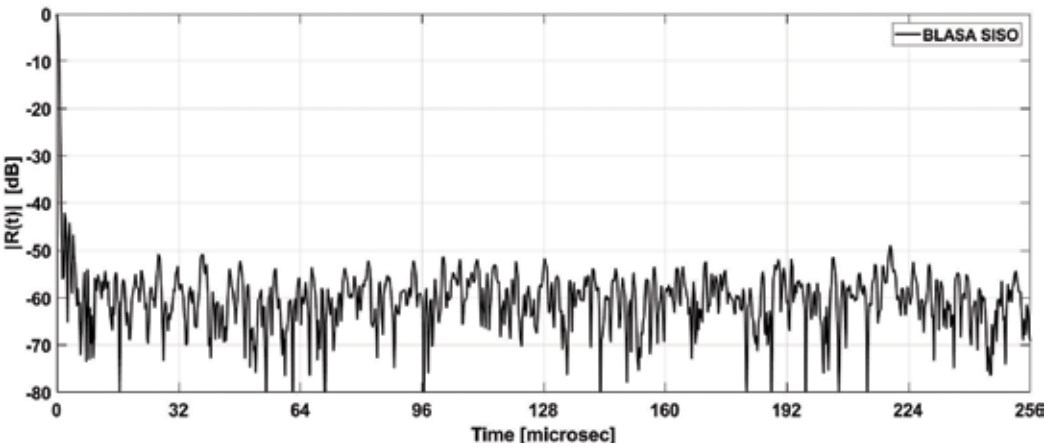

Figure 15. Unimodular noise compressed pulse: BLASA. $B = 1$ *MHz* and $T = 4096$ μs.

Algorithm	MIMO version	Sidelobe level and suppression interval	$\frac{B_{TOT}}{B_{-3dB}}$	Amplitude modulation
HNLFM	No	$-67\ dB$ at $BT = 4096$	400%	Pseudo trapezoidal AM
Unimodular Noise	No	$-23\ dB$ at $BT = 4096$	100%	Unimodular
SCAN	No	$-45\ dB$ at $BT = 4096$ (within 15%)	100%	Unimodular
BLASA SISO	No	$-50\ dB$ at $BT = 4096$	100%	Unimodular
BLASA MIMO	Yes	$-30\ dB$ at $BT = 256$ (within 12%), unimodular amplitude with $M = 2$	400%	Unimodular

Table 1. Comparison of algorithms.

the sidelobe level with respect to the not-averaged case and L is the number of coherently integrated returns.

Summing up all the considered waveforms, **Table 1** shows their comparison. Each algorithm is checked to verify whether it allows a MIMO version, the level of the sidelobes, the frequency occupancy, and its capability to be coherently integrated.

The column "MIMO version" refers to the capability of jointly generated M waveforms with a cross-correlation level comparable to the auto-correlation level. The frequency occupancy $\frac{B_{TOT}}{B_{-3dB}}$ gives the information of how much the mainlobe is enlarged by the algorithm.

6. Conclusions

Waveform design is a critical component in the design of an effective and efficient radar system. Various types of radar signals have been proposed and analyzed for over half a century, resulting in extensive literature on the subject matter. This chapter, after an overview of the various proposed waveforms, examined in more detail two particular classes of radar signals, that is a deterministic and a random one. The former is based on non-linear frequency modulation of the radar pulse, which, with a suited amplitude modulation added, can reach extremely low-*Range* sidelobes in the absence of Doppler shift. The latter class is used in the novel *noise radar technology,* still at research stage, where a suited tailoring of the noisy waveforms grants a fairly low sidelobe level. Pro and cons of both approaches are also discussed.

Author details

Gaspare Galati[1,2]* and Gabriele Pavan[1,2]

*Address all correspondence to: gaspare.galati@uniroma2.it

1 Tor Vergata University, Department of Electronic Engineering, Rome, Italy

2 CNIT, Interuniversity Consortium for Telecommunications, Italy

References

[1] Skolnik M.I. Introduction to Radar Systems. 3rd ed. New York: McGraw-Hill Education; 2015

[2] Nathanson F.E., Reilly J.P., Cohen M.N. Radar Design Principles: Signal Processing and the Environment. Mendham, New Jersey: Scitech Pub; 1999

[3] Turin G.L. An introduction to matched filters. IRE Transactions on Information Theory. 1960;**6**(3):311-329. DOI: 10.1109/TIT.1960.1057571

[4] North D.O. An analysis of the factors which determine signal/noise discrimination in pulsed carrier systems. Proceedings of the IEEE. 1963;**51**(7):1016-1027. DOI: 10.1109/PROC.1963.2383

[5] Galati G. 100 Years of Radar. 1st ed. Springer International Publishing; 2016. DOI: 10.1007/978-3-319-00584-3

[6] Galati G., van Genderen P. Special section on some less-well-known contributions to the development of radar: From its early conception until just after the second world war. The Radio Science Bulletin. 2016;**358**:12–108

[7] Barker R.H. Group synchronizing of binary digital systems. Communication Theory. London: Butterworth Sci. Pub; 1953:273-287

[8] Klauder J.R., Price A.C., Darlington S., Albefsheim W.J. The theory and design of chirp radars. Bell System Technical Journal. 1960;**39**:745-808

[9] Cook C.E., Bernfeld M. Radar Signals—An Introduction to Theory and Application. Norwood, MA, USA: Artech House; 1993

[10] Pioneer Award IEEE Trans. Aerospace and Electronic Systems. 2010;**46**:2139-2141

[11] Yanovsky F. Radar development in Ukraine. In: International Radar Symposium (IRS 2014); 16–18 June 2014; Gdansk, Poland; 2014. DOI: 10.1109/IRS.2014.6869179

[12] Woodward P.M. Probability and Information Theory with Applications to Radar. London: Pergamon Press; 1953

[13] Li J., Stoica P. MIMO Radar Signal Processing. Wiley/IEEE Press; 2008

[14] Galati G., Pavan G. Orthogonal and complementary radar signals for multichannel applications. In: EuRad 2011; 12–14 October 2011; Manchester (UK). 2011. pp. 178–181

[15] Galati G., Pavan G. On the Design of Waveforms for noise-MIMO radar. In: Noise Radar Technology, NRT-2012; 27-29 September 2012; Yalta, Crimea (Ukraine). 2012. p. 1–7

[16] Barbur G., Aubry P., Le Chevalier F. Space-time radar waveforms: Circulating codes. Hindawi Journal of Electrical and Computer Engineering. 2013. DOI: 10.1155/2013/809691

[17] He H., Li J., Stoica P. Waveform Design for Active Sensing Systems—A Computational Approach. Cambridge University Press; 2012

[18] Levanon N., Mozeson E. Radar Signals. Hoboken, NJ, USA: John Wiley & Sons; 2004

[19] Millett R.E. A matched-filter pulse-compression system using a nonlinear FM waveform. IEEE Transactions on Aerospace and Electronic Systems. 1970;**AES-6**:73-77

[20] Davenport W.B., Root W.L. An Introduction to the Theory of Random Signals and Noise. Wiley-Interscience; 1987

[21] Nuttall H.A. Some windows with very good sidelobe behavior. IEEE Transactions on Acoustics, Speech, and Signal Processing. 1981;**ASSP-29**(1):84-91

[22] Collins T., Atkins P. Nonlinear frequency modulation chirps for active sonar. IEE Proceedings Radar, Sonar and Navigation. 1999;**146**:312-316

[23] Zhiqiang G., Peikang H., Weining L. Matched NLFM pulse compression method with ultra-low sidelobes. In: 5th European Radar Conference; 30–31 October 2008; Amsterdam, The Netherlands. 2008. pp. 92–95

[24] Galati G., Pavan G. Range sidelobes suppression in pulse-compression radar using Golay pairs: Some basic limitations for complex targets. IEEE Transactions on Aerospace and Electronic Systems. 2012;**48**(3):2756-2760

[25] Costas J.P. A study of a class of detection waveforms having nearly ideal range-Doppler ambiguity properties. Proceedings of the IEEE. 1984;**72**(8):996-1009

[26] Alltop W.O. Complex sequences with low periodic correlations. IEEE Transactions on Information Theory. 1980;**IT-26**(3):350-354

[27] Krasnov O.A., Wang Z., Tigrek R.F., van Genderen P. OFDM waveforms for a fully polarimetric weather radar. In: ESAV'11; 12-14 September 2011; Capri (Italy). 2011. pp. 69–75

[28] Axelsson R.J. Noise radar using random phase and frequency modulation. IEEE Transactions on Geoscience and Remote Sensing. 2004;**42**(11):2370-2384

[29] Galati G., Pavan G. Waveform radar design using orthogonal and complementary codes. Prace Przemysłowego Instytutu Telekomunikacji. 2010;**145**:28-44

[30] Levanon N., Mozeson E. Modified Costas signal. IEEE Transactions on Aerospace and Electronic System. 2004;**40**(3):946-953

[31] Stove A., Galati G., Pavan G., De Palo F., Lukin K., Kulpa K., Kulpa J.S., Maślikowski Ł. The NATO SET-184 noise radar trials 2016. In: 17th International Radar Symposium; 10–12 May 2016; Krakow (Poland). 2016. DOI: 10.1109/IRS.2016.7497327

[32] Galati G. Coherent Radar. Patent PCT/IC2014/061454 ed. 15 May 2014

[33] Galati G., Pavan G., De Palo F., Stove A. Potential applications of noise radar technology and related waveform diversity. In: 17th International Radar Symposium. 10–12 May 2016; Krakow (Poland). 2016. DOI: 10.1109/IRS.2016.7497329

[34] Stove A., Galati G., De Palo F., Wasserzier C., Erdogan Y.A., Kubilay S., Lukin K. Design of a Noise Radar Demonstrator. In: 17th International Radar Symposium; 10–12 May 2016; Krakow (Poland). 2016. DOI: 10.1109/IRS.2016.7497328

[35] Kulpa K. Signal Processing in Noise Waveform Radar. Norwood, MA, USA: Artech House; 2013. ISBN 9781608076611.

[36] Marsaglia G., Tsang W.W. The ziggurat method for generating random variables. Journal of Statistical Software. 2000. DOI: 10.18637/jss.v005.i08

[37] De Palo F. Noise Radar Technology–Waveforms, Architectures, Application Cases [Dissertation]. Rome: Tor Vergata University; 2017. ISBN 978-88-90348259

Chapter 2

Space-Time Transmit-Receive Design for Colocated MIMO Radar

Guolong Cui, Xianxiang Yu and Lingjiang Kong

Additional information is available at the end of the chapter

http://dx.doi.org/10.5772/intechopen.71946

Abstract

This chapter deals with the design of multiple input multiple-output (MIMO) radar space-time transmit code (STTC) and space-time receive filter (STRF) to enhance moving targets detection in the presence of signal-dependent interferences, where we assume that some knowledge of target and clutter statistics are available for MIMO radar system according to a cognitive paradigm by using a site-specific (possible dynamic) environment database. Thus, an iterative sequential optimization algorithm with ensuring the convergence is proposed to maximize the signal to interference plus noise ratio (SINR) under the similarity and constant modulus constraints on the probing waveform. In particular, each iteration of the proposed algorithm requires to solve the hidden convex problems. The computational complexity is linear with the number of iterations and polynomial with the sizes of the STTW and the STRF. Finally, the gain and the computation time of the proposed algorithm also compared with the available methods are evaluated.

Keywords: multiple input multiple output (MIMO), space-time transmit code (STTC), space-time receive filter (STRF), signal-dependent interferences, signal to interference plus noise ratio (SINR)

1. Introduction

Multiple-input multiple-output (MIMO) radar emits multiple probing signals via its transmit antennas, which provides the greater flexibility for the design of the whole radar system, and boosts the development of more sophisticated signal processing algorithms [1]. On the basis of the configurations of transmitter/receiver antennas, MIMO radar systems can be classified into two categories: widely distributed [2, 3] and colocated [4, 5]. The former has different angles of view on the target owing to widely separated antennas, and this feature can be used to improve the performance of target detection and angle estimation, as well as the capabilities of target

identification and classification [6]. The latter shares the same aspect angle of the target by using tightly spaced antennas. However, colocated MIMO radar exploits the waveform diversity to form a long virtual array, thus providing better results concerning spatial resolution, target localization, and the interference rejection, as well as obtaining the degrees of freedom for the design of transmit beam pattern [1, 7, 8].

Recently, colocated MIMO radar waveform design is a hot and challenging topic and has received significant attention. In general, these works can be divided into two categories. The first category focuses on the fast-time waveforms design exploiting some a priori information. In particular, in [6], by using the a priori knowledge of target power spectral density, the minimax robust waveforms are designed based on the rules of the mutual information (MI) and minimum mean-square error (MMSE). In [9], MIMO waveforms for the case of an extended target are devised based on the maximization of signal-to-interference plus-noise ratio (SINR) through a gradient-based algorithm assuming the knowledge of both the target and signal-dependent clutter statistics. In [10], by considering MMSE as figure of merit, MIMO radar waveforms are synthesized under signal-dependent clutter. The join design of the transmit waveform and the receive filter is addressed for improving the extended target delectability in the presence of signal-dependent clutter, by employing a cycle iteration algorithm with ensuring convergence [11]. In [12], by designing the transmit waveform and the receive filter, two sequential optimization algorithms are proposed to maximize SINR subject to the constant modulus and similarity constraints. Based on the rule of the worst-case output SINR in the presence of unknown target angle, the robust joint design of transmit waveform and the receive filter is considered [13]. Some more works can be found in [7, 8, 14, 15].

The second category addresses the MIMO radar space-(slow) time code design for moving target scenarios. In particular, in [16], MIMO radar slow-time code shares the ability of improving the resolution in angle-Doppler images and obtaining enhanced moving target detection performance. In [17], the signal-dependent interference is alleviated by the space-time coding framework based on a beamspace space-time adaptive processing (STAP). In [18], based on the max-min SINR optimization criteria, the time-division beamforming signal is designed for a multiple target scenario. For a moving point-like target detection, based on the worst case SINR over the actual and signal-dependent clutter statistics, the robust joint design of the space-time transmit code (STTC) satisfying the energy and similarity constraints and the space-time receive filter (STRF) is addressed in [19].

This chapter handles the joint design of the STTC and STRF with the aim of enhancing the moving target detectability under signal-dependent interferences and white Gaussian noise. Unlike [19, 20], some knowledge of target and clutter statistics is assumed to be available. In particular, the SINR is considered as figure of merit to maximize subject to a constant modulus constraint on the transmit signal in addition to a similarity constraint. To deal with the resulting nonconvex design problem, an iterative algorithm ensuring convergence is proposed. Each iteration of the proposed algorithm involves the solution of hidden convex problems. Specifically, both a convex problem with closed-form solution and a set of fractional programming problems, which can be globally solved through the Dinkelback's algorithm, are solved. The resulting computational complexity is linear with the number of iterations and polynomial with the sizes of the STTC and the STRF.

The remainder of the chapter is organized as follows. In Section 2, the system model is formalized. In Section 3, the constrained optimization problem under constant modulus and similarity constraints is formulated. In Section 4, the new optimization algorithm is presented. In Section 5, the performance of the new procedure is evaluated. Finally, in Section 6, concluding remarks and possible future research tracks are provided.

2. System model

We focus on a colocated narrow band MIMO radar system consisting of N_T transmitters antennas and N_R receivers. Each transmitter emits a slow-time phase-coded coherent train with K pulses. Let $s(k) = [s_1(k), s_2(k), \cdots, s_{N_T}(k)]^T \in \mathbb{C}^{N_T}$, $k = 1, 2, \cdots, K$ denote the transmitted space code vector at the kth transmission interval, where $s_{n_t}(k)$ denotes the kth transmitted phase-code pulse of the n_tth transmitting antenna, for $n_t = 1, 2, \cdots, N_T$, $(\cdot)^T$ stands for the transpose, and $\mathbb{C}^N$ is the set of N-dimensional vectors of complex numbers. At each receiver, the received waveform is downconverted to baseband, undergoes a pulse matched filtering operation, and then is sampled. Hence, the observations of the kth slow-time sample for a far-field moving target at the azimuth angle θ_0 can be expressed as [21]

$$x(k) = \alpha_0 e^{j2\pi(k-1)v_{d_0}} \mathbf{A}(\theta_0)\, s(k) + d(k) + v(k), \tag{1}$$

where

- α_0 is a complex parameter taking into account the target radar cross section (RCS), channel propagation effects, and other terms involved into the radar range equation.
- v_{d_0} denotes the normalized target Doppler frequency, which is related to the radial velocity v_r via the equation $v_{d_0} = 2v_r T/\lambda$ with λ being the carrier wavelength and T being the pulse repetition time (PRT).
- $\mathbf{A}(\theta) = a_r^*(\theta) a_t{}^\dagger(\theta)$, in which $a_t(\theta)$ and $a_r(\theta)$ denote the transmit spatial steering vector and the receive spatial steering vector at the azimuth angle θ, respectively, and $(\cdot)^*$ and $(\cdot)^\dagger$ are the conjugate and the conjugate transpose operators, respectively. In particular, for the uniform linear arrays (ULAs), they are given by

$$a_t(\theta) = \frac{1}{\sqrt{N_T}} \left[1, e^{j2\pi\frac{d_T}{\lambda}\sin\theta}, \cdots, e^{j2\pi\frac{d_T}{\lambda}(N_T-1)\sin\theta}\right]^T, \tag{2}$$

$$a_r(\theta) = \frac{1}{\sqrt{N_R}} \left[1, e^{j2\pi\frac{d_R}{\lambda}\sin\theta}, \cdots, e^{j2\pi\frac{d_R}{\lambda}(N_R-1)\sin\theta}\right]^T \tag{3}$$

with d_T and d_R being the array interelement spacing of the transmitter and the receiver, respectively.

- $d(k) \in \mathbb{C}^{N_R}, k = 1, 2, \cdots, K$, considering M signal-dependent uncorrelated point-like interfering scatterers. Specifically, as shown in **Figure 1**, the angle space is discretized as $\Theta = \{0, 1, \cdots, L\} \times \frac{2\pi}{(L+1)}$. For the mth interfering source located at the range-azimuth bin

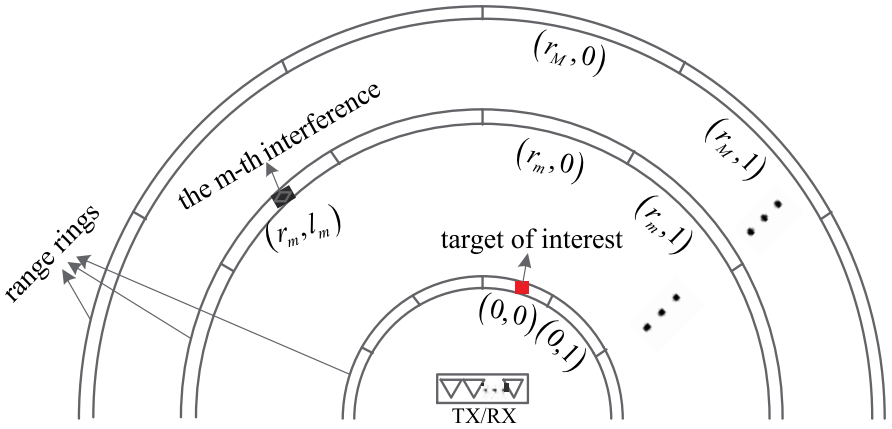

Figure 1. Range-azimuth bins (the target of interest is represented by the red (solid) circle).

(r_m, l_m), $r_m \in \{0, 1, \cdots, K-1\}$, $l_m \in \{0, 1, \cdots, L\}$, the received interfering vector $\boldsymbol{d}(k)$ can be expressed as the superposition of the returns from M interference sources, i.e.,

$$\boldsymbol{d}(k) = \sum_{m=1}^{M} \boldsymbol{\rho}_m e^{j2\pi v_{d_m}(k-1)} \mathbf{A}(\boldsymbol{\theta}_m)\, \boldsymbol{s}(k - r_m), \mathbf{0} \le r_m \le k-1, \tag{4}$$

with $\boldsymbol{\rho}_m$, v_{d_m}, and $\boldsymbol{\theta}_m$, respectively, the complex amplitude, the normalized Doppler frequency, and the look angle, given by $\boldsymbol{\theta}_m = \frac{2\pi}{(L+1)} l_m$, of the mth interferences. Furthermore, M is nominally equal to $K \times (L+1)$.

- $v(k) \in \mathbb{C}^{N_R}, k = 1, 2, \cdots, K$ denotes additive noise, modeled as independent and identically distributed (i.i.d.) complex circular zero-mean Gaussian random vector, i.e., $v(k) \sim \mathcal{CN}(\mathbf{0}, \sigma^2 \boldsymbol{I}_{N_R})$, where $\boldsymbol{I}_{N_R}$ denotes $N_R \times N_R$-dimensional identity matrix.

Let $\boldsymbol{x} = \left[\boldsymbol{x}^T(1), \cdots, \boldsymbol{x}^T(K)\right]^T$, $\boldsymbol{s} = \left[\boldsymbol{s}^T(1), \cdots, \boldsymbol{s}^T(K)\right]^T$, $\boldsymbol{d} = \left[\boldsymbol{d}^T(1), \cdots, \boldsymbol{d}^T(K)\right]^T$, and $\boldsymbol{v} = \left[\boldsymbol{v}^T(1), \cdots, \boldsymbol{v}^T(K)\right]^T$. Then, Eq. (1) can be expressed in a compact form as

$$\boldsymbol{x} = \boldsymbol{\alpha}_0 \widehat{\mathbf{A}}\left(v_{d_0}, \boldsymbol{\theta}_0\right) \boldsymbol{s} + \boldsymbol{d} + \boldsymbol{v}, \tag{5}$$

where

$$\widehat{\mathbf{A}}(v_d, \boldsymbol{\theta}_0) = \mathbf{Diag}(\boldsymbol{p}(v_d)) \otimes \mathbf{A}(\boldsymbol{\theta}_0) \tag{6}$$

with $\boldsymbol{p}(v_d) = \left[\mathbf{1}, e^{j2\pi v_d}, \cdots, e^{j2\pi(K-1)v_d}\right]^T$ being the temporal steering vector, $\otimes$ denotes the Kronecker product, and $\mathbf{Diag}(\cdot)$ denotes the diagonal matrix formed by the entries of the vector argument. Additionally, we assume that the noise vector $\boldsymbol{v}$ is a zero-mean circular complex Gaussian random vector with covariance matrix $\boldsymbol{\Sigma}_v = \mathbb{E}\left[\boldsymbol{v}\, \boldsymbol{v}^\dagger\right] = \sigma_v^2 \boldsymbol{I}_{N_R K}$. Finally, interference vector $\boldsymbol{d}$ can be expressed as

$$\boldsymbol{d} = \sum_{m=1}^{M} \boldsymbol{\rho}_m \mathbf{P}_{r_m} \widehat{\mathbf{A}}\left(v_{d_m}, \boldsymbol{\theta}_m\right) \boldsymbol{s}, \tag{7}$$

where $\mathbf{P}_{r_m}$ is given by

$$\mathbf{P}_{r_m} = \mathbf{J}^{r_m} \otimes \mathbf{I}_{N_R}, \tag{8}$$

in which $\mathbf{J}^r$ denotes the shift matrix [23], whose (k_1, k_2)th entry is defined as[1],

$$\mathbf{J}^r(k_1, k_2) = \begin{cases} 1 & k_1 - k_2 = r \\ 0 & k_1 - k_2 \neq r, \end{cases} \tag{9}$$

$r \in \{0, 1, \cdots, K-1\}$ and $(k_1, k_2) \in \{1, 2, \cdots, K\}^2$. In particular, we assume that $\boldsymbol{\rho}_m$, $m = 1, 2, \cdots, M$, and $\boldsymbol{\alpha}_0$ are a zero-mean uncorrelated random variables with, respectively, $\sigma_m^2 = \mathbb{E}\left[|\boldsymbol{\rho}_m^2|\right]$ and $\sigma_0^2 = \mathbb{E}\left[|\boldsymbol{\alpha}_0|^2\right]$. As to the normalized Doppler frequency of the interfering signals, we model v_{d_m} as a random variable uniformly distributed around a mean Doppler frequency $\overline{v}_{d_m}$, i.e.,

$$v_{d_m} \sim \boldsymbol{U}\left(\overline{v}_{d_m} - \frac{\boldsymbol{\varepsilon}_m}{2}, \overline{v}_{d_m} + \frac{\boldsymbol{\varepsilon}_m}{2}\right), m \in 1, 2, \cdots, M \tag{10}$$

where ε_m accounts for the uncertainty on v_{d_m}. Basing on the previous assumptions, the interference vector $\boldsymbol{d}$ has zero mean and covariance matrix

$$\boldsymbol{\Sigma}_d(\boldsymbol{s}) \quad = \mathbb{E}\left[\boldsymbol{d}\boldsymbol{d}^{\dagger}\right] = \sum_{m=1}^{M} (\mathbf{J}^{r_m} \otimes \mathbf{A}(\boldsymbol{\theta}_m)) \left[\left(\boldsymbol{s}\boldsymbol{s}^{\dagger}\right) \odot \boldsymbol{\Xi}_m\right] (\mathbf{J}^{r_m} \otimes \mathbf{A}(\boldsymbol{\theta}_m))^{\dagger}, \tag{11}$$

where

$$\boldsymbol{\Xi}_m = \sigma_m^2 \boldsymbol{\Phi}_{\varepsilon_m}^{\overline{v}_{d_m}} \otimes \boldsymbol{\Upsilon}_t, \tag{12}$$

in which

$$\boldsymbol{\Phi}_{\varepsilon_m}^{\overline{v}_{d_m}}(k_1, k_2) = e^{j2\pi\overline{v}_{d_m}(k_1 - k_2)} \frac{\sin\left[\pi\varepsilon_m(k_1 - k_2)\right]}{\pi\varepsilon_m(k_1 - k_2)}, \forall (k_1, k_2) \in \{1, 2, \cdots, K\}^2, \tag{13}$$

and $\boldsymbol{\Upsilon}_t = \mathbf{1}_t \mathbf{1}_t{}^T$ with $\mathbf{1_t} = [1, 1, \cdots, 1]^T$ being the $N_T \times 1$ vector, $\odot$ and $\mathbb{E}[\cdot]$ denote the Hadamard product and the statistical expectation, respectively. This expression, for the covariance matrix $\boldsymbol{\Sigma}_d(\boldsymbol{s})$, follows from the results obtained in ([19], Appendix 1).

Inspection of (11) and (12) reveals that the interference covariance matrix $\boldsymbol{\Sigma}_d(\boldsymbol{s})$ requires the knowledge of $\boldsymbol{\theta}_m$ and σ_m^2 as well as $\overline{v}_{d_m}$ and $\boldsymbol{\varepsilon}_m$, for $\boldsymbol{m} = 1, 2, \cdots, M$. These information can be obtained according to a cognitive paradigm [22–24] through exploiting a site-specific (possible dynamic) environment database, which involves a geographical information system (GIS),

[1]Notice that based on its definition, the shift matrix satisfies the condition $\mathbf{J}^r = \mathbf{J}^{-rT}$.

digital terrain maps, previous scans, tracking files, clutter models (in terms of electromagnetic reflectivity and spectral density), and meteorological information.

3. Problem formulation

This section formulates the joint design problem of the STTC and STRF based on the maximization of the output SINR considering practical constraints.

3.1. Output SINR

Letting the observations $\boldsymbol{x}$ be processed via the STRF $\boldsymbol{w} \in \mathbb{C}^{N_R K}$, the SINR $\widehat{\boldsymbol{\rho}}(\boldsymbol{s}, \boldsymbol{w})$ at the output of the receiver can be expressed as

$$\widehat{\boldsymbol{\rho}}(\boldsymbol{s}, \boldsymbol{w}) = \frac{\left|\alpha_0 \boldsymbol{w}^{\dagger} \widehat{\mathbf{A}}(v_{d_0}, \boldsymbol{\theta}_0)\boldsymbol{s}\right|^2}{\mathbb{E}\left[\left|\boldsymbol{w}^{\dagger}\boldsymbol{d}\right|^2\right] + \mathbb{E}\left[\left|\boldsymbol{w}^{\dagger}\boldsymbol{v}\right|^2\right]} = \frac{\sigma_0^2 \boldsymbol{w}^{\dagger} \widehat{\mathbf{A}}(v_{d_0}, \boldsymbol{\theta}_0)\boldsymbol{s}\boldsymbol{s}^{\dagger}\widehat{\mathbf{A}}^{\dagger}(v_{d_0}, \boldsymbol{\theta}_0)\boldsymbol{w}}{\boldsymbol{w}^{\dagger}\boldsymbol{\Sigma}_d(\boldsymbol{s})\boldsymbol{w} + \sigma_v^2 \boldsymbol{w}^{\dagger}\boldsymbol{w}}, \tag{14}$$

where we exploit

$$\mathbb{E}\left[\left|\boldsymbol{w}^{\dagger}\boldsymbol{d}\right|^2\right] = \boldsymbol{w}^{\dagger}\mathbb{E}\left[\boldsymbol{d}\boldsymbol{d}^{\dagger}\right]\boldsymbol{w} \tag{15}$$

and

$$\mathbb{E}\left[\left|\boldsymbol{w}^{\dagger}\boldsymbol{v}\right|^2\right] = \boldsymbol{w}^{\dagger}\mathbb{E}\left[\boldsymbol{v}\,\boldsymbol{v}^{\dagger}\right]\boldsymbol{w} \tag{16}$$

and assume $\boldsymbol{w} \neq \mathbf{0}$ and the independence between the disturbance and the noise random processes.

In particular, the numerator in (14) denotes the useful energy at the output of the STRF, $\boldsymbol{w}^{\dagger}\boldsymbol{\Sigma}_d(\boldsymbol{s})\boldsymbol{w}$ and $\sigma_v^2 \boldsymbol{w}^{\dagger}\boldsymbol{w}$ represent the clutter energy and noise energy, respectively, at the output of $\boldsymbol{w}$. Observe that the clutter energy $\boldsymbol{w}^{\dagger}\boldsymbol{\Sigma}_d(\boldsymbol{s})\boldsymbol{w}$ functionally relies on the STTC $\boldsymbol{w}$ and the STRF $\boldsymbol{s}$ through $\boldsymbol{\Sigma}_d(\boldsymbol{s})$ as well as the useful energy. Furthermore, we note that the objective function $\widehat{\boldsymbol{\rho}}(\boldsymbol{s}, \boldsymbol{w})$ requires that the exact angle $\boldsymbol{\theta}_0$ and normalized Doppler frequency v_{d_0} are known. However, from a practical point of view, the explicit knowledge of $\boldsymbol{\theta}_0$ and v_{d_0} cannot be available. To circumvent this drawback, the averaged SINR defined as $\boldsymbol{\rho}(\boldsymbol{s}, \boldsymbol{w}) = \mathbb{E}[\widehat{\boldsymbol{\rho}}(\boldsymbol{s}, \boldsymbol{w})]$ as figure of merit is exploited. More specifically, we suppose that v_{d_0} and $\boldsymbol{\theta}_0$ are independent random variables uniformly distributed around a mean Doppler frequency $\overline{v}_{d_0}$ and a mean azimuth $\overline{\boldsymbol{\theta}}_0$, respectively, i.e., $v_{d_0} \sim \boldsymbol{U}(\overline{v}_{d_0} - \frac{\varepsilon_0}{2}, \overline{v}_{d_0} + \frac{\varepsilon_0}{2})$, $\boldsymbol{\theta}_0 \sim \boldsymbol{U}(\overline{\boldsymbol{\theta}}_0 - \frac{\vartheta_0}{2}, \overline{\boldsymbol{\theta}}_0 + \frac{\vartheta_0}{2})$, where $\sim$ means "*distribute*" and $\boldsymbol{U}$ represents uniform distribution and ε_0 and ϑ_0 accounts for the uncertainty on v_{d_0} and $\boldsymbol{\theta}_0$, respectively. Interestingly, after some algebraic manipulations, the objective function $\boldsymbol{\rho}(\boldsymbol{s}, \boldsymbol{w})$ shares the following two equivalent expressions,

where

$$\Gamma(S) = \sigma_0^2 \mathbb{E}\Big[(\mathbf{Diag}(p(v_d)) \otimes \mathbf{A}(\theta_0)) S \Big((\mathbf{Diag}(p(v_d)))^{\dagger} \otimes \mathbf{A}^{\dagger}(\theta_0)\Big)\Big] \tag{17}$$

$$\Sigma_{dv}(S) = \sum_{m=1}^{M} (\mathbf{J}^{r_m} \otimes \mathbf{A}(\theta_m))(S \odot \Xi_m)(\mathbf{J}^{r_m} \otimes \mathbf{A}(\theta_m))^{\dagger} + \sigma_v^2 I_{N_R K} \tag{18}$$

$$\Theta(W) = \sigma_0^2 \mathbb{E}\Big[\Big((\mathbf{Diag}(p(v_d)))^{\dagger} \otimes A^{\dagger}(\theta_0)\Big) W (\mathbf{Diag}(p(v_d)) \otimes A(\theta_0))\Big] \tag{19}$$

$$\overline{\Sigma}_{dv}(W) = \sum_{m=1}^{M} (\mathbf{J}^{r_m} \otimes \mathbf{A}(\theta_m))^{\dagger} \big(W \odot \overline{\Xi}_m\big)(\mathbf{J}^{r_m} \otimes \mathbf{A}(\theta_m)) + \frac{\sigma_v^2 \mathbf{tr}(W) \mathbf{I}_{N_T K}}{E}, \tag{20}$$

While $S = ss^{\dagger} \in \mathbb{H}^{KN_T}$ and $W = ww^{\dagger} \in \mathbb{H}^{KN_R}$, Ξ_m is given by (12), E denotes the energy of s, $\overline{\Xi}_m = \sigma_m^2 \Psi_{\varepsilon_m}^{\overline{v}_{d_m}} \otimes \Upsilon_r$, $\Psi_{\varepsilon_m}^{\overline{v}_{d_m}}(k_1, k_2) = \Big(\Phi_{\varepsilon_m}^{\overline{v}_{d_m}}(k_1, k_2)\Big)^*$, $\forall (k_1, k_2) \in \{1, 2, \cdots, K\}^2$ and $\Upsilon_r = \mathbf{1}_r \mathbf{1}_r^T$ with $\mathbf{1}_r = [1, 1, \cdots, 1]^T \in \mathbb{C}^{N_R}$, and $\mathbf{tr}(\cdot)$ denotes the trace of square matrix. These expressions follow from the results obtained in ([19], Appendix 3).

Note that $\Gamma(S)$ and $\Theta(W)$ can be rewritten in block matrix form, i.e.,

$$\Gamma(S) = \big(\sigma_0^2 \Gamma_{m_1 m_2}\big)_{K \times K} \tag{21}$$

$$\Theta(W) = \big(\sigma_0^2 \Theta_{i_1 i_2}\big)_{K \times K} \tag{22}$$

where $\Gamma_{m_1 m_2} \in \mathbb{C}^{N_R \times N_R}$ and $\Theta_{i_1 i_2} \in \mathbb{C}^{N_T \times N_T}$ can be computed by (38) and (46) respectively, $\forall (m_1, m_2, i_1, i_2) \in \{1, 2, \cdots, K\}^4$, as shown in Appendix **A**.

3.2. Constant modulus and similarity constraints

In practical applications, the designed STTC is enforced to be unimodular (i.e., constant modulus) since the nonlinear property of radar amplifiers [24, 25]. To this end, we limit the modulus of each element of the code s as a constant. Precisely, the ith element s_i of s can be written as

$$s_i = \frac{1}{\sqrt{N_T K}} e^{j\varphi_i}, \; i = 1, 2, \cdots, N_T K, \tag{23}$$

with φ_i denoting the phase of s_i. Furthermore, K different similarity constraints are enforced on the N_T transmitting waveforms, namely

$$\|s(k) - s_0(k)\|_{\infty} \le \xi_k, \; k = 1, 2, \cdots, K, \tag{24}$$

where $s_0(k) \in \mathbb{C}^{N_T}$ is the reference code vector at the kth transmission interval, ξ_k is a real parameter ruling the extent of the similarity, and $\|x\|_{\infty}$ denotes the infinite norm.

Without loss of generality, we assume the same similarity parameter ξ_0 (i.e., $\xi_0 = \xi_1 = \cdots = \xi_K$) [12, 26, 28–30] on the sought STTC. Thus, Eq. (24) can be written as $\|\boldsymbol{s}-\boldsymbol{s}_0\|_\infty \le \xi_0$, where $\boldsymbol{s}_0 = \left[\boldsymbol{s}_0^T(\mathbf{1}), \cdots, \boldsymbol{s}_0^T(\boldsymbol{K})\right]^T$ is the reference code vector. Several reasons are presented to show the motivation to exploit the similarity constraints on radar codes. Actually, an arbitrary optimization of SINR via designing an STTC does not offer any kind of control on the shape of the resulting designed waveforms. Specifically, an pure optimization of the SINR can cause signals sharing high peak sidelobe levels and, in general, with an undesired ambiguity function feature. To this end, by exploiting the similarity constraint, when $\boldsymbol{s}_0$ possesses suitable properties, such as low peak sidelobe levels, and reasonable Doppler resolutions, the designed STTC can enjoy some of the good ambiguity function feature of $\boldsymbol{s}_0$. In other words, the similarity constraint compromises the performance between SINR improvement and suitable waveform features [31].

3.3. Design problem

Summarizing, the joint design of the STTC and the STRF can be formulated as the following constrained optimization problem:

$$\mathcal{P}_1 \begin{cases} \max\limits_{\boldsymbol{s},\boldsymbol{w}} & \boldsymbol{\rho}(\boldsymbol{s},\boldsymbol{w}) \\ \mathbf{s.t.} & \|\boldsymbol{s}(\boldsymbol{k})-\boldsymbol{s}_0(\boldsymbol{k})\|_\infty \le \xi_k, \boldsymbol{k} = \mathbf{1}, \mathbf{2}, \cdots, \boldsymbol{K}, \\ & |\boldsymbol{s}_i| = \dfrac{\mathbf{1}}{\sqrt{\boldsymbol{N_T K}}}, \boldsymbol{i} = \mathbf{1}, \mathbf{2}, \cdots, \boldsymbol{N_T K}, \\ & \|\boldsymbol{w}\|^{\mathbf{2}} = \mathbf{1}, \end{cases} \tag{25}$$

where $|\cdot|$ and $\|\cdot\|$, respectively, represent the modulus and the Euclidean norm. Without loss of generality, we add the constraint $\|\boldsymbol{w}\|^{\mathbf{2}} = \mathbf{1}$. $\mathcal{P}_1$ is a NP-hard problem [12, 28] whose optimal solution cannot be found in polynomial time. Next, we develop a new iterative algorithm to offer high-quality solution to the NP-hard problem (25).

4. STTC and STRF design procedure

This section focuses on the design of an iterative algorithm ensuring convergence properties, which is capable of offering high-quality solutions to the NP-hard problem $\mathcal{P}_1$ by sequentially improving the SINR. In particular, we exploit the pattern search framework to cyclically optimize the design variables $(\boldsymbol{w}, \boldsymbol{s_1}, \boldsymbol{s_2}, \cdots, \boldsymbol{s}_{N_T K})$.

4.1. STRF optimization

In this subsection, we deal with the STRF optimization for a fixed STTC $\boldsymbol{s}$. Specifically, we handle the optimization problem

$$\mathcal{P}_w \begin{cases} \max\limits_{w} & \dfrac{w^{\dagger}\boldsymbol{\Gamma}(ss^{\dagger})w}{w^{\dagger}\boldsymbol{\Sigma}_{dv}(ss^{\dagger})w} \\ \mathbf{s.t.} & \|w\|^2 = \mathbf{1}. \end{cases} \tag{26}$$

We observe that the optimal solution w_o to $\mathcal{P}_w$ is the maximum eigenvector of the matrix

$$\left(\boldsymbol{\Sigma}_{dv}(ss^{\dagger})\right)^{-1}\boldsymbol{\Gamma}(ss^{\dagger}),$$

i.e., to a generalized eigenvector of the matrices $\boldsymbol{\Gamma}(s\,s^{\dagger})$ and $\boldsymbol{\Sigma}_{dv}(s\,s^{\dagger})$ corresponding to the maximum generalized eigenvalue. Thus, a closed-form solution to $\mathcal{P}_w$ can be obtained by normalizing w_o.

4.2. STTC optimization

This subsection is devoted to the optimization of the STTC under a fixed STRF. Precisely, each code element in s is sequentially optimized under the fixed remaining N_TK-1 elements. Performing some algebraic manipulations to similarity constraints [26], the optimization problem $\mathcal{P}_{\bar{s}_i}$ with respect to the ith STTC variable, $i = 1, \ldots, N_TK$, is written by,

$$\mathcal{P}_{\bar{s}_i} \begin{cases} \max\limits_{\bar{s}_i} & \dfrac{s^{\dagger}\boldsymbol{\Theta}(ww^{\dagger})s}{s^{\dagger}\overline{\boldsymbol{\Sigma}}_{dv}(ww^{\dagger})s} \\ \mathbf{s.t.} & \arg\bar{s}_i \in [\gamma_i, \gamma_i+\delta], \\ & |\bar{s}_i| = \dfrac{1}{\sqrt{N_TK}}, \end{cases} \tag{27}$$

where $s = [s_1, s_2, \cdots, s_{i-1}, \bar{s}_i, s_{i+1}, \cdots, s_{KN_T}]^T$, $\gamma_i = \arg s_{0i} - \arccos(1-\xi^2/2)$, $\delta = 2\arccos(1-\xi^2/2)$, $\xi = \sqrt{N_TK}\xi_0$ with $0 \le \xi \le 2$, and s_{0i} is the ith element of s_0. Notice that for $\xi = 0$, the code s is equal to the reference code s_0, whereas the similarity constraint would become the constant modulus constraint with $\xi = 2$.

Remark: This procedure by resorting to pattern search framework offers a new strategy to address the code design problem under a fixed filter. In addition, this STTC optimization problem can be efficiently but approximatively settled by semidefinite relaxation (SDR) and randomization procedure with the computational complexity of $O\left((N_TK)^{3.5}\right) + O\left(L(N_TK)^2\right)$, where L is the number of randomization trials. However, the SDR technique usually shares a huge computational complexity, especially in large dimension N_TK, thus limiting its applications in real-time systems; moreover, the existing approach also needs the reasonable selection of L. On the other hand, it is shown that a higher quality solution can be further obtained via a sequential iteration optimization algorithm, which is capable of monotonically increasing the SINR value and achieving a stationary point of the formulated NP-hard problem [27].

Next, we focus on the proposed iteration algorithm to solve problem (27) in a polynomial time. In particular, performing some algebraic manipulations to the objective function in (27), $\mathcal{P}_{\bar{s}_i}$

can be equivalently rewritten as a fractional programming optimization problem by the following proposition.

Proposition 4.1 *The problem* $\mathcal{P}_{\bar{s}_i}$ *is equivalent to*

$$\begin{cases} \max\limits_{\bar{s}_i} & \dfrac{\Re(a_{1,i}\bar{s}_i)+a_{3,i}}{\Re(b_{1,i}\bar{s}_i)+b_{3,i}} \\ \mathbf{s.t.} & \bar{s}_i = \dfrac{1}{\sqrt{N_T K}} e^{j\varphi}, \varphi \in [\gamma_i, \gamma_i+\delta], \end{cases} \tag{28}$$

where

$$a_{3,i} = \frac{a_{0,i}}{N_T K}+a_{2,i}, b_{3,i} = \frac{b_{0,i}}{N_T K}+b_{2,i}, \tag{29}$$

and $a_{k,i}, b_{k,i}$ *are constants for* $k = 0, 1, 2$, $\Re(x)$ *denotes the real part of* x.

Proof. See Appendix **B**.

Problem (28) is solvable [32] since the objective function is continuous with $\Re(b_{1,i}\bar{s}_i)+b_{3,i}>0$ and the constraint is a compact set (closed and bounded set of $\mathbb{C}$). Thus, we consider the following parametric problem [32],

$$\begin{cases} \max\limits_{\bar{s}_i} & \varrho(\mu) = \{\Re(a_{1,i}\bar{s}_i)+a_{3,i}-\mu[\Re(b_{1,i}\bar{s}_i)+b_{3,i}]\} \\ \mathbf{s.t.} & \bar{s}_i = \dfrac{1}{\sqrt{N_T K}} e^{j\varphi}, \varphi \in [\gamma_i, \gamma_i+\delta]. \end{cases} \tag{30}$$

After some simple manipulations, problem (30) can be rewritten as

$$\begin{cases} \max\limits_{\bar{s}_i} & \Re(c_i\bar{s}_i) \\ \mathbf{s.t.} & \bar{s}_i = \dfrac{1}{\sqrt{N_T K}} e^{j\varphi}, \varphi \in [\gamma_i, \gamma_i+\delta], \end{cases} \tag{31}$$

where $c_i = a_{1,i}-\mu b_{1,i}$ and the constant $a_{3,i}-\mu b_{3,i}$ do not affect the optimal value.

Interestingly, problem (31) shares a closed-form solution whose phase φ^* is given by,

$$\varphi^* = -\varphi_{c_i}, -\varphi_{c_i} \in [\gamma_i, \gamma_i+\delta],$$

where φ_{c_i} is the phase of c_i; otherwise, the optimal solution φ^* is given by,

$$\varphi^* = \begin{cases} \gamma_i+\delta & \cos\left(\varphi_{c_i}+\gamma_i+\delta\right) \geq \cos\left(\varphi_{c_i}+\gamma_i\right) \\ \gamma_i & \cos\left(\varphi_{c_i}+\gamma_i+\delta\right) < \cos\left(\varphi_{c_i}+\gamma_i\right). \end{cases} \tag{32}$$

We observe that problems (28) and (30) are relevant in each other via Lemma 2.1 of [32]. Specifically, we can find a solution to problem (28) by obtaining a solution of the equation

$\varrho(\mu) = \mathbf{0}$ concerning $\bar{s}_i$. To this end, the Dinkelbach-type procedure [32, 33] summarized in Algorithm 1 is introduced to solve problem (27).

Algorithm 1. Dinkelbach-type algorithm for solving $\mathcal{P}_{\bar{s}_i}$

Input: $a_{1,i}$, $a_{3,i}$, $b_{1,i}$, $b_{3,i}$, γ_i and δ;

Output: An optimal solution $\widehat{s}_i$ to $\mathcal{P}_{\bar{s}_i}$;

1. Randomly generate $\bar{s}_{i,0}$ within the feasible sets;
2. Compute $\mu_1 = \frac{\Re\left(a_{1,i}\bar{s}_{i,0}\right)+a_{3,i}}{\Re\left(b_{1,i}\bar{s}_{i,0}\right)+b_{3,i}}$ and let $k := 1$;
3. Find the optimal solution $\bar{s}_{i,k}$ by solving problem (30),
4. If $\varrho(\mu_k) = \mathbf{0}$, then $\bar{s}_{i,k}$ is an optimal solution of $\mathcal{P}_{\bar{s}_i}$ with optimal value μ_k and stop. Otherwise, go to step 5;
5. Let $\mu_k = \frac{\Re\left(a_{1,i}\bar{s}_{i,k}\right)+a_{3,i}}{\Re\left(b_{1,i}\bar{s}_{i,k}\right)+b_{3,i}}$ and $k := k+1$; Then go to step 2.

Algorithm 1 sharing a linear convergence rate [34] is needed to handle the problem (30) in each iteration. The objective value of the generated sequence of points has a monotonic convergence property, and the optimal value of (28) can be achieved eventually. We set the exit condition $\varrho(\mu) = \mathbf{0}$, actually, which can be replaced by $\varrho(\mu) \le \varsigma$, with ς being a prescribed accuracy.

4.3. Transmit-receive system design

This subsection reports the iteration optimization procedure for the STTC and STRF in Algorithm 2. In particular, Algorithm 2 guarantees that the SINR monotonically increases[2]. Furthermore, we need to point out that the maximum block improvement (MBI) [24] framework could be used to ensure the convergence to a stationary point of problem $\mathcal{P}_1$.

The global computation consume of the Algorithm 2 is linear to the number of iterations and polynomial with the sizes of the STTC and the STRF. More specifically, each iteration of the proposed algorithm involves the computational cost associated with the solution to problems (26) and $\mathcal{P}_{\bar{s}_i}$, for $i = 1, 2, \cdots, N_T K$. The former requires to solve the generalized eigenvalue decomposition with the order of $O\left((N_R K)^3\right)$ (see [35], p. 500). Similarly, the latter is linear to polynomial with the size of the STTC, while each iteration needs the solution of a generalized fractional programming problem with the computational complexity of $O\left((N_T K)^2\right)$. We need to point out that SOA2, based on the SDR and randomization method, can also be used to the solution of problem (25). However, it cannot guarantee the convergence to a stationary point due to the use of randomized approximations. Moreover, from computational complexity, each iteration of SOA2 has the order of $O\left((N_R K)^3\right) + O\left((N_T K)^{3.5}\right) + O\left(L(N_T K)^2\right)$, whereas Algorithm 2 is $O\left((N_R K)^3\right) + O\left((N_T K)^3\right)$.

[2]Notice that the similar convergence analysis can be obtained in [23].

Algorithm 2. Algorithm for the joint STTC $\boldsymbol{s}$ and STRF $\boldsymbol{w}$ design

Input: $\overline{\theta}_0$, ϑ_0, s_0, ξ, σ_m, r_m, $\overline{v}_{d_m}$, ε_m, for $m = 0, 1, \cdots, M$, and θ_p, for $p = 1, 2, \cdots, M$;

Output: An optimal solution (s^*, w^*) to $\mathcal{P}_1$;

1. Construct γ_m, δ, $m = 1, 2, \cdots, N_T K$ exploiting s_0;
2. For $n = 0$ and initialize $s^{(n)} = s_0$;
3. Compute $w^{(0)} = \frac{w_o^{(0)}}{\|w_o^{(0)}\|}$ and $\rho_0 = \rho\left(s^{(0)}, w^{(0)}\right)$;
4. n:=n+1 and $i = 0$;
5. Compute $\overline{\Sigma}_{dv}\left(w^{(n)} w^{(n)\dagger}\right)$ and $\Theta\left(w^{(n)} w^{(n)\dagger}\right)$ by (20) and (22), respectively;
6. i:=i+1;
7. Compute $a_{k,i}$ and $b_{k,i}$ by (50) and (51), $k = 0, 1, 2$, respectively;
8. Find $a_{3,i}$ and $b_{3,i}$ by (29);
9. Exploit **Algorithm 1** to update s_i by maximizing the problem (27);
10. If $i = N_T K$, output $s^{(n)} = [s_1, s_2, \cdots, s_{KN_T}]^T$. Otherwise, return to step 7;
11. Compute $\Sigma_{dv}\left(s^{(n)} s^{(n)\dagger}\right)$ and $\Gamma\left(s^{(n)} s^{(n)\dagger}\right)$ by (18) and (21), respectively;
12. Find the generalized eigenvector $w_o^{(n)}$ of matrices $\Gamma\left(s^{(n)} s^{(n)\dagger}\right)$ and $\Sigma_{dv}\left(s^{(n)} s^{(n)\dagger}\right)$ corresponding to the maximum generalized eigenvalue;
13. Compute $w^{(n)} = \frac{w_o^{(n)}}{\|w_o^{(n)}\|}$ and $\rho_n = \rho\left(s^{(n)}, w^{(n)}\right)$;
14. If $|\rho_n - \rho_{n-1}| \le \kappa$, where κ is a user selected parameter to control convergence, output $s^* = s^{(n)}$ and $w^* = w^{(n)}$; Otherwise, repeat step 5 until convergence.

5. Numerical results

This section focuses on assessing the capability of the proposed algorithm for designing optimized STTC and STRF in signal-dependent interference for both a nonuniform and an uniform point-like clutter environment. In particular, for both scenarios, we consider an L-band radar with operating frequency $f_c = 1.4$ GHz, which is equipped with an ULA of $N_T = 4$ transmit elements and $N_R = 8$ receive elements under an interelement spacing $d_t = d_r = \lambda/2$. We set the code length $K = 13$ for each transmitter and the orthogonal linear frequency modulation (LFM[3]) is used as the reference waveform s_0 [12] with the (n_t, k)th entry of the reference $S^{(0)}$ given by,

[3]Notice that LFM waveforms have good properties in the pulse compression and ambiguity feature.

$$S^{(0)}(n_t,k)=\frac{\exp\left\{j2\pi n_t(k-1)/N_T\right\}\exp\left\{j\pi(k-1)^2/N_T\right\}}{\sqrt{KN_T}} \tag{33}$$

where $n_t=1,2,\cdots,N_T$ and $k=1,2,\cdots,K$. Hence, the reference code is derived as $s_0=vec\left(S^{(0)}\right)$. Moreover, we assume the target located at range-azimuth bin of interest (0,0) with power $\sigma_0^2=10$ dB. In addition, we set a mean azimuth $\overline{\theta}_0=0^\circ$ with azimuth uncertainty $\vartheta/2=1^\circ$, and a normalized mean Doppler frequency $\overline{v}_{d_0}=0.4$ with Doppler uncertainty $\varepsilon_0/2=0.04$ for the presence of target. We set the noise variance to $\sigma_v^2=0$ dB. Finally, the exit condition[4] $\varsigma=10^{-3}$ for Algorithms 1 and 2 is $\kappa=10^{-3}$, i.e.,

$$|\rho_n-\rho_{n-1}|\le 10^{-3}. \tag{34}$$

All simulations are performed using Matlab 2010a version, running on a standard PC (with a 3.3 GHz Core i5 CPU and 8 GB RAM).

5.1. Nonuniform point-like clutter environment

This subsection focuses on a scenario where three disturbances, respectively, are located at the spatial angles $\theta_1=-55^\circ,\theta_2=-20^\circ,\theta_3=40^\circ$, with corresponding range bins $r_i=0,i=1,2,3$ and powers $\sigma_1^2=30\text{dB}$, $\sigma_2^2=28\text{dB}$, $\sigma_3^2=25$ dB. Moreover, we suppose $\overline{v}_{d_1}=-0.35$, $\overline{v}_{d_2}=-0.15$, $\overline{v}_{d_3}=0.25,\varepsilon_m/2=0.04,m=1,2,3$ for the presence of the disturbances.

For comparison purpose, we also perform simulations for the SOA2 with constant modulus and similarity constraints as well as the algorithm in [19] with energy constraint (i.e., $\|s\|^2=1$), respectively. In particular, **Figure 2** shows the SINR versus the iteration number for different ξ by also comparing the results obtained via Algorithm 2 and SOA2 considering L = 100 and exploiting the CVX toolbox [36] to handle the semidefinite programming (SDP) involved in SOA2. The results exhibit that the SINR values achieved using Algorithm 2 and SOA2 increase as the iteration number increases. In addition, the SINR increases as ξ increases owing to the higher degrees of freedom available at the design stage. Precisely, Algorithm 2 is superior to SOA2 for $\xi=0.1,0.5,1.3$. It is interesting to note that Algorithm 2 and SOA2 share almost the same SINR for $\xi=2$, whereas both obtain lower SINR than the case considering energy constraint. Finally, it is worth pointing out that a loss of SINR caused by constant constraint can be observed since the gap of SINR between $\xi=2$ and energy constraint is about 1 dB.

Table 1 reports the achieved SINR values, iterations number, and global computation time of Algorithm 2 and SOA2 supposing a target with $-\pi/180\le\theta_0\le\pi/180$, $0.36\le v_{d_0}\le 0.44$ for $\xi=0.1,0.5,1.3,2$ and setting the same exit condition for SOA2. We observe that Algorithm 2 and SOA2 both converge very fast. Additionally, Algorithm 2 is superior to SOA2 concerning

[4]Notice that we consider the exit condition $A/10^4$ both for Algorithms 1 and 2, where A denotes the upper bound of the objective function neglecting the signal-dependent interference (for example, $A=10$ is considered in this simulation).

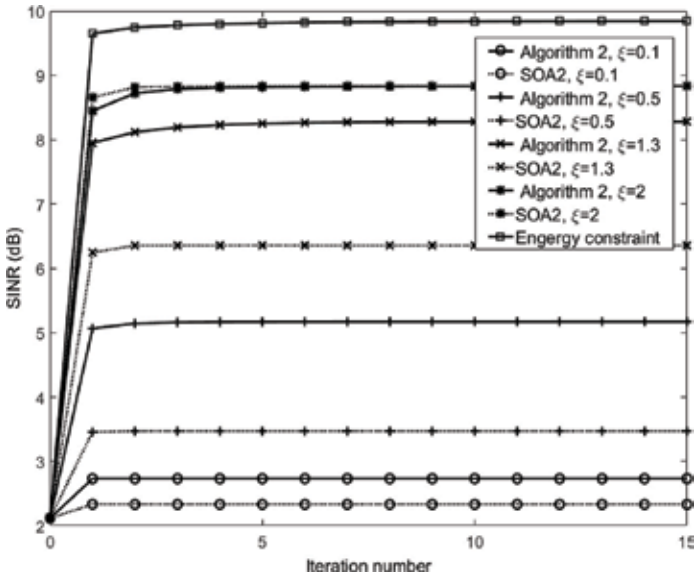

Figure 2. The SINR behavior versus iteration number assuming a target with $-\pi/180 \leq \theta_0 \leq \pi/180$, $0.36 \leq v_{d_0} \leq 0.44$ for $\xi = 0.1, 0.5, 1.3, 2$, s_0 as the initial point.

Algorithm 2				**SOA2**		
ξ	SINR	n	Time	SINR	n	Time
0.1	2.7	2	0.3236	2.3	3	4.0145
0.5	5.2	6	0.8942	3.5	3	3.9688
1.3	8.3	12	1.7175	6.3	4	5.3498
2	8.8	13	1.8102	8.8	7	9.3621

Table 1. SINR values (in dB), iterations number, and global computation time (in seconds) of Algorithm 2 and SOA2 assuming a target with $-\pi/180 \leq \theta_0 \leq \pi/180$, $0.36 \leq v_{d_0} \leq 0.44$ for $\xi = 0.1, 0.5, 1.3, 2$, s_0 as the initial point.

the achieved SINR value for $\boldsymbol{\xi = 0.1, 0.5, 1.3}$ and concerning the required computational cost for $\boldsymbol{\xi = 0.1, 0.5, 1.3, 2}$.

In the following, the joint frequency and azimuth behavior of STTC and STRF are considered corresponding to $\boldsymbol{\xi = 2}$ supposing $\boldsymbol{-\pi/180 \leq \theta_0 \leq \pi/180}$, $\boldsymbol{0.36 \leq v_{d_0} \leq 0.44}$ for different iteration numbers, by using the contour map of the slow-time cross ambiguity function (CAF) [19],

$$g^{(n)}\left(\boldsymbol{s}^{(n)}, \boldsymbol{w}^{(n)}, \boldsymbol{r}, v, \theta\right) = \left|\boldsymbol{w}^{(n)\dagger}\mathbf{P}_r\widehat{\mathbf{A}}(v, \theta)\boldsymbol{s}^{(n)}\right|^2, \tag{35}$$

where $\widehat{\mathbf{A}}(v, \theta)$ and $\mathbf{P}_r$ are obtained by exploiting Eqs. (6) and (8), respectively. **Figure 3** plots the contour map of the Doppler-azimuth plane of CAF at $\boldsymbol{r = 0}$ versus the iteration number $\boldsymbol{n = [0, 1, 4, 15]}$ for Algorithm 2. As expected, the lower and lower values in the regions of (highlighted by black ellipses) $\boldsymbol{\theta_1 = -55^\circ}$ and $\boldsymbol{-0.39 \leq v \leq -0.31}$, $\boldsymbol{\theta_2 = -20^\circ}$ and $\boldsymbol{-0.19 \leq v \leq}$

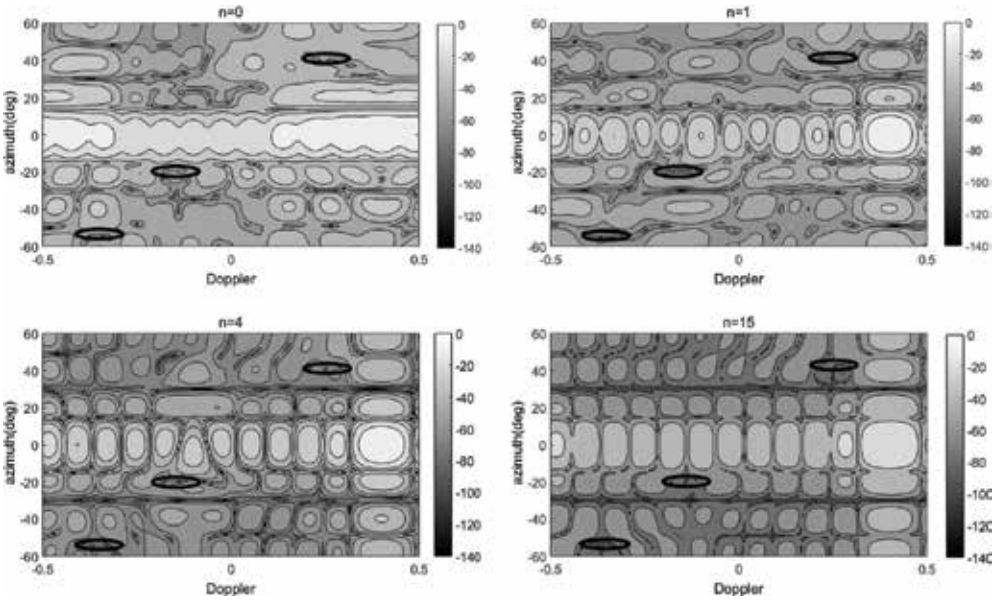

Figure 3. Doppler-azimuth plane of CAF at $r = 0$ for $\xi = 2$ of Algorithm 2 for $n = [0, 1, 4, 15]$ assuming a target with $-\pi/180 \le \theta_0 \le \pi/180$, $0.36 \le v_{d_0} \le 0.44$ (black ellipses represent the locations of three interference sources), s_0 as the initial point.

$-\mathbf{0.11}$, and $\boldsymbol{\theta_3 = 40^\circ}$ and $\mathbf{0.21 \le v \le 0.29}$ are achieved, with the increase of $\boldsymbol{n}$. Thus, it is worth pointing out that the proposed algorithm can suitably shape the CAF to resist interferences.

For the uniform distribution, we define both standard deviations $\sigma_{v_{d_0}}$ and σ_{θ_0} of target Doppler and azimuth as, respectively,

$$\sigma_{v_{d_0}} = \varepsilon_0/\sqrt{12}, \sigma_{\theta_0} = \vartheta_0/\sqrt{12}.$$

Figure 4 shows the SINR behaviors versus the standard deviations $\sigma_{v_{d_0}}$ (**Figure** 4**a**) and σ_{θ_0} (**Figure** 4**b**) supposing $\overline{\theta}_0 = 0^\circ$, $\overline{v}_{d_0} = 0.4$, respectively. Our curves highlight that the proposed algorithm can further improve SINR gain in comparison with SOA2 for $\xi = 0.1, 0.5, 1.3$. We also observe that the higher $\sigma_{v_{d_0}}$ and σ_{θ_0} and the lower SINR can be obtained due to the larger inaccuracies on the knowledge of Doppler and azimuth of the actual target. Finally, we need to point out that the proposed design procedure still has the better robustness against a large uncertain set in comparison with SOA2.

5.2. Uniform clutter environment

This subsection focuses on a scenario where we consider a homogeneous range-azimuth ground clutter interfering with the range-azimuth bin of interest (0,0). Specifically, for each range-azimuth ground clutter bin, a clutter to noise ratio (CNR) of 25 dB and a normalized Doppler frequency $\overline{v} = 0$ with Doppler uncertainty $\varepsilon/2 = 0.04$ are considered. We suppose

$M = 50$ range-azimuth ground clutter bins located within the azimuth angular sector $[-\pi/2, \pi/2]$. Moreover, we set the range ring $r_i = 0$ for all range-azimuth ground clutter bins.

In **Figure 5**, we show the SINR of Algorithm 2 and SOA2 for $\xi = 0.1, 0.5, 1.3, 2$ supposing a target $-\pi/180 \le \theta_0 \le \pi/180$, $0.36 \le v_{d_0} \le 0.44$. The SINR values increases both for Algorithm 2 and SOA2 with the increasing iteration number n. Furthermore, we observe the higher ξ, the better SINR values reflecting the larger and larger feasible set. Interestingly, Algorithm 2 significantly outperforms SOA2 for all the considered ξ, except for $\xi = 2$ where they both

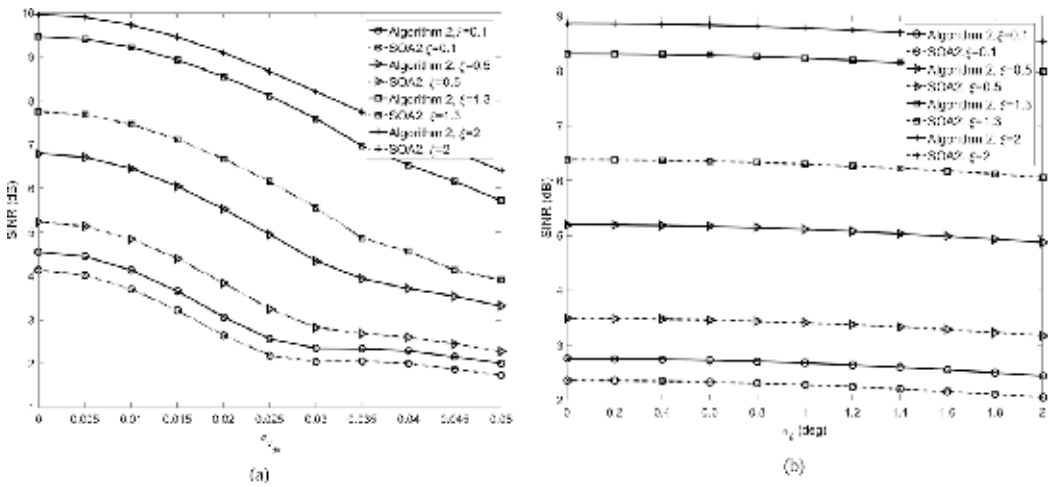

Figure 4. The SINR behaviors versus the standard deviations $\sigma_{v_{d_0}}$ (**Figure 4a**) and σ_{θ_0} (**Figure 4b**) of Doppler and azimuth of target with $\overline{\theta}_0 = 0^\circ$, $\overline{v}_{d_0} = 0.4$ considering $\xi = 0.1, 0.5, 1.3, 2$, respectively, s_0 as the initial point.

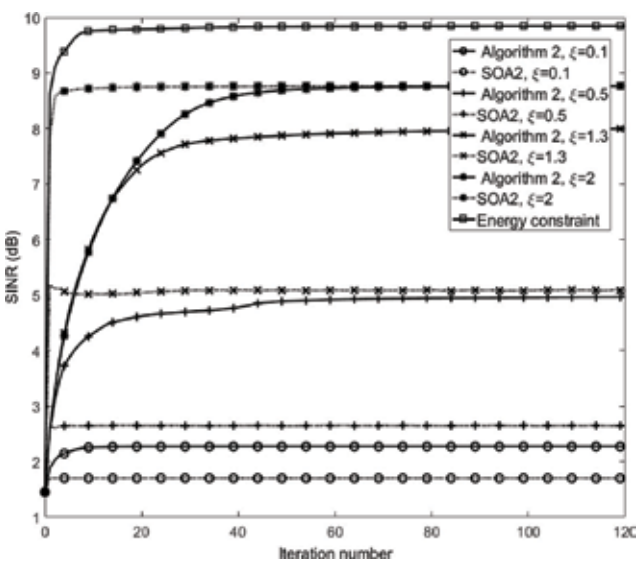

Figure 5. The SINR behavior versus iteration number assuming a target with $-\pi/180 \le \theta_0 \le \pi/180$, $0.36 \le v_{d_0} \le 0.44$ in uniform clutter environment for $\xi = 0.1, 0.5, 1.3, 2$, s_0 as the initial point.

achieve the same SINR value. In particular, we see that the gap between $\boldsymbol{\xi = 2}$ and energy constraint is about 1.1 dB because of the introduction of constant modulus constraint. We also observe that in this scenario, Algorithm 2 needs a higher number of iterations to achieve convergence compared with that in **Figure 2**. For instance, for $\boldsymbol{\xi = 0.1}$, Algorithm 2 converges with about 12 iterations in **Figure 5**, whereas in **Figure 2** after about 2 iterations.

In **Table** 2, we summarize the SINR values, iterations number, and the global computation time of Algorithm 2 and SOA2. In particular, Algorithm 2 shows a lower computational time for $\boldsymbol{\xi = 0.1, 2}$. Furthermore, it is observed that the gains of 2.3 and 3 dB are achieved using Algorithm 2 with a slightly higher computational cost for $\boldsymbol{\xi = 0.5, 1.3}$, respectively.

Figure 6 shows the joint frequency and azimuth behavior of STTC and STRF concerning CAF. Specifically, the contour map of the Doppler-azimuth plane of CAF at $\boldsymbol{r = 0}$ against the

Algorithm 2				**SOA2**		
ξ	SINR	n	Time	SINR	n	Time
0.1	2.3	12	2.6325	1.7	3	4.3007
0.5	4.9	68	13.0183	2.6	8	11.4606
1.3	8.0	120	21.4875	5.0	10	14.5547
2	8.8	82	15.8699	8.8	24	35.0873

Table 2. SINR values (in dB), iterations number, and global computation time (in seconds) of Algorithm 2 and SOA2 assuming a target with $-\pi/180 \le \theta_0 \le \pi/180$, $0.36 \le v_{d_0} \le 0.44$ in uniform clutter environment for $\xi = 0.1, 0.5, 1.3, 2$, s_0 as the initial point.

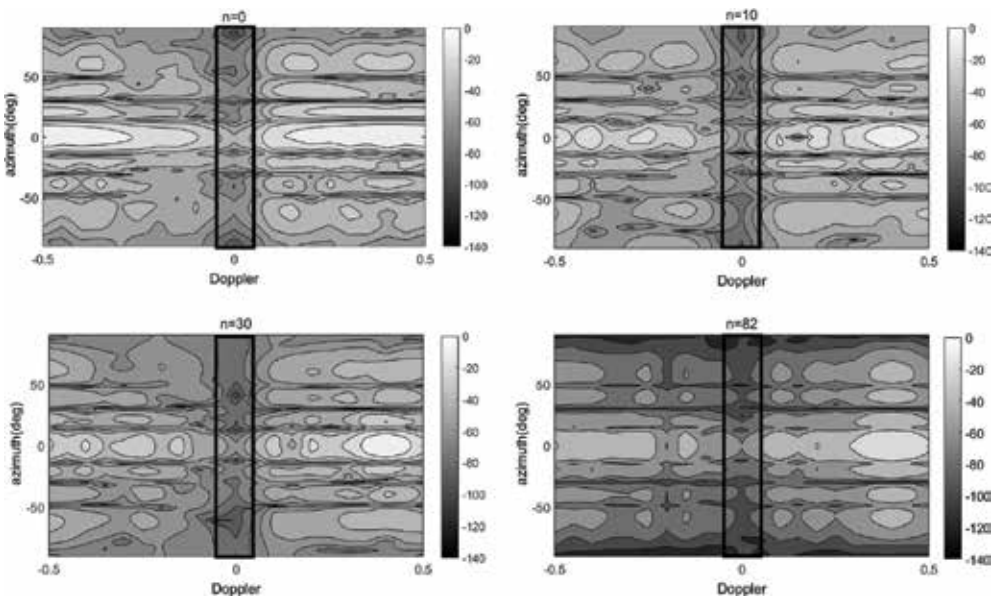

Figure 6. Doppler-azimuth plane of CAF at $r = 0$ for $\xi = 2$ of Algorithm 2 for $n = [0, 10, 30, 82]$ assuming a target with $-\pi/180 \le \theta_0 \le \pi/180$, $0.36 \le v_{d_0} \le 0.44$ in uniform clutter environment (black rectangles represent the locations of uniform clutter), s_0 as the initial point of Algorithm 2 and SOA2.

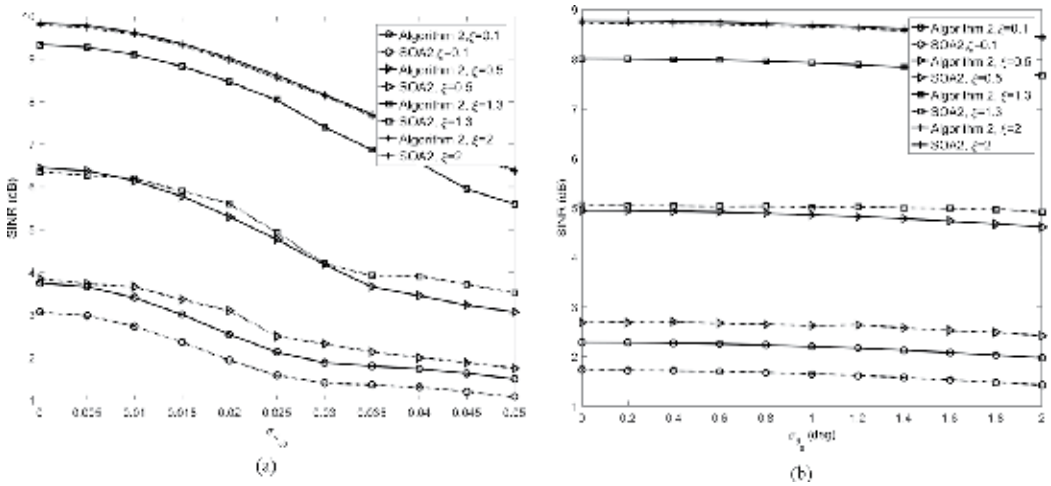

Figure 7. The SINR behaviors versus the standard deviations $\sigma_{v_{d_0}}$ (a) and σ_{θ_0} () of Doppler and azimuth of target with $\overline{\theta}_0 = 0^\circ$, $\overline{v}_{d_0} = 0.4$, respectively, s_0 as the initial point of Algorithm 2 and SOA2.

iteration number ($\boldsymbol{n} = [\mathbf{0}, \mathbf{10}, \mathbf{30}, \mathbf{82}]$) considering $\boldsymbol{\xi} = \mathbf{2}$ for Algorithm 2 is plotted. We observe that $g^{(n)}\left(\boldsymbol{s}^{(n)}, \boldsymbol{w}^{(n)}, \boldsymbol{r}, v, \boldsymbol{\theta}\right)$ obtains lower and lower values in the region of $-\boldsymbol{\pi/2} \leq \boldsymbol{\theta} \leq \boldsymbol{\pi/2}$, $-\mathbf{0.04} \leq \boldsymbol{v} \leq \mathbf{0.04}$ (highlighted by black rectangles) with the increase of iteration number $\boldsymbol{n}$. This performance behavior highlights that the proposed algorithm of joint design STTC and STRF possesses the ability of sequentially refining the shape of the CAF to achieve better and better clutter suppression levels.

Figure 7 plots the SINR versus the standard deviations $\boldsymbol{\sigma_{v_{d_0}}}$ (**Figure 7a**) and $\boldsymbol{\sigma_{\theta_0}}$ (**Figure 7b**) of Doppler and azimuth of target with $\overline{\boldsymbol{\theta}}_{\mathbf{0}} = \mathbf{0}^\circ$, $\overline{\boldsymbol{v}}_{\boldsymbol{d}_0} = \mathbf{0.4}$, respectively. Again, we see that Algorithm 2 obtains a higher SINR gain than SOA2 for $\boldsymbol{\xi} = \mathbf{0.1}, \mathbf{0.5}, \mathbf{1.3}$, whereas they both fulfill the near same gain at $\boldsymbol{\xi} = \mathbf{2}$. Interestingly, we also observe that a decreasing trend in gain with the increase in standard deviation. This is reasonable due to that the larger standard deviation results in the larger uncertainty on the knowledge of target.

6. Conclusions

This chapter has considered the joint STTC and STRF design for MIMO radar under signal-dependent interference. We focus on a narrow band colocated MIMO radar with a moving point-like target considering imprecise a prior knowledge including Doppler and azimuth. Summarizing,

- We have devised an iterative algorithm to maximize the SINR accounting for both a similarity constraint and constant modulus requirements on the probing waveform. Each iteration of the algorithm requires the solution of hidden convex problems. The consequent computational complexity is linear with the number of iterations and polynomial with the sizes of the STTC and the STRF.

- We have assessed the performance of the proposed iteration algorithm through numerical simulations. The results have manifested that the larger the similarity parameter (i.e., the weaker the similarity constraint), the larger the output SINR due to the expanded feasible set. Moreover, we observed that the devised iteration procedure can provide a monotonic improvement of SINR and ensuring convergence to a stationary point, which possesses excellent superiority in computation complexity and performance gain compared with the related SOA2. The numerical examples also have revealed the capability of the developed procedure to sequentially refine the shape of the CAF both in nonuniform point-like clutter environment and uniform clutter environment.

Possible future work tracks might extend the proposed framework to consider spectral constraint [37] and MIMO radar beampattern design by optimizing integrated sidelobe level (ISL) with practical constraints.

Acknowledgements

This work was supported by the National Natural Science Foundation of China under Grants 61771109 and 61501083. The authors like to thank Dr. Augusto Aubry for his constructive comments.

Appendices

Appendix A: Computation of $\boldsymbol{\Gamma}(\mathbf{S})$ and $\boldsymbol{\Theta}(\mathbf{W})$

Let us denote $\boldsymbol{S}$ in block matrix form, i.e.,

$$\boldsymbol{S} = (\boldsymbol{S}_{n_1 n_2})_{K\times K}, \tag{36}$$

where the block matrix $\boldsymbol{S}_{n_1 n_2} \in \mathbb{C}^{N_T \times N_T}$ can be computed as

$$\boldsymbol{S}_{n_1 n_2} = \boldsymbol{s}(n_1)\boldsymbol{s}^{\dagger}(n_2),\ (n_1, n_2) \in \{1, 2, \cdots, K\}^2. \tag{37}$$

Hence, exploiting the fact that v_{d_0} and $\boldsymbol{\theta_0}$ are statistically independent random variables, the block matrix $\boldsymbol{\Gamma}_{m_1 m_2}$ of $\boldsymbol{\Gamma}(\boldsymbol{S})$ in (21) can be expressed as

$$\boldsymbol{\Gamma}_{m_1 m_2} = \sigma_0^2 \mathbb{E}\left[e^{j2\pi(m_1-m_2)v_{d_0}}\right] \mathbb{E}\left[\boldsymbol{A}(\boldsymbol{\theta_0})\boldsymbol{S}_{m_1 m_2}\boldsymbol{A}^{\dagger}(\boldsymbol{\theta_0})\right],\ (m_1, m_2) \in \{1, 2, \cdots, K\}^2. \tag{38}$$

Since v_{d_0} is a uniformly distributed random variable, e.g., $v_{d_0} \sim \boldsymbol{U}\left(\overline{v}_{d_0} - \frac{\varepsilon_0}{2}, \overline{v}_{d_0} + \frac{\varepsilon_0}{2}\right)$, the first expectation of (38) can be computed as

$$\mathbb{E}\left[e^{j2\pi(m_1-m_2)v_{d_0}}\right] = \frac{1}{\varepsilon_0} \int_{\overline{v}_{d_0}-\frac{\varepsilon_0}{2}}^{\overline{v}_{d_0}+\frac{\varepsilon_0}{2}} e^{j2\pi(m_1-m_2)v_{d_0}} dv_{d_0} = e^{j2\pi\overline{v}_{d_0}(m_1-m_2)} \frac{\sin\left[\pi\varepsilon_0(m_1-m_2)\right]}{\pi\varepsilon_0(m_1-m_2)}, (m_1, m_2) \in \{1, 2, \cdots, K\}^2. \tag{39}$$

Let $\boldsymbol{\Phi}_{\vartheta_0}^{\overline{\theta}_0}$ denote the second expectation of (38) whose (q_1, q_2) entry is given by

$$\boldsymbol{\Phi}_{\vartheta_0}^{\overline{\theta}_0}(q_1,q_2) \quad = \mathbb{E}\left[\tilde{a}_{q_1}^T(\theta_0)S_{m_1m_2}\tilde{a}_{q_2}^*(\theta_0)\right] = tr\left(S_{m_1m_2}\overline{\boldsymbol{\Phi}}_{q_1q_2}\right), \qquad (q_1,q_2)\in\{1,2,\cdots,N_R\}^2, \quad (40)$$

where

$$\tilde{a}_q(\theta_0) = \frac{1}{\sqrt{N_R}}e^{-j\frac{2\pi\sin\theta_0}{\lambda}d_r(q-1)}a_t{}^*(\theta_0), \quad q\in\{1,2,\cdots,N_R\}, \qquad (41)$$

and

$$\overline{\boldsymbol{\Phi}}_{q_1q_2} = \mathbb{E}\left[\tilde{a}_{q_2}^*(\theta_0)\tilde{a}_{q_1}^T(\theta_0)\right]. \qquad (42)$$

Based on θ_0 as a uniformly distributed random variable, e.g., $\theta_0\sim U\left(\overline{\theta}_0-\frac{\vartheta_0}{2},\overline{\theta}_0+\frac{\vartheta_0}{2}\right)$, the (q_1,q_2) entry of expectation $\overline{\boldsymbol{\Phi}}_{q_1q_2}$ can be computed as

$$\overline{\boldsymbol{\Phi}}_{q_1q_2}(p_1,p_2) = \frac{1}{N_TN_R\vartheta_0}\int_{\overline{\theta}_0-\frac{\vartheta_0}{2}}^{\overline{\theta}_0+\frac{\vartheta_0}{2}} e^{j\frac{2\pi\sin\theta_0}{\lambda}\left[d_r(q_2-q_1)+d_t(p_1-p_2)\right]}d\theta_0 (q_1,q_2)\in\{1,2,\cdots,N_R\}^2,\ (p_1,p_2)\in\{1,2,\cdots,N_T\}^2. \qquad (43)$$

As to the computation of (43), we can adopt numerical integration.

Next, we focus on the computation of $\boldsymbol{\Theta}(W)$. Similarly, let us write W in block matrix structure, given by

$$W = (W_{i_1i_2})_{K\times K}, \qquad (44)$$

where block matrix $W_{i_1i_2}\in\mathbb{C}^{N_R\times N_R}$ is given by

$$W_{i_1i_2} = w(i_1)w^\dagger(i_2), \qquad (i_1,i_2)\in\{1,2,\cdots,K\}^2. \qquad (45)$$

As a consequence, based on the statistical independence of v_{d_0} and θ_0, the block matrix $\boldsymbol{\Theta}_{i_1i_2}$ of $\boldsymbol{\Theta}(W)$ in (22) is

$$\boldsymbol{\Theta}_{i_1i_2} = \sigma_0^2\mathbb{E}\left[e^{-j2\pi(i_1-i_2)v_{d_0}}\right]\mathbb{E}\left[A^\dagger(\theta_0)W_{i_1i_2}A(\theta_0)\right], \qquad (i_1,i_2)\in\{1,2,\cdots,K\}^2. \qquad (46)$$

Following the same lines of reasoning in (39) and (43), both expectations in (46) can be evaluated.

Appendix B: Proof of (25)

The $\boldsymbol{\Theta}(w\,w^\dagger)$ can be rewritten as

$$\boldsymbol{\Theta}(ww^\dagger) = [a_1,a_2,\cdots,a_{KN_T}], \qquad (47)$$

where $a_n = [\alpha_{n,1},\alpha_{n,2},\cdots,\alpha_{n,KN_T}]^T\in\mathbb{C}^{KN_T}$, for $n = 1,2,\cdots,KN_T$. Hence, the $s^\dagger\boldsymbol{\Theta}(ww^\dagger)s$ can be expressed as

$$\bar{s}^{\dagger}\Theta(ww^{\dagger})\bar{s} = \sum_{\substack{n=1 \\ n\neq i}}^{KN_T} \bar{s}^{\dagger}a_n s_n + \bar{s}^{\dagger}a_i\bar{s}_i = \sum_{\substack{n=1 \\ n\neq i}}^{KN_T} \bar{s}_i^{*}\alpha_{n,i}s_n + \bar{s}^{\dagger}a_i\bar{s}_i + \sum_{\substack{k=1 \\ k\neq i}}^{KN_T}\sum_{\substack{l=1 \\ l\neq i}}^{KN_T} s_l^{*}\alpha_{k,l}s_k. \tag{48}$$

Using the property $\alpha_{n,i} = \alpha_{i,n}^{*}$ since $\Theta(ww^{\dagger})$ is a positive semidefinite matrix, (48) can be computed as

$$\bar{s}^{\dagger}\Theta(ww^{\dagger})\bar{s} = \alpha_{i,i}|\bar{s}_i|^2 + \Re\left\{\sum_{\substack{n=1 \\ n\neq i}}^{KN_T} 2\bar{s}_i\alpha_{i,n}s_n^{*}\right\} + \sum_{\substack{k=1 \\ k\neq i}}^{KN_T}\sum_{\substack{l=1 \\ l\neq i}}^{KN_T} s_l^{*}\alpha_{k,l}s_k. \tag{49}$$

Hence, we obtain

$$a_{0,i} = \alpha_{i,i}, a_{1,i} = 2\sum_{\substack{n=1 \\ n\neq i}}^{KN_T} \alpha_{i,n}s_n^{*}, a_{2,i} = \sum_{\substack{k=1 \\ k\neq i}}^{KN_T}\sum_{\substack{l=1 \\ l\neq i}}^{KN_T} s_l^{*}\alpha_{k,l}s_k. \tag{50}$$

Following the same line of reasoning, the coefficients b_0, b_1, b_2 are given by,

$$b_{0,i} = \beta_{i,i}, b_{1,i} = 2\sum_{\substack{n=1 \\ n\neq i}}^{KN_T} \beta_{i,n}s_n^{*}, b_{2,i} = \sum_{\substack{k=1 \\ k\neq i}}^{KN_T}\sum_{\substack{l=1 \\ l\neq i}}^{KN_T} s_l^{*}\beta_{k,l}s_k \tag{51}$$

where $\beta_{m,n}$ denotes the (m,n)th entry of $\overline{\Sigma}_{dv}(ww^{\dagger})$.

Author details

Guolong Cui*, Xianxiang Yu and Lingjiang Kong

*Address all correspondence to: cuiguolong@uestc.edu.cn

School of Electronic Engineering, University of Electronic Science and Technology of China, Chengdu, China

References

[1] Li J, Stoica P. MIMO Radar Signal Processing. Hoboken, NJ, USA: Wiley; 2009

[2] Haimovich AM, Blum RS, Cimini LJ. Mint:MIMO radar with widely separated antennas. IEEE Signal Processing Magazine. 2008;**25**:116-129. DOI: 10.1109/MSP.2007.909532

[3] Fishler E, Haimovich AM, Blum RS, Cimini LJ Jr, Chizhik D, Valenzuela RA. Spatial diversity in radars-models and detection performance. IEEE Transactions on Signal Processing. 2006;**54**:823-838. DOI: 10.1109/TSP.2005.862813

[4] Li J, Stoica P. MIMO radar with colocated antennas. IEEE Signal Processing Magazine. 2007;**24**:106-114. DOI: 10.1109/MSP.2007.904812

[5] Forsythe K, Bliss D, Fawcett G. Multiple-input multiple-output (MIMO) radar: Performance issues. In: Proceedings 38th Asilomar Conference Signals, Systems and Computers (ASILOMAR04); 7-10. Nov. 2004. Pacific Grove, CA, USA: IEEE; 2004. pp. 310-315

[6] Yang Y, Blum RS. Minimax robust MIMO radar waveform design. IEEE Journal of Selected Topics in Signal Processing. 2007;**1**:147-155. DOI: 10.1109/JSTSP.2007.897056

[7] Aubry A, De Maio A, Huang Y. MIMO radar Beampattern design via PSL/ISL optimization. IEEE Transactions on Signal Processing. 2016;**64**:3955-3967. DOI: 10.1109/TSP.2016.2543207

[8] Ahmed S, Alouini MS. MIMO-radar waveform covariance matrix for high SINR and low side-lobe levels. IEEE Transactions on Signal Processing. 2014;**62**:2056-2065. DOI: 10.1109/TSP.2014.2307282

[9] Friedlander B. Waveform design for MIMO radars. IEEE Transactions on Aerospace and Electronic Systems. 2007;**43**:1227-1238. DOI: 10.1109/TAES.2007.4383615

[10] Naghibi T, Behnia F. MIMO radar waveform design in the presence of clutter. IEEE Transactions on Aerospace and Electronic Systems. 2011;**47**:770-781. DOI: 10.1109/TAES.2011.5751224

[11] Chen CY, Vaidyanathan PP. MIMO radar waveform optimization with prior information of the extended target and clutter. IEEE Transactions on Signal Processing. 2009;**57**:3533-3544. DOI: 10.1109/TSP.2009.2021632

[12] Cui G, Li H, Rangaswamy M. MIMO radar waveform design with constant modulus and similarity constraints. IEEE Transactions on Signal Processing. 2014;**62**:343-353. DOI: 10.1109/TSP.2013.2288086

[13] Zhu W, Tang J. Robust design of transmit waveform and receive filter for colocated MIMO radar. IEEE Signal Processing Letters. 2015;**22**:2112-2116. DOI: 10.1109/LSP.2015.2461460

[14] Jiu B, Liu H, Wang X, Zhang L, Wang Y, Chen B. Knowledge-based spatial-temporal hierarchical MIMO radar waveform design method for target detection in heterogeneous clutter zone. IEEE Transactions on Signal Processing. 2015;**63**:543-554. DOI: 10.1109/TSP.2014.2366714

[15] Imani S, Ghorashi SA. Transmit signal and receive filter design in co-located MIMO radar using a transmit weighting matrix. IEEE Signal Processing Letters. 2015;**22**:1521-1524. DOI: 10.1109/LSP.2015.2411676

[16] Xue M, Zhu X, Li J, Vu D, Stoica PMIMO. Radar waveform design. In: De Maio A, Gini FL P, editors. Waveform Design and Diversity for Advanced Radar Systems. 2012. pp. 89-120. DOI: 10.1049/PBRA022.ch4

[17] Mecca VF, Krolik JL, Robey FC. Beamspace slow-time MIMO radar for multipath clutter mitigation. IEEE International Conference on Acoustics, Speech and Signal Processing 31 March-4 April 2008. Las Vegas, Nevada, USA: IEEE; 2008. p. 2313-2316

[18] Duly AJ, Krogmeier JV. Time-division beamforming for MIMO radar waveform design. IEEE Transactions on Aerospace and Electronic Systems. 2013;**49**:1210-1223. DOI: 10.1109/TAES.2013.6494408

[19] Karbasi SM, Aubry A, Carotenuto V, Naghsh MM, Bastan MH. Knowledge-based design of space-time transmit code and receive filter for a multiple-input-multiple-output radar in signal-dependent interference. IET Radar, Sonar, Navigation. 2015;**9**:1124-1135. DOI: 10.1049/iet-rsn.2014.0527

[20] Yu X, Cui G, Kong L, Carotenuto V. Space-time transmit code and receive filter Design for Colocated MIMO radar. IEEE radar conference; 2-6 May 2016; Philadelphia, Pennsylvania, USA. IEEE. 2016:1-6

[21] Cui G, Yu X, Carotenuto V, Kong L. Space-time transmit code and receive filter design for colocated MIMO radar. IEEE Transactions on Signal Processing. 2017;**65**:1116-1129. DOI: 10.1109/TSP.2016.2633242

[22] Guerci JR. Cognitive radar: The knowledge aided fully adaptive approach. IEEE radar conference; 10-14 May 2010; Washington, DC, USA. IEEE. 2010:1365-1370

[23] Aubry A, De Maio A, Farina A, Wicks M. Knowledge-aided (potentially cognitive) transmit signal and receive filter design in signal-dependent clutter. IEEE Transactions on Aerospace and Electronic Systems. 2013;**49**:93-117. DOI: 10.1109/TAES.2013.6404093

[24] Aubry A, De Maio A, Jiang B, Zhang S. Ambiguity function shaping for cognitive radar via complex quartic optimization. IEEE Transactions on Signal Processing. 2013;**61**:5603-5619. DOI: 10.1109/TSP.2013.2273885

[25] Cui G, Fu Y, Yu X, Li J. Local ambiguity function shaping via unimodular sequence design. IEEE Signal Processing Letters. 2017;**24**:977-981. DOI: 10.1109/LSP.2017.2700396

[26] De Maio A, De NS, Huang Y, Luo Z, Zhang S. Design of phase codes for radar performance optimization with a similarity constraint. IEEE Transactions on Signal Processing. 2009;**57**:610-621. DOI: 10.1109/TSP.2008.2008247

[27] Aubry A, Carotenuto V, De Maio A. Forcing multiple spectral compatibility constraints in radar waveforms. IEEE Signal Processing Letters. 2016;**23**:483-487. DOI: 10.1109/LSP.2016.2532739

[28] Aubry A, De Maio A, Piezzo M, Farina A, Wicks M. Cognitive design of the receive filter and transmitted phase code in reverberating environment. IET Radar, Sonar, Navigation. 2012;**6**:822-833. DOI: 10.1049/iet-rsn.2012.0029

[29] Cui G, Yu X, Foglia G, Huang Y, Li J. Quadratic optimization with similarity constraint for unimodular sequence synthesis. IEEE Transactions on Signal Processing. 2017;**65**:4756-4769. DOI: 10.1109/TSP.2017.2715010

[30] Yu X, Cui G, Ge P, Kong L. Constrained radar waveform design algorithm for spectral coexistence. IET Electronic Letters. 2017;**53**:558-560. DOI: 10.1049/el.2016.4524

[31] Li J, Guerci JR, Signal XL. Waveforms optimal-under-restriction design for active sensing. IEEE Signal Processing Letters. 2016;**13**:565-568. DOI: 10.1109/SAM.2006.1706159

[32] Barros AI, Frenk JBG, Schaible SA. New algorithm for generalized fractional programs. Mathematical Programming. 1996;**72**:147-175. DOI: 10.1109/CC.2017.7942327

[33] Crouzeix JP, Ferland JA, Schaible S. An algorithm for generalized fractional programs. Journal of Optimization Theory and Applications. 1985;**47**:35-49. DOI: 10.1109/IPDPS.2017.22

[34] Aubry A, De Maio A, Naghsh MM. Optimizing radar waveform and Doppler filter bank via generalized fractional programming. IEEE Journal of Selected Topics in Signal Processing. 2015;**9**:1387-1399. DOI: 10.1109/JSTSP.2015.2469259

[35] Golub G H and Loan C F V. Matrix Computations. 4th ed. Baltimore, MD: The Johns Hopkins University Press; 2013

[36] Grant M and Boyd S. CVX Package [Internet]. March 2017. Available from: http://www.cvxr.com/cvx.r

[37] Aubry A, De Maio A, Huang Y, Piezzo M, Farina A. A new radar waveform design algorithm with improved feasibility for spectral coexistence. IEEE Transactions on Aerospace and Electronic Systems. 2015;**52**:1029-1038. DOI: 10.1109/TAES.2014.140093

Chapter 3

Waveform Design for MIMO Radar and SAR Application

Stéphane Méric and Jean-Yves Baudais

Additional information is available at the end of the chapter

http://dx.doi.org/10.5772/intechopen.71300

Abstract

Remote sensing applications using radar systems require specific signal processing to obtain high resolution for radar imagery. This high resolution is essential in detection and imaging processing and is provided by using synthetic aperture radar (SAR) processing. This chapter describes the application of the multiple-input multiple-output (MIMO) configuration and the orthogonal frequency-division multiplexing (OFDM) concept to overcome some existing limitations with conventional imaging systems as well as to assess the improvements achieved.

Keywords: remote sensing, synthetic aperture radar (SAR), multiple-input multiple-output (MIMO) SAR, orthogonal frequency-division multiplexing (OFDM) SAR, waveform design

1. Introduction

Nowadays, airborne or satellite systems are essential for monitoring and observing the evolution of the Earth. Radar imaging systems make this observation possible through acquiring various information about observed regions. A radar system illuminates a region by transmitting electromagnetic waves at different frequency bands, such as L, S, C or X ones, and this system receives the diffused waves from this region in monostatic configuration. In the case of bistatic configuration, the receiving system is located at another place of the transmitting one. In case of monostatic, one of the greatest advances in radar imaging is the principle of aperture synthesis from a moving radar system in order to obtain high-resolution images. This technique is widely known as synthetic aperture radar (SAR). A SAR system provides required data for different applications such as polarimetry, interferometry and tomography. These techniques make it possible to collect various information about the region of interest. Thus, we can retrieve intrinsic characteristics such as soil properties (roughness, moisture), vegetation information (type of vegetation and height of vegetation) or urban density. However, radar imaging techniques are dependent on the characteristics of the SAR imaging system.

Among other parameters, capabilities to obtain the information of the region of interest depend on the spatial resolutions of the imaging system and the global signal-to-noise ratio (SNR). Actually, high resolution for a radar system is essential for detection and image processing and a high SNR is the first condition to achieve good spatial resolutions. Specific geometric configurations and signal processing provide opportunities to reach high spatial resolutions and to enhance system performances. This chapter describes the application of the multiple-input multiple-output (MIMO) configuration and the orthogonal frequency-division multiplexing (OFDM) concept to overcome some existing limitations with conventional imaging systems. Moreover, we propose how to assess the achieved improvements.

The chapter is divided into three sections. In Section 2, we briefly explain the basic characteristics of a radar imaging system and the signal processing applied to obtain radar images. This introduction is important to exhibit the challenges of the MIMO configuration and the OFDM concept. We describe the steps providing a SAR image and the corresponding paragraph deals with the description of a radar system and the respected geometric configuration. The SAR signal processing is also addressed to describe the SAR image characteristics. In Section 3, we present the MIMO configuration. The MIMO principle is based on several transmitting antennas and several receiving antennas. This transmission/reception configuration is widely used in digital communication applications. For radar applications, this kind of configuration leads to numerous improvements such as moving target identification or radar resolutions. In this section, we synthesise the different approaches of the MIMO radar in a colocalised configuration and we describe the SAR processing relied on. Also, we present different opportunities to exploit the spatial diversity given by the MIMO radar. We evaluate performances of different methods by analysing the effect of the SAR resolution and the noise robustness. The processing assessment is essentially based on the peak sidelobe ratio (PSLR) and the integrated sidelobe ratio (ISLR). Finally, some examples through simulations (basic system and operating spaceborne system) and measurements (ground-based SAR system) are provided to illustrate our developments. Section 4 deals with the OFDM signal. For digital communications, OFDM signals have shown many advantages such as the allocated bandwidth optimisation or the robustness against impulsive noise. For radar applications, using OFDM signals is essential in context of MIMO radar to reach the transmitted signal orthogonality. In this section, we present the use of OFDM signals for SAR imagery by describing OFDM single-input single-output (SISO) SAR configuration. Moreover, we propose to illustrate the range ambiguity in radar images and the way to remove the unexpected phenomena. Thus, we design OFDM radar signals to reduce range ambiguity in SAR images based on radar image parameter such as PSLR and ISLR. At the end of this section, we give examples through simulations (basic system and operating spaceborne radar). Finally, we combine OFDM waveforms and the MIMO configuration to achieve a SAR image in Section 5. Section 6 concludes this chapter.

2. SAR processing

The SAR technique is well-known as a high spatial resolution signal processing. In other words, this technique makes possible to obtain resolutions in range and azimuth of the radar

image less than around 30 cm in both dimensions [1]. This method is based on the signal focusing both along range axis and azimuth axis. The high resolution in range is obtained by using the properties of the transmitted signal and especially the bandwidth of this signal. Along the azimuth axis, the high resolution is related to the combination of different signals received at different times that induces the radar sensor to move along the azimuth axis. We propose to deal with the SAR processing with respect to the performances we address in this chapter. In our case, these performances are relied to SAR image characteristics such as range ambiguity and radar image resolutions. The radar signal processing is the way to reach these requested SAR image characteristics. Moreover, these image characteristics are based on the radar geometric configuration.

2.1. Radar geometric configuration

Let us consider the geometric configuration described in **Figure 1**. The geometry related to the radar sensor is partially described by the antenna aperture angles both in elevation β_e and azimuth β_{az}. These angles determine the footprint of the radar. On the one hand, the angle β_e determines the swath width W_s of the radar along the range axis and the elevation angle α_e aligns the illuminated area away the azimuth axis with respect to the height H of the radar sensor. On the other hand, the angle β_{az} determines the azimuth swath width W_{az}. The distance and azimuth swath widths determine the maximum observation distances of the radar along these dimensions. The single ground scatterer n is located on the illuminated area at the coordinates $\left(x_{sol\_n}, y_{sol\_n}\right)$ with respect to the range-azimuth plane. When the radar imaging process is applied, the region of interest is imaged regarding the line-of-sight (slant). Consequently, the image of the ground scatterer n located on the ground is then projected onto this axis of sight and is depicted with the coordinates $\left(x_n, y_n\right)$ in the slant-azimuth area. The following descriptions deal with SAR images, which are referenced in the slant-azimuth area unless otherwise specified. The transformation from the slant-azimuth area to the range-azimuth area is carried out by means of a projection of the ground plane onto the slant plane.

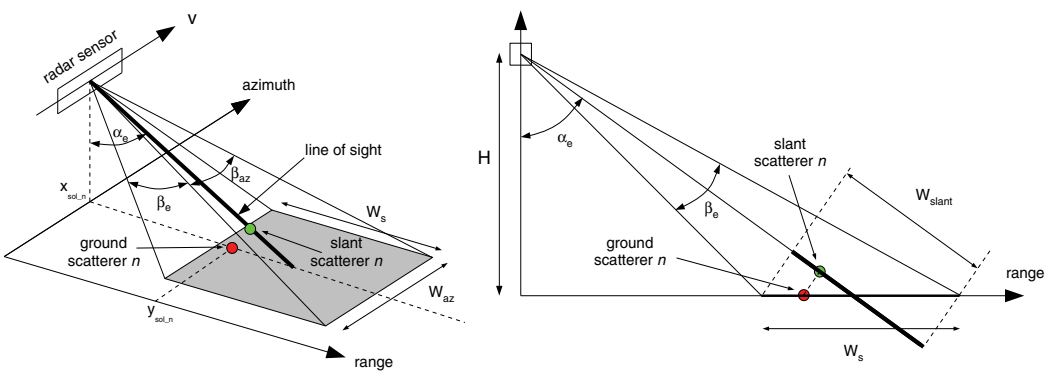

Figure 1. SAR geometric configuration.

2.2. SAR signal processing

As mentioned before, the spatial resolutions δ_{az} along the azimuth axis and δ_{rg} along the range axis require a transmitted bandwidth B and a radar motion v. The considered geometric configuration (see **Figure 1**) is that of a stripmap radar image. The elements we describe are useful in the following sections to deal with MIMO configurations and waveform design.

2.2.1. Pulse compression

The transmitted signal is $s_e(t)$ as a frequency-modulated periodic signal (chirp) of magnitude A_0 and having a bandwidth B centred around the carrier frequency f_c. This signal is defined with

$$s_e(t) = A_0 \,\mathrm{rect}\left(\frac{t}{T_p}\right) \exp\left(i2\pi\left(f_c t + Kt^2\right)\right) \tag{1}$$

where $\mathrm{rect}\left(t/T_p\right)$ is the rectangular window of T_p duration and K is the frequency slope of the chirp, that is, $K = B/T_p$. Finally, the signal $s_e(t)$ is transmitted with a rate of pulse repetition frequency (PRF), which is considered to be much lower than $1/T_p$. Considering a single ground scatterer located at a distance R away from the radar and characterised with a radar cross section (RCS) σ, the received signal obtained after a matched filter processing based on the transmitted signal (Eq. (1)) is given by

$$s_{rc}(t) = A\sigma T_p \exp\left(-i\Phi\right) \mathrm{sinc}\left[KT_p\left(t - \frac{2R}{c}\right)\right] \exp\left[i2\pi f_c\left(t - \frac{2R}{c}\right)\right] \tag{2}$$

where $\Phi = \pi B\left(t - \frac{2R}{c}\right)$ and the coefficient A includes all the propagation losses and the other elements involved in the radar equation. We can deduce the range resolution related to the mainlobe width of the sinc function in Eq. (2) with

$$\delta_{rg} = \frac{c}{2B} \tag{3}$$

It is worth to notice the influence of the bandwidth B on the SNR of the radar sensor [2]. Actually, if we consider P_t as the transmitted power (in our case, $P_t = \mathrm{PRF}\ \ T_P A_0^2/2$) before pulse compression through G_a (the antenna gain) and for the wavelength $\lambda_c = c/f_c$, the SNR after matched filtering by the radar sensor is described with

$$\mathrm{SNR} = \frac{P_t G_a^2 \lambda_c^2 \sigma}{(4\pi)^3 R^4 P_n} B T_p \tag{4}$$

Because the noise is uncorrelated to the transmitted pulse, the noise power is not modified by the pulse compression processing contrary to the transmitted signal involved in the pulse compression processing, which is amplified by a factor $B T_p$.

2.2.2. Synthetic aperture along azimuth axis

In this work, we use the backprojection algorithm to focus the reflected signals acquired along the moving path of the radar. In the slant-range plane, the geometric configuration is reminded in **Figure 2**. The reflected signal is acquired along the azimuth path limited by the length L, which is also called the synthetic antenna length. The backprojection method is based on the temporal correlation between the theoretical response of each pixel of the final image corresponding to the coordinates (x, y) on the region of interest with the set of received signals $s_r(t, u)$ for each u position. The coordinates are calculated regarding the reference point $(X_c, 0)$. Let us consider a single point scatterer located at (x_n, y_n) coordinates. At a given u position, the received signal is then defined with

$$s_r(t,u) = A\sigma \,\mathrm{rect}\left(\frac{y_n - u}{W_{az}}\right) s_e\left(t - \frac{2R(u)}{c}, u\right) \tag{5}$$

The distance $R(u)$ varies as a function of u and is equal to $R(u) = \sqrt{x_n^2 + (y_n - u)^2}$. The rectangular window limits the visualisation of the scattering reflecting point by the radar system as a function of its u position and the y_u azimuth position of the reflector point: if $|y_n - u| > W_{az}/2$, then this point is not seen by the radar. Finally, the correlation is carried out by means of matched filters with respect to the geometric configuration. The focused image function $f(x, y)$ corresponds simultaneously to matched filter processing both along range axis and azimuth axis.

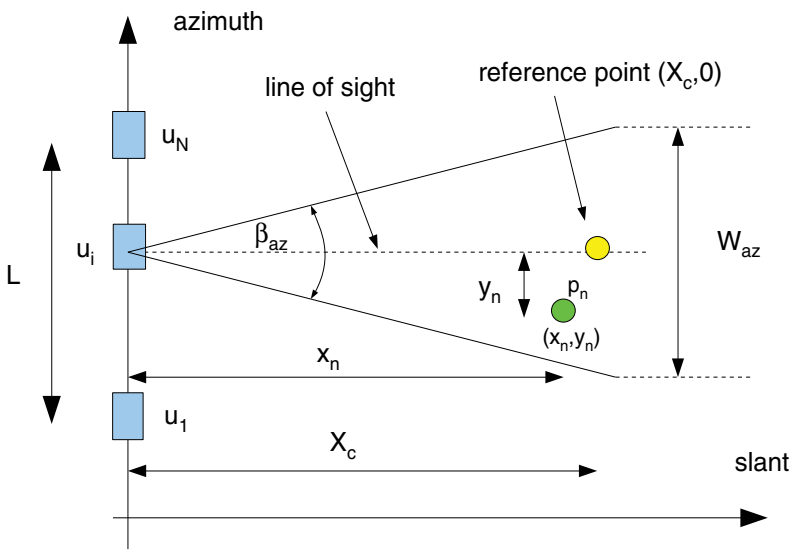

Figure 2. SAR geometric configuration in the slant-range area.

2.3. SAR image characteristics

The two-dimension matched filtering is finally given with

$$f(x,y) = \exp\left(-i2\pi f_c \frac{2x}{c}\right) \int_{y_n - W_{az}/2}^{y_n + W_{az}/2} s_{rc}(\tau(x,y),u) \exp\left(-i2\pi f_c \tau(x,y)\right) du \tag{6}$$

where $\tau(x,y) = 2R(x,y)/c$. Based on the formulation of Eq. (6), one can express the theoretical azimuth resolution δ_{az} [3]:

$$\delta_{az} = \frac{D}{2} \tag{7}$$

if the value of L is sufficient to entirely cover the area under image processing. We can note that Eq. (6) is described with respect to the delay $\tau(x,y)$ and the u position. Thus, the sampling of the range compressed signal achieves the adaptation to the $(\tau(x,y),u)$ samples by means of an oversampling operation (so-called zero-padding operation in the spectral domain) and a linear interpolation. The backprojection procedure is described in **Figure 3** and a result of this procedure is also exhibited in **Figure 3** for nine point scatterers.

Until now, the radar system is presented as an ideal one. Actually, the electromagnetic wave used to make a radar image undergoes perturbations due to different factors [2]. The first kind of disturbances affects the received power:

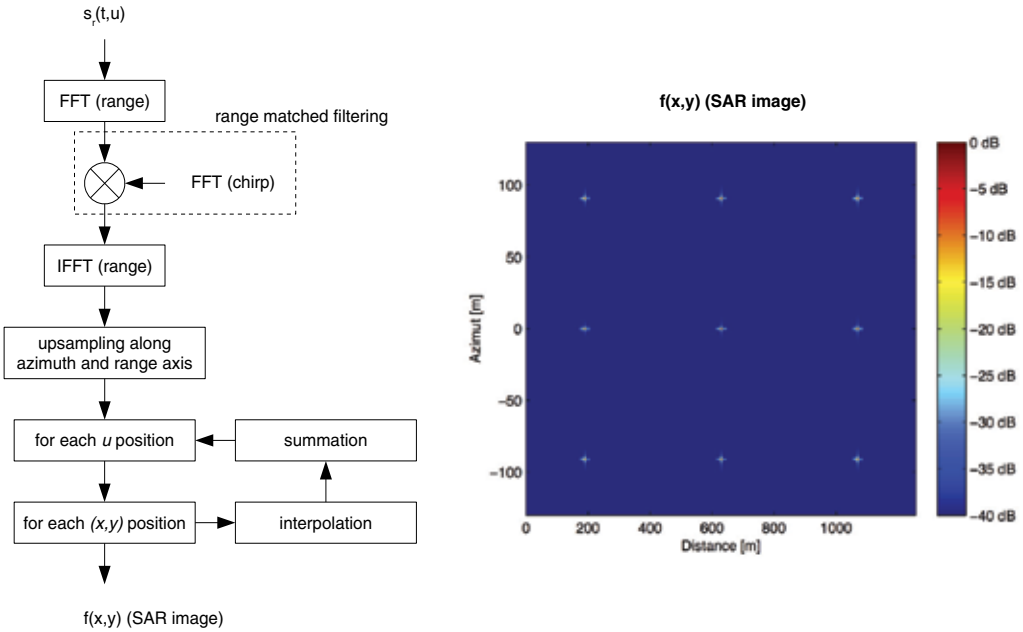

Figure 3. Backprojection procedure and nine point scatterers SAR image.

- Power loss related to the transmitter during the transportation of the transmitted signal between the signal generator and the antenna. The use of coaxial cables or waveguides implying a loss in the transmitted power compared to that generated (loss around 3 or 4 dB according to the signal characteristics, to the wavelength of the carrier, to length of the cable or of the waveguide…);
- Power loss related to the media that the electromagnetic wave run through during the transmission. The electromagnetic wave passes through different media with different attenuation and phase shift properties. As an example, in the case where the wave passes through the atmospheric medium, it suffers losses, which are expressed in dB per km. This loss is related to the interaction between the electromagnetic wave and the molecules contained in the atmosphere and depends on the carrier frequency of the transmitted wave;
- Power loss related to the receiver during the reception of the electromagnetic wave by the antenna during the transmission to the information sampling and storage components. This transfer involves losses of the same order as during transmission.

Other perturbations are possible such as:

- Noise related to on-board electronics (example of receiver noise),
- Electromagnetic waves diffused by reflectors in the area to be imaged (example of the speckle phenomenon visible on a radar image),
- Electromagnetic waves from reflectors not in the area to be imaged but creating ambiguities in range or azimuth on the radar image,
- Electromagnetic waves coming from other applications, and which disrupt the radar image interpretation (example of jammers).

The following section of this chapter mainly focus on either the different MIMO configuration to make radar system more robust against noise through the SAR processing and range ambiguities, which can be mitigated by using specific waveform design such as OFDM.

3. MIMO configuration

In this section, we present firstly the limitations regarding the SISO SAR configuration relied to the chirp waveform transmitted signal. We introduce some processing and system design solutions based on the MIMO principle, to overcome these limitations. This principle is addressed through the various radar configurations and its application to SAR imagery, called MIMO SAR. Comparing with SISO radar, we focus on the robustness of signals to noise and interference and on azimuth resolution. We describe the SNR to assess the influence of the MIMO configuration comparing to the SISO one. The SNR expression we propose is based on the lossless radar equation as described with Eq. (4). Many ways to reduce the noise influence are based on using bandpass filters [4] with low bandwidth that drives thermal noise at the receiver systems down. Other methods exist by using multiple antenna configurations as multiple-input single-output (MISO) for transmitting approach or single-input multiple-output

(SIMO) for receiving approach. In case of a complete combination (M receiving antenna and N transmitting antenna), which is the MIMO configuration, the SNR equation yields [5]:

$$\mathrm{SNR}_{\mathrm{MIMO}} = N^2 M^2 \frac{P_e G_a^2 \lambda_c^2 \sigma}{(4\pi)^3 R^4 P_n} B T_p \tag{8}$$

Thus, we notice easily that by increasing the number of transmitting and receiving antennas, we obtain an improvement of the SNR in relation to the number of antenna.

Nevertheless, concerning the problem related to radar imagery, the SNR coefficient does not make the measurement of radar image quality possible. It is therefore necessary to use other parameters, which take into account the imaged region of interest. These parameters measure the effect of disturbances on the radar image. Thus, two SAR image parameters are commonly used to assess the image quality: the so-called PSLR and ISLR. Considering a SAR image composed of discrete elements z_n, that is, the pixel, we introduce these two image quality parameters with [6]:

1. The ratio between the amplitude of the most powerful sidelobe and the amplitude of the mainlobe. This ratio is called PSLR and is expressed with:

$$\mathrm{PSLR} = \frac{\max\limits_{n \in I \setminus I_0} |z_n|^2}{\max\limits_{n \in I_0} |z_n|^2} \tag{9}$$

where $|z_n|$ is the magnitude of the pixel n in the image, I is the set of all the pixels belonging to all the image (mainlobe and secondary lobes), and I_0 is the set of the pixels belonging to the mainlobe;

2. The ratio between the energy contained in the secondary lobes and the energy in the mainlobe. This ratio is called ISLR and is formulated with:

$$\mathrm{ISLR} = \frac{\sum\limits_{n \in I \setminus I_0} |z_n|^2}{\sum\limits_{n \in I_0} |z_n|^2} \tag{10}$$

These two parameters are defined on the basis of the impulse response, that is to say by considering the presence of a single scatterer on the region of interest. In the case of the PSLR parameter, we measure the radar system capability to image scatterers having a low RCS with respect to scatterers having a much stronger RCS. Indeed, the secondary lobes associated with a scatterer having a strong RCS may mask the presence of scatterers having a much lower RCS. The PSLR parameter, thus reflects the appearance of a parasitic object on the region of interest. In the case of no artefact, the PSLR parameter value is obtained from the first secondary lobe of the impulse response related to the image of the point scatterer. In the case of ISLR, we measure the interference amount and noise located in the region of interest [7]. By taking into account the relation between the number of antenna and the SNR formulated in case of MIMO

configuration (Eq. (8)), it is therefore possible to decrease the ISLR value more efficiently than with a SIMO or a MISO configuration.

3.1. Coherent MIMO radar and SAR processing

In this paragraph, we consider a coherent MIMO radar system (C-MIMO) composed of a linear array with M transmitting antennas and a linear array of N receiving antennas (**Figure 4**). The C-MIMO means that the distance between the radar and the target is high compared to the distance between antennas. The transmitting antennas are separated from each other with a distance d_T and the receiving antennas with a distance d_R. The transmitting (receiving) antennas are close enough to each other to consider the transmitting (receiving) angles of the transmitted and received signals, respectively, equal to the same angle θ (see **Figure 4**) that means the distance of the scene far away the radar is more greater than d_R and d_T.

Moreover, each of the M antennas transmit signals $(\phi_i(t))_{i\in[1,M]}$ that are orthogonal to each other. In case of non-orthogonal waveforms, we have to design $\phi_i(t)$ signals with the lowest correlation level to each other. The SAR processing that we applied to this MIMO configuration is based on applying matched filters in range that makes it possible to separate different transmitted signal at the reception. After this step, $M \times N$ signals with a low cross-correlation level are available on which we apply matched filters in azimuth with respect to the SAR geometric configuration as described in Section 2.

The MIMO SAR system concept is widely described and different design strategies for the receiver are proposed in the literature [5, 8, 9]. The MIMO imaging procedure is mainly based on applying SAR processing (back projection or Omega-K method) on the signals available at the matched filters (range and azimuth). Also, the MIMO SAR system is made to obtain a better SNR and consequently a better robustness against noise and better resolution in azimuth with respect to the SISO configuration possible. Another strategy is the joint use of specific waveforms (rather than the chirp one) and new kind of reception filters [10, 11]. This strategy improves the PSLR and ISLR levels and therefore makes the radar system more robust.

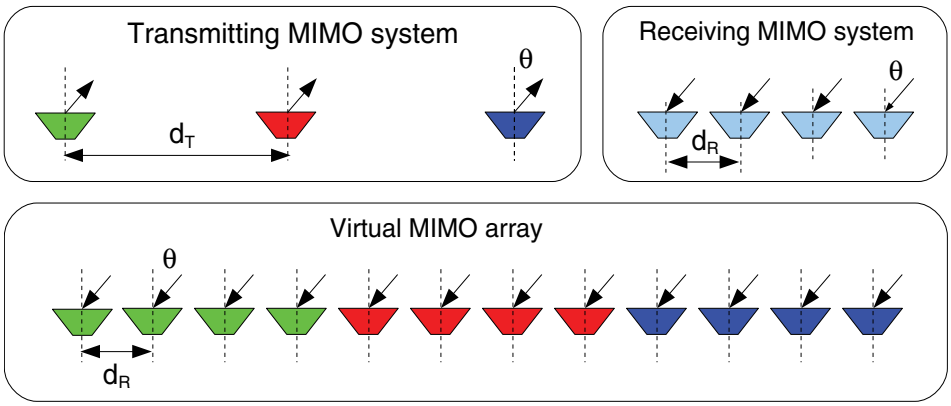

Figure 4. Uniform virtual MIMO array principle.

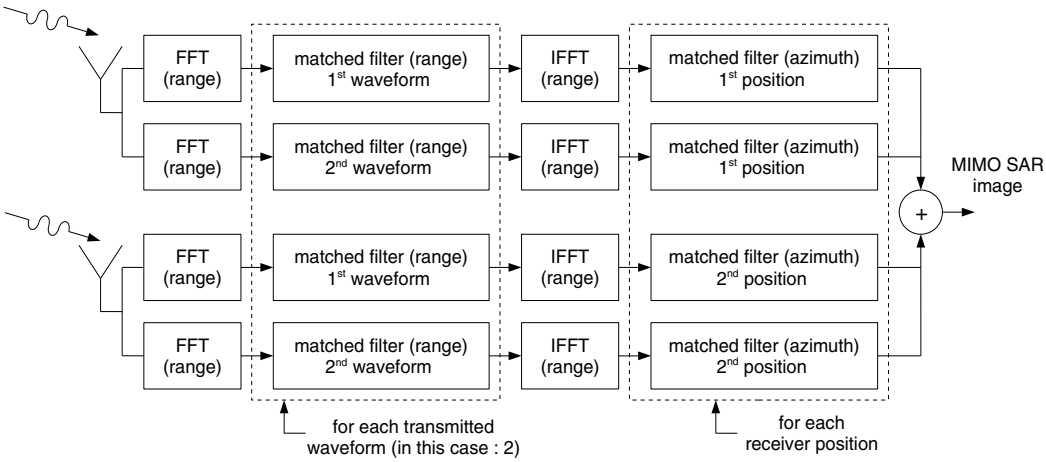

Figure 5. SAR images coherent sum.

Although many receiver designs were examined in [12], we propose to describe the results we obtain with the receiver design exhibited in **Figure 5**. The applied method uses $M \times N$ couples of transmitter and receiver combinations. For each couple, a SAR image is provided through a basic SAR processing and the final MIMO SAR image is given after a scalar sum of each SAR image.

3.2. Method assessment

To evaluate the robustness of the MIMO configuration, we compare the results we obtained for the SISO and MIMO configurations. These assessments are based on the PSLR and ISLR measurements, defined in Eqs. (9) and (10), respectively. Moreover, we extract the azimuth resolution δ_{az} by evaluating the mainlobe width at -3 dB for a point-like target respons along the azimuth axis.

3.2.1. Simulation

The geometric configuration is shown in **Figure 6**. The radar imaging system consists of two transmitting antennas and two receiving antennas. The transmitted signals are of the chirp type (up and down-modulated) whose carrier frequency f_c is 6 GHz. The bandwidth B of these chirps is 1 GHz and is centred around the carrier frequency f_c. The transmit antennas identified with (1) and (2) in **Figure 6** are spaced 1 m apart, that is, $40 \times \lambda_c/2$, and the receiving antennas identified with (3) and (4) in **Figure 6** are spaced 12 cm apart, that is, approximately $2 \times \lambda_c/2$ This configuration matches the co-located condition because the maximum range is about 2.5 m. The imaging system is located at a height $H = 2.40$ m from the ground with an incidence angle α_e of 45°. The azimuth aperture angle for each antenna is β_{az} = 54°. The point-like scatterer is located at a slant range of 4.55 m and at -0.22 m in azimuth. Finally, we consider a radar data collection along a 3 m azimuth distance (± 1.5 m). As the azimuth displacement is limited to 3 m, the considered antennas for the SISO configuration are located at position (3) and (4) in **Figure 6**

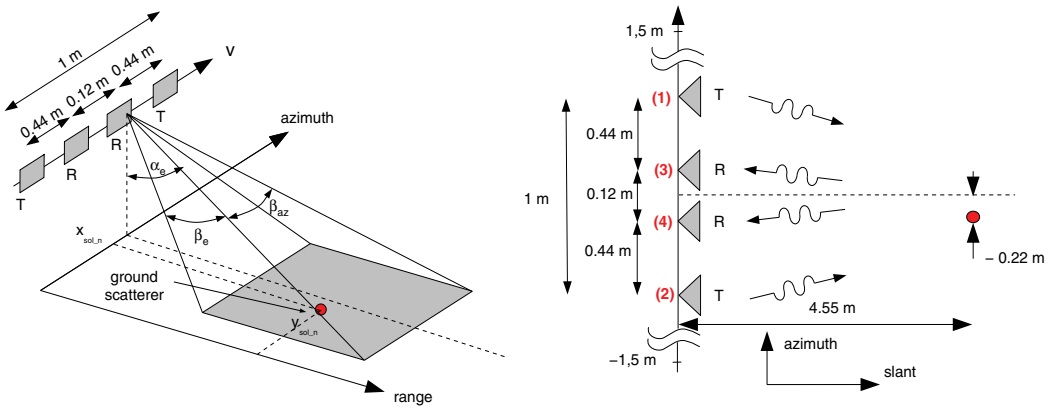

Figure 6. Geometric configuration used in simulation.

for the receiver and the transmitter, respectively. When white Gaussian noise is considered for simulations, the SNR level is set up to −30 dB at the receiving stage. Also, we have SAR images for both SISO and MIMO configurations, which are exhibited in **Figure 7**.

Moreover, the results we obtained in noisy conditions or not, for the azimuth resolution, ISLR and PSLR, are given in **Table 1**.

As a conclusion, the azimuth resolution is slightly improved for the MIMO situation that could be planned because of the coherent summation of different SAR images. Moreover, we obtained lower PSLR and ISLR levels for MIMO configuration than for the SISO one that means the better robustness of MIMO system against noise for radar imaging.

3.2.2. Measurement

The experimental system is shown in **Figure 8**.

The radar system uses a vector network analyser (VNA) transmitting a step frequency continuous waveform. The SAR processing is based on a stop & go configuration. The experimental settings match those used by the simulation: the carrier frequency is 6 GHz, the transmitted bandwidth is 1 GHz and this MIMO radar system is also composed of four antennas, which are arranged as described in **Figure 6**. In the same way, the radar scene consists of a metallic trihedral arranged on the ground to obtain the same experimental conditions described in **Figure 6**. The VNA is placed on a 3 m rail that provides the displacement to perform the SAR processing. The images provided by this experimental system are then obtained for SISO and MIMO configurations and are exhibited in **Figure 9**.

Consequently, different values for the azimuth resolution, PSLR and ISLR are obtained and shown in **Table 2**. As mentioned in Section 3.2.1, the results obtained with the experimental measurements confirm those obtained with the simulated configuration even if the values are slightly different, that is mainly due to the measurement conditions.

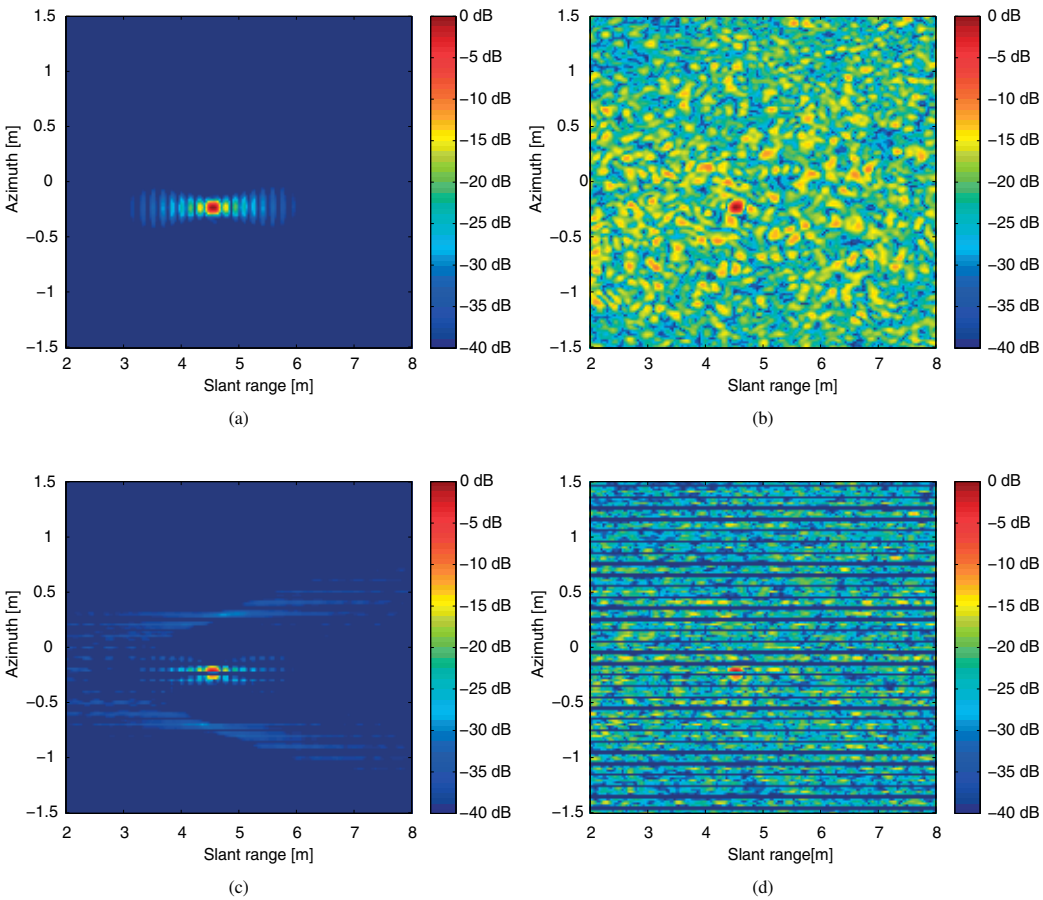

Figure 7. SISO and MIMO SAR images provided by simulation.

	Azimuth resolution (m)	PSLR (dB)	ISLR (dB)	PSLR (dB)	ISLR (dB)
		Without noise		With noise	
SISO	0.056	−13.9	−31	−9.5	−11.7
MIMO	0.048	−14.2	−31	−11.2	−14.4

Table 1. Simulation results of the azimuth resolution, PSLR and ISLR for SISO and MIMO configuration.

3.3. Discussion

Section 3 proposes an application of the MIMO principle to SAR imagery. Simulations and experimental measurements are conducted to quantify the gain we are able to obtain by using a MIMO configuration rather than a SISO one. For the given receiver design, the performance improvements are noticeable whether by simulation or by measurement. Thus, the use of the MIMO principle in SAR imagery reinforces the robustness of the radar system against noise.

http://dx.doi.org/10.5772/intechopen.71300

Figure 8. Overview of the measurement system.

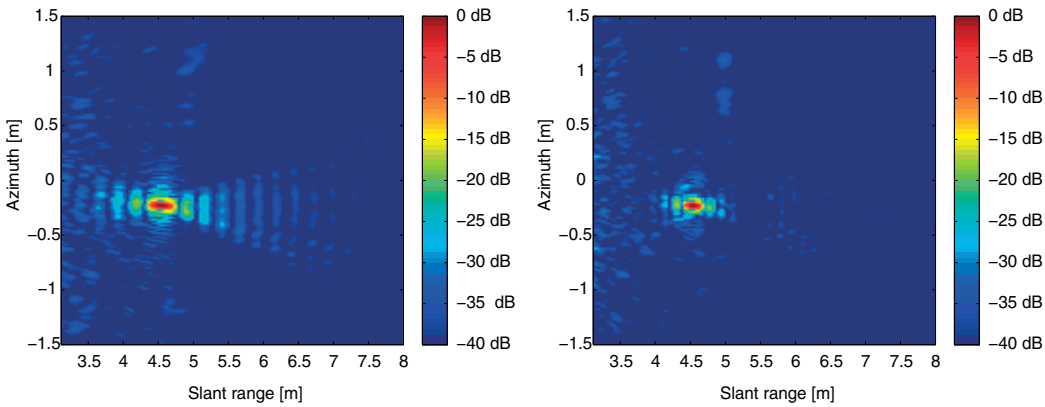

Figure 9. SISO and MIMO SAR images provided by measurements.

	Azimuth resolution [m]	PSLR [dB]	ISLR [dB]
SISO	0.043	−13.6	−31.4
MIMO	0.038	−15.3	−34.8

Table 2. Measurement results of the azimuth resolution, PSLR and ISLR for SISO and MIMO configuration.

Moreover, the MIMO principle does indeed to improve the azimuth resolution even this improvement is low and may be considered as negligible in the case of 2-by-2 MIMO configuration.

At this point, it is worth to notice that these improvements can be achieved under the orthogonal transmitted waveform condition. In this section, the up- and down-modulated chirp makes it possible to partially reach this orthogonal condition. Nevertheless, many applications require a better orthogonality criterion or need more than two transmitted waveforms. For this purpose, frequency modulation techniques are useful to get low correlation level between two signals.

4. OFDM design

The OFDM is based on frequency division multiplexing (FDM) in which subchannels overlap without interfering and with the minimal frequency spacing. It is a modulation technique widely used in wireless communication systems such as access networks, cellular networks, broadcast networks and also in wireline communication systems such as digital subscriber line (DSL) and powerline communications (PLC). With OFDM, the data are transmitted in parallel subchannel, which means that the channel distortion experienced by each subchannel decreases. The channel equalisation procedure at receiver side is then simplified with the respective complexity increase counterpart at transmitter size. With the availability of efficient software and electronic technologies, the modulation at the transmitter side is efficiently realised with the inverse fast Fourier transform (iFFT). The continuous baseband signal using N subchannels, also called subchannels, and transmitting N complex data symbols a_i is defined with

$$s_e(t) = \frac{A_0}{\sqrt{N}} \sum_{i=1}^{N} a_i \exp\left(i2\pi f_i t\right) \mathrm{rect}\left(\frac{t}{T_p}\right) \tag{11}$$

where the subchannel spacing $|f_i - f_{i+1}|$ is equal to the inverse of the symbol time length $1/T_p$. The OFDM transmission mainly consists in iFFT transform of the data a_i at the sampling time T_p/N. The data symbols are recovered with an FFT at receiver side.

One of the major benefits of OFDM transmission is the spectrum design. Holes in the spectrum can be simply created by turning off some subchannels obtained with $a_i = 0$ for the corresponding subchannel i, as shown in **Figure 10**.

This key advantage is used in waveform radar design to increase the localisation and the tracking of targets in noisy environment [13], to increase the robustness of target detection in jamming scenarios [14], to improve efficient computational performance in 2D SAR imaging scenarios [15] and the OFDM is also considered as one proper waveform for communication-radar integrated system [16]. These few examples show the potential of the OFDM waveform to meet the needs of radar and especially SAR applications.

The first capability measure of the OFDM waveform for radar application is the ambiguity function. With respect to the delay τ and the frequency Doppler ν, this ambiguity function using Eq. (11) and in the case where $f_i = \left(i - \frac{N+1}{2}\right)\frac{1}{T_p}$ is [17]

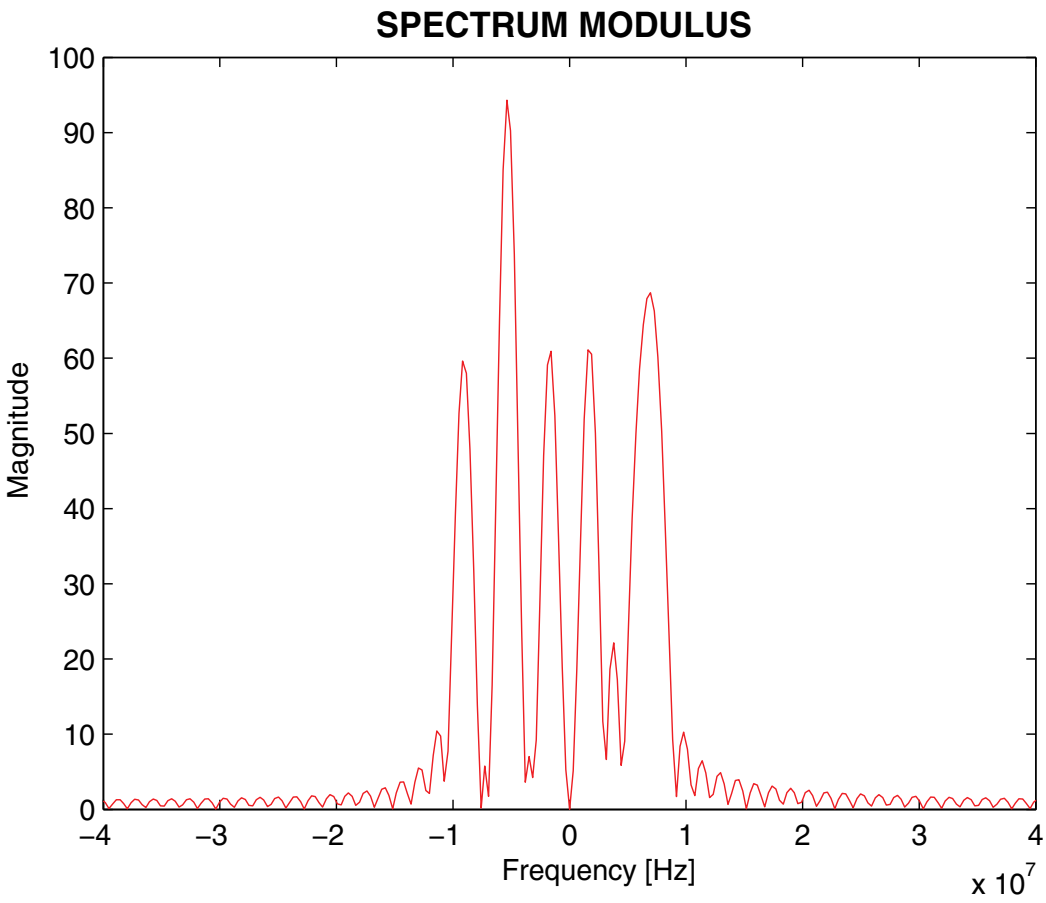

Figure 10. OFDM signal spectrum with $(a_i)_{i=1}^{13} = [1011010100110]$.

$$\chi(\tau,\nu) = \left(T_p - |\tau|\right)\frac{A_0^2}{N}\sum_{i=1}^{N}\sum_{j=1}^{N} a_i a_j^* \exp\left(i\pi\left(i-j+\nu T_p\right)\right)\exp\left(i\pi\left(i+j-N-1+\nu T_p\right)\frac{\tau}{T_p}\right) \times \operatorname{sinc}\left(\pi\left(i-j+\nu T_p\right)\frac{|T_p-\tau|}{T_p}\right) \tag{12}$$

This ambiguity function is described in **Figure 11** with $N = 17$[1]. The increase of the number N of subchannels causes a decrease of the mainlobe size in the Doppler domain but does not change the mainlobe size in the delay domain. We will see that the choice of the line vector $[a_1, \cdots, a_N]$ with $a_i \in \{0,1\}$ is important and is managed by the goals of the application. We present in this chapter the case of OFDM waveform design for range ambiguity cancellation.

[1] In this case, the OFDM is not generated with an iFFT but with a inverse digital Fourier transform (iDFT).

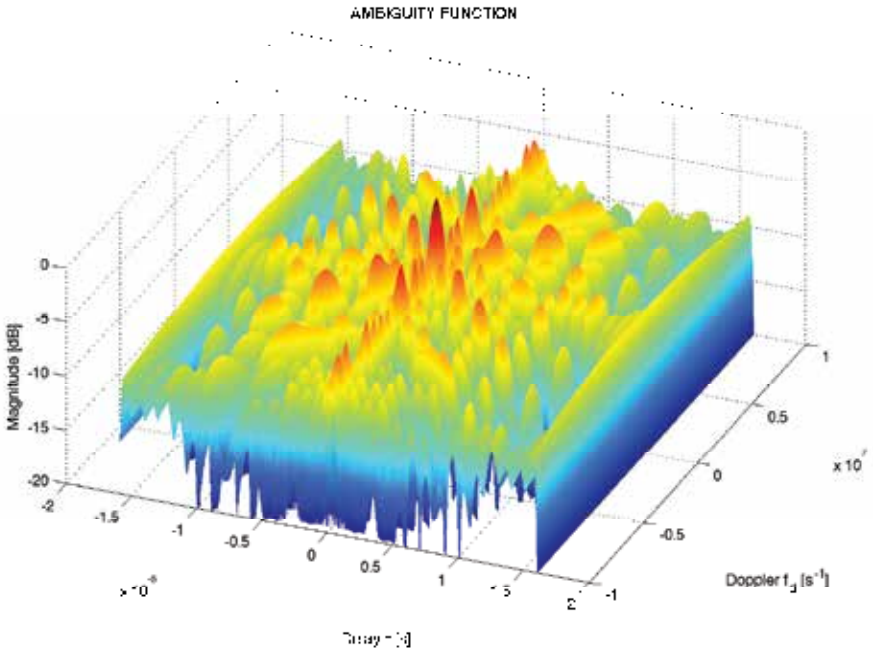

Figure 11. OFDM ambiguity function.

But, before designing the waveform for this task, the OFDM signal has to be characterised regarding the range and azimuth resolutions.

4.1. SAR OFDM signal

The OFDM signal expressed in Eq. (11) has a bandwidth per subchannel equal to $1/T_p$, the inverse of the rectangular pulse time duration. The OFDM signal is composed of N orthogonal subchannels, its total -3 dB bandwidth when all the a_i are set to one is $B = N/T_p$. If $N = KT_p^2$, where K is the frequency slope of the chirp given in Eq. (1), the range resolution of the OFDM signal is same as the chirp one and is given by Eq. (3). The compression and the range resolution driven by the parameter K with the chirp are driven by the parameter N with the OFDM. In both signal cases, the increase of the parameter increases the signal bandwidth and the range resolution.

Considering a single ground scatterer, as in Eq. (2), the range compressed OFDM signal is obtained after the matched filter. With the RF transposition of the baseband signal expressed in Eq. (11) at the frequency f_c, the compressed signal is

$$s_{rc}(t) = A_0^2 \sigma T_p \exp\left(-i2\pi f_c \frac{2R}{c}\right) \frac{1}{N} \sum_{i=1}^{N} \sum_{j=1}^{N} a_i a_j^* \exp\left(i2\pi \left(f_j t - f_i \frac{2R}{c}\right)\right) \operatorname{sinc}\left(f_i - f_j\right) T_p \tag{13}$$

With a full OFDM signal, that is, $\forall i\ a_i = 1$, the pulse compression processing amplifies the SNR by a factor BT_p, as the chirp case does and the SNR is also given by Eq. (4).

As previously mentioned, one of the benefits of the OFDM signal is the spectrum flexibility. The question is then what appends if some a_i are null? In the simple case, where the null subchannels are on the edge of the OFDM spectrum, the signal bandwidth is proportional to the number N_a of active subchannels and the range resolution is

$$\delta_{rg} = \frac{cT_p}{2N_a} = \frac{c}{2B}\frac{N}{N_a} \geq \frac{c}{2B} \tag{14}$$

To obtain the minimal range resolution, active subchannels on the edge of the spectrum are obviously required. The question is now to know if it is possible to create holes in the spectrum without decreasing the range resolution. **Figure 12** gives results in two cases, with $N = 65$.

On **Figure 12a**, the range resolution is plotted versus the number of null subchannels in the middle of the spectrum. When this number of null subchannels is equal to zero, all the subchannels are active and the range resolution is the optimal one given by Eq. (3). With a number of null subchannels lower than 25, the range solution remains the optimal one whereas only 40 % of the subchannels are active. On **Figure 12b**, only two subchannels are active and the range resolution is plotted versus the number of null subchannels between these two active subchannels. When the number of null subchannels between the two active subchannels is equal to zero, the range resolution is given by Eq. (14) with $N_a = 2$. When the number of null subchannels between the two active subchannels increases, the resolution first decreases and secondly increases near the range resolution given by Eq. (14) with $N_a = 2$. Excessive increase of the size of the hole in the spectrum does not allow to keep the minimal range resolution given by the full bandwidth use.

We can conclude that if all the spectrum cannot be used, the OFDM design solution is to keep active the subchannels on the edge of the spectrum and to allow relative small hole within the

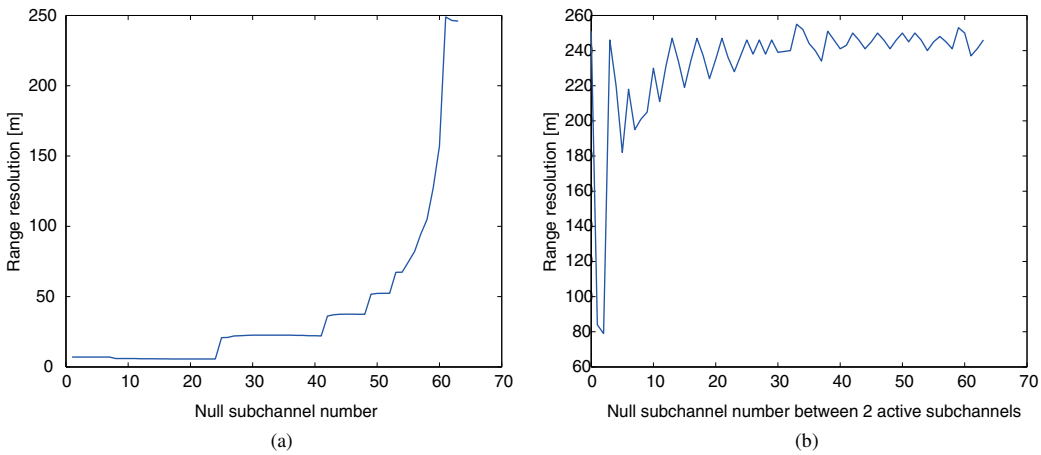

Figure 12. Range resolution versus active subchannels in OFDM signal.

spectrum. This strategy ensures an optimal range resolution. To retain the SNR in Eq. (4), the amplitude A_0 has to be scale to ensure a transmitting power independent of N_a.

4.2. Range ambiguity

The range ambiguity is well-known and studied in radar system [18]. This drawback mainly appears with high wide swath in satellite configuration and results from trade-off between high and low PRF. On the one hand, high PRF induces azimuth ambiguities while reducing the range ambiguities; on the other hand, low PRF induces range ambiguities while reducing the azimuth ambiguities. For example, let PRF_0 be the proper PRF, as shown in **Figure 13**. This PRF is set up to have the maximum swath width without ambiguities. In this case, a scatterer located far out the swath is well imaged as seen in **Figure 14a**.

If the PRF is larger than PRF_0, the scatterer becomes ambiguous as shown in **Figure 14b** and it is then considered as interference. The signal focusing also fails to operate along the azimuth axis and defocusing phenomenon occurs. A scatterer appears in the image at a range andazimuth where there is no scatterer.

The idea of range ambiguity suppression by alternating up and down chirp modulation is often discussed since it is obvious and easy to implement [19]. The goal is to keep a high PRF and to alternate waveforms with cross-correlation values as low as possible. With two different waveforms, the size of the unambiguous delay window is then multiplied by two, compared to the size obtained with the same PRF and with only one waveform. The unambiguous region can then be extended to the overall observed scene. As shown in **Figure 14c**, obtained with up and down chirp modulation, the scatterer is further well localised, as in the left unambiguous image, but a ghost appears due to the finite cross-correlation rejection values, roughly equal to 20 dB. Flexibility of the waveform is then required to improve the cross-correlation properties

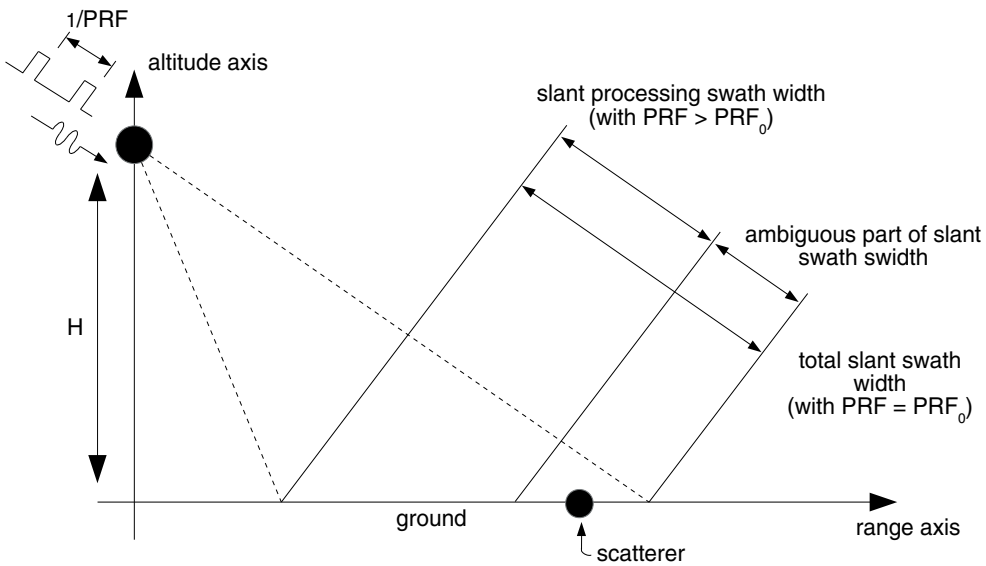

Figure 13. SAR imaging slant geometry taking range ambiguity into account.

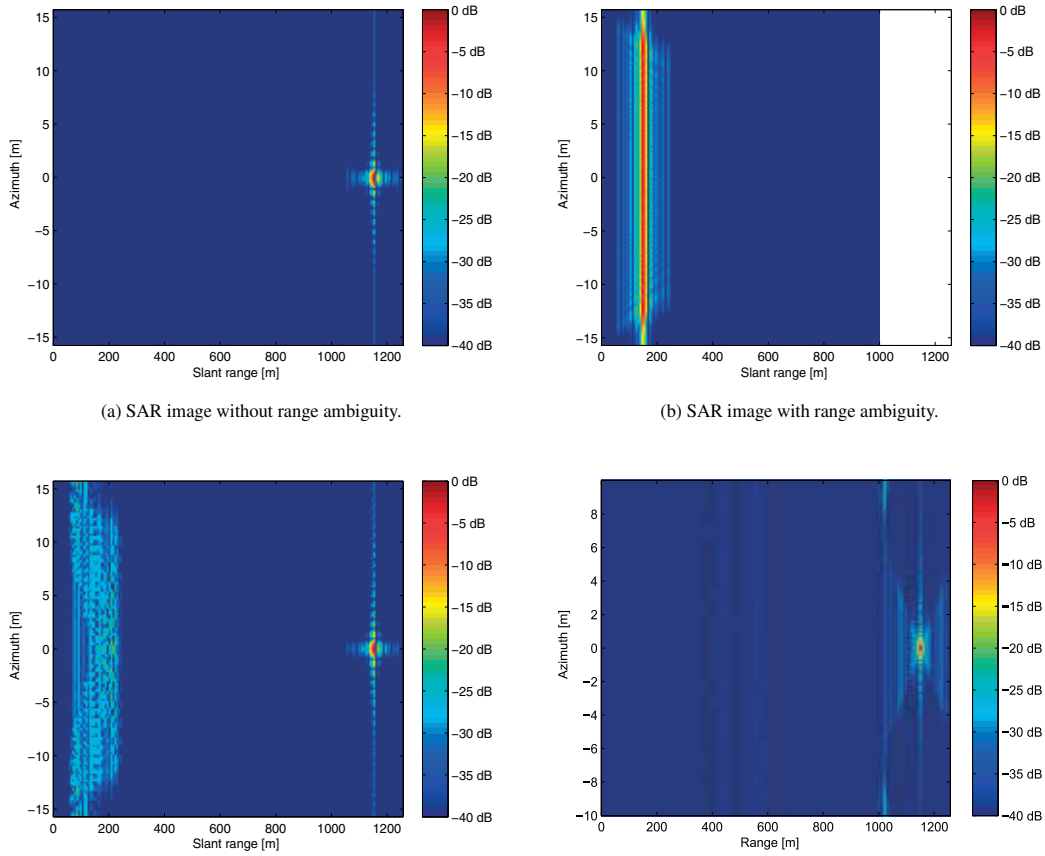

(a) SAR image without range ambiguity.

(b) SAR image with range ambiguity.

(c) SAR image with up and down chirp range ambiguity correction.

(d) SAR image with OFDM range ambiguity correction.

Figure 14. SAR images describing range ambiguity effects and a cancellation of them.

and to reduce the ghost level. The subchannel turning off and turning on capability of the OFDM offers this flexibility.

4.3. OFDM waveform design strategy

To cancel or reduce the range ambiguity phenomenon, we need multiple orthogonal signals or signals with good cross-correlation properties. It is now straightforward that OFDM is a good candidate to ensure this task: it is easy to create orthogonal signals using holes in the OFDM spectrum and at the same time to keep optimal range resolution for SAR applications. We provide an OFDM waveform design in the case of two generated signals, but the method can be extended to a larger number of orthogonal signals.

4.3.1. Signal requirements

To simplify the SAR imaging signal processing, the two signals must have the same characteristics: same carrier frequency, same subchannel frequency and same bandwidth.

The orthogonality of the OFDM spectrum simplify the generation of two orthogonal waveforms. Let $J = \{1, \cdots, N\}$ be the set of indexes of subchannels and two subsets J_a and J_b corresponding to the active subchannels of the signals. If $J_a \subset J$ is the set of active subchannels of the first OFDM signal, that is, $\forall i \in J_a\ a_i = 1$ and $\forall i \notin J_a\ a_i = 0$, then $J_b = J \setminus J_a$ is the set of active subchannels of the second OFDM signal. The orthogonality does not mean that the cross-correlation, given by Eq. (12) with $a_j = b_j = 1 - a_j$ and $\nu = 0$, is equal to zero for all the delay τ. This orthogonality is guaranteed when $\tau = \nu = 0$ and then we obtained easily $\chi_{a,b}(0,0) = 0$ with OFDM signals. However, this orthogonality is not enough to ensure good ambiguity rejection, the maximal relative cross-correlation amplitude should also be taken into account to optimise the signal waveform. This relative cross-correlation amplitude is defined as

$$\Delta\chi(a) = \max_{\tau} \frac{|\chi_{a,b}(\tau, 0)|}{|\chi_{a,a}(0,0)|} \tag{15}$$

and it is a function of a only, because b is completely determined by a.

To ensure optimal range resolution, the subchannels on the edge of the spectrum have to be active for both OFDM signals. However, to keep the orthogonality property, if a subchannel is active in one signal, it should be inactive in the other one. It has been proposed to set $a_1 = a_{N-1} = 1$ and $a_2 = a_N = 0$ in one OFDM signal and $b_2 = b_N = 1$ and $b_1 = b_{N-1} = 0$ in the other one [20]. The range resolution given in Eq. (14) becomes

$$\delta_{rg} = \frac{c}{2B}\left(1 + \frac{1}{N-1}\right) \tag{16}$$

which can be approximated by Eq. (3) when $N \gg 1$.

4.3.2. Optimisation strategy

The objective is to provide high-resolution SAR image. We have introduced two image quality parameters, the ISLR and PSLR, and we have added another parameter, the maximal relative cross-correlation amplitude in Eq. (15).

For spectrum equilibrium reason, N is odd and the subchannel in the middle is set to 0 in all the OFDM signals. Four other subchannels, two at each end of the spectrum, are fixed for range resolution reason. Then, it remains to allocate $N - 5$ subchannels in two OFDM signals. To have equal number of active subchannels per OFDM signal, each signal will have $(N-5)/2$ active subchannels and $(N-5)/2$ null subchannels. One have to choose $(N-5)/2$ active subchannels between $N - 5$ ones and the number of possible couples of OFDM signals are

$$N_{\text{couple}} = \frac{1}{2}\frac{(N-5)!}{\left(\frac{N-5}{2}!\right)^2} \tag{17}$$

With $N = 13$, the number of couples is 35. This low number allows exhaustive performance comparison to find the best couple. However, with higher number of subchannels, allowing higher design flexibility, the exhaustive search of the optimal couple solution becomes

unfeasible. For example, the value $N = 65$ leads to around 60 peta possible couples. To solve this search problem, genetic algorithm has been proposed [21]. This algorithm is based on a population of couple of OFDM signals iteratively modified to converge to the best couple solution. A fitness function is used to evaluate the performance of each couple and it is defined by

$$\psi(a) = \sum_{i=1}^{3} \alpha_i \frac{|\phi_i(a) - \phi_{i,0}|}{\phi_{i,0}} \tag{18}$$

where α_i is the weighting coefficient related to the objective function $\phi_i(a)$, which is equal to the PSLR given by Eq. (9) for $i = 1$, to the ISLR given by Eq. (10) for $i = 2$ and it is equal to the relative cross-correlation amplitude given by Eq. (15) for $i = 3$. The value of the objective functions is normalised by the reference values $\phi_{i,0}$ equal to or lower than $\min_a \phi_i(a)$.

The genetic algorithm is composed of five steps:

1. *Initialisation.* The first population of couples is randomly chosen. It is called the first generation;
2. *Evaluation.* The fitness function is calculated for each couple of the population;
3. *Selection.* It is a roulette-wheel selection and the selected couples are retained for the next generation. The selection is based on the value of the fitness function. The couples with high fitness function values are more likely to be selected for the next generation;
4. *Mutation.* Each selected couple is modified with a specific mutation probability. It means that each element of the vector a has the specific mutation probability to have its value changed;
5. *End condition.* The algorithm stops when the number of desired generations is reached, otherwise a new cycle of evaluation, selection and mutation starts. As the aim of the genetic algorithm is not to search for the all possible solutions, the ending condition limits the searching sub-space dimension by defining the expected number of generations.

To ensure the convergence of the algorithm to a local optimum, the couple with the lowest value of the fitness function in one generation is added unchanged to the next generation, that is, without mutation.

4.4. Simulation results

Although the range ambiguity mainly appears with high wide swath in satellite configuration, we consider an airborne configuration to evaluate the performance of the SAR imaging system in reasonable time. High value of the PRF is then chosen to increase the ambiguity phenomena. The carrier frequency of the transmitted signal is $f_c = 6$ GHz, the -3 dB signal bandwidth is 20 MHz and the number of subchannels of the OFDM signal is $N = 65$. The radar pulse length is $T_p = 3.25$ μs and the azimuth aperture angle is $\beta_{az} = 14.44^\circ$. The imaging system is located at a height $H = 3678$ m from the ground with an incidence angle $\alpha_e = 43.66^\circ$ is 1258 m whereas the PRF is 26.92 kHz, which leads to a unambiguous slant swath of 1000 m. This configuration

leads to an ambiguous configuration illustrated in **Figure 14**. The mutation parameter of the genetic algorithm is 20%, which ensures the search of a new solution close to the ones already found. The simulations are performed with the reference value $\phi_{i,0}$ given in **Table 3** and the weighting coefficients α_i are set to 1.

Figure 15 gives the lowest value of the fitness function for each generation. The genetic algorithm is applied five times to produce five optimised couples. The lowest value of the fitness function becomes quite flat after 15 iterations. We can conclude that this number of generation is enough to ensure a good optimised couple and **Table 3** gives the value of the objective function for each optimised couple. This table shows that the OFDM optimised signals outperform the chirp signals for all objective functions. **Figure 14d** shows the SAR

Optimisation	**PSLR [dB]**	**ISLR [dB]**	$\Delta\chi$ **[dB]**
#1	−18.5	−43.6	−11.3
#2	−18.5	−43.6	−11.4
#3	−18.5	−43.5	−11.6
#4	−18.5	−43.6	−11.0
#5	−18.3	−43.4	−12.1
Full OFDM	−16.4	−48.1	
Chirp couple	−13.9	−40.8	−9.2
$\phi_{i,0}$	−20	−48	−14

Table 3. PSLR, ISLR and $\Delta\chi$ for the different OFDM optimised couples (#1–#5) and a comparison with others transmitted signals.

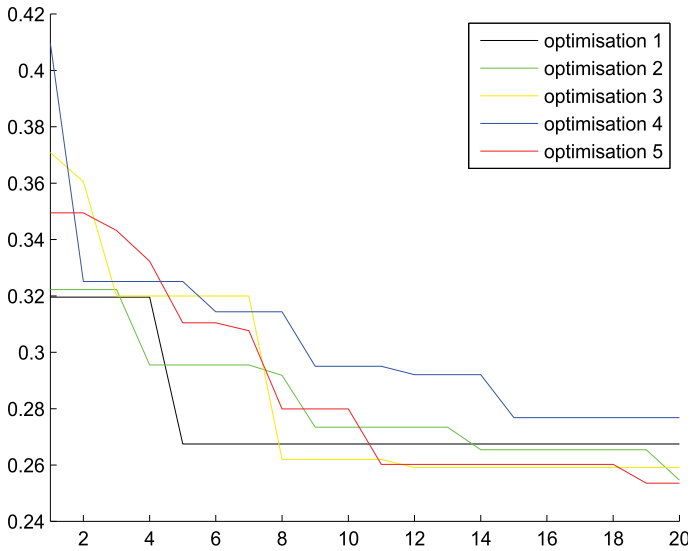

Figure 15. Objective function versus the generation number for 5 optimisation procedures.

image results with OFDM signals where the ghost has been largely reduced compared to **Figure 14c** obtained with chirp signal.

4.5. Discussion

The OFDM signals offer a good image quality improvement. The simulations are performed with $\forall i\ \alpha_i = 1$, which means that no priority is given to the objective function. Depending on the SAR application, priorities can be easily introduced to emphasis the desired parameter. We also focus on configurations with two OFDM signals. As mentioned, more than two signals with good cross-correlation properties can be generated with OFDM waveforms, which is not possible with the chirp signals. However, the OFDM signal has a main drawback that is not considered in this chapter: it has a high peak-to-average power ratio (PAPR). Two solutions can be provided. The first one consists to introduce a fourth objective function in Eq. (18) that takes into account the PAPR. The couple of the OFDM signals given by the genetic algorithm will minimise the PSLR, the ISLR, the cross-correlation amplitude and the PAPR. The other solution is to use complex symbols instead of 1, that is, the active subchannels are such that $a_i = e^{i\theta_i}$. The angle θ_i can also be introduced as a parameter to optimise in the genetic algorithm but random values lead high PAPR reductions [17].

5. MIMO OFDM SAR extension

As the previous procedure makes possible to set up orthogonal signals through the OFDM modulation, we propose to achieve SAR images in MIMO configuration. Some artefacts, that appear in MIMO SAR images, are due to the fact that the up- and down-modulated chirps do not provide the lowest cross-correlation level. Thus, we are interested to use OFDM signals for SAR applications in a MIMO context. The optimised OFDM pair provided by the optimisation procedure is then used in a MIMO configuration composed of two transmitting and receiving antennas.

As previously done in Section 4, an optimised OFDM couple composed of 65 subchannels are obtained with the use of the genetic algorithm. These OFDM signals are then associated with the SAR MIMO method exposed in Section 3. The results thus obtained are compared with those obtained in the case of the use of the MIMO SAR method with chirps signals and those obtained in the case of the use of an SISO configuration. The geometric configuration described in Section 3 is the same for this comparison and a metallic trihedral placed in the region of interest is considered to be at a 3.53 m range, that is, 5 m along the line-of-sight axis. In the two reference configurations without noise, the images shown in **Figure 16a** for the SISO SAR configuration and **Figure 16c** for the SAR MIMO configuration using transmitted chirps are obtained.

By analysing the SAR MIMO configuration with the chirps signals, the artefact appears along the azimuth axis on both sides of the metallic trihedral and the maximum level of this artefact is equal to -27 dB. The position of these phenomena is related to the position of the transmitting and receiving antennas. In our case, the artefacts are located at the coordinates

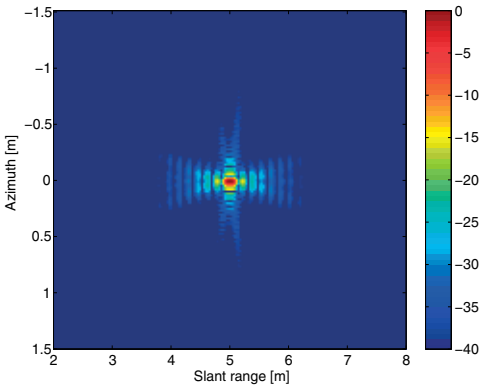

(a) SISO SAR image.

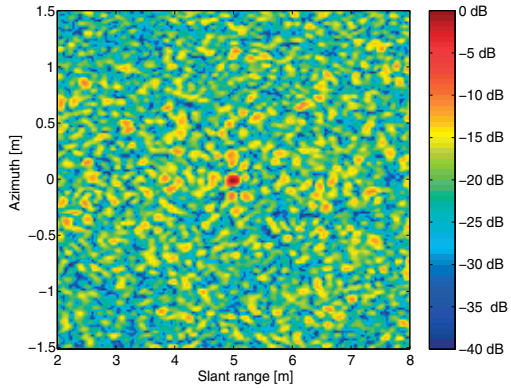

(b) SISO SAR image with noise.

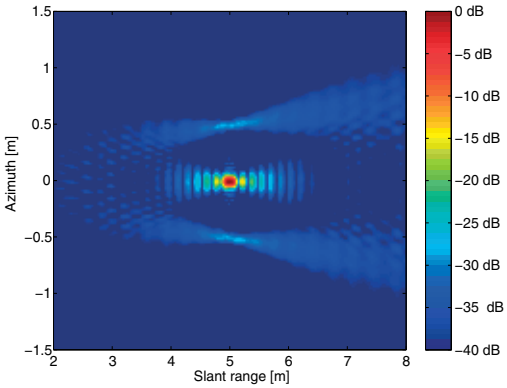

(c)

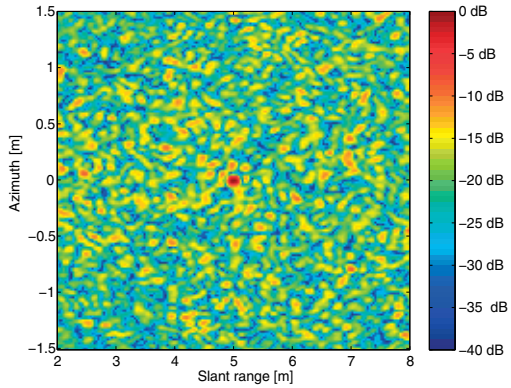

(d) MIMO SAR image with chirp transmitted waveforms and noise.

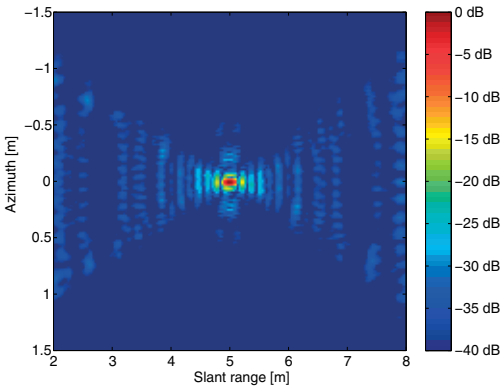

(e) MIMO SAR image with OFDM transmitted waveforms.

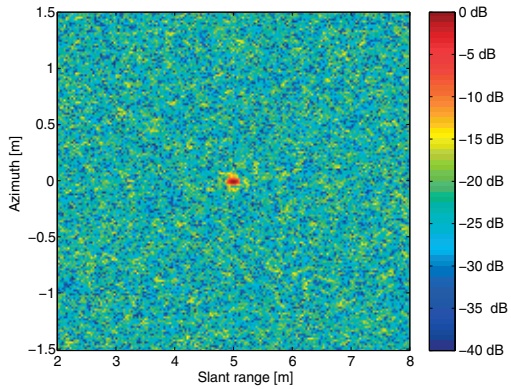

(f) MIMO SAR image with OFDM transmitted waveforms and noise.

Figure 16. SAR images provided by three different configurations without and with noise.

	Azimuth resolution (m)	PSLR (dB)	ISLR (dB)	PSLR (dB)	ISLR (dB)
		Without noise		With noise	
SISO	0.056	−13.8	−31	−9.5	−11.7
chirps MIMO	0.048	−14.2	−31	−11.2	−14.4
OFDM MIMO	0.037	−14.9	−32.4	−12.0	−17.3

Table 4. Simulation results of the azimuth resolution, PSLR and ISLR for different SAR configuration.

($x = 0$ m, $y = 0.56$ m) and ($x = 0$ m, $y = -0.56$ m). In the case of the MIMO OFDM SAR configuration, which is shown in **Figure 16e**, the azimuth artefacts have been largely reduced. Moreover, we are able to produce the similar results by adding noise resulting in a -30 dB SNR for the received signal. The corresponding SAR images are exhibited in **Figure 16b, d, f**. The imagery parameters are obtained and summarised in **Table 4**.

The azimuth resolution equal to 0.037 m is obtained. The azimuth resolution is improved by using the MIMO configuration together with the OFDM signals. However, the values of the other parameters, ISLR and PSLR, are modified. These improvements are due to the use of optimised OFDM transmitted signals. In the context of SAR MIMO imaging, the use of OFDM signals optimised in transmission makes it possible to greatly reduce the phantom phenomenon in azimuth. Moreover, in the case of a noisy environment, the use of OFDM signals coupled with MIMO techniques induces a stronger resistance to noise.

6. Conclusion

Based on the concepts from digital communications, this chapter discusses the improvement of the SAR processing performances provided by a MIMO-type configuration on the one hand and an OFDM-type waveform on the other hand. In order to illustrate the benefits of these approaches, we address some performances as the system robustness of SAR system, the azimuth resolution of SAR images and the range ambiguity of SAR processing.

First, the principle of SAR imaging is shown. The performances under study, which are achieved for the SISO SAR configuration with the chirp waveform, are also detailed. We assess the improvements that we apply, through differents parameters as PSLR, ISLR and azimuth resolution. These parameters make possible to describe the capabilities of system configuration and waveform design to improve the SAR images. The section about the MIMO configuration analysis describes the procedure for a coherent system regarding the geometric situation. Based on the backprojection SAR processing, some simulations achieve a coherent addition of SAR images to each other that induces an increase in noise resistance. The described procedure is validated by the use of an experimental system. This study of the receiver part of the MIMO

SAR shows us the possibility of improving the azimuth resolution and the robustness of the imaging system by using a MIMO configuration. The next section deals with the use of OFDM signals to solve a limitation related to range ambiguity phenomena. This method is then validated by simulation using a pair of chirps (up- and down-modulated chirps). Nevertheless, these transmitted signals are not totally orthogonal artefacts appear in the SAR image along the azimuth axis. Thus, a procedure is proposed in order to determine the optimum OFDM signal couple to solve the ambiguity in range and at the same time to reduce the presence of artefacts in the final image. An optimization procedure based on a genetic algorithm is used and validated for 65 subchannels. Finally, the use of the OFDM signals is proposed with the MIMO concept. In the same way as for range ambiguity, the MIMO SAR focusing methods are all based on the use of matched filters in range. By using the optimal OFDM couple determined to solve the range ambiguity, it is possible to improve the SAR image.

This chapter indicates a number of avenues for future research directions and gives first answers to the problem we investigate. For example, some lines of research seem interesting to explore. It would be interesting to increase the number of transmitting or receiving antennas in order to increase the robustness of the radar system against noise. Another application of OFDM for SAR imaging is the use of OFDM signals coupled with polarimetry because it is often necessary to increase the PRF to make a second acquisition by changing the transmitted polarisation.

Author details

Stéphane Méric* and Jean-Yves Baudais

*Address all correspondence to: stephane.meric@insa-rennes.fr

Institute of Electronics and Telecommunications of Rennes, Rennes, France

References

[1] Cumming IG, Wong FH. Digital Processing of Synthetic Aperture Radar Data. Norwood, USA: Artech House Inc.; 2005

[2] Richards MA, Scheer J, Holm WA. Principles of Modern Radar: Basic Principles. Rayleigh, USA: SciTech Publishing Inc; 2010

[3] Soumekh M. Synthetic Aperture Radar Signal Processing. New-York, USA: Wiley-Interscience Inc.; 2004

[4] Chevalier FL. Application to radar. In: Principles of Radar and Sonar Signal Processing. Norwood, USA: Artech House Inc.; 2005. pp. 39-106

[5] Klare J, Saalmann O, Wilden H, Brenner AR. First experimental results with the imaging MIMO radar MIRA-CLE X. In: European Conference on Synthetic Aperture Radar. 2010. pp. 374-377

[6] Martínez A, Marchand JL. SAR Image quality assessment. Revista de Teledetección. 1993 Nov;**1993**(2):1-7

[7] Levanon N, Mozeson E. Radar Signals. New-York, USA: Wiley-interscience Inc.; 1999

[8] Klare J, Saalmann O, Wilden H, Brenner A. Environmental monitoring with the imaging MIMO radars MIRA-CLE and MIRA-CLE X. In: IEEE International Geoscience and Remote Sensing Symposium. 2010. pp. 3781-3784

[9] Ender JHG, Klare J. System architectures and algorithms for radar imaging by MIMO-SAR. In: Radar Conference. Pasadena, CA, USA. 2009. pp. 1-6

[10] Li SF, Chen J, Zhang LQ, Zhou YQ. Application of complete complementary sequence in orthogonal MIMO SAR system. Progress in Electromagnetics Research C. 2010;**13**:51-66

[11] Li J, Zheng X, Stoica P. MIMO SAR imaging: Signal synthesis and receiver design. In: International Workshop on Computational Advances in Multi-Sensor Adaptive Processing. 2007. pp. 89-92

[12] Riché V, Méric S, Pottier É. Study of receiver design in a MIMO SAR configuration. International Journal of Microwave and Wireless Technologies. 2012;**4**(3):335-339

[13] Kauffman K, Raquet J, Morton Y, Garmatyuk D. Enhanced feature detection and tracking algorithm for UWB-OFDM SAR navigation. National Aerospace and Electronics Conference. 2011:261-269

[14] Hossain MA, Elshafiey I, Alkanhal MA, Mabrouk A. Anti-jamming capabilities of UWB-OFDM SAR. In: European Radar Conference. Manchester, UK. 2011. pp. 313-316

[15] Garmatyuk D, Brenneman M. Adaptive multicarrier OFDM SAR signal processing. IEEE Transactions on Geoscience and Remote Sensing. 2011 Oct;**49**(10):3780-3790

[16] Liu X, Liu Y, Wang X, Zhou J. Application of communication OFDM waveform to SAR imaging. In: Radar Conference. 2017. pp. 1757-1760

[17] Baudais JY, Méric S, Riché V, Pottier É. MIMO-OFDM signal optimization for SAR imaging radar. EURASIP Journal on Advances in Signal Processing. 2016;**2016**:1-11

[18] Curlander JC, McDonough RC. Synthetic aperture radar: Systems and signal processing. New-York, USA: Wiley-Interscience Inc.; 1991

[19] Mittermayer J, Martínez JM. Analysis of range ambiguity suppression in SAR by up and down chirp modulation for point and distributed targets. In: IEEE Internationnal Geoscience and Remote Sensing Symposium. Toulouse, France. 2003. pp. 4077-4079

[20] Riché V, Méric S, Baudais JY, Pottier É. OFDM signal design for range ambiguity suppression in SAR configuration. In: IEEE International Geoscience and Remote Sensing Symposium. Munich, Germany. 2012. pp. 2156-2159

[21] Riché V, Méric S, Baudais JY, Pottier É. Optimization of OFDM SAR signals for range ambiguity suppression. In: European Radar Conference. Amsterdam, Netherlands. 2012. pp. 278-281

Section 2

SAR Applications

Chapter 4

A 94-GHz Frequency Modulation Continuous Wave Radar Imaging and Motion Compensation

Jiwoong Yu, Sumin Kim and Min-Ho Ka

Additional information is available at the end of the chapter

http://dx.doi.org/10.5772/intechopen.74692

Abstract

A compact and lightweight synthetic aperture radar (SAR) that can be loaded on a miniature unmanned aerial vehicle (UAV) was recently developed. The higher the frequency is, the smaller is the antenna size and the microwave characteristics are improved. Thus, a high frequency is favorable for miniaturization and weight reduction. In this chapter, a method of obtaining a radar image through a 94-GHz frequency modulation continuous wave (FMCW) radar is proposed. In addition, a method of motion compensation is described, and the W-band SAR image after motion compensation is confirmed. This kind of SAR imaging can provide geographic information and characteristics of extreme environments, disaster scenes, and information on sites where human access is difficult.

Keywords: synthetic aperture radar (SAR), frequency modulation continuous wave (FMCW), radar, imaging, W-band, motion compensation

1. Introduction

Airborne and space-borne synthetic aperture radar (SAR) images are used in various fields of remote sensing [1]. There are various applications in using high-resolution radar images. Several imaging algorithms were developed in the laboratory, which depend on the given geometry [2–4]. SAR technology can be used to acquire images of disaster areas or other dangerous sites where direct human access is difficult. Traditional optical images have limitations, such as being weather- and environment-dependent, being too bright, or having no range information. As an alternative imager, the SAR can be loaded onto an unmanned aerial vehicle. SAR equipment was once too heavy and bulky for such an application. However, owing to recent technological improvements, radar has become smaller and more lightweight [5–7]. In particular, frequency

modulation continuous wave (FMCW) radar was developed as a chip and is lightweight, has a small size, and offers low power consumption, which has advantageous qualities for being mounted on a drone. FMCW radar can also be used at a close range. Attempts are being made to replace conventional radars with FMCW types for small and close-range systems. The higher the frequency is, the smaller is the antenna size. Thus, a high frequency is favorable for miniaturization and weight reduction [8–10]. In this chapter, FMCW radar with a center frequency of 94 GHz is used. FMCW radar is commonly employed for relatively short distances. Also, a high-range resolution can be obtained, even though it has a low sampling rate [11, 12]. The developed FMCW radar only measures real components; nevertheless, it can obtain complex data by using the Hilbert transform [13–16].

The higher frequency used in the proposed W-band SAR causes a narrower antenna beam width. Because the range is short and the width is narrow, range migration in SAR data can be ignored. In a short range, the matched filter phase for azimuth compression should change with the range. In this study, based on the range-variant azimuth chirp rate of the range Doppler algorithm (RDA), a SAR algorithm at a close range was developed and a resolution analysis of an impulse target was performed.

In the airborne SAR, the movement of the aircraft greatly affects SAR focusing. Motion compensation is important because small and slow-flying objects have less inertia and are thus more notably affected by disturbances. Therefore, to obtain decent SAR images, the motion must be compensated. Motion information is acquired by navigation sensors and used for focusing SAR images by compensating them. The quality of the reconstructed image is very sensitive to the geometry determination accuracy. This factor has led to the development of autofocusing techniques.

Several methods for autofocusing exist, such as entropy minimization [17], an FMCW analytic method [18], contrast optimization [19] in ISAR, phase gradient autofocusing (PGA) [20, 21], and prominent point processing (PPP) [22] in SAR. These methods consist of range alignment and phase compensation. Moreover, they are applicable to circular synthetic aperture radar (CSAR) with wideband SAR [23]. A SAR or ISAR autofocusing method using a prominent target was proposed [22, 24]. However, this method requires a prominent target, and it is difficult to find an ideal point target. Nonetheless, this method is faster than contrast maximization [19] or entropy minimization [17, 25]. The algorithm based on contrast maximization is slow because of a high computing cost. It is difficult to apply these autofocusing methods because focusing cannot be performed when the motion is large. Therefore, navigation sensors that can provide position and velocity information, such as GPS and IMU, are needed to compensate for motion.

The purpose of the proposed algorithm is to implement a video SAR with a high frame rate through fast signal processing. It is possible to obtain SAR images, such as videos, using W-band. The video SAR helps intuitively recognize moving objects. Recent research has contributed to the increase in the real-time frame rate [26–28]. Therefore, a simple SAR focusing algorithm and motion compensation should be implemented.

This chapter describes a method of compensating the motion caused by disturbance of the W-band SAR platform. Focusing from the SAR received data with arbitrary movement is

http://dx.doi.org/10.5772/intechopen.74692

evaluated in the laboratory, where arbitrary movement can be applied by using the motor controller. As the wavelength becomes short, the motion compensation of the aircraft should become more precise. Therefore, precise IMU and GPS navigation sensors are required. The motion obtained from the sensors must be compensated to obtain the SAR image.

An experiment was conducted in which it was assumed that accurate position information is obtained by using the motor controller. In the experiment, a 94-GHz FMCW radar developed by Yonsei University using an FPGA was used. Section 2 describes the radar architecture. Section 3 presents the proposed method for W-band SAR imaging at a close range. Section 4 describes the process of measuring SAR in well-known motions and compensating for the movements in an anechoic chamber. Section 5 provides a summary.

2. W-band radar architecture

The 94-GHz radar consists of three major parts: a transceiver, power board, and processing board. The transceiver generates the waveform, up-converts the signal to a radio frequency (RF), and radiates the signal. The power board provides power to the transceiver. The processing board samples the beat signal and transmits the data. A functional diagram of the modules is presented in **Figure 1**.

2.1. Transceiver

As shown in **Figure 2**, the transceiver consists of three parts: an antenna, front-end module, and phase-locked-loop (PLL) board. The antenna is a gold-plated brass horn antenna with linear polarization. It has 25-dBi gain at 94-GHz frequency, and an approximately 10-degree half-power beam width. The antenna is connected to the front-end module with a rectangular

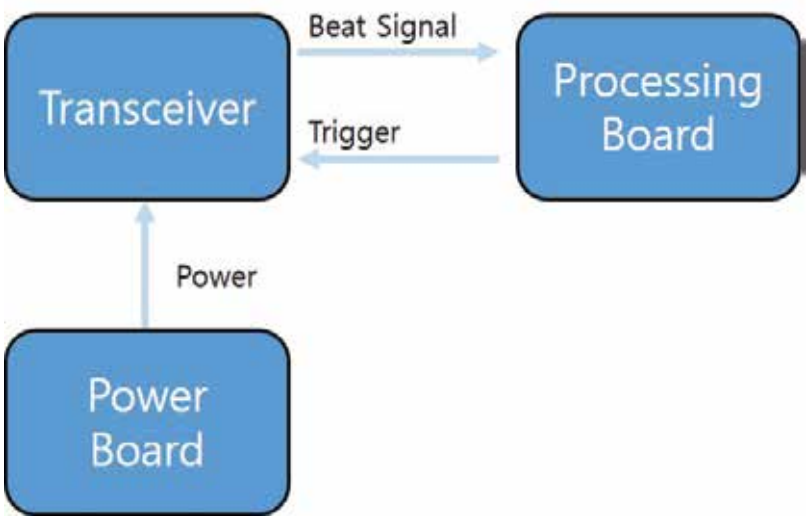

Figure 1. Functional diagram of developed radar.

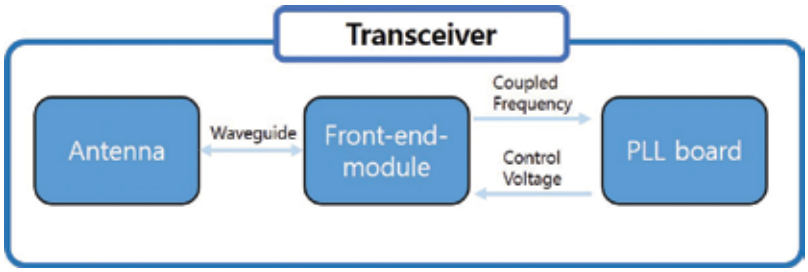

Figure 2. Functional diagram of a transceiver.

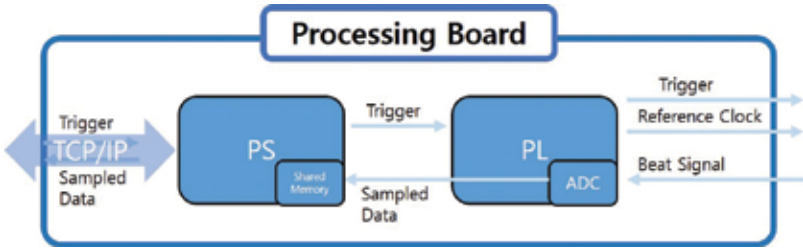

Figure 3. Functional diagram of the processing board.

waveguide interface [13]. The front-end module consists of a voltage-controlled oscillator (VCO), power amplifier, frequency multiplier, bypass mixer, and multistage low-noise amplifier. Its output center frequency is 94 GHz with a sweep bandwidth of 1.4 GHz, which is adequate for providing a resolution up to 0.12 m. The RF output power is 1.5–2 mW. Its receiver low-noise amplifier (LNA) gain can be selected from 23 to 46 dB. To synchronize the front-end module with the processing board, a PLL board is used. The PLL board synchronizes the oscillation from the front-end module with the processing board's clock. It also provides the voltage sweep required to sweep the VCO output frequency.

2.2. Processing board

The processing board utilizes the Xilinx Zynq-7000 chip for analog-to-digital conversion (ADC), synchronization with the PLL board, triggering the PLL board, and data transmission. The chip is divided into two parts: programmable logic (PL) and a processor (PS) [14]. Its functional diagram is presented in **Figure 3**. The processing board's main tasks are to provide the trigger and clock for the PLL, sample the beat signal from the transceiver, and send the raw data via TCP/IP. The beat signal from the front-end module is sampled by an analog-to-digital converter inside the PL at a sampling rate of 940 KHz. When the PL receives the radar command from the PS, the latter writes the sampled data to the shared memory. The PS then reads the sampled data from the shared memory and transmits the raw data via TCP/IP [29].

Figure 4 shows the FMCW radar block diagram. **Figure 5** shows the radar module, processing board, power board, PLL, front-end module, and antenna.

http://dx.doi.org/10.5772/intechopen.74692

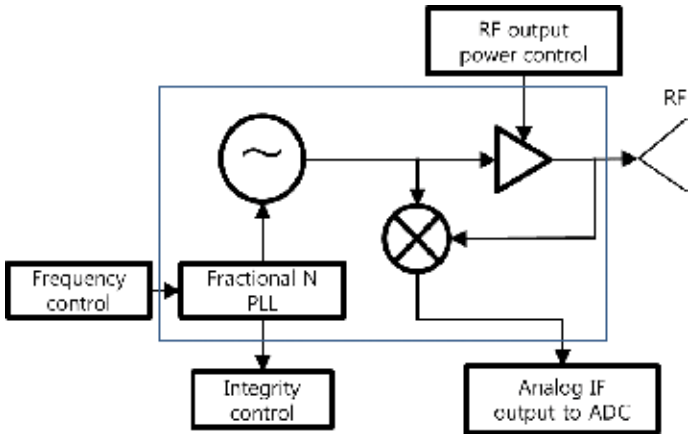

Figure 4. Flow diagram of FMCW radar.

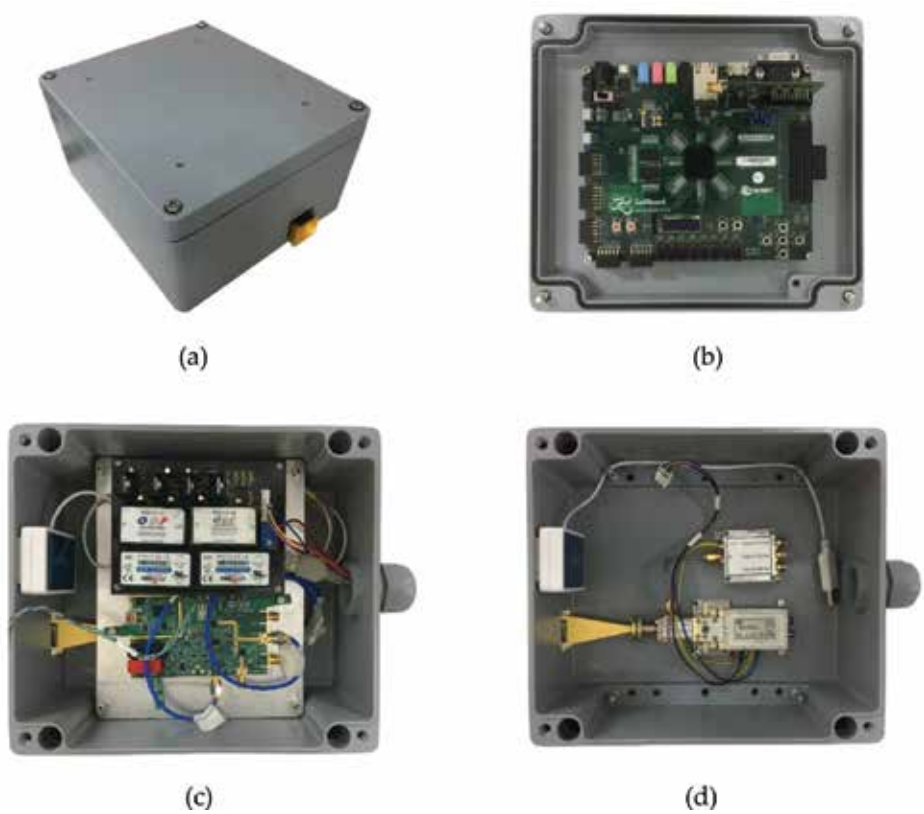

Figure 5. Developed 94-GHz radar: (a) radar module, (b) FPGA signal-processing board, (c) PLL and power board, and (d) front-end module and antenna.

2.3. Power board

The power board consists of four power converters and four regulators. It was designed to provide the transceiver with the required power for each module. After providing the transceiver with its appropriate voltage level, the power consumption of the radar is approximately 10 W.

2.4. FMCW radar performance

An FMCW [30–34] is a signal whose frequency is continuously modulated. The transmitted signal can be represented by.

$$s(t) = e^{2\pi j\left(f_0 t+\frac{1}{2}kt^2\right)} \tag{1}$$

where f_0 is the carrier frequency and k is the chirp rate. The echo signal is mixed with the transmitted signal to from the received signal. The received signal from a single target can be represented as.

$$s_r(t) = e^{2\pi j\left(f_0 t+\frac{1}{2}kt^2\right)} \cdot ae^{2\pi j\left(f_0(t-\tau)+\frac{1}{2}k(t-\tau)^2\right)} = ae^{2\pi j\left(f_0\tau+\frac{1}{2}k\tau^2\right)}e^{-2\pi jkt\tau} = ae^{j\varphi}e^{-2\pi jkt\tau} \tag{2}$$

where ϕ is the constant phase. The received signal for a single target is sinusoidal and its frequency depends on the target range. The transmitted signal of the FMCW radar is modulated with respect to time, and the received signal from the impulse target is a beat frequency, f_b, which is the difference between the transmit frequency and the received frequency. The beat frequency is proportional to the range of the target and is represented as.

$$f_b = k\tau = \frac{BW}{t_r}\frac{2R}{c} \tag{3}$$

The FMCW radar repeatedly and continuously transmits the waveform given in Eq. (1). The waveform is classified into saw-tooth and triangular waveforms according to the repeated form. The time it requires to sweep the frequency is called the ramp time, t_r. Then, the bandwidth of the FMCW is defined as.

$$BW = kt_r \tag{4}$$

The radar used in the experiment was FMCW radar with a center frequency of 94 GHz. The radar transmitted the linear frequency modulation (LFM) signal through the antenna, and it sampled the echo signal mixed with the transmitted signal. The chirp of the LFM signal used was an up-ramp saw-tooth waveform. The chirp rate, k, was 1400 MHz/ms and the ramp (sweep) time was 1 ms. The sampling rate was 940 KHz. The bandwidth was 1.4 GHz, and the signal could be sampled 940 times in a single period. According to Eq. (3), the range can be represented by the function of the beat frequency as.

$$R = \frac{cf_b}{2k} \tag{5}$$

The received signal is converted to a range profile by inverse fast Fourier transform (IFFT). The range profile of a single target is obtained using Eq. (3), which is shown as.

$$S_r(f,R) = ae^{j\varphi}\int_{-\infty}^{\infty} w(t_r)e^{-2\pi jkt\tau}\cdot e^{2\pi jft}dt = ae^{j\varphi}\mathrm{sinc}(tf-k\tau) \tag{6}$$

where the window, $w(t_r)$, serves only to take one period of the signal, and sinc(x) is a normalized sinc function. In the case of saw-tooth FMCW, the beat frequency is obtained by performing the FFT on the range profile.

Taking the displacement on both sides of Eq. (5) gives Eq. (7). The range resolution is determined by a sinc function of the range profile.

$$\Delta R = \frac{c\Delta f}{2k} = \frac{ct_r\Delta f}{2BW} = \frac{cNt_s\Delta f}{2BW} = \frac{c}{2BW} \tag{7}$$

where t_s is the sampling interval, 1.06 μs, and N is the number of samples in an echo, 940. The beat frequency resolution is 1.49 MHz. The theoretical properties of the point target response for FMCW radar is a 1.4-Ghz bandwidth or a resolution of approximately 0.093 m. If the bandwidth increases, a profile with a high-range resolution can be obtained. The FMCW radar does not require a sampling rate above the bandwidth to avoid degrading resolution.

$$\Delta R_0 = \frac{r_r f_s}{N_{IFFT}}\frac{c}{2BW} \tag{8}$$

The range resolution depends on zero padding. However, according to the Fourier transform properties, Nt_s is equal to 1/Δf. The range cell thus had a spacing of 0.15 m. Therefore, 8912 samples were used for FFT after padding 7912 zeros. The range cell spacing after zero padding was 0.015 m. The range cell spacing after zero padding was sufficiently smaller than the range resolution.

There is no minimum range limit in FMCW radar. However, the maximum range is limited by two parameters. For one, the maximum range is limited by the sampling rate. This is because the beat frequency is determined by the Nyquist frequency, which is equal to half the sampling rate. Another criterion is the range ambiguity. For FMCW, when the delay time becomes half of the ramp time, the resolution doubles. Depending on the conditions, this value may vary; however, in Eq. (9), 10% was chosen [35]. Usually, in FMCW radar, the ramp time is adequately long and the target signal exists only within the radar range of interest. Thus, the maximum range is determined by the sampling rate.

$$R_{\max} = \begin{cases} \dfrac{ct_r f_{\max}}{2BW} = \dfrac{ct_s f_s}{4BW} = \dfrac{cN}{4BW} & \text{for the Nyquist criterion} \\ 0.1\dfrac{ct_r}{2} & \text{for the range ambiguity} \end{cases} \tag{9}$$

Because the sampling rate is high, the distance information of farther targets can be obtained if the beat frequency resolution increases. The maximum range criterions are sufficiently longer than the length of the chamber. Therefore, aliasing will not occur. The maximum range of

FMCW radar is 15,000 m for the ambiguous range and 477 m for the Nyquist criterion. The chamber subjected to the experiment had a length of approximately 7 m.

The radar performance was analyzed using a trihedral corner reflector target. The experimental settings are shown in **Figure 6**. The target and the radar were placed inside an anechoic chamber with a target distance of 2.8 m.

As shown in **Figure 4**, the radar samples the echo signal multiplied by the transmitted signal. The sampled signal is the de-ramped signal of the echo, where the frequency components are sampled. Therefore, when conducting an inverse Fourier transformation (IFT), the symmetric value of the time or range domain can be obtained. Because only the in-phase component can be obtained, only the real number or in-phase components of Eq. (2) can be obtained as the received data. Through the Hilbert transformation, a quadratic component (imaginary part) can be generated. The Hilbert transformation is a method for generating a signal that has the same magnitude but is orthogonal to the original signal [15]. As shown in Eq. (10), the Hilbert transformation is used to obtain an in- phase/quadratic (I/Q) signal. When performing the IFT with this method, the phase information can be obtained, and the symmetrical information, which can be generated as a mistaken IFT, can be prevented.

$$s_h(t,n) = s(t,n) + jH_h(s(t,n)) \tag{10a}$$

$$S_r(f,n) = IFFT[s_h(t,n)]_t \tag{10b}$$

The experimental results from a point target are shown in **Figure 7**. Theoretically calculated side-lobe level, resolution and experimental results are almost identical.

The side-lobe level, null-to-null resolution, and 3-dB resolution of the impulse target were analyzed [36]. The measured resolution of the FMCW radar, as shown in **Figure 7**, is expressed in **Table 1**, which describes the resolution in the range direction. It can be observed that the theoretical resolution of 0.09 m and the measured resolution (3 dB) are very close.

Figure 6. Experiment settings for the impulse target.

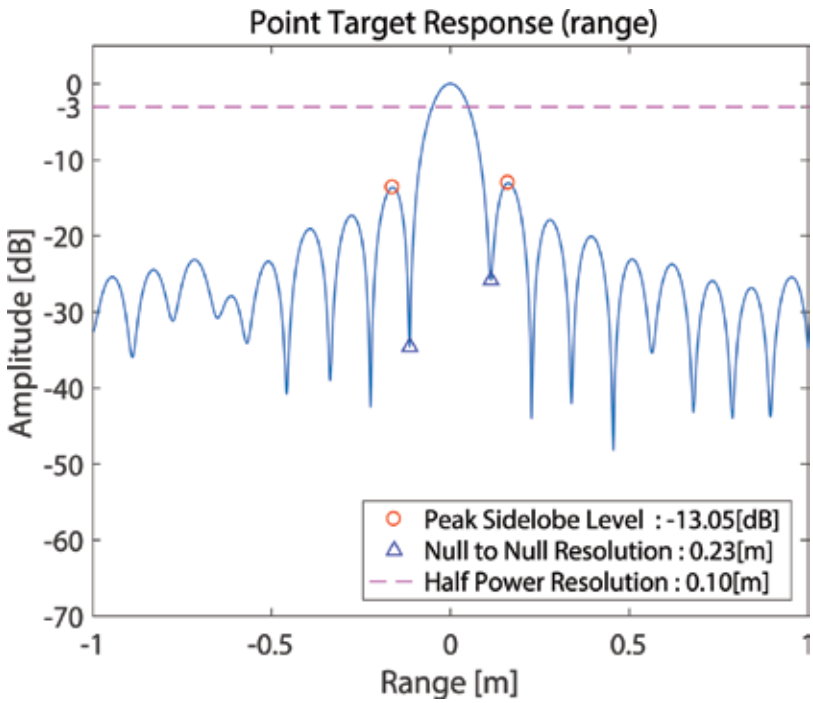

Figure 7. Point target response in the range direction.

Peak side-lobe level	**−13.05 dB**
Null-to-null resolution	0.23 m
3-dB resolution	0.10 m

Table 1. Measured resolution of the range direction.

3. SAR image formation

3.1. Experimental settings

SAR experiments were conducted using the FMCW radar described in Section 2. An experimental diagram is shown in **Figure 8**. The experiment was conducted inside an anechoic chamber with a maximum range of 7 m. The broadside-facing radar was placed on a rail moving in a cross-range direction to the target. The total synthetic length was 2 m and the target was in a range of 2.8 m. The target was a trihedral corner reflector. **Figure 9** depicts the experimental settings, which assumed a non-squint radar geometry and that the antenna was oriented perpendicular to the track direction during motion. The rail motion was controlled by a motor. As shown in **Figure 8**, the radar platform moved along the rail. Because its flying

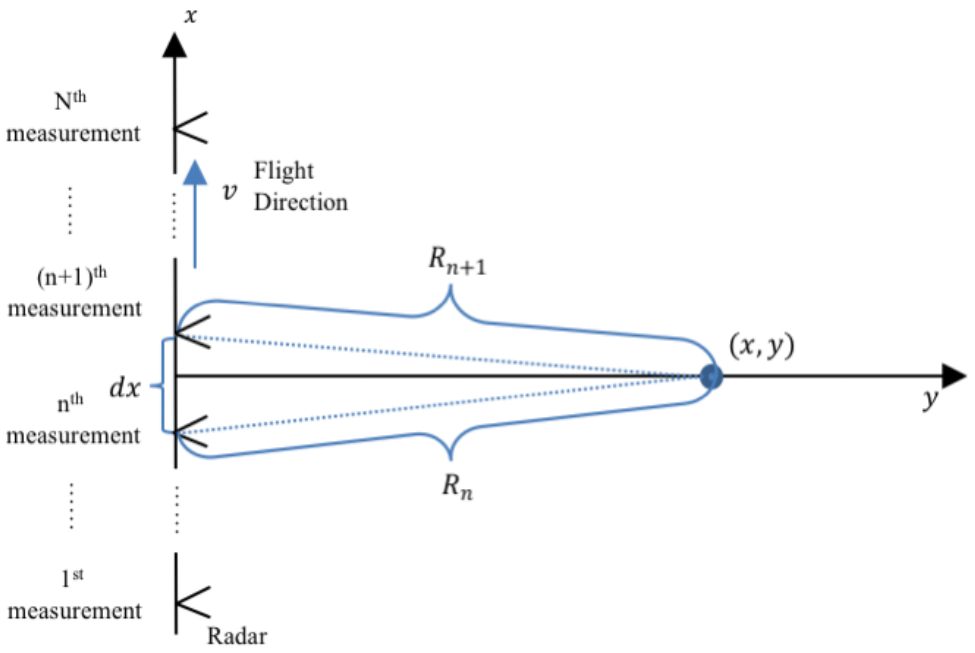

Figure 8. Diagram of SAR experiment settings.

speed was low, the interval on the rail was set to 0.001 m. The total number of measurements was 2001.

3.2. Range profile

The transmitted signal was scattered by the target. The n^{th}-received signal from the impulse target after IFFT was $S_r(n)$ and is written as Eq. (11). As shown in Eq. (2), the phase delayed received signal can be represented. Herein, R_i refers to the distance between the antenna and the target, and a_i refers to the i^{th}-scattering coefficient and antenna pattern with respect to the observation angle. In addition, p(f) refers to the impulse response without a delay and λ refers to the signal wavelength. The range profiles of all 2001 measurements are shown in **Figure 11**.

$$S_r(f, n, R_i; x_i, y_i) = \sum_{i=1}^{N} a_i(n)p(f)e^{-4\pi j R_i/\lambda} = \sum_{i=1}^{N} a_i(n)p(f)e^{-4\pi j\sqrt{x_i^2+y_i^2}/\lambda} \quad (11)$$

A single range profile at the center of the synthetic aperture is shown in **Figure 10**. The target signal is visible at a range of 2.8 m. Such range profiles can be stacked with regard to the antenna position to form a two-dimensional range profile, which is shown in **Figure 11**. As the figure illustrates, a frequency of 94 GHz and a narrow beam width of approximately 10° were used. The target with a relatively short distance was measured.

http://dx.doi.org/10.5772/intechopen.74692

Figure 9. Configuration of experimental settings.

$$\delta R = \frac{R}{\cos\theta/2} - R = \Delta R \tag{12}$$

The difference between the bore sight range and the antenna of 3-dB edge sight range can be represented as Eq. (12). The range cell migration can be neglected because the difference is sufficiently less than the range resolution.

3.3. Azimuth compression

The target signal phase changes with respect to the antenna position. From **Figure 8**, the phase history of the point target located at x_0 and y_0 can be derived as Eq. (13).

$$\theta\left(n, R_0 = \sqrt{x_0^2 + y_0^2}\right) = \frac{4\pi}{\lambda}\sqrt{(x_0 + ndx)^2 + y_0^2} \approx \frac{4\pi}{\lambda}\left[\frac{x_0^2}{2y_0} + \frac{(ndx)^2}{2y_0} + \frac{x_0}{y_0}ndx + y_0\right] \tag{13}$$

The azimuth compression can be performed by using Eq. (13) to create a matched filter along the cross-range direction. Since the curvature of phase in Eq. (12) varies with range, a

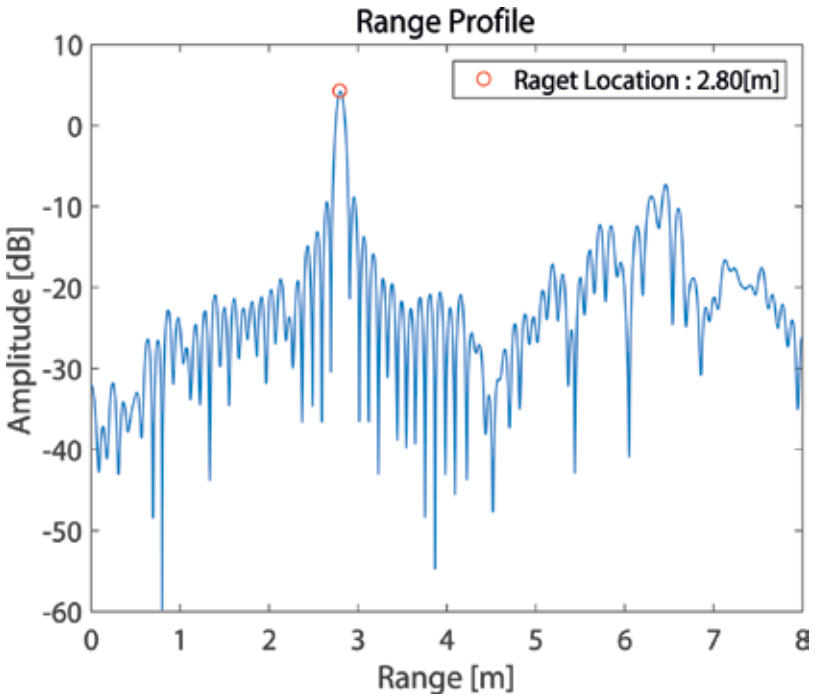

Figure 10. Range profile of the impulse target.

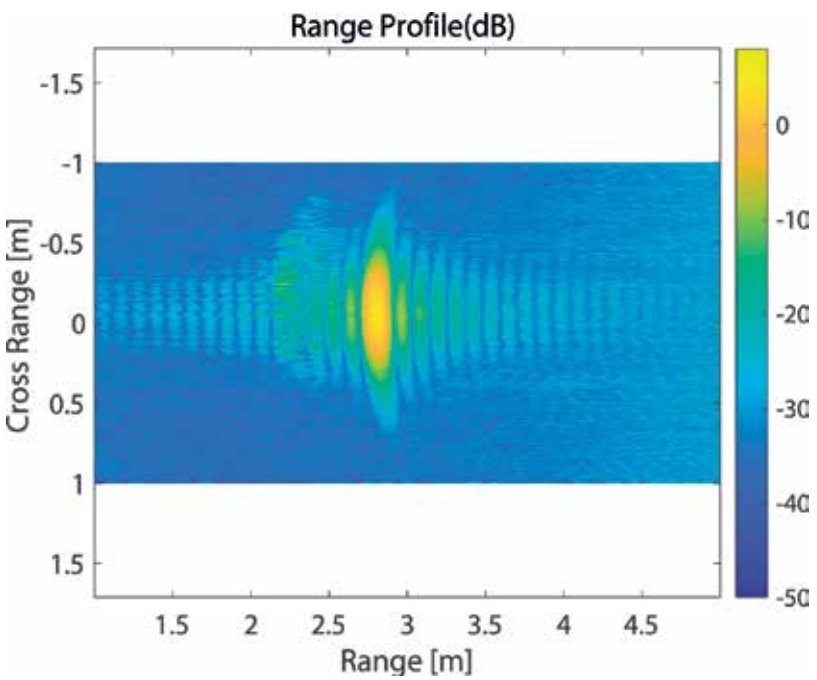

Figure 11. Measured range profile in two dimensions.

http://dx.doi.org/10.5772/intechopen.74692

different azimuth-matched filter must vary with the range. **Figure 13** shows the azimuth compression filter.

$$\begin{aligned} S_{SAR}(f,n) &= IFFT\left[FFT[S_r(f,n)]_n * FFT[S_{MF}(y,n)]_n^*\right] \\ &= IFFT\left[FFT[S_r(f,n)]_n * FFT\left[e^{j\theta(y,n)}\right]_n^*\right] \end{aligned} \tag{14}$$

The SAR image is obtained through the azimuth compression, as shown in Eq. (13). The process of obtaining the SAR image using the FMCW radar is shown in the flow chart in **Figure 12**.

After applying the azimuth compression filter (**Figure 13**) to the two-dimensional range profile (**Figure 11**), the azimuth-compressed SAR image of the impulse target is obtained, as shown in **Figures 14** and **15**.

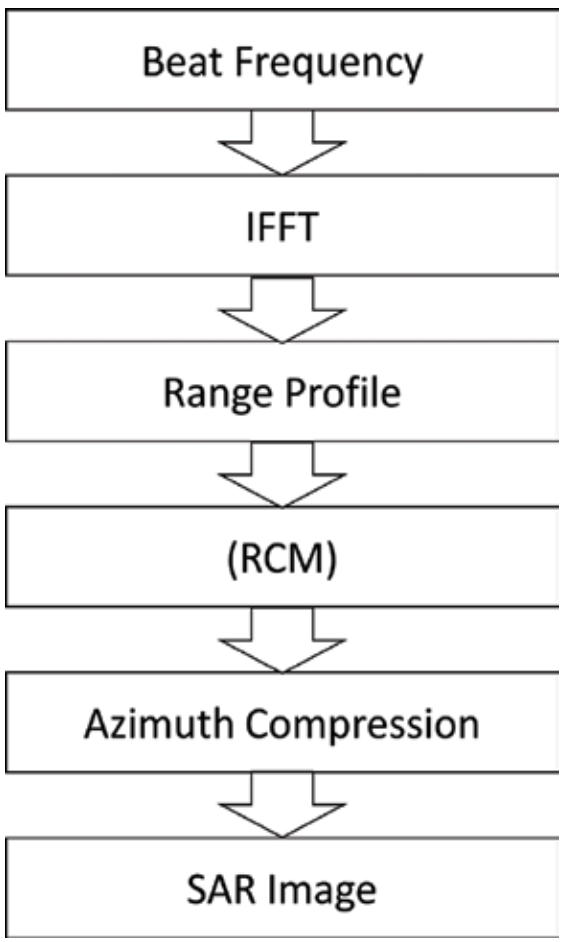

Figure 12. Flow diagram of SAR imaging. In the W-band, RCM does not have to be used depending on the range and the antenna beam width.

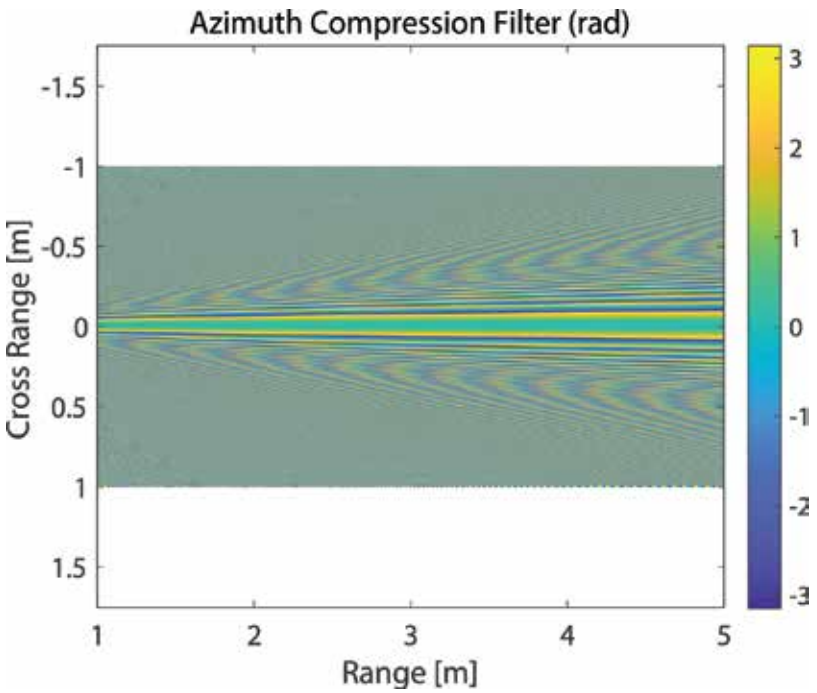

Figure 13. Azimuth compression filter.

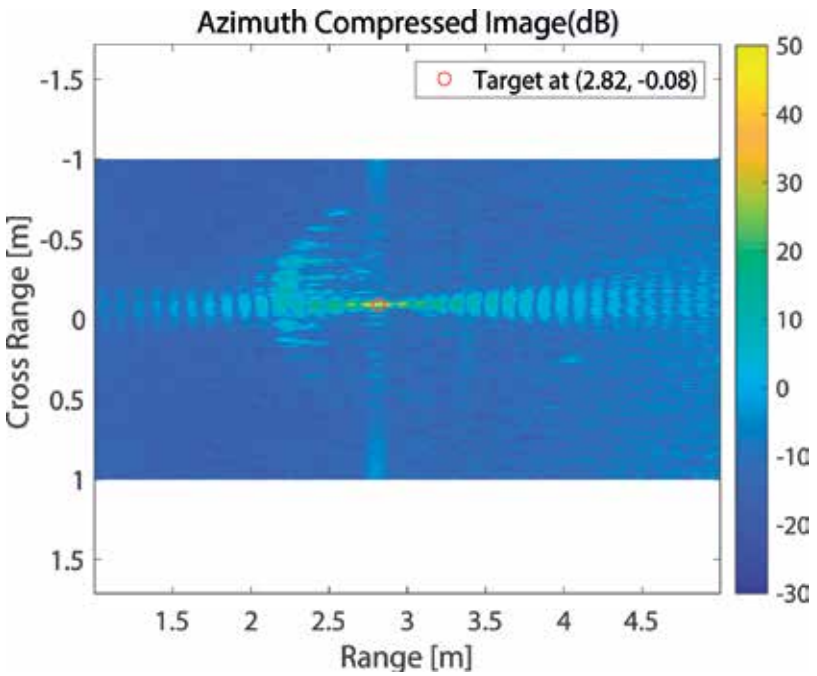

Figure 14. Azimuth-compressed SAR image.

http://dx.doi.org/10.5772/intechopen.74692

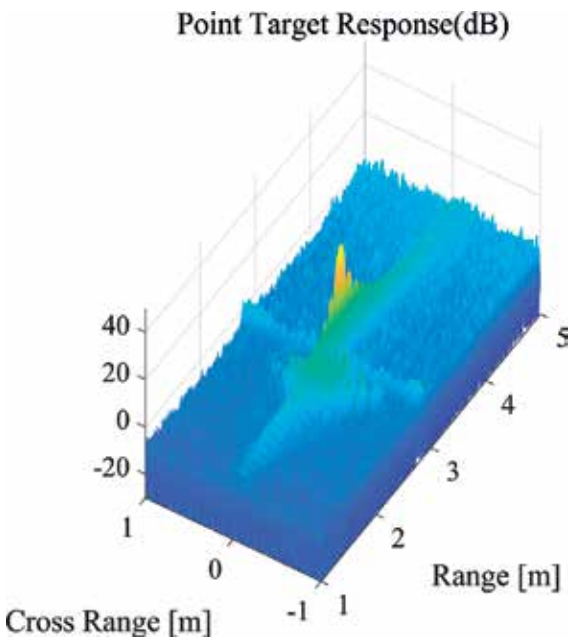

Figure 15. Azimuth-compressed SAR image shown in three dimensions.

The range profile in the SAR image can be represented in **Figures 16** and **17**. The range resolution of the SAR image is lower than the impulse range response shown in **Figure 7**. This degradation is estimated to be due to azimuth compression and may be improved via a precise range cell migration.

3.4. Cross-range profile

The cross-range profile at a target range can be obtained by taking a column from the SAR image. This profile with the target location is shown in **Figure 18**.

A detailed analysis of the point target is shown in **Figure 19**, including the side-lobe level and resolution. The theoretical null-to-null cross-range resolution of the SAR image can be calculated using Eq. (14) [37].

$$\delta y_{nn} = \frac{\lambda}{2\theta} = 0.0183 \text{ m} \tag{15}$$

Because the target range is small, the synthetic length is governed not by the antenna position but by the antenna beam width. The 3-dB beam width of the antenna, that is, 10°, was used for the calculation. **Table 2** outlines the resolution in the cross-range direction. The cross-range null-to-null resolution is 0.0183 m, and the cross-range half-power resolution (3 dB) is 0.0076 m, as measured by the SAR experiment using the impulse target, as shown in **Figure 19**. The experimental null-to-null resolution matches the theoretical expectation of 0.0183 m from Eq. (15).

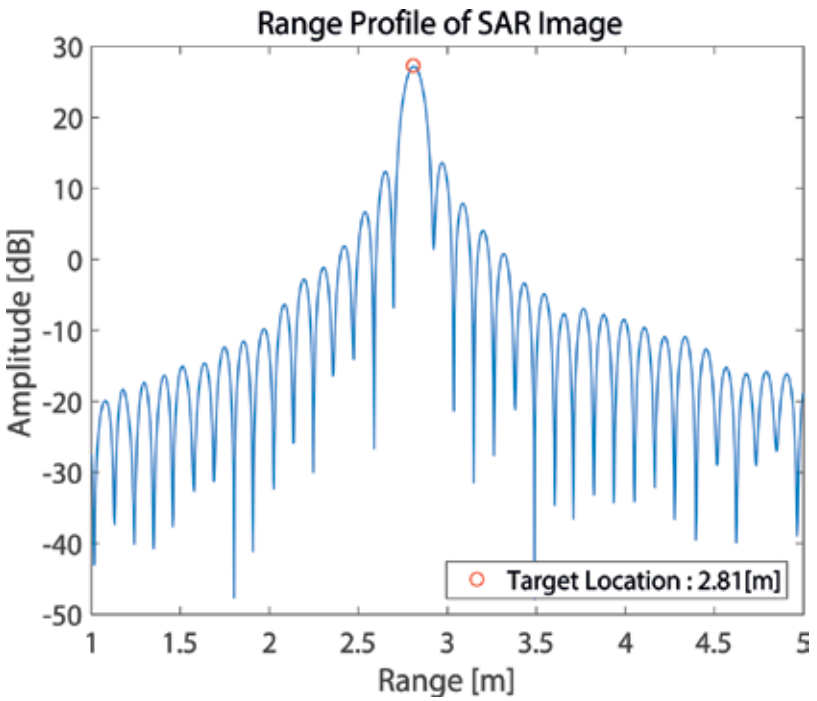

Figure 16. Range profile in SAR image.

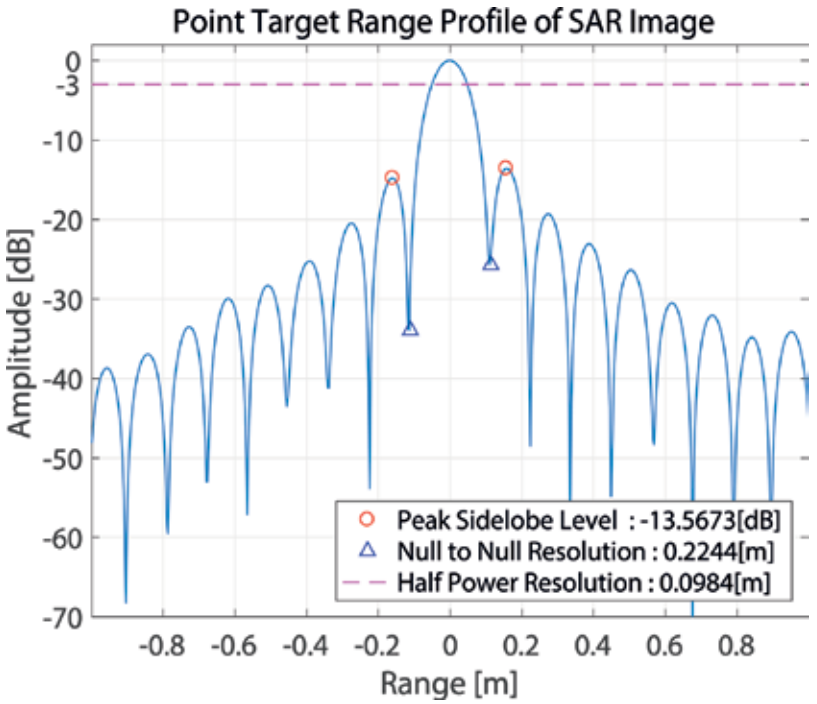

Figure 17. Point target profile in SAR image.

http://dx.doi.org/10.5772/intechopen.74692

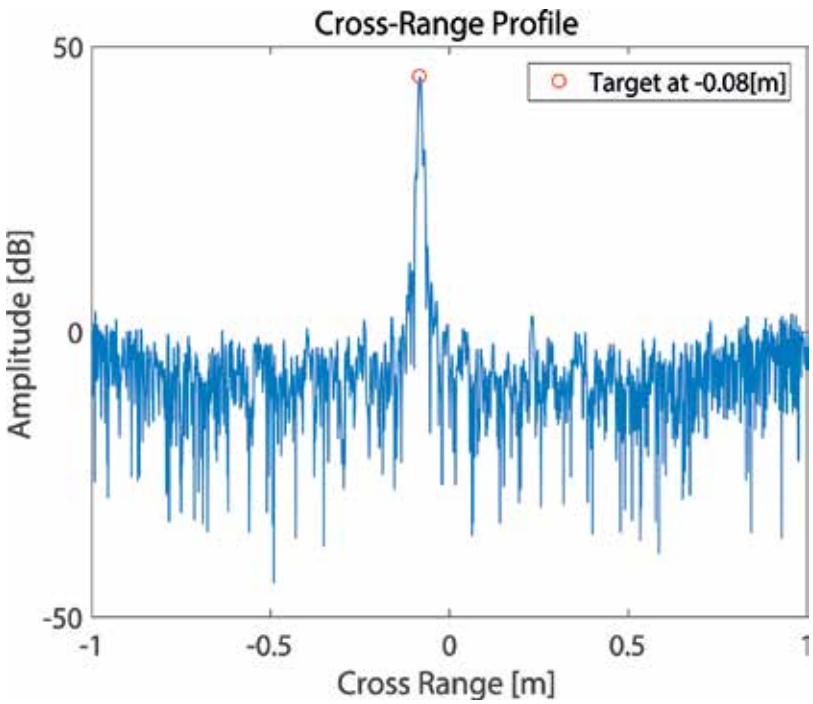

Figure 18. Cross-range profile of the impulse target.

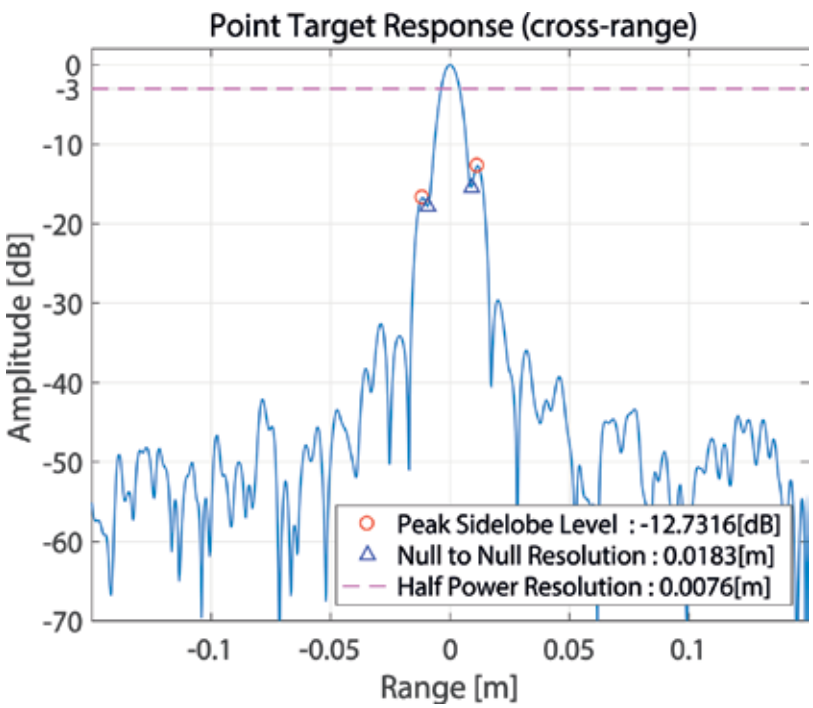

Figure 19. Detailed analysis on the cross-range profile of the impulse target.

Peak side-lobe level	**−12.73 dB**
Null-to-null resolution	0.0183 m
3 dB resolution	0.0076 m

Table 2. Measured cross-range resolution of SAR.

Figure 20. Experimental settings of multiple targets.

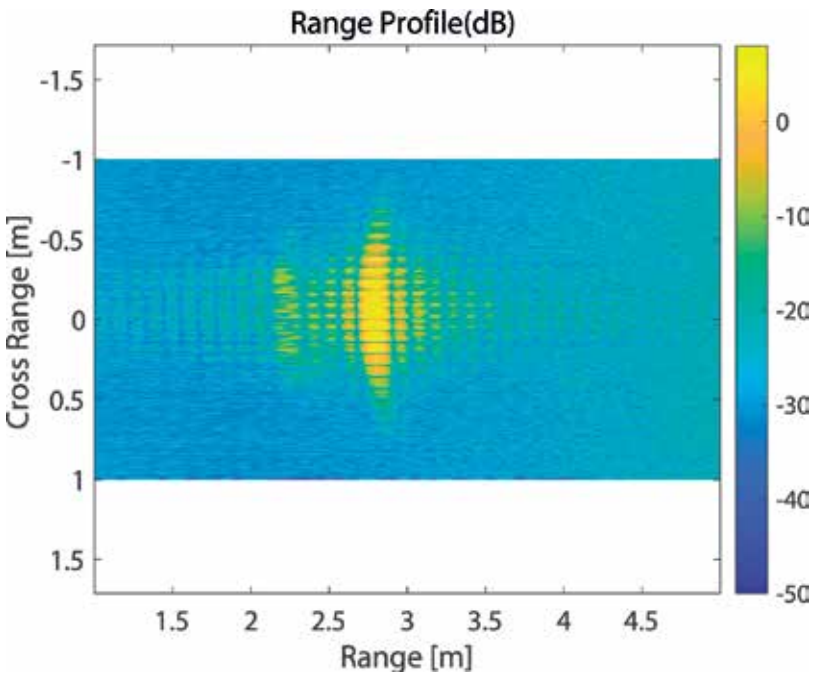

Figure 21. Measured range profile for three corner reflectors.

http://dx.doi.org/10.5772/intechopen.74692

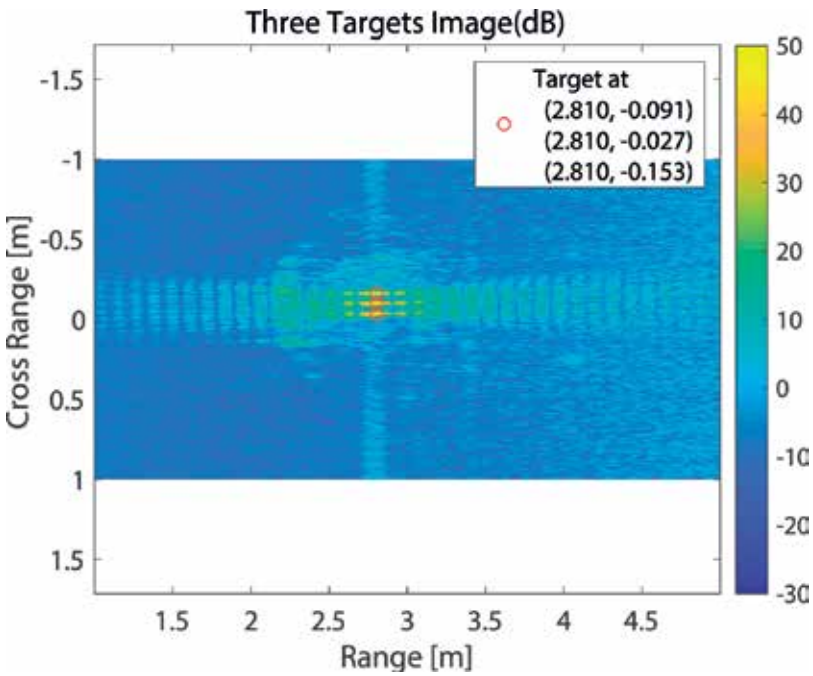

Figure 22. SAR image of multiple targets.

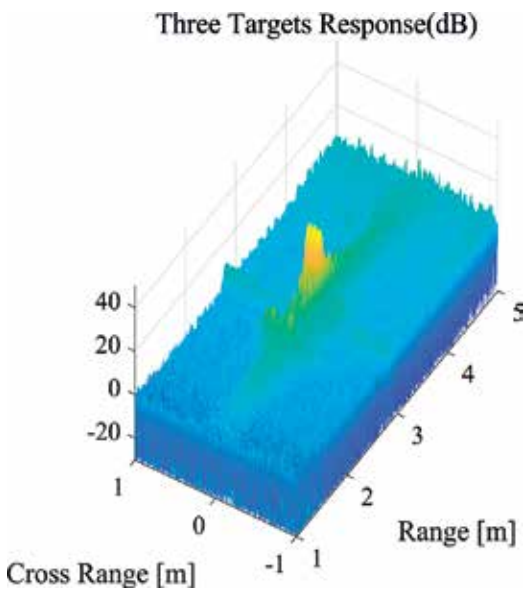

Figure 23. Azimuth-compressed SAR image of the multiple targets shown in three dimensions.

3.5. Multiple targets

An experiment was conducted in which three corner reflectors 0.06 m apart from each other were placed at a range of 2.8 m. The target settings are shown in **Figure 20**.

By using the same processing in Section 3.3, a SAR image of multiple targets was obtained. The range profile for the three corner reflectors is shown in **Figure 21**. Using the azimuth compression method in Section 3.3, the SAR images were obtained. The SAR image is shown in **Figure 22**, where its magnitude is in the decibel scale. The three-dimensional SAR image is shown in **Figure 23**. The positions of the corner reflectors are approximately 0.06 m apart in the cross-range direction. The targets are located close to the cross-range direction; nevertheless, they are clearly distinguishable. Any arbitrary object can acquire SAR images using the above SAR-focusing method. This SAR-imaging method is very simple; however, it is a powerful method for acquiring real-time SAR images.

4. Motion compensation

In the case of the airborne SAR, movement due to external disturbances can easily occur. Navigation devices, such as GPS and IMU, can record such motion. To focus the SAR image, the motion must be compensated. Motion compensation has been studied for decades, as described in [38–41]. Since W-band has a short wavelength, accurate motion compensation is

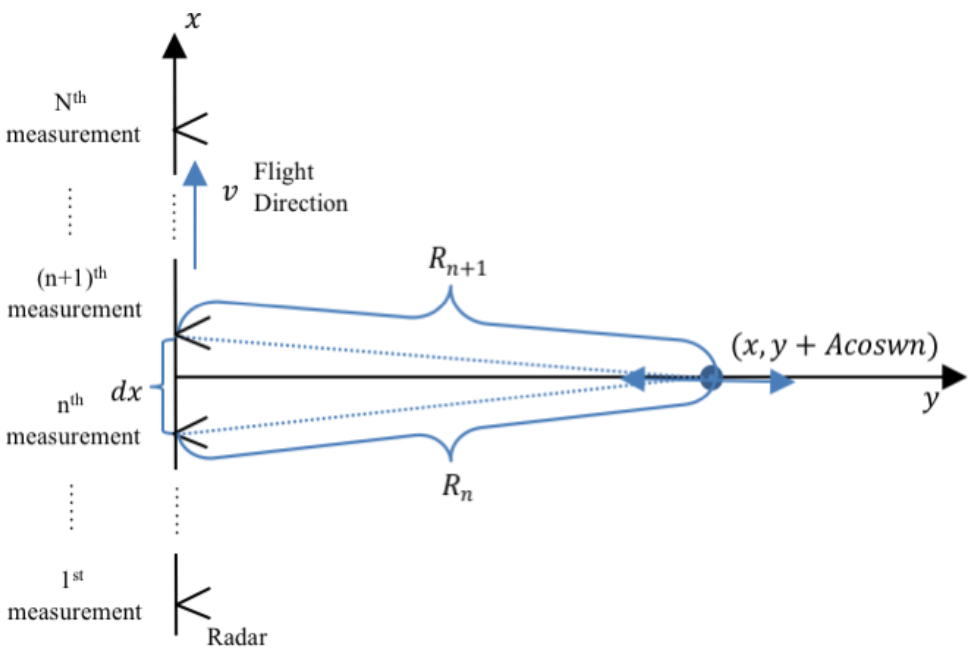

Figure 24. SAR geometry with motion.

http://dx.doi.org/10.5772/intechopen.74692

required. A method of applying and verifying the motion compensation to the simple SAR focusing shown in Section 3.3 is herein introduced.

To verify the motion compensation algorithm, the target was measured by adding motion to the SAR technique, as shown in **Figure 24**. Similar to the experiments in Section 3, the radar moved in the cross-range direction. However, in this case, the target also moved in the range direction. In practical situations, the radar has a movement in the range direction with stationary targets.

The above conditions are that the target is moving and general conditions move the platform, which are equivalent. Thus, for experimental convenience, the experiment in which the target moved was conducted. The target had a sinusoidal motion with an amplitude of 0.4 m, as shown in **Figure 25**. The amplitude of this motion was several times larger than both the range cell and the wavelength. Therefore, it was necessary to compensate for the range bin and phase in the range profile of the received signal.

The other conditions were the same as those in the experiments noted in Section 3. The SAR image acquisition method is now discussed with compensation for this motion. The motion of azimuth direction is known to be compensated by interpolation [39, 42, 43]. Thus, it is not considered in this experiment. The motion (or acceleration) in azimuth direction can be compensated by equal-spacing azimuth sampling using interpolation. Also, the interpolation can also be used to increase the sample in azimuth direction at a high velocity of the platform.

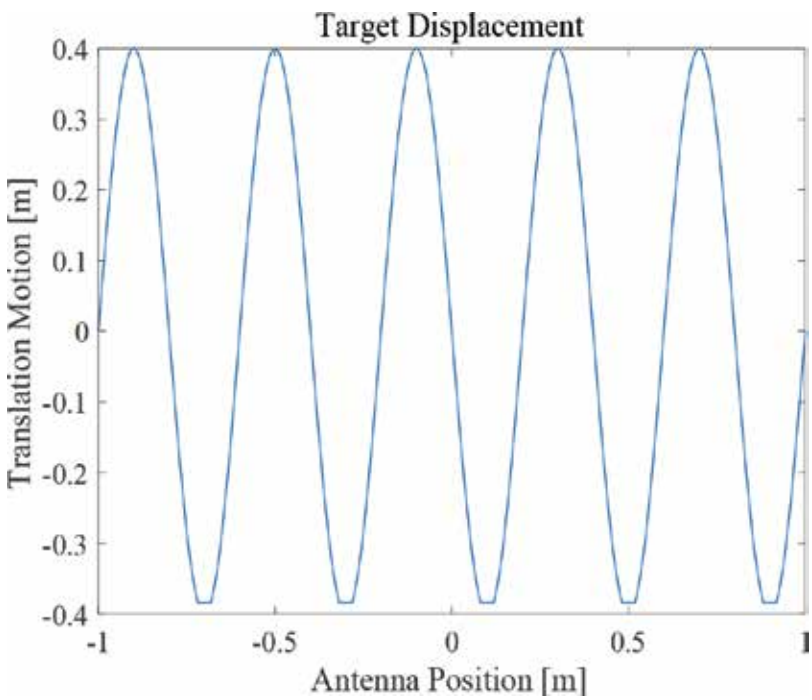

Figure 25. Movement applied to the target in the range direction.

4.1. Range bin alignment

The range profile of the impulse target located at 4.3 m and obtained under the mentioned sinusoidal motion is shown in **Figure 26**. In the figure, it can be observed that the locus of the scatterer moves in a sinusoidal direction.

The phase, including the motion in the azimuth direction, can be expressed as Eq. (16).

$$\begin{aligned}\theta'\left(n, R_0 = \sqrt{x_0^2 + y_0^2}\right) &= \frac{4\pi}{\lambda}\sqrt{(x_0 + ndx)^2 + \left(y_0 + d(n)\right)^2} \\ &\simeq \frac{4\pi}{\lambda}\left[\frac{x^2}{2y_0} + \frac{(ndx)^2}{2y_0} + \frac{x_0}{y_0}ndx + y_0 + Y_{des} + \frac{Y_{des}(n)^2}{2y_0}\right] \\ &\simeq \frac{4\pi}{\lambda}Y_{des} + \theta(n, y_0)\end{aligned} \tag{16}$$

The quadrature term of the phase in Eq. (12) and motion can be approximately represented as linear combinations. Therefore, the motion can be compensated independently of the azimuth compression.

For azimuth compression, the range bin should be aligned in the received signal (before IFFT). In the frequency domain, the delay function is represented by the phase shift. Accordingly, the received signal is compensated by the phase delay as much as the y-direction movement of the target. The phase delay for the range alignment is represented as Eq. (17).

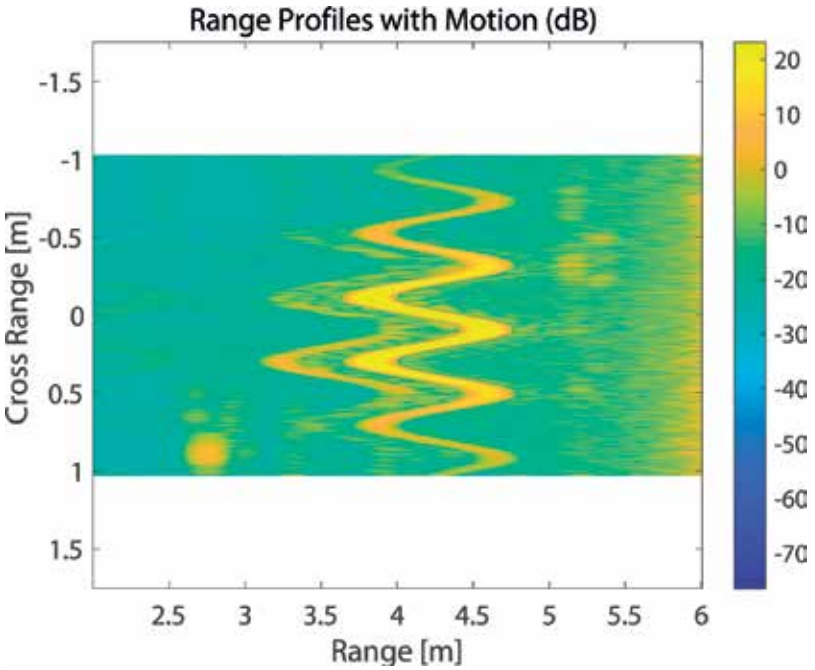

Figure 26. Range profile of a single target with motion.

http://dx.doi.org/10.5772/intechopen.74692

$$S_{MOCO1}(n_x, n) = e^{-2\pi j\left(\frac{Y_{des}(n)}{dr}\frac{n_x}{N_x}\right)} \tag{17}$$

where the range cell size is dr, the target movement is Y_{des}, the number of range bins is n_x, and the total number of range bins is N_x.

The compensation of the phase delay calculated by Eq. (17) to the range profile from Eq. (10) can be expressed as Eq. (18). The aligned range profile is expressed as $s_1(f, n)$, and the range profile after applying motion compensation in Eq. (18) is shown in **Figure 27**. As shown in the compensated range profile in **Figure 27**, most of the scatterers are aligned near the range bin.

$$S_1(f, n) = IFFT[s_h(t, n) * S_{MOCO1}(n_x, n)]_t \tag{18}$$

4.2. Phase compensation

The range must be compensated after bin alignment. Using the given motion, the range profile obtained in Eq. (18) can be compensated as Eq. (19).

$$S_2(f, n) = IFFT\left[FFT[S_1(f, n)]_f * e^{-\frac{4\pi j f_0}{c}Y_{des}(n)}\right]_f \tag{19}$$

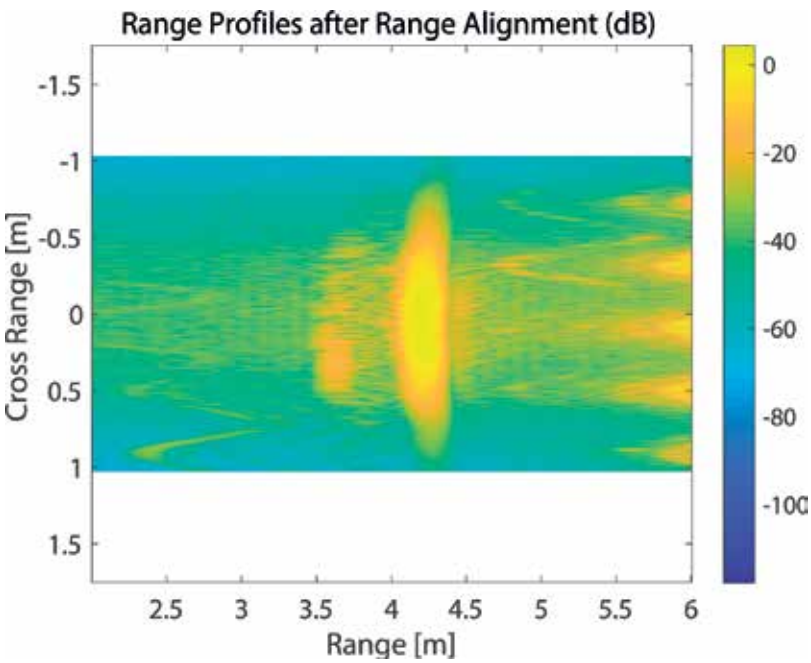

Figure 27. Range profiles after the range bin alignment.

The phase-compensated range profile, $s_2(f, n)$, performs azimuth compression in the same way as SAR imaging without motion. The SAR image can be obtained by performing azimuth compression, as shown in Eq. (20).

$$S_{SAR}(t,n) = IFFT\left[FFT[S_2(f,n)]_n * FFT[S_{MF}(n,y)]_y^*\right]_n \tag{20}$$

The process of motion compensation and SAR imaging can be represented by the flow chart shown in **Figure 28**.

4.3. SAR image after motion compensation

After compensating the motion for the single corner reflector, the SAR image was obtained by azimuth compression. The SAR image is shown in **Figure 29**; the magnitude is in decibel units. The image is depicted in three dimensions in **Figures 30** and **31**. **Figure 32** shows the range direction profile of the SAR image for a point target at a distance of approximately 4.3 m in the range direction. A detailed analysis of **Figure 32** is provided in **Figure 33**.

Table 3 compares and analyzes the resolutions obtained from motion compensation and the general SAR resolution. The motion compensation decreases the level of the peak to side lobe,

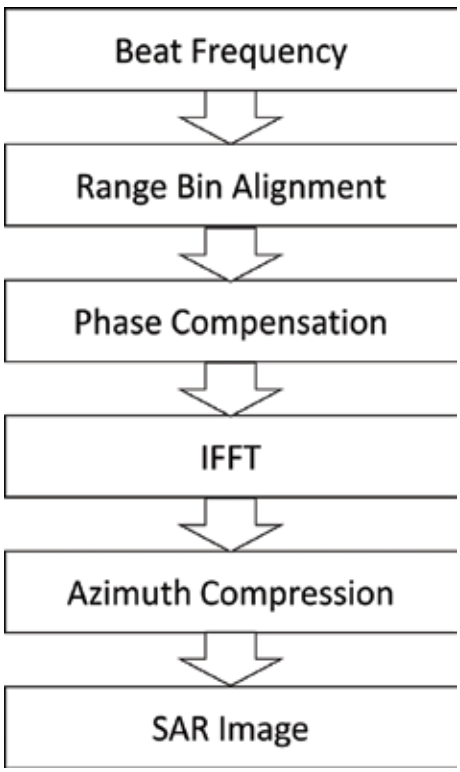

Figure 28. SAR motion compensation block diagram.

http://dx.doi.org/10.5772/intechopen.74692

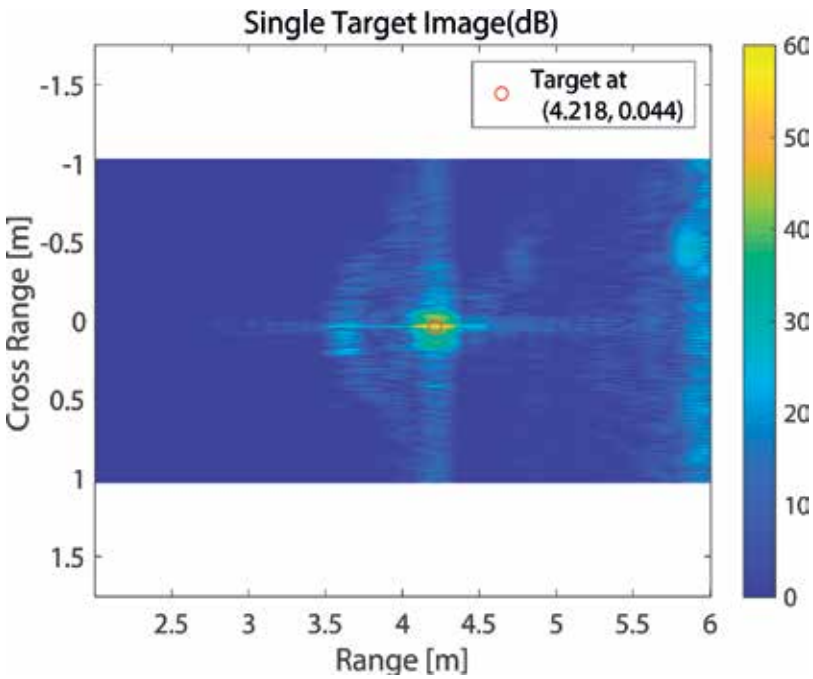

Figure 29. SAR image of the impulse target with motion compensation.

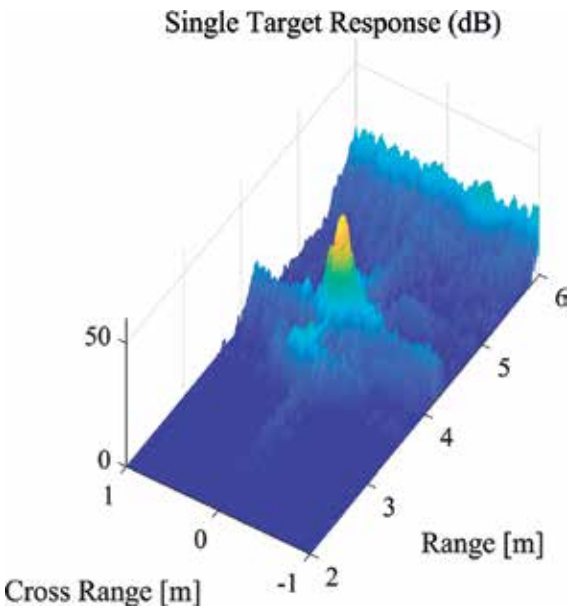

Figure 30. SAR image of the impulse target with motion compensation in three dimensions.

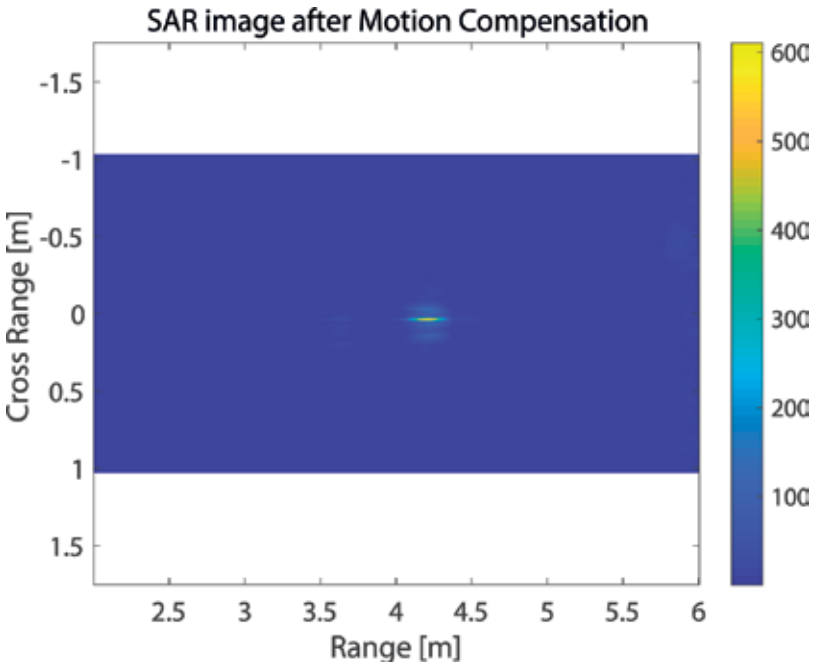

Figure 31. Azimuth-compressed SAR image of the impulse target with motion compensation.

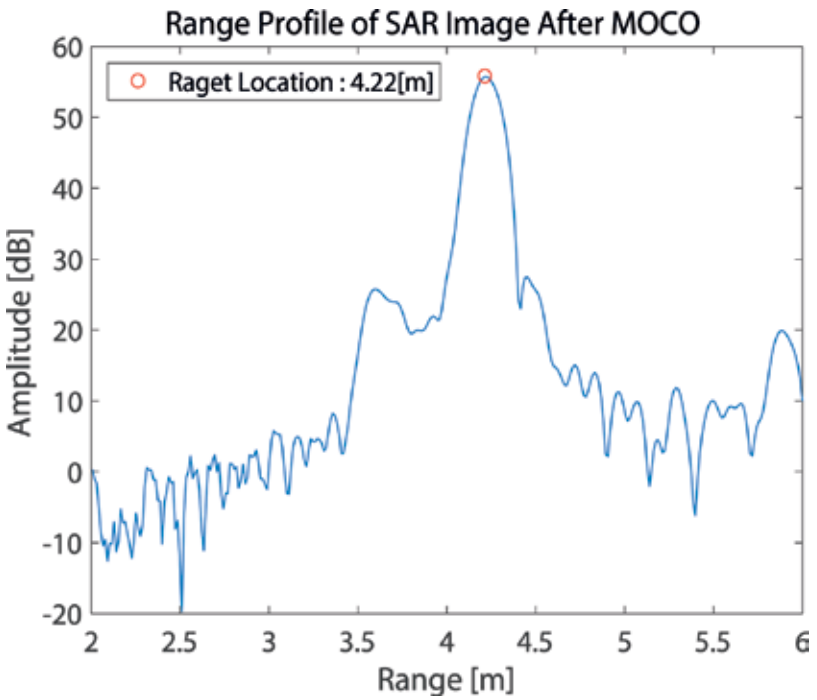

Figure 32. Range profile of the SAR image of the impulse target with motion compensation.

http://dx.doi.org/10.5772/intechopen.74692

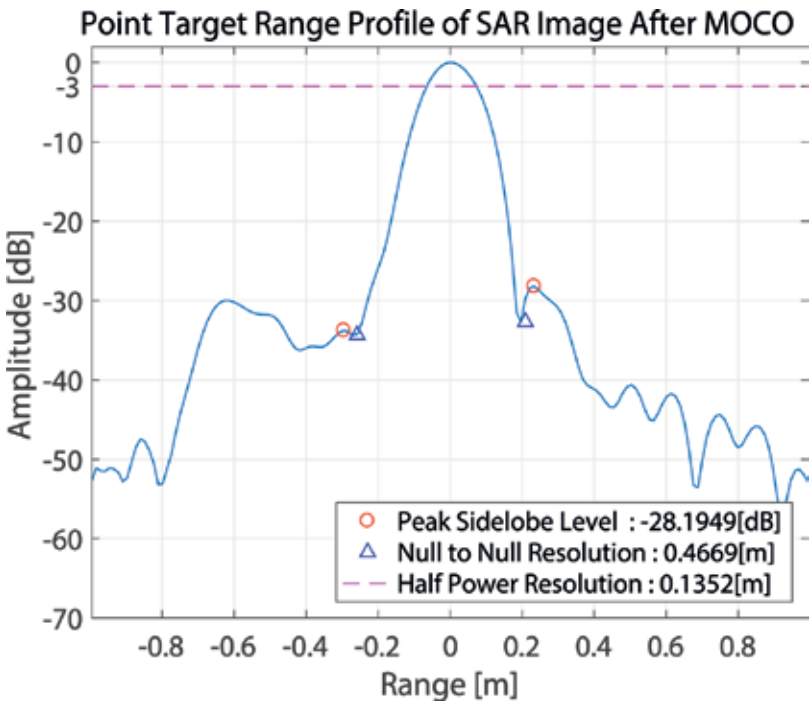

Figure 33. Detailed analysis of the impulse target range profile with motion compensation.

		w/o motion	Motion compensation
Range	Peak side-lobe level	−12.73 dB	−28.1949 dB
	Null-to-null resolution	0.2244 m	0.4669 m
	3-dB resolution	0.0984 m	0.1352 m
Cross-range	Peak side-lobe level	−12.73 dB	−11.22 dB
	Null-to-null resolution	0.0183 m	0.0268 m
	3-dB resolution	0.0076 m	0.0134 m

Table 3. Measured resolution of SAR after motion compensation.

and the resolution in the range direction increases. Furthermore, the resolution in the cross-range direction is degraded.

Furthermore, the cross-range profile at the target range was obtained by taking a column from the SAR image after motion compensation. The cross-range profile with the target location is shown in **Figure 34**. A detailed analysis on the point target is shown in **Figure 35**, including the side-lobe level and resolution.

In addition, experiments with multiple targets were performed as in Section 3.5. The target movement in the range direction was the same as in the above experiment. Three corner

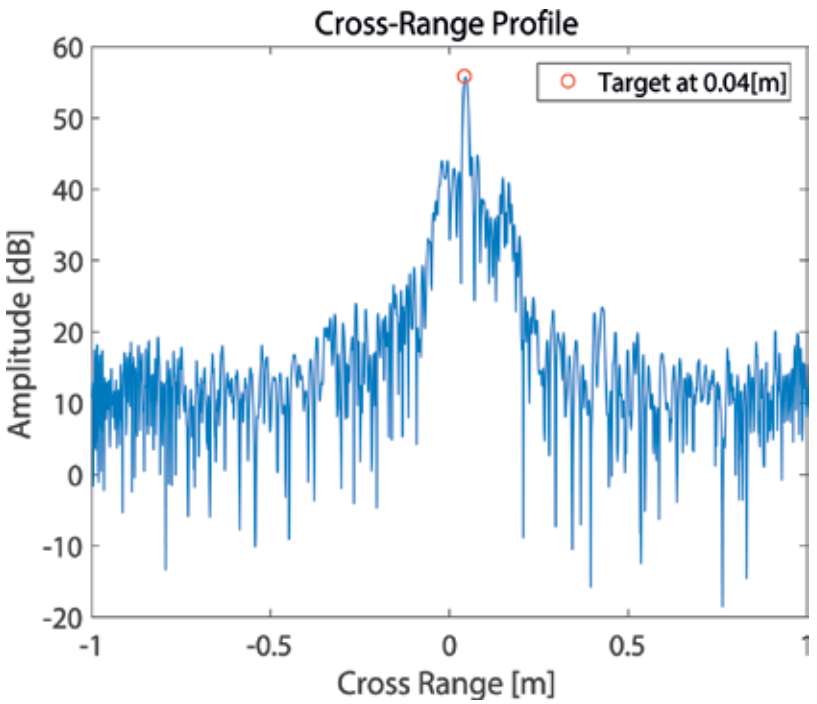

Figure 34. Cross-range profile of the impulse target with motion compensation.

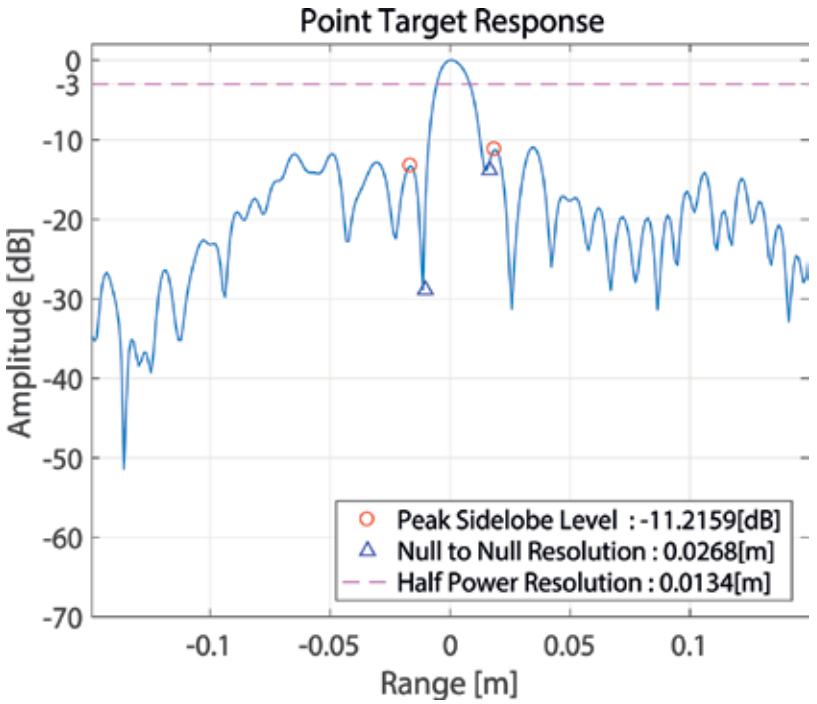

Figure 35. Detailed analysis on the impulse target cross-range profile with motion compensation.

http://dx.doi.org/10.5772/intechopen.74692

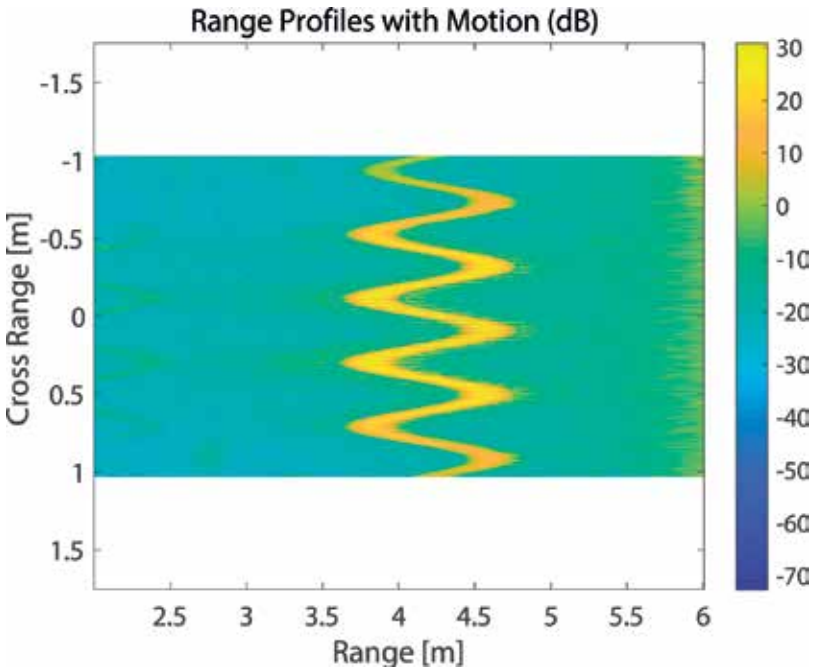

Figure 36. Measured range profile of multiple targets with motion.

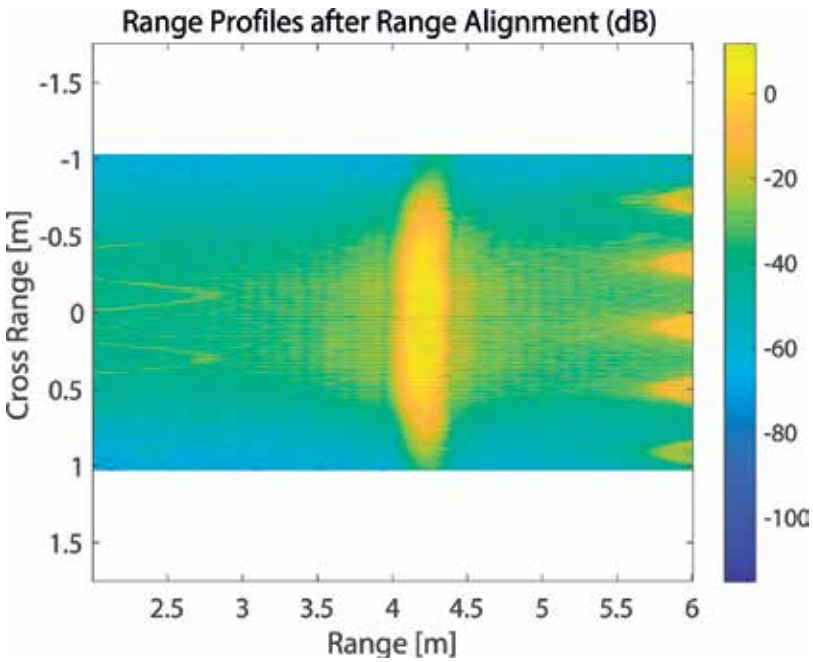

Figure 37. Range profile of multiple targets after range alignment.

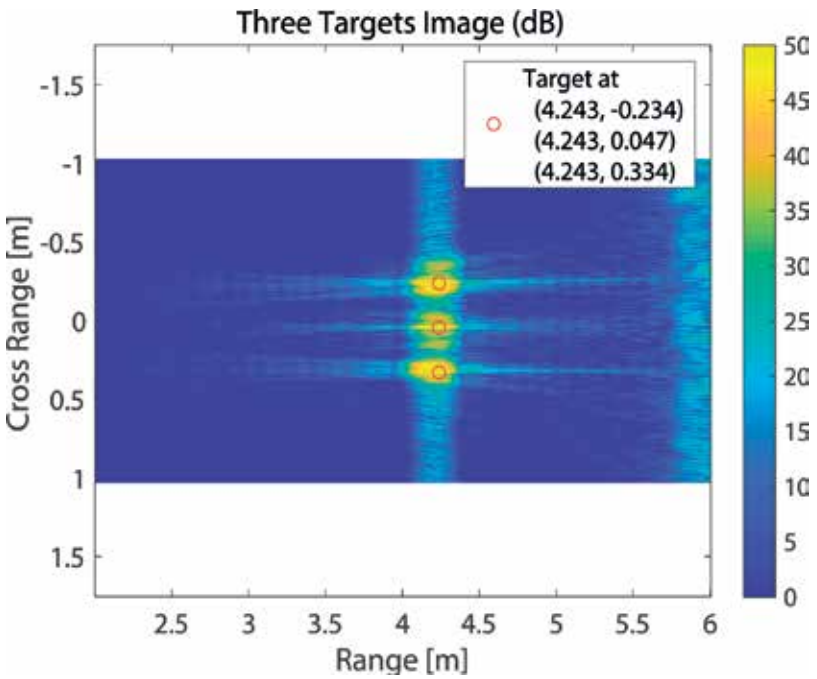

Figure 38. SAR image of multiple targets with motion compensation.

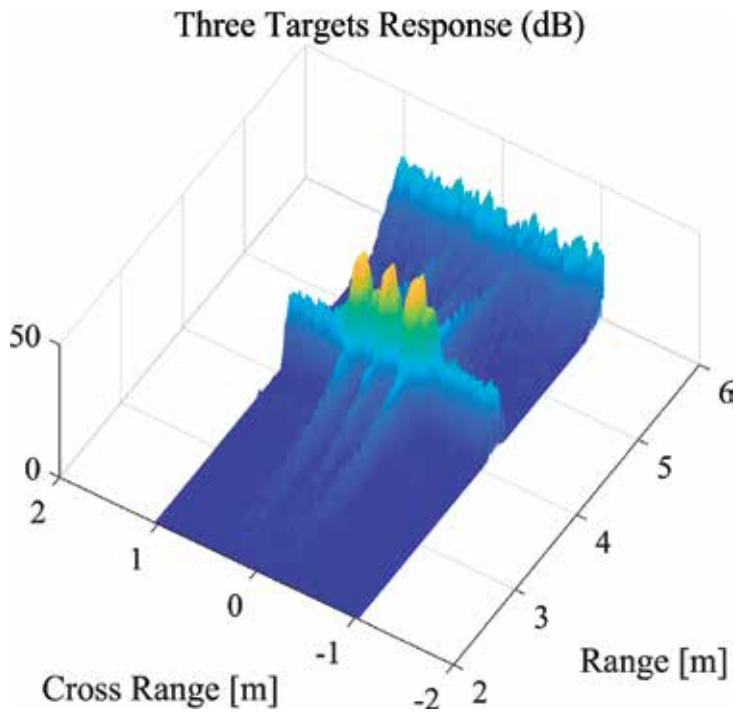

Figure 39. SAR image of multiple targets in three dimensions.

http://dx.doi.org/10.5772/intechopen.74692

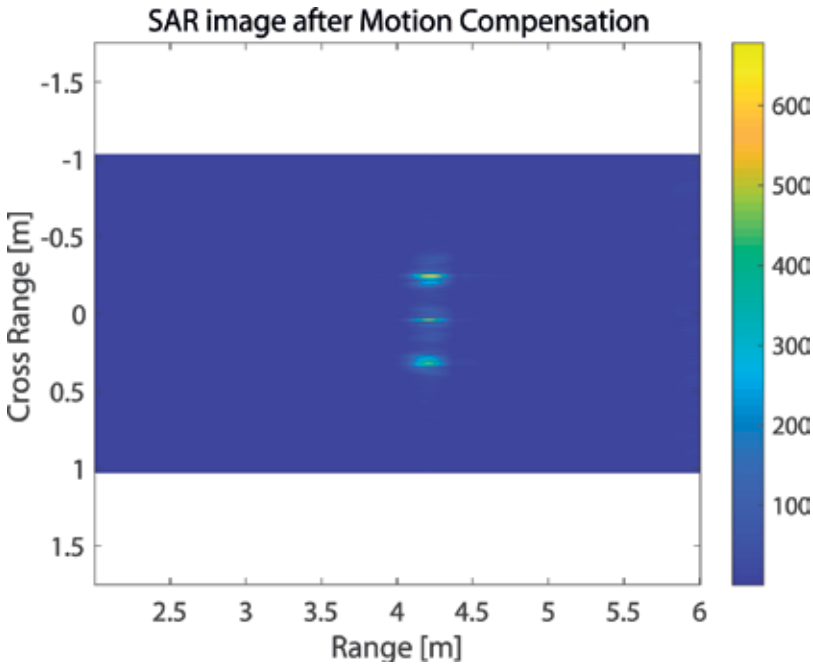

Figure 40. Azimuth-compressed SAR image with motion compensation.

reflectors, which were approximately 0.26 m apart in the azimuth direction and located approximately 4.3 m in the range direction, were used. The range profile is shown in **Figure 36**.

The range profile for the range bin compensation is shown in **Figure 37**. The SAR image for three targets after motion compensation was obtained in decibel units, as shown in **Figure 38**. The three-dimensional SAR image is illustrated in **Figure 39**; the SAR image is depicted in **Figure 40**.

5. Conclusions

A simple SAR algorithm for the W-band and a method for motion compensation of a disturbance-containing signal were presented. A SAR-imaging method in a situation with motion in the range direction was additionally presented. The FMCW radar continuously transmits signals of a predetermined period. If a constant speed along the track is maintained, the moving distance or a period is also maintained. In a conducted experiment, the distance interval was a function of the along-track velocity. With a constant pulse repeat frequency (PRF), the faster the radar is, the longer is the time (or distance) interval between the range profiles. Disturbance of the along-track (azimuth direction) was not considered in this chapter because it can be easily compensated by interpolation. Movement in the range direction has a significant effect on SAR imaging. The proposed method can be used with the exact knowledge of the radar movement.

The described SAR algorithm is based on the RDA with the range variant FM rate. The FMCW radar can be used in a relatively close range and has a low computing cost. In addition, motion compensation can be easily performed using the given position information, even though the RDA method is used. Owing to the W-band characteristics, the RCM can be ignored; however, very precise position information and the motion compensation are required since short wavelengths are used. In the W-band, the beam width is narrow and the synthetic aperture length is short. Therefore, long-term position information is not required; nonetheless, position information that is more precise than the wavelength is required. On account of the short synthetic aperture length, motion may be compensated based on simple parameters. This phenomenon is useful for video SAR because it can increase the frame rate of the SAR image.

Owing to the limitations of navigation sensors, there is a limit to the motion compensation. Precise navigation devices are very expensive and physically difficult to mount on a small aircraft. Therefore, it is necessary to calculate motion and compensate it from received data. In this experiment, although the motor controller had a precision of several millimeters, it was not perfectly compensated by the inaccuracy of the position information. In future studies, the actual flight measurements will be performed and motion compensation will be conducted from the received data. Unlike the experiment in the laboratory, field measurements can be used in the long range. Hence, the SAR algorithm can become more simple, and it is expected to be a real-time-processing approach.

Furthermore, there are many methods for autofocusing based on received data. However, there remains a limit to the autofocusing method. The minimum entropy method is precise as a contrast-based method; however, it has a large computing cost and difficulty in finding the global minimum. With respect to PPP or PGA, there may not be a suitable target in the image, and it is difficult to use in complex structures or extended targets. It may not be particularly suitable for a narrow beam of W-band. Moreover, it is difficult to use in the case wherein the image frame rate is as high as the video SAR.

In this experiment, as a result of the motion compensation, the level of the side lobe was lowered and the resolution of the cross-range was reduced. However, the resolution in the range direction of the SAR image increased. This result requires further investigation and elaborate experimentation. The resolution of the azimuth direction will increase in proportion to the range variation within the synthetic aperture length. Therefore, if motion is exactly known, the azimuth resolution can increase further when there is external motion. Currently, the azimuth resolution is relatively higher than the range resolution. If the resolution is the same for the range and azimuth, and the size of the image is reduced in the azimuth direction, the frame rate can be sufficiently increased.

Experiments in the laboratory are useful for W-band radar development, radar performance validation, and SAR algorithm verification. By using FMCW radar, low power consumption and miniaturization can be achieved. By using high frequency, small antenna and RF devices can be used, which is advantageous when mounting the radar to a flight vehicle. In addition, accurate motion can be applied in the laboratory. However, physical distance constraints exist. Based on the measurements in the laboratory, it was possible to develop W-band

FMCW radar based on FPGA, and the good performance was confirmed. In addition, the SAR algorithm and motion compensation were shown to have good performance in the experiments.

Furthermore, the Hilbert transform returned the component orthogonal to the real component. The Hilbert transform removed symmetric components in the range profile after the IFT. This is useful when only the real component is received in the FMCW radar. However, it should be used when I and Q data are not actually received.

In this chapter, the development of a high-resolution W-band radar based on FPGA is described, and W-band SAR images can be obtained via the motion compensation. The motion compensation method in W-band has been described as accurate phase compensation. As a result, the SAR images are obtained in the laboratory using developed W-band radar, and the SAR images are consistent with the theoretical resolution. Although the resolution of the SAR image is slightly lower than that of the motion compensation, the SAR image can be obtained almost the same as the theory.

Acknowledgements

This research was supported by the MSIT (Ministry of Science and ICT), Korea, under the ICT Consilience Creative program (IITP-2017-2017-0-01015) supervised by the IITP (Institute for Information & Communications Technology Promotion), the Civil Military Technology Cooperation Program, and the Institute for Information & Communications Technology Promotion (IITP) grant funded by the Korea government (MSIT) (2017–0-00678, A Development of SAR for small-sized UAV).

Author details

Jiwoong Yu[1,2*], Sumin Kim[1] and Min-Ho Ka[1]

*Address all correspondence to: jiwoong.yu@yonsei.ac.kr

1 School of Integrated Technology, Yonsei Institute of Convergence Technology, Yonsei University, South Korea

2 Satellite Technology Research Center, Korea Advanced Institute of Science and Technology, South Korea

References

[1] Moreira A et al. A tutorial on synthetic aperture radar. IEEE Geoscience and Remote Sensing Magazine. 2013;**1**(1):6-43

[2] Yu J, Dewantari A, Ka M-H. Measurement of the rotation center from the received signals for ultrahigh-resolution radar imaging. IEEE Antennas and Wireless Propagation Letters. 2017;**16**:2266-2269

[3] Yu J, Ka M-H. Precision near-field reconstruction in the time domain via minimum entropy for ultra-high resolution radar imaging. Remote Sensing. 2017;**9**(5):449

[4] Kim S, Yu J, Jeon SY, Dewantari A, Ka M-H. Signal processing for a multiple-input, multiple-output (MIMO) video synthetic aperture radar (SAR) with beat frequency division frequency-modulated continuous wave (FMCW). Remote Sensing. 2017;**9**(5):491

[5] Metasensing. Airborne Sar [Online]. Available: http://www.metasensing.com/wp/index.php/products/airborne-sar/minisar-sensor/

[6] ImSAR. Imsar's Collision-Avoidance Radar for Small Uas Expected to be Available Late 2016, [Online]. Available: http://www.imsar.com/pages/news.php?article = imsars collision-navoidance radar for small uas expected to be available late; 2016

[7] Raney RK, Cahill JT, Patterson G, Bussey DBJ. The m-chi decomposition of hybrid dual-polarimetric radar data. In: Geoscience and Remote Sensing Symposium (IGARSS), 2012 IEEE International. IEEE; 2012. pp. 5093-5096

[8] Sakai F, Suzuki H, Sato H, Sawaya K, Mizuno K. High resolution millimeter-wave imaging radar using inline tx/rx antennas. In: Radar Conference, 2008, EuRAD 2008. European, IEEE; 2008. pp. 156-159

[9] Goshi D, Liu Y, Mai K, Bui L, Shih Y. Recent advances in 94 ghz fmcw imaging radar development. In: Microwave Symposium Digest, 2009, MTT'09. IEEE MTT-S International, IEEE; 2009. pp. 77-80

[10] Palm S, Wahlen A, Stanko S, Pohl N, Wellig P, Stilla U. Real-time onboard processing and ground based monitoring of fmcw-sar videos. In EUSAR 2014; 10th European Conference on Synthetic Aperture Radar; Proceedings of, VDE; 2014. pp. 1-4

[11] Meta A, Hoogeboom P, Ligthart LP. Signalprocessingforfmcw sar. Geoscience and Remote Sensing, IEEE Transactions. 2007;**45**(11):3519-3532

[12] Ribalta A. Time-domain reconstruction algorithms for fmcw-sar. Geoscience and Remote Sensing Letters, IEEE. 2011;**8**(3):396-400

[13] SAGE Millimeter, SAR-2507-10-S2. [Online]. Available from: https://www.sagemillimeter.com/content/datasheets/SAR-2507-10-S2.pdf

[14] Xilinx, Zynq-7000 All Programmable SoC Data Sheet: Overview, [Online]. Available from: https://www.xilinx.com/support/documentation/data_sheets/ds190-Zynq-7000-Overview.pdf

[15] Charvat GL, Kempel LC. Synthetic aperture radar imaging using a unique approach to frequency-modulated continuous-wave radar design. Antennas and Propagation Magazine, IEEE. 2006;**48**(1):171-177

[16] Charvat GL, Kempell LC, Coleman C. A low-power high- sensitivity x-band rail sar imaging system [measurement's corner]. Antennas and Propagation Magazine, IEEE. 2008;**50**(3):108-115

[17] Xi L, Guosui L, Ni J. Autofocusing of isar images based on entropy minimization. IEEE Transactions on Aerospace and Electronic Systems. 1999;**35**(4):1240-1252

[18] Giusti E, Martorella M. Range doppler and image autofocusing for fmcw inverse synthetic aperture radar. IEEE Transactions on Aerospace and Electronic Systems. 2011;**47**(4):2807-2823

[19] Berizzi F, Corsini G. Autofocusing of inverse synthetic aperture radar images using contrast optimization. IEEE Transactions on Aerospace and Electronic Systems. 1996;**32**(3): 1185-1191

[20] Wahl D, Eichel P, Ghiglia D, Jakowatz C Jr. Phase gradient autofocus-a robust tool for high resolution sar phase correction. IEEE Transactions on Aerospace and Electronic Systems. 1994;**30**(3):827-835

[21] Otten MPG, Van Rossum WL, Van Bree RJP. Extended pga for range migration algorithms. IEEE transactions on Aerospace and electronic systems. 2006;**42**(2):478-488

[22] Werness S, Carrara W, Joyce L, Franczak D. Moving target imaging algorithm for sar data. IEEE Transactions on Aerospace and Electronic Systems. 1990;**26**(1):57-67

[23] Dungan KE, Nehrbass JW. Wide-area wide-angle sar focusing. Aerospace and Electronic Systems Magazine, IEEE. 2014;**29**(1):21-28

[24] Chen C-C, Andrews HC. Target-motion-induced radar imaging. IEEE Transactions on Aerospace and Electronic Systems. 1980;(1):2-14

[25] Cao P, Xing M, Sun G, Li Y, Bao Z. Minimum entropy via subspace for isar autofocus. Geoscience and Remote Sensing Letters, IEEE. 2010;**7**(1):205-209

[26] Wallace H, Gorman J, Maloney P. Video Synthetic Aperture Radar (Visar); 2012

[27] Johannes W, Stanko S, Wahlen A, Sommer R, Pohl N, Wellig P, Sennhauser C, Meier E, Kallfass I. Implementation of a 35 ghz sar sensor and a high resolution camera to enable real-time observation. In: EUSAR 2014; 10th European Conference on Synthetic Aperture Radar; Proceedings of, pp. 1-4, VDE. 2014

[28] Doerry AW, Dubbert DF, Thompson M, Gutierrez VD. A portfolio of fine resolution ka-band sar images: Part i. In: Defense and Security, pp. 13–24, International Society for Optics and Photonics. Proceedings of SPIE. Vol. 5788. Bellingham, WA: SPIE; 2005

[29] Avnet. ZedBoard Hardware User's Guide [Online]. Available from: https://reference.digilentinc.com/_media/zedboard:zedboard_ug.pdf

[30] Charvat GL. Small and short-range radar systems. Boca Raton, FL: Taylor & Francis Group, CRC Press; 2014

[31] IMST GmbH imst radar -small and flexible 24 ghz radar modules. http://www.radar-sensor.com/?navanchor = 2,110,039. [Accessed: April 07, 2017]

[32] Infineon Technologies AG 24ghz rdar - industrial. https://www.infineon.com/cms/en/product/rf-and-wireless-control/mmwave-mmic/24-ghz-radar-industrial/channel.html?channel = 5546d46145f1f3a40146140e9c1c1956. [Accessed: April 07, 2017]

[33] SIVERS IMA fmcw Radar Sensors fron end, 24 ghz to 77 ghz-sivers ima. https://siversima.com/products/radar-sensors/. [Accessed: April 07 2017]

[34] InnoSenT Application of Radar Systems. http://www.innosent.de/en/applications/. [Accessed: April 07, 2017]

[35] Mahafza BR. Radar signal analysis and processing using MATLAB. New York: Taylor & Francis Group, CRC Press; 2016

[36] Richards MA. Fundamentals of signal processing to fundamentals of radar signal processing, USA. pp. 171-183, 581-582; 2015

[37] Ozdemir C. Inverse Synthetic Aperture Radar Imaging with Matlab Algorithms. Wiley; 2012. pp. 139-140

[38] Moreira A, Huang Y. Airborne SAR processing of highly squinted data using a chirp scaling approach with integrated motion compensation. IEEE Transactions on Geoscience and Remote Sensing. 1994;**32**(5):1029-1040

[39] Fornaro G, Franceschetti G, Perna S. On center-beam approximation in SAR motion compensation. IEEE Geoscience and Remote Sensing Letters. 2006;**3**(2):276-280

[40] Xing M et al. Motion compensation for UAV SAR based on raw radar data. IEEE Transactions on Geoscience and Remote Sensing. 2009;**47**(8):2870-2883

[41] Buckreuss S. Motion compensation for airborne SAR based on inertial data, RDM and GPS. Geoscience and Remote Sensing Symposium, 1994. IGARSS'94. Surface and Atmospheric Remote Sensing: Technologies, Data Analysis and Interpretation., International. Vol. 4. IEEE; 1994

[42] Carrara R, Goodman R. Spotlight Synthetic Aperture Radar: Signal Processing Algorithms. Norwood, MA: Artech House; 1995

[43] Cumming IG, Wong FH. Digital processing of synthetic aperture radar data. Artech house 1.2.2005: 3

Chapter 5

Analysis of Coastal Areas Using SAR Images: A Case Study of the Dutch Wadden Sea Region

Corneliu Octavian Dumitru, Gottfried Schwarz,
Daniela Espinoza-Molina, Mihai Datcu,
Herman Hummel and Christiaan Hummel

Additional information is available at the end of the chapter

http://dx.doi.org/10.5772/intechopen.70855

Abstract

The increased availability of civil synthetic aperture radar (SAR) satellite images with different resolution allows us to compare the imaging capabilities of these instruments, to assess the quality of the available data and to investigate different areas (e.g., the Wadden Sea region). In our investigation, we propose to explore the content of TerraSAR-X and Sentinel-1A satellite images via a data mining approach in which the main steps are patch tiling, feature extraction, classification, semantic annotation and visual-statistical analytics. Once all the extracted categories are mapped and quantified, then the next step is to interpret them from an environmental point of view. The objective of our study is the application of semi-automated SAR image interpretation. Its novelty is the automated multiclass categorisation of coastal areas. We found out that the north-west of the Netherlands can be interpreted routinely as land surfaces by our satellite image analyses, while for the Wadden Sea, we can discriminate the different water levels and their impact on the visibility of the tidal flats. This necessitates a selection of time series data spanning a full tidal cycle.

Keywords: classification, coastal areas, SAR imaging, semantic labelling, Wadden Sea

1. Introduction

The Wadden Sea (Dutch: Waddenzee, German: Wattenmeer, Danish: Vadehavet) is a coastal area with extensive tidal flats in the south-eastern part of the North Sea (see **Figure 1**). It lies between the coast of N-W continental Europe and the range of Frisian Islands, forming a shallow body of water with tidal flats and wetlands [1], protected by a 450 km long chain of

Figure 1. The Dutch-German-Danish Wadden Sea area (with the kind permission of the common Wadden Sea secretariat, CWSS [18]).

barrier islands, the Wadden Islands [2]. The Wadden Sea region measures about 22,000 km^2 divided between land and sea. About 63% of the region lies in Germany, with about 30% in the Netherlands and 7% in Denmark [3].

- *Environment:* Most of the landforms in the Wadden Sea region have essentially been created from a marine [2] or tidal [4, 5] environment. The main exception being the Dutch Wadden island of Texel, the centre of which is a glacial relict. The islands are characterised by dunes and wide, sandy beaches to the North Sea, and a low, tidal coast to the Wadden Sea. It also consists of large intertidal areas, of which two thirds are emergent at low tide. Most of these flats are bare, mainly consisting of sand, but locally along the mainland, and in estuaries, mudflats and salt marshes occur [6].

- *Fauna:* The Wadden Sea is famous for its rich fauna, such as birds: waders, ducks and geese; that use the Wadden Sea area as a migration stopover or wintering site and also gulls and terns [7]. Typical of the Wadden Sea are large tidal flats, which are characterised by very high benthic biomass and productivity, dominated by molluscs and polychaetes [8]. The Wadden Sea houses a variety of habitats that support diverse fish communities, providing an important nursery and feeding area for many fish of commercial importance [9, 10]. Also, a large population of harbour seals (*Phoca vitulina*) lives in the Wadden Sea [11].

http://dx.doi.org/10.5772/intechopen.70855

- *Conservation:* In 2009, the Dutch-German Wadden Sea was inscribed on the UNESCO World Heritage List, and the Danish part was added later in 2014.

Our interest in this contribution is on the use of remote sensing in the Dutch part of the Wadden Sea, which is a protected area under European legislation [12]. This area is part of the Natura 2000 network [13] (see **Figure 2**) and is one of the protected areas being analysed in [14]. Natura 2000 covers 18% of the EU's land area and 6% of its marine territory. The aim of the network is to ensure the long-term survival of Europe's most valuable and threatened species and habitats [15].

In the coastal area research literature, there are several studies treating the Wadden Sea area along the years (for an interdisciplinary overview, see [2, 5]). The Wadden Sea area faces a strong economic impact due to recreation, fisheries and maritime traffic. The last impact is due to, for example, the ports of Bremerhaven, Hamburg and Rotterdam, whereby the traffic runs through or nearby this area, which makes that monitoring of sand banks and any decrease of the water depth in this area is a critical topic for maritime security.

In order to understand the Wadden Sea dynamics, we exploited a number of recent publications already using remote sensing images and addressing the issue of SAR satellite image classification and interpretation [16, 17] in these coastal areas.

For a more detailed description of coastal areas, the work of [19] is focused on morphological changes (e.g., river estuaries) using X-band radar data. Here, TerraSAR-X Spotlight and

Figure 2. Natura 2000 network viewer of the Dutch Wadden Sea and surrounding areas (the colour legend is available in [13]).

StripMap images [20] are used to monitor river channel and coastline/waterline changes. However, this data set only covers the Island of Helgoland (North Sea, Germany) and the river Elbe estuary.

An extension of [19] is presented in [21], where the authors perform automated land-waterline detection with a high level of accuracy using TerraSAR-X StripMap and ScanSAR images. This latter data set covers two areas, the south of Trischen Island and Pellworm Island. The proposed detection technique provides a fast and useful way to identify changes in the coastal topography.

Further, [22] describes a waterline extraction algorithm, which allows a near real-time determination of changes of coastal outlines of the North Sea using TerraSAR-X and Sentinel-1A images.

In [23], the authors use a waterline detection method to produce the topography of tidal flats by using 70 SAR images taken between 1996 and 1999 at different water levels. The investigated area is along the North Sea coast of Germany between Schleswig-Holstein and Lower Saxony.

In addition, [24] investigates the characteristics of five tests areas (Amrum, Pellworm, Wesselburen, Jadebusen and Norderney) using TerraSAR-X and C-band RADARSAT-2 [25] data acquired in 2012 and 2013. The authors demonstrate that the analysis of TerraSAR-X images provides valuable information about the intertidal flats when monitoring the Wadden Sea area. For the detection of small changes (in waterline and morphology), a combination of X-band data with C-band data helps to obtain reliable conclusions. Promising results are also obtained for dual polarisation SAR images, when the images are acquired at incidence angles exceeding 40°.

The organisation of this contribution is as follows. Section 2 presents the characteristics of our data set. Section 3 outlines our image analysis methodology used to generate visual-statistical analytics. Section 4 describes the image classification and annotation results using the methodology presented in Section 3. Finally, Section 5 gives an environmental interpretation and quality assessment of the results from Section 4, while Section 6 contains a conclusion and a comparison of results with Sentinel-2 data.

2. Test and validation dataset

The different resolutions of high-resolution data from TerraSAR-X [20] and medium-resolution data from Sentinel-1A [26] allow us to compare the imaging capabilities of these instruments, to assess the quality of the available data and to monitor periodically different areas. Therefore, we analysed both TerraSAR-X and Sentinel-1A amplitude data from the Wadden Sea and its surrounding neighbour areas (outside of the zone marked in purple in **Figure 2**).

TerraSAR-X is a German radar satellite launched in June 2007. It operates in X-band and is a side-looking SAR instrument that offers a wide selection of operating modes and product-generation options [20]. TerraSAR-X has a repeat period of 11 days. We selected high-resolution

http://dx.doi.org/10.5772/intechopen.70855

mode images (High resolution Spotlight (HS), or StripMap (SM)) with vertical (VV) polarisation, because they provide the best resolution data of the target areas. As for the product-generation options, we took from the available modes the multi-look ground range detected (MGD) level 1b mode, because this is not affected by geometrical interpolation effects over hilly terrain and is well suited for feature extraction. This was also the reason for choosing the radiometrically enhanced (RE) product option that is optimised with respect to radiometry (i.e., reduced speckle).

On the other hand, Sentinel-1 is a C-band radar satellite mission funded by the European Union and operated by the European Space Agency (ESA). It comprises a constellation of two satellites, Sentinel-1A launched in April 2014 and Sentinel-1B launched 2 years later in April 2016. These Sentinels have a repeat period of 6 days for the twin constellation. We selected Sentinel-1A images because they are readily available for our investigated area. Level-1 products are recommended for land cover analysis. For a fair comparison with TerraSAR-X, we chose the interferometric wide (IW) swath mode and its GRD (ground range detected) option containing medium-resolution data. We limited ourselves to single polarisation (VV) data.

When comparing the classification potential of both missions, it turns out that the high-resolution TerraSAR-X data not only provide more detailed object morphologies but also allow more classes to be discriminated with good classification quality. We suppose that this is due to the good signal-to-noise characteristics of the TerraSAR-X radiometrically enhanced products.

Figure 3 shows the geographical locations of all SAR images from our data set. The footprints of three TerraSAR-X image products are marked with red rectangles. Together with these TerraSAR-X images, another two Sentinel-1A image products are analysed in our evaluation. All images were acquired within a short time interval and are projected on a map (see **Figure 3**) using QGIS [27].

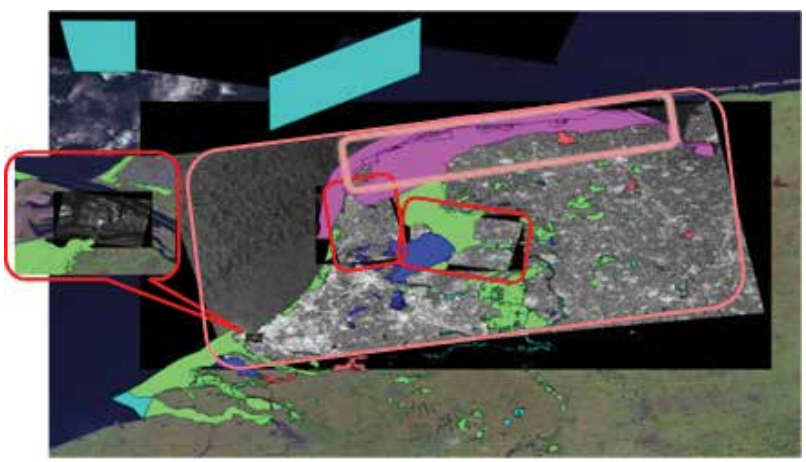

Figure 3. Locations of our SAR images and the Natura 2000 protected areas of the Netherlands.

The scenes were selected based on their availability, their content and their typical diversity of categories. The data set mainly covers the protected area of the Wadden Sea (its Dutch part) and its surrounding areas. The corresponding image parameters are listed in **Table 1**. All images were tiled into a series of patches with a size of 200 × 200 pixels (in the case of TerraSAR-X) and 128 × 128 pixels (in the case of Sentinel-1A). In total, we obtained 10,834 patches for TerraSAR-X and 34,900 patches for Sentinel-1A and classified them into several categories by using an existing semantic annotation catalogue [28]. Finally, we overlaid the Natura 2000 data [13] of the Dutch part of the Wadden Sea.

SAR instrument	**TerraSAR-X**	**TerraSAR-X**	**Sentinel-1A**
Image location	Flevoland (Image-1)	Port of Rotterdam (Image-3)	Wadden Sea, Lake IJssel, Marker Lake and the surrounding areas (Image-4) Lake IJssel, Marker Lake, Flevoland, and North Holland (Image-5)
	North Holland (Image-2)		Wadden Sea (Image-6)
Acquisition time	13-05-2015 (Image-1) 15-05-2015 (Image-2)	Sept. 21, 2009 (Image-3)	15-05-2015 (Image-4, 5, 6)
SAR band	X-band	X-band	C-band
Instrument mode	StripMap (SM)	High-resolution spotlight (HS)	Interferometric wide swath (IW)
Polarisation	VV	VV	VV and VH (Image-4, 5, 6 only VV)
Orbit branch	Ascending (Image-1) Descending (Image-2)	Descending	Ascending
Incidence angle	31°	48°	39°
Product type	Multi-look ground range detected (MGD)	Multi-look ground range detected (MGD)	Ground range detected high resolution (GRDH)
Enhancement	Radiometrically enhanced (RE)	Radiometrically enhanced (RE)	—
Ground range resolution	6.28 m	2.9 m	20 m
Pixel spacing	2.75 m	1.25 m	10 m
Equivalent number of looks (range × azimuth)	2.7 × 2.2	3.7 × 2.6	20 × 22
Full image size (cols × rows)	20,560 × 11,697 (Image-1)	2119 × 2651 (Image-3)	25,601 × 16,698 (Image-4) 10,001 × 8941 (Image-5)
	14,087 × 11,674 (Image-2)		18,944 × 5013 (Image-6)

Table 1. SAR image parameters.

http://dx.doi.org/10.5772/intechopen.70855

The protected areas are shown in **Figure 3** with different colours corresponding to the different tranches in which they became assigned as Natura 2000: tranche 1 (green) per January 2007, tranche 2 (purple) per May 2007, tranche 3 (dark blue) per September 2008, tranche 4 (reddish) per September 2009, and later tranches (light blue) per 2011 to 2016.

3. Image analysis methodology

In the following, we demonstrate that very good results in SAR image classification and semantic annotation can be obtained, if we follow a systematic feature extraction and classification approach described in [29]. Our image classification system is basically composed of the following main modules: data model generation (DMG), database management system (DBMS), knowledge discovery in databases (KDD), and statistical analytics.

The DMG module transforms the original format of original Earth observation products into smaller and more compact product representations that include image descriptors, metadata, image patches, etc.

The DBMS module is used for storing all the generated information and allows querying and retrieval of the available image data.

The KDD module is in charge of finding patterns of interest from the processed data and presenting them to the user. Moreover, the KDD module allows annotating the image content by using machine learning algorithms and human interaction resulting in physical categories.

The statistical analytics module provides classification maps of each dataset, distribution results of the retrieved categories in an image, and the classification accuracy of selected descriptors (primitive features) by computing different metrics.

These four modules are operated automatically and interactively with and without user interaction.

The DMG module represents an automated processing chain that produces data items from an Earth observation product. The main functionality of DMG is metadata extraction, tiling the images with multiple resolutions (resulting in different patch sizes, as described in Section 2), generation of high-resolution quick-look images and primitive feature extraction. The DMG process starts by reading the product data files and extracting the relevant metadata entries. In the next step, the full product image is cut into square-shaped patches, and for each patch, a high-resolution quick-look image is generated. Later, different feature extraction methods can be applied to the generated patches in order to obtain descriptors that characterise the image content. These feature extraction methods are able to describe texture, colour, spectral features, etc. In this study, we use Gabor filters [30] for feature extraction with five scales and six orientations. The final output of DMG consists of image content descriptors in the form of primitive feature vectors, metadata entries, image patch descriptions and high-resolution quick-look image patches; all this generated information is stored into our database (DBMS).

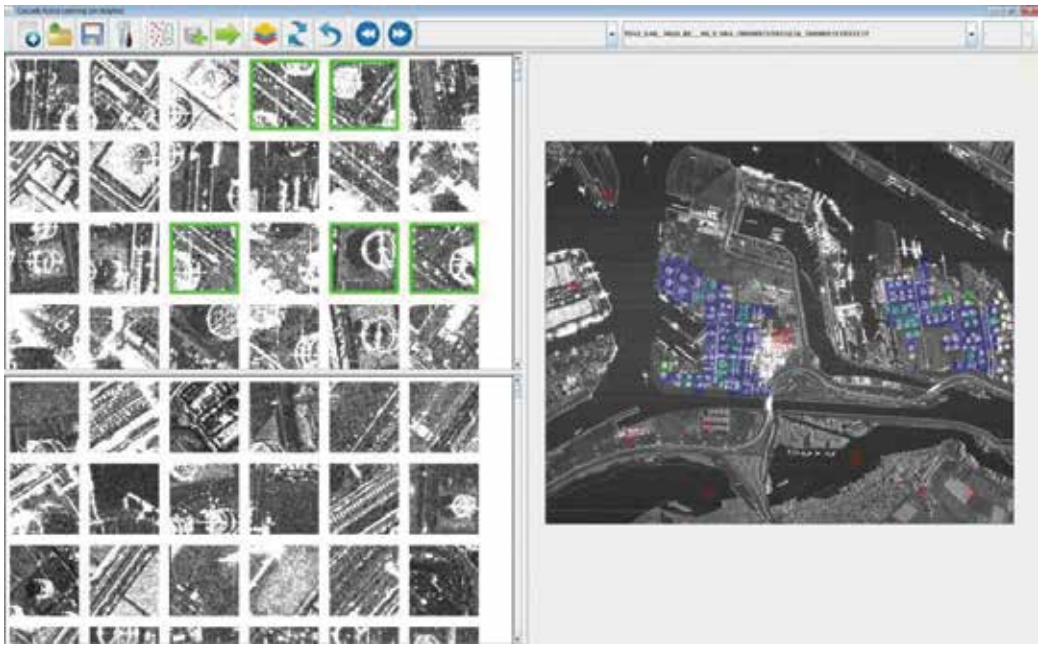

Figure 4. Our tool interface used to retrieve existing categories from an image or images. The top left panel shows the most relevant retrieved patches (e.g., storage tanks), while the bottom left panel shows irrelevant retrieved patches. The large right panel shows the image being analysed (here, the Port of Rotterdam, Netherlands) that can be zoomed. Through this panel, users can see the distribution of the retrieved patches and all the training samples. The users can also verify the selected training samples by checking the surrounding context as there is a relation between the patches in the upper left and right panel. Training samples can be selected from all three panels.

In the next step, since all the generated information (i.e., primitive features, patches, metadata entries, etc.) is available in the DBMS, the interactive KDD module is enabled and allows us to search for specific images in the DBMS repository. This module implements data mining, machine learning and relevance feedback methods. In particular, it uses an interactive support vector machine (SVM) for active learning support with a χ^2 kernel that makes highly accurate classifications even with a small number of examples for each given image annotation category [31]. For more detailed information about the attainable classification quality, see Section 4.

The KDD process is triggered interactively by a user; it accesses the database and selects the image patches and their primitive feature vectors to be used for subsequent classification. In the next step, the quick-look images of the patches are presented to the user via a graphical user interface (GUI). After selection of a target category (from the list of labels available from the semantic catalogue [28]), the user selects patches with interesting content as positive examples and patches with undesired content as negative examples. This set of positive and negative examples is leveraged as our training data set and passed to the SVM. Then, the SVM is used for training, creates a model for classifying the whole dataset and generates predictions for the remaining patches. The classification results are ordered according to the prediction rankings. In the next step, the ranked results are updated on the screen, and the

classified patches are marked in colour, so that the user can perform a new training (with more selected examples) or stop the training (see **Figure 4**). Finally, when the user is satisfied with the classification results, he/she stops the training and selects a label from the semantic catalogue to annotate this classification, and then, the software stores the classified patches and their semantic label into the database.

Finally, by interactively applying different statistical analytics to the database, we are able to generate analytics about the image content and present these results in different charts, to generate classification maps or change maps (in the case of image time series) and to compute classification accuracy metrics (e.g., precision/recall).

4. SAR image classification and annotation

Once new images are available for further analysis, they are processed as described in Section 3. The annotation methodology is semi-automated, that is, the following functions of the methodology are fully automated: patch tiling, metadata extraction, quick-look generation, feature extraction and insertion of the results into the database. In contrast, the final classification and annotation functions require manual operator interaction. They require interaction because our classification includes an operator to rank the patches via human–machine interaction (i.e., active learning), and the semantic annotation calls for the selection of proper labels for each category.

For high-resolution SAR images of our target areas (e.g., TerraSAR-X data), our annotation scheme has 3 levels with, in total, 150 categories (9 general high-level categories, 73 more specific mid-level categories and 68 categories belonging to a very detailed low level). The very detailed categories describe details of manmade infrastructure, while the categories describing natural environments do not have these refinements.

For medium-resolution and low-resolution SAR images (e.g., Sentinel-1), this annotation scheme can be adapted by concentrating on all categories from high level and some from mid-level.

To each tiled patch, we attach a semantic label. Typically, the total number of categories that can be identified in a high-resolution SAR image varies from 10 to 20 categories depending on the content of the image (e.g., as a function of geographical location and local architecture). In the case of medium-resolution SAR images, the total number of categories varies from 5 to 14 [32].

Figures 5 and **6** show one representative patch per category of one TerraSAR-X and one Sentinel-1A image, while **Figure 7** shows the distribution of categories for TerraSAR-X images, and **Figures 8–10** depict the corresponding classification maps. In **Figures 11–13**, we demonstrate, as in the case of TerraSAR-X, the distribution of categories and the classification maps of the Sentinel-1A data set. Here, one can see the effects of the geometrically coarse classification grid resulting from the unique label patch classification (e.g., **Figure 10**). A typical classification example of natural scenes is the Wadden Sea image shown in **Figure 14**.

Figure 5. (From left to right and from top to bottom) One patch of 200 × 200 pixels for each category retrieved from a selected TerraSAR-X image (Image-2): Dams, Channels, Coastal areas, Deltas/Lakes, Harbour infrastructure, Industrial buildings, Low-density residential areas, Medium-density residential areas, Mixed forest, Ploughed agricultural land and Sea.

Figure 6. (From left to right and from top to bottom:) One patch of 128 × 128 pixels for each category retrieved from a selected Sentinel-1A image (Image-4): Airports-runways; Wind mills; Dams; Channels; Coastal areas; Deltas/Tidal flats; Firth; Harbour infrastructure; Inhabited built-up areas; Lakes; Mixed forest; Agricultural land; and Sea/Fresh waters.

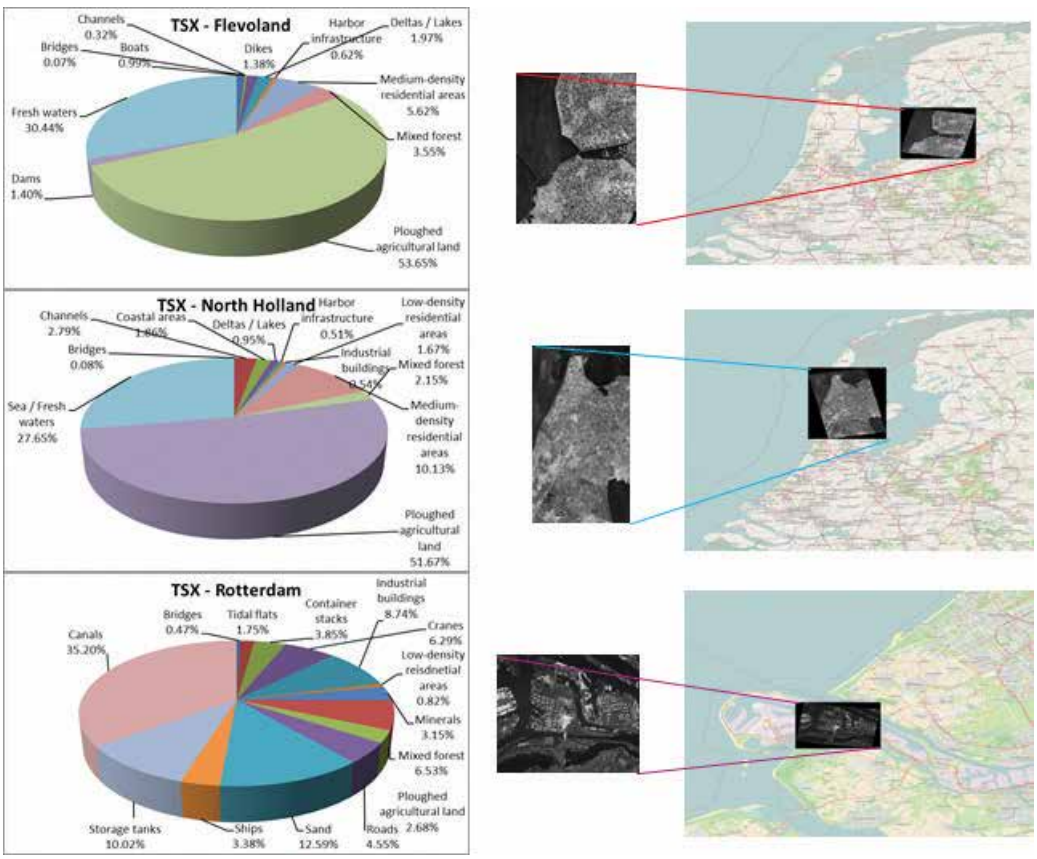

Figure 7. Diversity of categories identified in the case of TerraSAR-X (TSX), for areas with partial or total overlapping with Sentinel-1A (S1A) in **Figure 11**. On the right side of each pie-chart is the quick-look image of the SAR image, and the location of the image projected on OpenStreetMap [33]. From top to bottom (from **Table 1**) are: Image-1, Image-2 and Image-3.

http://dx.doi.org/10.5772/intechopen.70855

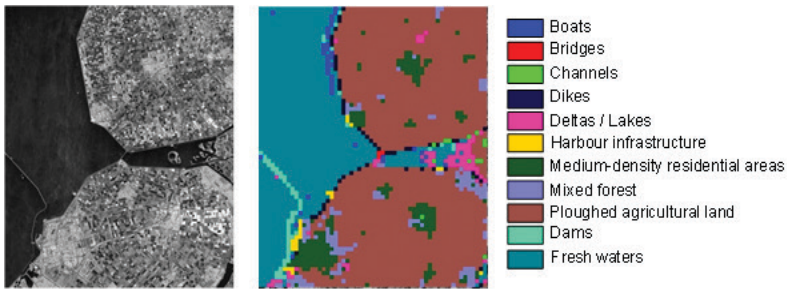

Figure 8. TerraSAR-X quick-look view (left) and classification map (right) for an image of Flevoland (Image-1).

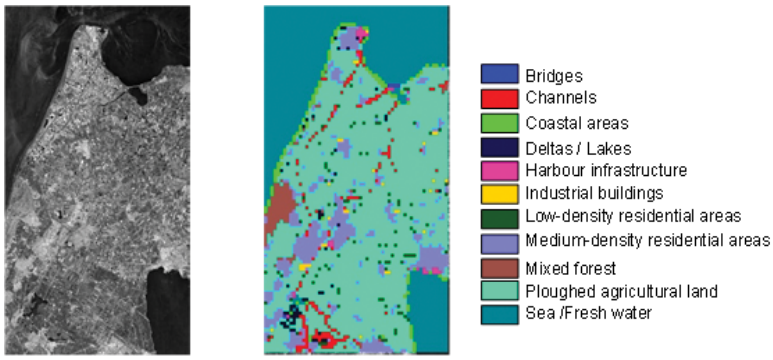

Figure 9. TerraSAR-X quick-look view (left) and classification map (right) for an image of North Holland (Image-2).

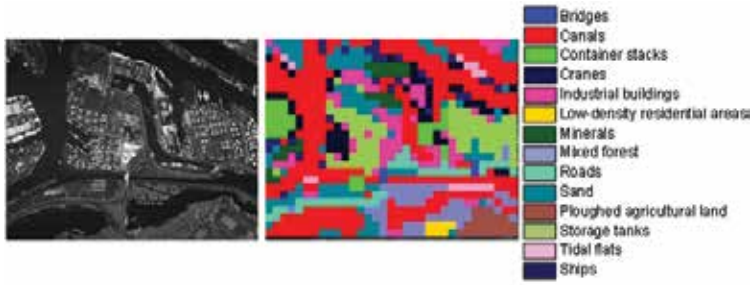

Figure 10. TerraSAR-X quick-look view (left) and classification map (right) for an image of the Port of Rotterdam (Image-3).

An interesting phenomenon contained in the figures is the higher number of categories found for TerraSAR-X images (the corresponding Sentinel-1A sub-scenes cover the same area on ground). This phenomenon can be explained by a greater discrepancy between the (visually hidden) feature vectors and by the architectural and geographical locations of these images [30].

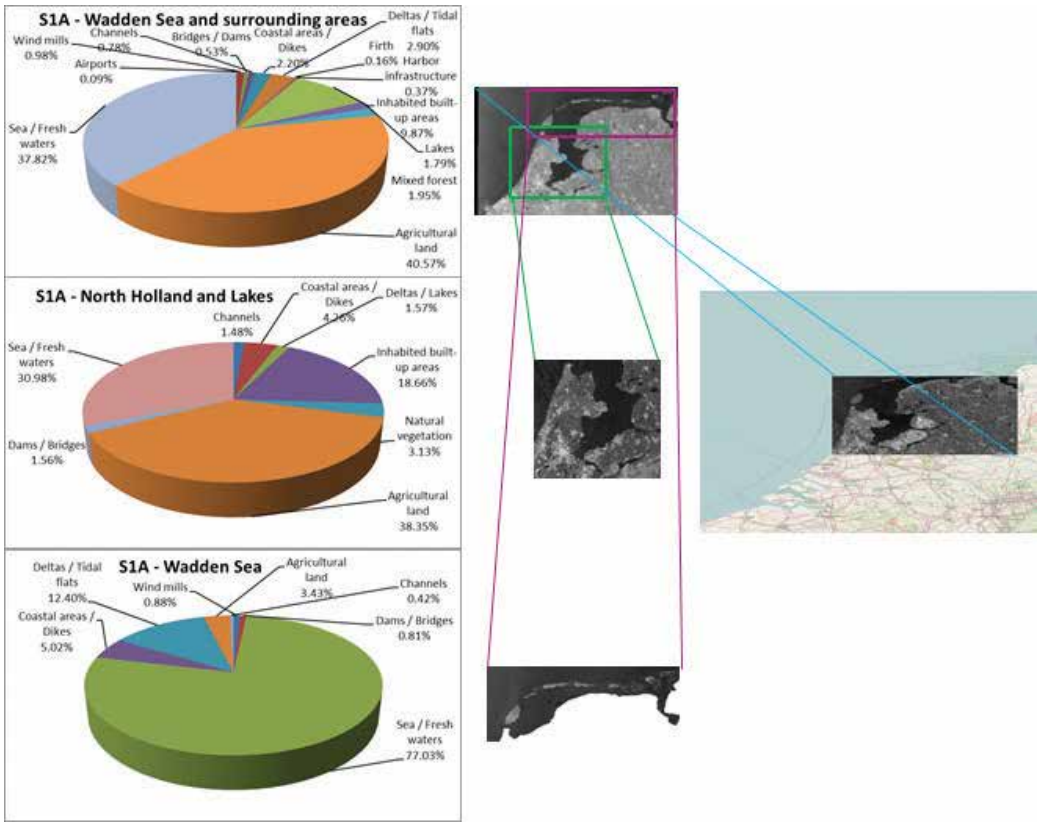

Figure 11. Diversity of categories identified in the case of sentinel-1A (S1A) (Image-5 and Image-6 embedded in Image-4). On the right side of each pie-chart is the quick-look image of the SAR image and the location of the Image-4 projected on Open Street Map [33].

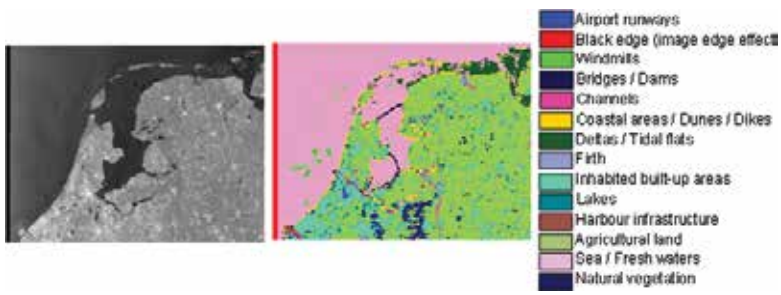

Figure 12. Sentinel-1A quick-look view (left) and classification map (right) for an image of the Wadden Sea, Lake IJssel and Marker Lake and the surrounding areas (Image-4).

Figure 13. The Dutch part of the Wadden Sea: Adapted from Natura 2000 [13] (left), sentinel-1A quick-look view (centre) (Image-6) and classification map (right). The colour legend labels are the ones from **Figure 12**.

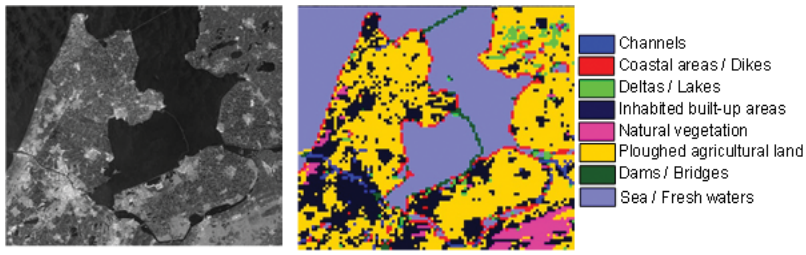

Figure 14. Sentinel-1A quick-look view (left) and classification map (right) for an image of Lake IJssel, Marker Lake and North Holland (Image-5).

Another phenomenon to be mentioned are the detailed semantic categories that are obtained in the case of TerraSAR-X (e.g., *Medium-density residential areas*, *Mixed forest*, etc.) in contrast to the categories in the case of Sentinel-1A (e.g., *Inhabited built-up areas*, *Natural vegetation*, etc.). This is due to the higher ground resolution of TerraSAR-X (see **Table 1**). In total, for TerraSAR-X, there are 23 semantic categories belonging to level 2 and 3 [28], and, for Sentinel-1A, 16 semantic categories belonging to level 1 and 2 [28].

Please note that we refer to *coastal areas* as the areas on both sides of a coastline, while we understand *dams* as (drivable) barriers separating two water basins and *dikes* as barriers for holding back flood waters.

Presently, we have reached a stable state of classification accuracy (a precision/recall) rate of 95%/90% for TerraSAR-X and 90%/85% for Sentinel-1A.

In addition, for Sentinel-1A, we plan to include the analysis and combination of its VV and VH polarisation data in order to increase the attainable classification accuracy.

5. Environmental interpretation

The landscapes of the western and northern part of the Netherlands are the result of an ongoing balance between natural processes on the one hand and increasing anthropogenic impact on the other hand at the edge of sea and land (overview in [2, 4, 5]). This resulted in a fine-meshed mosaic of natural habitats and man-made structures. In an alternating series of transgressions and regressions of the sea, especially from 3000 to 1000 years BC, along the Dutch coast, a series of barrier beaches and dunes, interrupted by rivers, were formed [34, 35]. Behind the beaches and dunes, huge packages of silt and clay were deposited and vast packages of peat developed in the (salt, brackish, and fresh) marshes. After that period, the first humans settled in that area, without interfering too much with the natural habitat. Only from 1000 AD, during a transgression of the sea, the interference with the natural landscape became stronger [4, 36]. Dikes were built, at ever increasing heights, and thereby more and more territory was reclaimed, the so-called polders. In those impoldered areas, protected with dikes, cities and agricultural lands developed more and more, as, for example, in the district of North Holland around the city of Amsterdam (**Figure 9**). In the areas not fully protected by dikes at several locations, the gulleys in between dunes became deeper, and the marshes behind were washed away, in the north of the Netherlands leading to the formation of today's

landscape of the Wadden Sea. That landscape became dominated by a series of islands with sandy beaches and dunes at the seaside and marshes at the landside, with large tidal flats and deep gulleys in between.

With the industrial revolution during the last 200 years, the impact on the landscape became even stronger, especially in those areas nearby ports, as in Rotterdam, one of the world's largest harbours. Moreover, the land reclamation continued until the last century, with even the closure of the Southern Sea (NL: Zuiderzee) with a 32 km long dike in 1932, giving rise to a huge fresh water lake, Lake IJssel (NL: IJsselmeer), of more than 3300 km^2. In this lake during the last decades, several polders were reclaimed for agriculture and new cities and villages now known as the Flevoland district.

We have thus focused on a couple of examples of these different types of habitats with different histories. Firstly, the transect in the Flevoland district (**Figure 8**) reflects the land reclamation during the last decades. Secondly, the transect of the harbour area of Rotterdam (**Figure 10**) reflects an area strongly modified since the industrial revolution. Thirdly, the transect in the district of North-Holland (**Figure 9**) reflects the land reclamation and impacts of the last 500 years and fourthly, the Wadden Sea area (**Figure 14**) represents the most natural habitat in the north of the Netherlands that arose after a transgression of the sea around 1000 AD.

In Flevoland, the reclaimed polders, in the midst of the fresh water Lake IJsselmeer, were mainly set up as agricultural areas together with some locations for residential areas as is also clear from our satellite image analyses (**Figures 7** and **8**). Agricultural areas (including forestry) covered 57% of the surface, open water 34% and residential areas 6%. These relative surface-values coincide largely with the inventories of the official Netherlands Statistics office (CBS) [37], being 51, 41 and 5%, respectively.

The industrialised area of the port Rotterdam is strongly dissected by canals with ships (36% of the surface) (**Figures 7** and **10**), which corroborates the value issued by the harbour authorities of the port of Rotterdam (38% for water surfaces) [38]. Further, the harbour territory is mainly covered with industrial structures (48% including container stacks, industrial buildings, cranes, minerals, barren sands, storage tanks), which is similar to the 47% according to the harbour authorities of the port of Rotterdam [38], leaving only little remnants of the coastal estuarine area it was in earlier days.

In the district of North Holland, the surface for residential areas is larger (12%) than in the previous areas, although agriculture (52%) and water (32%) still take a big portion (**Figures 7** and **9**). These values coincide with those of the Netherlands Statistics office (CBS) (Statistics, 2016), being 12, 46 and 35%, respectively. Nevertheless, care has to be taken especially in this district in the analysis of the water areas, since from the images, it is not feasible to distinguish between fresh water and sea water. Moreover, it is difficult to make a distinction between some detailed habitats in the coastal areas of this district, such as man-made dikes (in the northern and eastern part of this district) and natural dunes (in the western part).

For the Wadden Sea and its nearby surroundings, a completely different division of the major habitats is found than in the previous regions, indicating its natural value and marine character (**Figures 11** and **12**). The share of deltas or tidal flats (13%) and water (77%) is much

higher than in the previous areas, whereas agriculture has only a small share (4%). In earlier inventories of the Dutch Wadden Sea [35], an almost equal share of 43% for tidal flats and 43% for water was indicated (the other 14% belongs to islands). The lower share of tidal flats in our study is caused by the fact that the Wadden Sea is subject to alternating tidal water levels and therefore dependent on the acquisition time of the individual images.

A more generalised analysis (**Figures 11** and **12**) of the north-west of the Netherlands shows that there are two different sides of a coin. The heavily anthropogenically impacted regions (**Figures 11** mid and **13**), (i.e., the west Netherlands encompassing also the Rotterdam harbour area, Flevoland and the North Holland district) differentiate strongly from the more original and natural region in the north of the Netherlands, including the Wadden Sea and its direct surroundings (**Figures 11** bottom and **14**). The major differences can be found in the surface zones classified as agriculture, inhabited built-up areas and water.

6. Conclusion

The main habitats and structures for the moderately or strongly impacted areas in the north-west of the Netherlands (Flevoland, Rotterdam port, North Holland) are in general interpreted correctly by means of our satellite image analyses. For the Wadden Sea, one has to take into account the relative distribution of tidal flats versus water surface. A potential solution can be to acquire a series of images covering the full tidal cycle. It is also important to take care about the fact that in the Wadden Sea, although most of the tidal flats are barren, some may be overgrown with sea grasses and some are covered by seaweeds in summer, whereby these may be classified wrongly as agricultural land, assigning them to another category (e.g., agricultural). Again, images from different seasons can be compared to overcome this issue.

Altogether, we conclude that the majority of the habitats, man-made structures as well ecological features, can be classified rather accurately irrespective of a strongly different historic context and different levels of anthropogenic impact of the areas being studied. Nevertheless, it should be taken into account that due to its dynamic history, areas like the north-west Netherlands

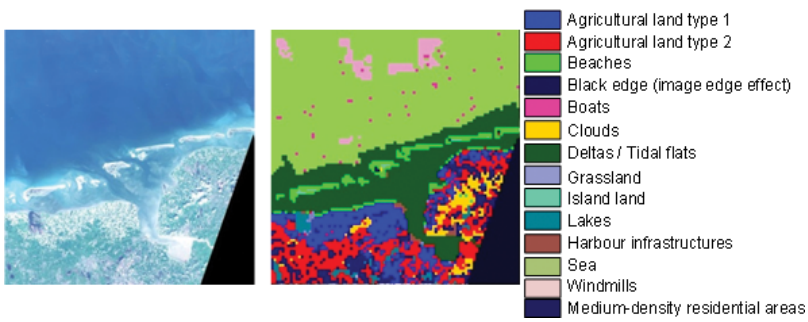

Figure 15. Sentinel-2A RGB quick-look view (left) and classification map (right) for an image of the Dutch and German part of the Wadden Sea.

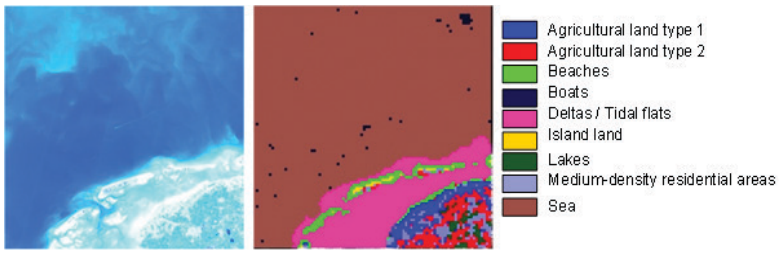

Figure 16. Sentinel-2A RGB quick-look view (left) and classification map (right) for an image of the Dutch part of the Wadden Sea.

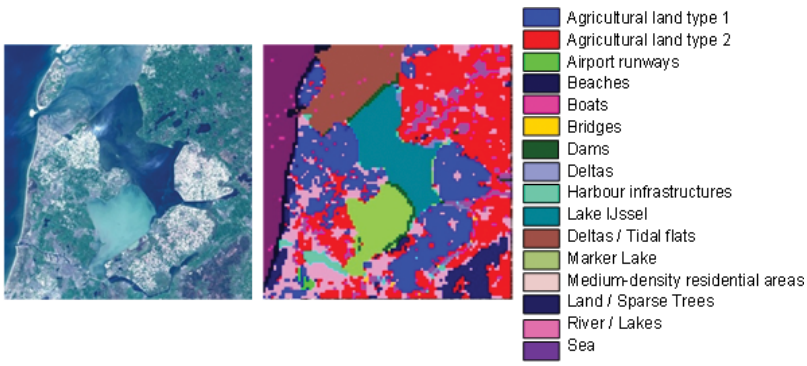

Figure 17. Sentinel-2A RGB quick-look view (left) and classification map (right) for an image of Lake IJssel, marker Lake and North Holland.

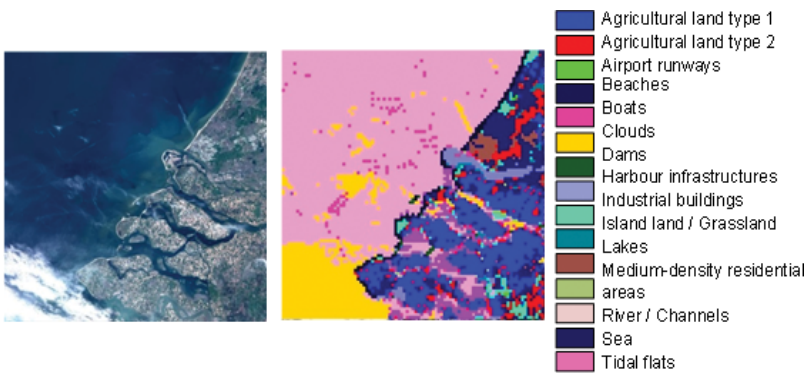

Figure 18. Sentinel-2A RGB quick-look view (left) and classification map (right) for an image of the port of Rotterdam and surrounding areas.

do call for carefulness regarding the interpretation of some features as, for example, water being fresh or salt and coastal defence structures being anthropogenic dikes or natural dunes and beaches. A further analysis is needed to distinguish between these ecologically rather different habitat types. Therefore, for a proper interpretation and ecological fine-tuning of satellite images, the cooperation with environmental researchers or managers with field experience remains a prerequisite.

http://dx.doi.org/10.5772/intechopen.70855

After the determination of the classification accuracy of our SAR images, we also determined the pros and cons of including optical sensors such as multispectral Sentinel-2 images [39]. On the one hand, one can automatically download selectable quadrants from large images and obtain image patch relationships that are much easier to understand and classify; on the other hand, we face the problem of potential cloud cover that can persist for a number of days. **Figures 15–19** illustrate these relationships for some selected quadrants that cover similar areas as the SAR images. Combining optical sensors with SAR sensors can be a solution to solve the open points arisen in our study, such as the separation between fresh water and sea water (see in **Figure 17**, the classification results of an optical image that cover an area with these two types of water).

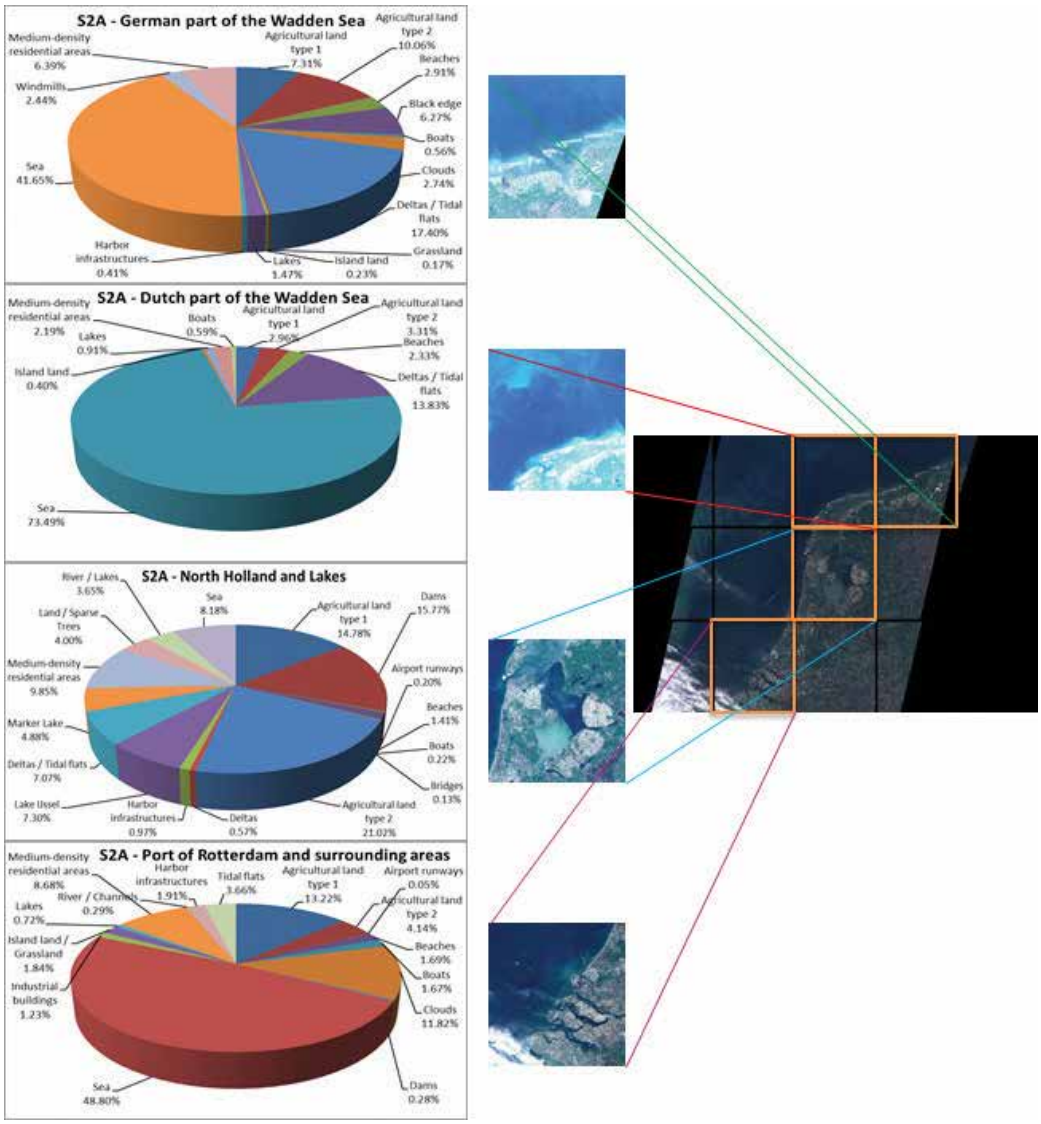

Figure 19. Diversity of categories identified in the case of sentinel-2A (S2A). On the right side of each pie-chart is the RGB quick-look image of the multispectral image and the location of each quadrant.

Acknowledgements

This work was supported by the TerraSAR-X Science Service System (proposals MTH-1118 and LAN-3156) and by the H2020 ECOPOTENTIAL project (grant agreement no. 641762).

Author details

Corneliu Octavian Dumitru[1]*, Gottfried Schwarz[1], Daniela Espinoza-Molina[1], Mihai Datcu[1], Herman Hummel[2,3] and Christiaan Hummel[2,3]

*Address all correspondence to: corneliu.dumitru@dlr.de

1 Remote Sensing Technology Institute, German Aerospace Center (DLR), Wessling, Germany

2 Department of Estuarine and Delta Studies, Royal Netherlands Institute for Sea Research, Yerseke, The Netherlands

3 Utrecht University, The Netherlands

References

[1] ECOSTRESS project (Ecological Coastal Strategies and Tools for Resilient European Societies) [Internet]. 2017. Available from: http://www.eucentre.it/ecostress-project/?lang=en

[2] Wolff WJ. Ecology of the Wadden Sea. Rotterdam: Balkema; 1983. DOI: 10.4319/lo.1984.29.6.1348

[3] Wadden Sea World Heritage [Internet]. 2017. Available from: http://www.waddensea-worldheritage.org/

[4] Abrahamse J, Joenje W, van Leeuwen-Seelt N. Waddenzee Natuurgebied van Nederland, Duitsland en Denemarken. Harlingen, Netherlands: Landelijke vereniging tot behoud van de Waddenzee (in Dutch); 1976

[5] Abrahamse J, Joenje W, van Leeuwen-Seelt N. Wattenmeer, Ein Naturraum der Niederlande, Deutschlands und Dänemarks (in German). Wachholtz, Neumünster, Germany; 1977

[6] Dijkema KS, Bossinade JH, Bouwsema P, de Glopper RJ. Salt marshes in the Netherlands Wadden Sea: Rising high-tide levels and accretion enhancement. In: Beukema JJ, Wolff WJ, Brouns JJWM, editors. Expected Effects of Climatic Change on Marine Coastal Ecosystems. Dordrecht: Kluwer Publishers; 1990. p. 173-188. DOI: 10.1007/978-94-009-2003-3

[7] von Nordheim H, Andersen ON, Thissen J. Red lists of biotopes, flora and fauna of the trilateral Wadden Sea area. Helgol Meeresunters. 1996;**50**:1-136

[8] Dankers N, Kuehl H, Wolff W. Invertebrates of the Wadden Sea. In: Report 4 of the Wadden Sea Working Group. Leiden, The Netherlands: Stichting Veth Tot Steun Aan Waddenonderzoek; 1981

[9] Dankers N, Wolff W, Zijlstra JJ. Fishes and fisheries of the Wadden Sea. In: Report 5 of the Wadden Sea Working Group. Leiden, The Netherlands: Stichting Veth Tot Steun Aan Waddenonderzoek; 1978

[10] Lozan JL. Zur Geschichte der Fischerei im Wattenmeer und in Küstennähe. Warnsignale aus dem Wattenmeer (in German). Berlin: Blackwell; 1994. p. 215-226

[11] Drescher HE. Spatial distribution of the harbour seal in the Wadden Sea during the breeding season. In: Proceedings of ICES, Copenhagen. 1979. 6

[12] Government of the Netherlands. Nature and biodiversity [Internet]. 2017. Available from: https://www.government.nl/topics/nature-and-biodiversity/contents/protected-nature-areas

[13] Natura 2000 network [Internet]. 2017. Available from: http://natura2000.eea.europa.eu/#

[14] ECOPOTENTIAL project [Internet]. 2017. Available from: http://www.ecopotential-project.eu/2016-05-24-14-52-12/protected-areas

[15] Baltsavias E, Gruen A, van Gool L, editors. Automatic Extraction of Man-Made Objects from Aerial and Space Images (III). Tokyo: Balkema Publishers; 2001. DOI: 10.1007/978-3-0348-9242-1

[16] Oliver C, Quegan S. Understanding Synthetic Aperture Radar Images. Raleigh, USA: SciTech Publishing; 2004

[17] Maître H, editor. Processing of Synthetic Aperture Radar (SAR) Images. New Jersey, USA: John Wiley & Sons; 2010. DOI: 10.1002/9780470611111.biblio

[18] The Trilateral Cooperation on the Protection of the Wadden Sea. © 1998-2013 Common Wadden Sea Secretariat (CWSS) [Internet]. 2017. Available from: http://www.wadden-sea-secretariat.org/

[19] Brusch S, Lehner S. Monitoring river estuaries and coastal areas using TerraSAR-X. In: Proceedings of OCEANS, Bremen. 2009. p. 1-4. DOI: 10.1109/OCEANSE.2009.5278248

[20] TerraSAR-X basic product specification document, issue 1.9. [Internet]. 2013. Available from: http://sss.terrasar-x.dlr.de/pdfs/TX-GS-DD-3302.pdf

[21] Wiehle S, Lehner S. Automated waterline detection in the Wadden Sea using high-resolution TerraSAR-X images. Hindawi Journal of Sensors. 2015;**450857**:1-6. DOI: 10.1155/2015/450857

[22] Wiehle S, Lehner S, Pleskachevsky A. Waterline detection and monitoring in the German Wadden Sea using high resolution satellite-based radar measurements. In: Proceedings of the 36th International Symposium on Remote Sensing of Environment, Berlin. 2015. p. 1029-1033. DOI: 10.5194/isprsarchives-XL-7-W3-1029-2015

[23] Heygster G, Dannenberg J, Notholt J. Topographic mapping of the German tidal flats analyzing SAR images with the waterline method. IEEE Transactions on Geoscience and Remote Sensing. 2010;**48**(3):1019-1030. DOI: 10.1109/TGRS.2009.2031843

[24] Gade M, Mechionna S. The use of high-resolution RADARSAT-2 and TerraSAR-X imagery to monitor dry-fallen intertidal flats. In: Proceedings of IGARSS, Quebec. 2014. p. 1218-1221. DOI: 10.1109/IGARSS.2014.6946651

[25] RADARSAT-2 [Internet]. 2017. Available from: http://www.asc-csa.gc.ca/eng/satellites/radarsat2/

[26] Sentinel-1 [Internet]. 2017. Available from: http://www.copernicus.eu/main/sentinels

[27] QGIS tool [Internet]. 2017. Available from: http://www.qgis.org/en/site/

[28] Dumitru C, Schwarz G, Datcu M. Land cover semantic annotation derived from high-resolution SAR images. IEEE Journal of Selected Topics in Applied Earth Observations and Remote Sensing. 2016;**9**(6):2215-2232. DOI: 10.1109/JSTARS.2016.2549557

[29] Espinoza-Molina D, Manilici V, Dumitru O, Reck C, Cui S, Rotzoll H, Hofmann M, Schwarz G, Datcu M. The earth observation image Liberian (EOLIB): The data mining component of the TerraSAR-X payload ground segment. In: Proceedings of BiDS, Santa Cruz de Tenerife. 2016. p. 228-231. DOI: 10.2788/854791

[30] Dumitru C, Cui S, Datcu M. Information content of very high resolution SAR images: Semantics, geospatial context, and ontologies. IEEE Journal of Selected Topics in Applied Earth Observations and Remote Sensing. 2014;**8**(**4**):1635-1650. DOI: 10.1109/JSTARS.2014.2363595

[31] Costache M, Maître H, Datcu M. Categorization based relevance feedback search engine for earth observation images repositories. In: Proceedings of IGARSS, Denver. 2006. p. 13-16. DOI: 10.1109/IGARSS.2006.8

[32] Dumitru C, Schwarz G, Datcu M. Improved image classification by proper patch size selection: TerraSAR-X vs. sentinel-1A. In: Proceedings of IWSSIP, Bratislava. 2016. p. 1-4. DOI: 10.1109/IWSSIP.2016.7502739

[33] Map of the Earth [Internet]. 2017. Available from: https://www.openstreetmap.org/

[34] Veenstra HJ. In: Introduction to the geomorphology of the Wadden Sea area. Ecology of the Wadden Sea. Rotterdam: Balkema; 1983. p.1. 8-19. DOI: 10.4319/lo.1984.29.6.1348

[35] Dijkema KS. Large-scale geomorphologic pattern of the Wadden Sea area. Ecology of the Wadden Sea. Rotterdam: Balkema; 1983. p. 1. 72-80. DOI: 10.4319/lo.1984.29.6.1348

[36] Eisma D, Wolff WJ. The development of the westernmost part of the Wadden Sea in historical time. Ecology of the Wadden Sea. Rotterdam: Balkema; 1983. p. 1. 95-103. DOI: 10.4319/lo.1984.29.6.1348

[37] Statistics Netherlands (Centraal Bureau van de Statistiek—CBS), publication 70262ned [Internet]. 2016. Available from: opendata.cbs.nl/dataportaal/portal.html?_la=en&_catalog=CBS

[38] Port of Rotterdam [Internet]. 2016. Available from: www.portofrotterdam.com/en/the-port/port-facts-and-figures/port-infrastructure

[39] Sentinel-2 [Internet]. 2017. Available from: https://sentinel.esa.int/web/sentinel/user-guides/sentinel-2-msi

Section 3

Mixed Signal Processing Applications

Chapter 6

Adaptive Clutter Cancellation Techniques for Passive Radars

Tamás Pető and Rudolf Seller

Additional information is available at the end of the chapter

http://dx.doi.org/10.5772/intechopen.71289

Abstract

In radar systems, the ambiguity function of the applied illuminator signal essentially determines the detection capabilities. Zero Doppler interference (ZDI) or close targets returns can mask weak target reflections from higher distances. This is particularly the case for passive radars where the illuminator signal is not under the control of the radar designer. In recent times, great efforts have been carried out to research and develop efficiently working filter algorithms. These adaptive algorithms aim to cancel the undesired interference components in order to enhance the useful dynamic range. A number of different algorithms are operating in the space and also in the time domain. Spatial algorithms apply beamforming techniques, while temporal algorithms utilize the available reference signal to suppress the interferences. The main goal of this chapter is to present and compare the available spatial and temporal adaptive interference cancellation techniques in terms of filtering efficiency and computation cost on real-life data.

Keywords: passive radar, DPIS, ZDI suppression, clutter cancellation, adaptive algorithm

1. Introduction

Passive radar systems utilize the so-called illuminator of opportunity (IO) for target detection. These transmissions are inherently not designed for radar purposes. The direct consequence of the inappropriate illumination is the presence of ambiguities and high sidelobes in the range-Doppler map. In addition, the received surveillance signal is often dominated by the direct and multipath Zero Doppler interference (ZDI) signals from the illuminator. The sidelobes of these unwanted high power clutter components can mask the weak target echoes [1]. The main goal of the adaptive clutter cancellation algorithms in passive radar applications is to get rid of the masking effect.

In recent times a number of research and development works aim to find the most adequate filtering technique. The most important aspects are the filtering performance, the capability for real-time operation and the purity of the resultant range-Doppler map. Filtering is performed typically in two different domain. Space-domain suppression techniques apply beamforming methods to deal with the high power interferences. The adaptive optimum beamformer for passive radar application has been investigated in [2, 3]. Methods which utilize the eigen-structure of the spatial correlation matrix have been proposed in [4, 5]. Moscardini et al. [6] have made efforts to identify the most suitable multi-channel processing architecture. Their work focuses on the optimum beamformer for digital video broadcasting-terrestrial (DVB-T)-based systems. Villano et al. examined the non-adaptive beam steering and null-steering methods as well as the adaptive correlation matrix inversion-based methods [5].

Beside the application of spatial filtering by means of digital beamforming, the temporal algorithms also has great importance. These filtering algorithms utilize the available reference signal to cancel out the time delayed and Doppler shifted replicas of the illuminator signal on the surveillance channel. When it comes to time domain filtering, the Wiener filtering problem is solved without exception. Among the first, Cardinali et al. have investigated the application of the least mean square (LMS), normalized least mean square (NLMS), recursive least squares (RLS), extensive cancellation algorithm (ECA) and sequential cancellation algorithm (SCA) in passive radar scenario [7]. In their work they used simulated data with assuming FM transmitter. A similar study with more extensive examinations on real life data can be found in [8]. Garry et al. [8] examined the ECA, CLEAN, NLMS, fast block LMS (FBLMS) and RLS algorithms using DVB-T IO.

The main objective of this chapter is to evolve a common basis of discussion for the clutter cancellation algorithms. In this present study, the ECA, ECA-B, ECA-S, LMS, NLMS, RLS and block LMS methods are investigated. The supplemented autocorrelation matrix method for the block type algorithms and the weight inheritance technique for the iterative algorithm are also presented. Beside the evaluation of the clutter suppression capabilities, the survey of the required resources has fundamental importance. The assessment of the computational costs provides support for the selection of the adequate algorithm for every specific scenario.

2. Signal model

Before we start to discuss the operation of different algorithms, the proper signal model is constructed at the first place.

Figure 1 illustrates the considered signal model. The signal transmitted from the illuminators is received on a number of different signal paths. We can separate the individual signal contributions on the surveillance channel to three different types. These are the reference signal correlated interferences, the useful target reflections and the uncorrelated receiver noise. The signal processing steps are implemented digitally in all real cases, thus we use a discrete time domain description. Let us denote the illuminator signal with $s[n]$, where $n = 0 \ldots N$ is a discrete time index, and the signal is samples with f_s sampling frequency. The number of samples in

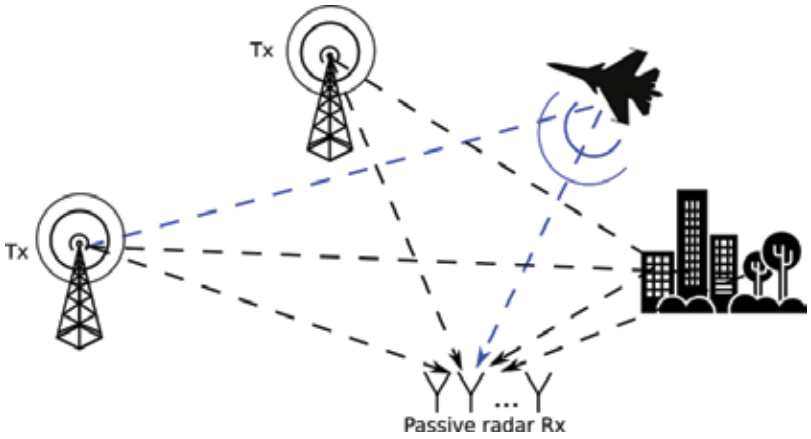

Figure 1. Signal model for the passive radar scenario.

coherent processing interval (CPI) is denoted by N. Eq. (1) describes the signal received on the passive radar antenna array for one target reflection.

$$\boldsymbol{x_a}[n] = \sum_{k=0}^{K-1} \alpha_k s[n-k] e^{j2\pi \frac{f_k}{f_s} n} \boldsymbol{a}(\theta_k) + \alpha_t s[n-t] e^{j2\pi \frac{f_t}{f_s} n} \boldsymbol{a}(\theta_t) + \boldsymbol{\xi}[n] \tag{1}$$

We are taking the following assumptions. The direct and multipath clutter components are received on the first K range cell. Each signal component has a propagation factor, which is described by the α parameter. The f_k, $k=0 \ldots K-1$ parameters describe the Doppler frequency of the considered clutter component. For static reflections, $f_k=0$ and they are also called as the ZDI components. $\boldsymbol{a}(\theta)$ denotes the spatial signature of the current signal component, that is arriving to the antenna array from the θ angle. Correspondingly, the target reflection has the α_t, f_t, θ_t parameters. Finally, the uncorrelated thermal noise vector collected by the receiver array is denoted with $\boldsymbol{\xi}[n]$. The received signal array $\boldsymbol{x_a}[n]$ is an M dimension array, where M is the number of antenna elements in the receiver array. For an M element equidistant linear antenna array the array response vector has the following form:

$$\boldsymbol{a}(\theta) = \left[1 \;\; e^{j\beta d\cos(\theta)} \;\; e^{j\beta d\cos(\theta)2} \;\; \ldots \;\; e^{j\beta d\cos(\theta)(M-1)}\right]^T \in \mathbb{C}^{Mx1}, \tag{2}$$

where θ is the incident angle of the impinging signal and β is the wavenumber. The detection stage is often preceded by the channel preparation algorithms, which aims to produce the clean reference and surveillance channels. On the reference channel, it is desired to receive only the direct path signal. Thus, in ideal case the reference signal has the following form:

$$x_r[n] = s[n] + \mu[n], \tag{3}$$

where $\mu[n]$ is the thermal noise. This can be often guaranteed by the use of high-gain antennas or the application of reference signal reconstruction algorithms [9]. Signal reconstruction

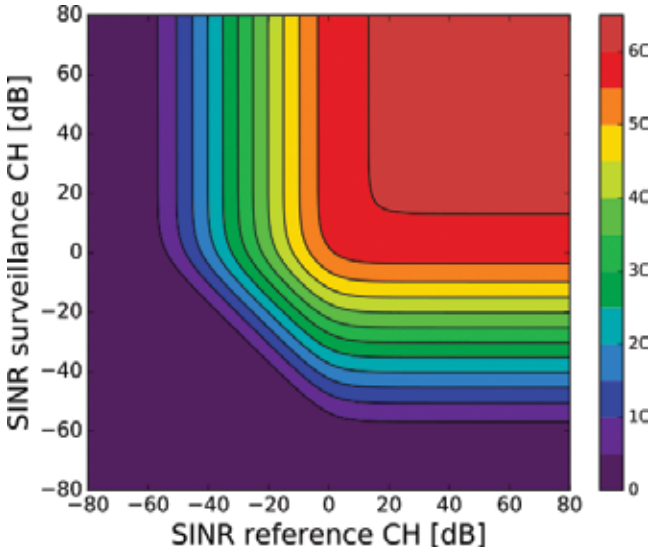

Figure 2. Target SINR (dB) in the function of the reference and surveillance signal purity.

algorithms are mainly used for illuminators, that use digital modulation techniques such as the digital audio broadcasting (DAB), DVB-T, digital video broadcasting: satellite (DVB-S), universal mobile telecommunications system (UMTS), long-term evolution (LTE) signals.

On the other hand, the surveillance channel must contain only the signal component reflected from the moving target in order to prevent performance degradation at the detection stage. It can be proved by analytical investigations that the detection performance is affected by both the reference and surveillance signal purity [10]. Assuming white noise illuminator, the signal-to-interference plus noise ratio (SINR) of the target can be described as the function of the SINR of the reference and surveillance signals.

$$SINR_{target} = \frac{1 + SINR_{ref} + SINR_{surv} + N\, SINR_{ref} SINR_{surv}}{1 + SINR_{ref} + SINR_{surv} + SINR_{ref} SINR_{surv}} \tag{4}$$

The dependencies of the observed target SINR on the range-Doppler surface can be calculated according to Eq. (4) and illustrated in **Figure 2**. In **Figure 2**, the number of samples in a CPI is $N = 2^{20}$. In this present chapter, we focus our attention to the filtering and preparation of the surveillance channel.

3. Algorithm evaluation methodology

In this section, the way of comparing the performances of the inspected algorithms is described in detail. The performance of the different clutter cancellation techniques is evaluated on real-life measured data.

3.1. Reference receiver system

The receiver system used to obtain the raw data is a quad channel software defined receiver especially designed for passive radar application. The system receives the surveillance signals on a quad channel fractal patch antenna system. On this surveillance antenna array, the elements are placed equidistantly with having 0.628λ spacing between each other, where λ denotes the wavelength of the center frequency. Among the four antenna elements, only three are connected to the receiver and the remaining one receiver channel is dedicated to the reference channel. This channel is connected to a Yagi antenna that receives the direct path signal. The detailed description and the design considerations of the software defined receiver can be found in [11]. During the measurements, the receiver system was only able to record the received multichannel signal in data chunks instead of streaming. This limitation results in short signal gaps between the consecutive CPIs. The CPI used in these investigations is $T_{CPI}=0.126s$. The duration of the signal gaps is dependent on the sample download speed, but its average is approximately $T_{gap}\approx 0.6s$.

3.2. Measurement scenario

The measured data were recorded near an airport using DVB-T signal as the illumination. During measurement, there were three illuminators operating in single frequency network mode at 634 *MHz*, and with a useful bandwidth of 7.61 MHz. In this analysis, the data acquired on Dec 21, 2015 have been processed and examined. The recorded data contains observations from several landing airplanes. After performing the initial processing steps, a long range target have been selected as the reference target for algorithm performance evaluations. For the analysis 25 CPIs have been processed.

3.3. Performance metrics

The clutter cancellation performance of the investigated algorithms can be measured on a wide variety of metrics. Choosing the proper metric is essential to obtain an objective comparison. Cardinali et al. [7] introduced the clutter attenuation (CA), which measures the averaged power ratio of the original and the filtered surveillance signal.

$$CA = \frac{\sum_{n=0}^{N-1} \left|x_f[n]\right|^2}{\sum_{n=0}^{N-1} \left|x_s[n]\right|^2} \tag{5}$$

In some cases, the applied surveillance channel filter unintentionally suppresses the target reflection beside the clutter. As the CA metric does distinguish the target reflection and the clutter higher CA value may represent worst filter performance. Also, Garry et al. [8] pointed out that CA is not reliably for the estimation of the RD map noise floor reduction. Instead of the CA, they proposed to measure the ratio of the estimated noise floor reduction in the RD map. To obtain this metric, they designated certain area on the RD map where no target reflection and dominant clutter components are expected. The noise floor reduction can be estimated over the specified region using the following equation.

$$R_{NF} = \frac{\sum_{\tau \in T, f \in F} \left|\chi\left(\tau, f, x_f\right)\right|^2}{\sum_{\tau \in T, f \in F} \left|\chi(\tau, f, x_s)\right|^2}, \tag{6}$$

where T and F defines the sets of the considered time delays and Doppler frequencies of the region of interest. The range-Doppler cell having τ time delay and f Doppler shift is calculated as follows:

$$\chi(\tau, f, x) = \sum_{n=0}^{N-1} x[n] x_r[n]^* e^{-j2\pi \frac{f}{f_s} n} \tag{7}$$

In contrast to the CA, the noise floor reduction metric isolates the clutter and the target echo contributions however, it still does not prove information about the impact of the filter on the useful target reflection. To overcome this limitation in [3, 8, 12], the SINR improvement of a detected target has been used as a metric. For the estimation of the target SINR we have

$$SINR_{target}(x) = \frac{\left|\chi\left(\tau_{0,} f_{0,} x\right)\right|^2}{\frac{1}{Q}\sum_{\tau \in T, f \in F} \left|\chi(\tau, f, x)\right|^2}, \tag{8}$$

where τ_0 and f_0 are the time delay and the Doppler shift of the detected target correspondingly. T and F sets contains the time delay and Doppler shift values of the neighboring range-Doppler cells, and Q denotes the number of cells used to estimate the clutter power. The improvement of the target SINR is defined as the ratio of the estimated values between the filtered and the original surveillance signals.

$$R_{SINR} = \frac{SINR_{target}\left(x_f\right)}{SINR_{target}\left(x_s\right)} \tag{9}$$

The target SINR improvement can be used effectively to evaluate the operation of different algorithms, however, its limitation must also be taken into account. The SINR of a detected target is dependent both on the purity of the reference and the surveillance signals. In case the reference signal has low quality, the achievable target SINR is limited, regardless of the interference suppression performance on the surveillance channel. Beside this, the relation between the surveillance signal purity and the target SINR is not linear, thus even a dramatical increase in the clutter suppression may result in slight target SINR improvement. Both of the highlighted limitations can be observed in **Figure 2**.

In the following presented analysis, the target SINR improvement is displayed as the main performance metric. According to preliminary results, we can declare that the observed and estimated values have large variation along the evaluated CPIs. To exclude this effect the performance metrics are evaluated on several consecutive CPIs along the target trajectory and the mean value of the metrics are indicated and compared.

3.4. Computation cost analysis

The computation cost of the examined algorithms is determined by specifying the necessary floating point operations (FLOPs) to calculate the filtered output signal. The cost of a complex

addition and a multiplication is taken into consideration as 2 and 6 FLOPs, respectively. Several algorithms perform matrix inversion to determine the coefficients used for the filtering. To estimate its requirements, $8J^3$ FLOPs are accounted for the inversion of a J dimensional matrix. The computational requirements are analyzed for each of the algorithms with considering their possible parameter settings.

4. Space domain filtering

During the process of space domain filtering, the M antenna channels are combined together. The coefficient vector of the beamformer ($\boldsymbol{w_{sd}} \in \mathbb{C}^{MxL}$) is calculated in a way to add the interference component out of phase while summarize target energy in-phase from the separate antenna channels. The beam-space processed output signal is calculated using Eq. (10).

$$y_{sd}[n] = \boldsymbol{w_{sd}^H x_a}[n] \tag{10}$$

The algorithms operating in the space-domain can be either data dependent adaptive algorithms or non-adaptive fixed beamformers. The main advantage of data independent methods is the fast output calculation. In this section, we only deal with beamformers that do not alter the coefficient vector during CPI.

4.1. Maximum signal-to-interference ratio

The maximum signal-to-interference ratio (SIR) is a data independent method, where the beampattern is manually calculated specifying the necessary constraints. These constraints are the incident angles and the desired responses of the antenna system in the specified directions. One can calculate the corresponding coefficients that fulfill the constraints using Eq. (11).

$$\boldsymbol{w_{sd-fix}}^{\boldsymbol{H}} = \boldsymbol{u}^T \boldsymbol{A}^H \left(\boldsymbol{A}\boldsymbol{A}^H + \sigma_n^2 \boldsymbol{I}\right)^{-1}, \tag{11}$$

where $\boldsymbol{u}$ is an L dimensional constraint vector and $\boldsymbol{A}$ is the array response matrix created from the specified directions, $\boldsymbol{I}$ is the identity matrix and σ_n^2 is the power of added noise that is used to prevent instability [13].

$$\boldsymbol{A} = [\,\boldsymbol{a}(\theta_0) \quad \ldots \quad \boldsymbol{a}(\theta_{L-1})\,] \in \mathbb{C}^{MxL} \tag{12}$$

Note that, the degrees of freedom of the beamformer is equal to the number of elements in the antenna system, thus only L constraints can be set ($L \leq M$) For passive radar application, the constraint vector and the array response matrix can be set as follows:

$$\boldsymbol{u} = [\,1 \quad 0 \quad \ldots \quad 0\,] \tag{13}$$

$$\boldsymbol{A} = [\,\boldsymbol{a}(\theta_t) \quad \boldsymbol{a}(\theta_1) \quad \ldots \quad \boldsymbol{a}(\theta_{L-1})\,] \tag{14}$$

The target is expected at θ_t angle and $\theta_l, l = 1 \ldots L-1$ are the incident angles of the clutter components.

4.1.1. *Fixed max SIR*

In this case the beampattern is not changing, thus the cofficient vector is set at the beginning of the processing and it used for all CPIs. In this case, the θ_l interference angles can be determined and set from preliminary information about the positions of the radar and the illuminators. This solution suffers from the inaccurate incident angle estimations and it is not able to deal with interference sources that change their positions over the surveillance time.

4.1.2. *DOA estimation supported max SIR*

Another way to configure the $\boldsymbol{A}$ array response matrix is to estimate the DOA of the dominant signal components in the received signal vector $\boldsymbol{x_a}[n]$. Thus the beamformer gets the opportunity to deal with all interference sources and to adapt to the changing environment. Note that in practical cases, the target reflection has low power relative to the ZDI and the other interferences, thus it does not affect the DOA estimation of these components. The choice of the DOA estimation technique has great importance as the performance of the interference suppression depends on its accuracy.

4.2. Adaptive optimum

Different optimization criteria such as the minimum variance distortionless response (MVDR) or the maximum signal to interference plus noise ratio (MSNR) leads to the well-known optimum weight vector calculation method described by Eq. (15).

$$\boldsymbol{w_{sd-opt}} = \boldsymbol{R_s^{-1}}\boldsymbol{a}(\theta_t) \tag{15}$$

In Eq. (15), $\boldsymbol{R_s} \in \mathbb{C}^{MxM}$ denotes the spatial correlation matrix of the interference components. It is often approximated by the correlation matrix of the full received signal, which is defined as

$$\boldsymbol{R_s} = \frac{1}{N}\sum_{n=0}^{N-1} \boldsymbol{x_a}[n]\boldsymbol{x_a}[n]^H \tag{16}$$

To calculate the corresponding beampattern, the expected incident angle of the target and the spatial autocorrelation matrix is required. In case the DOA of the target is not known precisely, the target reflection may be suppressed unintentionally. That is the so called pointing error. Another group of problem arise from the fact that the spatial correlation matrix contains other signal components than the interferences. Moscardini et al. [6] made progress on this problem with estimating the spatial autocorrelation matrix of the interferences from the corresponding range-Doppler cells after performing the cross-correlation. They report 2dB improvement over the conventional methods.

4.3. Subspace-based technique

Eigen-subspace-based beamforming techniques for passive radar application is proposed in [4, 5]. According to these works, the spatial correlation matrix can be decomposed to the

signal subspace and the noise subspace. In practical cases, the target echo having relatively low power resides in the noise subspace. Also we can assume that the unwanted disturbances will determine the dominant eigenvalues of the spatial correlation matrix. Then it is possible to suppress the interferences by projecting the array response vector of the target to the noise subspace.

$$\boldsymbol{w}_{sd-eig} = \boldsymbol{Q}\boldsymbol{Q}^{H}\boldsymbol{a}(\theta_t), \tag{17}$$

where the columns of the $\boldsymbol{Q}$ matrix are the eigenvectors assigned to the smallest eigenvalues of the spatial correlation matrix, that are the vectors of the noise subspace. The computation intensive eigenvalue calculation can be avoided by using the Power of R (POR) method proposed in [4]. Villano et al. [5] suggested to select the noise subspace as the subspace orthogonal to the eigenvectors that is assigned to the principal eigenvalues. In the current investigation, it is found that the best result is achieved by constraining the principal eigensubspace dimension to one.

4.4. Comparison of the space-domain filters

Table 1 summarizes the obtained SINR improvements for the different beamformers. As it can be seen, the fixed maximum SIR beamformer has the lowest performance. This beamformer has no ability to react to the changed environment. When the information from DOA estimation is utilized continuously this beamformer can clearly achieve gain over the non-adaptive case. The adaptive optimum method has the highest average gain. The adaptive principal eigenvalue beamformer in most cases performs worse than the optimum beamformer. This is due to the fact that only one dominant clutter component is canceled and most of the clutter power remains unsuppressed in the beam-space processed signal (**Figure 3**).

In [2] Di Lallo et al. have measured $13-25$dB suppression using two antennas and FM illumination. A wide-ranging study of the beamforming algorithms application for the Metropolitan Beacon System (MBS) illuminator can be found in [14]. Navrátil et al. investigated the effectiveness of the direct signal separation utilizing the elevation angle difference of the target and the illuminator. Using four antennas they achieved 10 dB improvement measured on the SINR of a detected target.

Beamformer	SINR gain (dB)
Fixed max SIR	3.9
DOA supported max SIR	4.5
Adaptive optimum	5.4
Principal eigenvalue	5.2

Table 1. Obtained SINR improvements of the different beamformer algorithms.

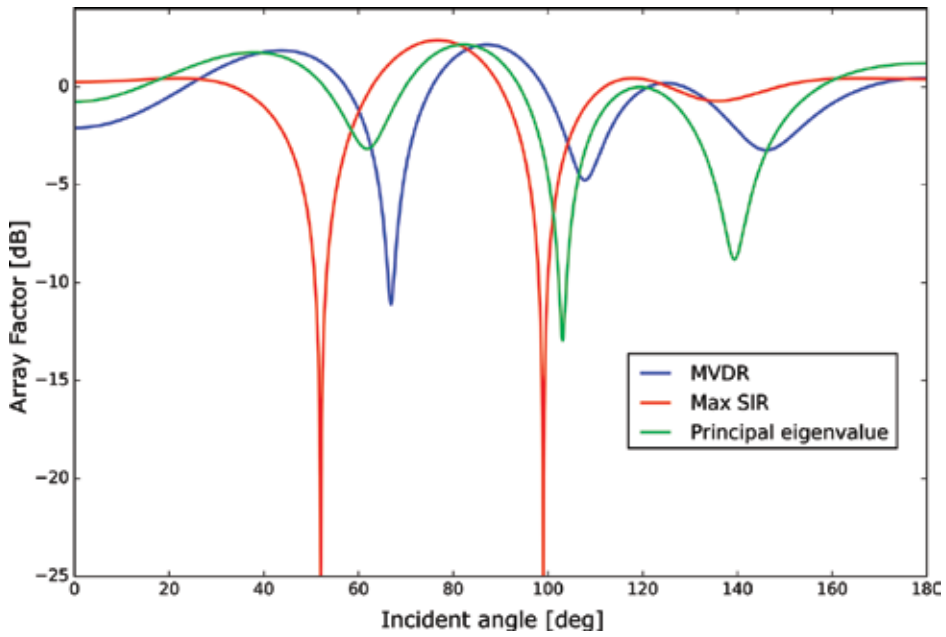

Figure 3. Obtained radiation patterns of the different beamformers.

5. Time domain filtering

The adaptive temporal algorithms rely on the fact that the ZDI signal components in the surveillance channel can be reproduced and subtracted by the use of the reference channel. According to the considered signal model, a FIR filter is able prepare the properly weighted and time delayed replicas of the reference signal. The n-th sample of the time domain filtered signal is calculated with

$$\begin{aligned} y_{td}[n] &= \boldsymbol{w}_{td}^H \boldsymbol{x}_r[n], \\ &\Downarrow \\ y_{td}[n] &= \boldsymbol{x}_s[n] - \boldsymbol{w}_{td}^H \boldsymbol{x}_r[n], \end{aligned} \tag{18}$$

where $\boldsymbol{w}_{td} \in \mathbb{C}^{Jx1}$ is the coefficient vector of the time domain filter and J is the tap size of the filter. J is set to the range of the farthest expected clutter component. We can obtain the temporal coefficient vector in the minimum mean squared error (MMSE) sense by using the well-known solution of the Wiener-Hopf equations [15]. In matrix form we have

$$\boldsymbol{w}_{td} = \boldsymbol{R}_t^{-1} \boldsymbol{r}_t \tag{19}$$

$\boldsymbol{R}_t \in \mathbb{C}^{JxJ}$ denotes the so called temporal autocorrelation matrix and $\boldsymbol{r}_t \in \mathbb{C}^{Jx1}$ is the temporal cross correlation vector. These are defined as follows

$$\begin{aligned} \boldsymbol{R}_t &= E\{\boldsymbol{x}_r[n] \boldsymbol{x}_r[n]^H\} \\ \boldsymbol{r}_t &= E\{\boldsymbol{x}_r[n] x_s[n]^*\}, \end{aligned} \tag{20}$$

where $\boldsymbol{x_r}[n]$ contains the last J samples of the reference signal and $x_s[n]$ is the n th sample of the surveillance signal.

$$\boldsymbol{x_r}[n] = [\, x_r[n] \quad x_r[n-1] \quad \dots \quad x_r[n-J+1] \,]^T \tag{21}$$

In practical cases, the temporal autocorrelation matrix and cross correlation vector is not known preliminary and thus it is inevitable to estimate them from the measured data. The algorithms discussed thus far can be partitioned into two main groups. The block type algorithms estimate and apply the coefficient vector of the filter on larger data chunks, while the iterative type algorithms update the used coefficient vector from sample to sample. In this chapter, the investigated and presented block type algorithms are the Wiener-SMI, ECA, ECA-B and ECA-S methods and the iterative methods are the LMS, NLMS, RLS and BLMS. In the presented investigations, the dimension of the temporal filters is uniformly set to $J = 128$ tap. This choice ensures that most of the clutter contributions are removed and also grants fast calculations to the analysis. Note that, the tap size of the temporal filter must be fitted to the environment in every specific case.

5.1. Wiener: sample matrix inversion (SMI)

The most-simple algorithm is the direct application of Wiener filtering technique with the sample average estimation of the temporal autocorrelation matrix and cross-correlation vectors.

$$\boldsymbol{R_t} = \frac{1}{N}\sum_{n=0}^{N-1} \boldsymbol{x_r}[n]\boldsymbol{x_r}[n]^H \tag{22}$$

$$\boldsymbol{r_t} = \frac{1}{N}\sum_{n=0}^{N-1} \boldsymbol{x_r}[n]x_s[n]^* \tag{23}$$

The filter has only one parameter, which is the tap size. This parameter controls the number of considered clutter components. **Figure 4** illustrates the mean value of the obtained target SINRs for different filter tap sizes. As we increase the filter tap size we can achieve higher filtering performance.

After reaching a certain filter tap-size the rate of the achievable further improvements decreases. In real systems, the optimal choice of the filter dimension can be set according to such an analysis. Note that the curve of the achieved improvements in the function of the filter dimension is fundamentally determined by the clutter profile of the environment. An exhaustive study on the clutter profile for FM-based passive radar can be found in [16].

The Wiener filter implemented with the SMI technique leads to solution of the LS filter. The LS filter minimizes the squared error of the filtered output signal array.

$$\min_{w_{\mathrm{td}}} \left\{ \left[\!\left[\boldsymbol{x_s} - \boldsymbol{X}\boldsymbol{w_{td}} \right]\!\right]^2 \right\} \tag{24}$$

The filtered surveillance signal that satisfies Eq. (24) can be calculated using Eq. (25)

$$\boldsymbol{x_f} = \boldsymbol{x_s} - \boldsymbol{X}\boldsymbol{w_{td}} = \left(\boldsymbol{I_N} - \boldsymbol{X_{SMI}}\left(\boldsymbol{X_{SMI}^H}\boldsymbol{X_{SMI}}\right)^{-1}\boldsymbol{X_{SMI}^H}\right)\boldsymbol{x_s}, \tag{25}$$

where $\boldsymbol{X_{SMI}}$ is the reference signal subspace matrix, that is composed of the time delayed replicas of the reference signal array.

$$\boldsymbol{X_{SMI}} = \left[\boldsymbol{x_r}\ \boldsymbol{D}\boldsymbol{x_r}\boldsymbol{D}^2\boldsymbol{x_r}\ldots\boldsymbol{D}^{J-1}\boldsymbol{x_r}\right] \in \mathbb{C}^{NxJ} \tag{26}$$

In Eq. (26) $\boldsymbol{x_r}$ denotes the vector of the reference signal samples from the whole CPI.

$$\boldsymbol{x_r} = [\,x_r[0] \quad x_r[1] \quad \ldots \quad x_r[N-1]\,]^T \in \mathbb{C}^{Nx1} \tag{27}$$

The $\boldsymbol{D}$ matrix performs the time delay by shifting the elements of the reference signal vector $\boldsymbol{x_r}$. It has a size $N \times N$ and the elements are defined by the following expression:

$$d_{i,j} = \begin{cases} 1\ , i = j+1 \\ 0\ , otherwise \end{cases} \tag{28}$$

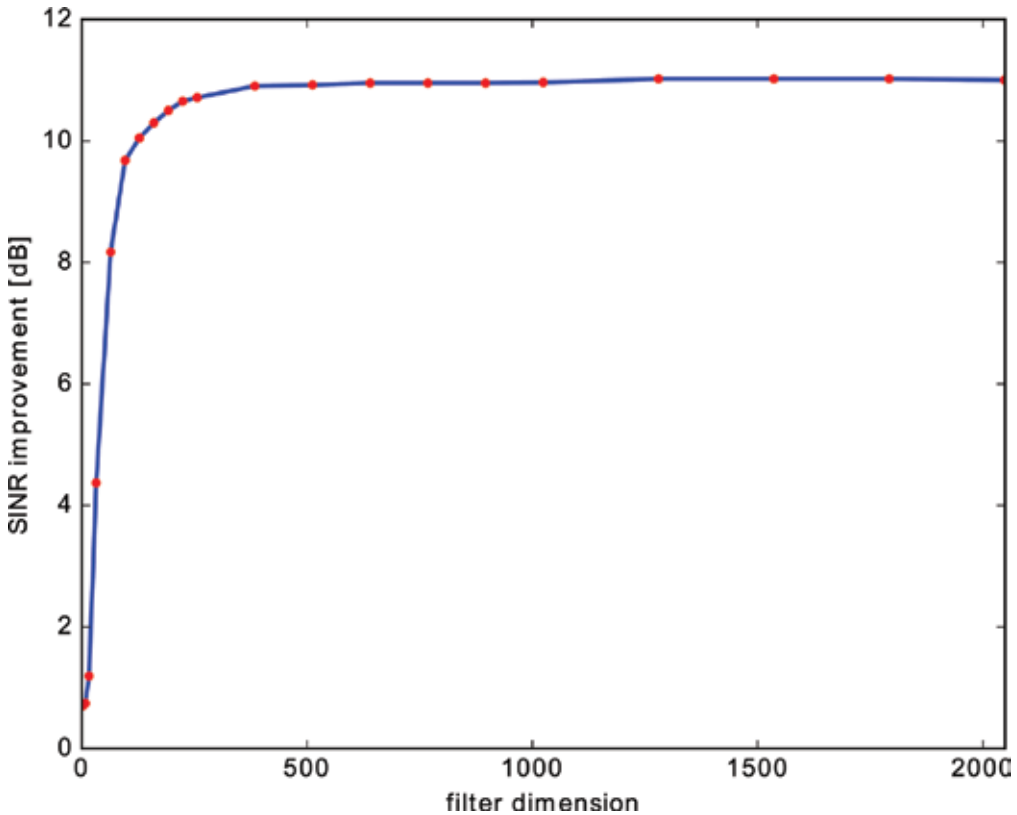

Figure 4. Wiener-SMI filtering performance with different tap-sizes.

In its form of the filter it can be considered as a projection. The Wiener-SMI algorithm projects the surveillance signal array to a subspace orthogonal to the reference signal and its time delayed replicas [17].

The processing demands for the Wiener-SMI algorithm can be written as

$$C_{Wiener-SMI} = 8\left(J^3 + J^2 + J^2N + 2JN\right) + 2N \tag{29}$$

Figure 5 illustrates the computational costs for different filter dimensions. The algorithm is relatively computational intensive, however using the method described in section the requirements can be greatly reduced.

5.2. Extensive cancellation algorithm (ECA)

The ECA algorithm is first introduced by Colone et al. in [17, 18].They realized that beside the ZDI a portion of the disturbances resides in the low Doppler frequency region. The main reason is that vegetation and slowly varying environment spreads the clutter energy around

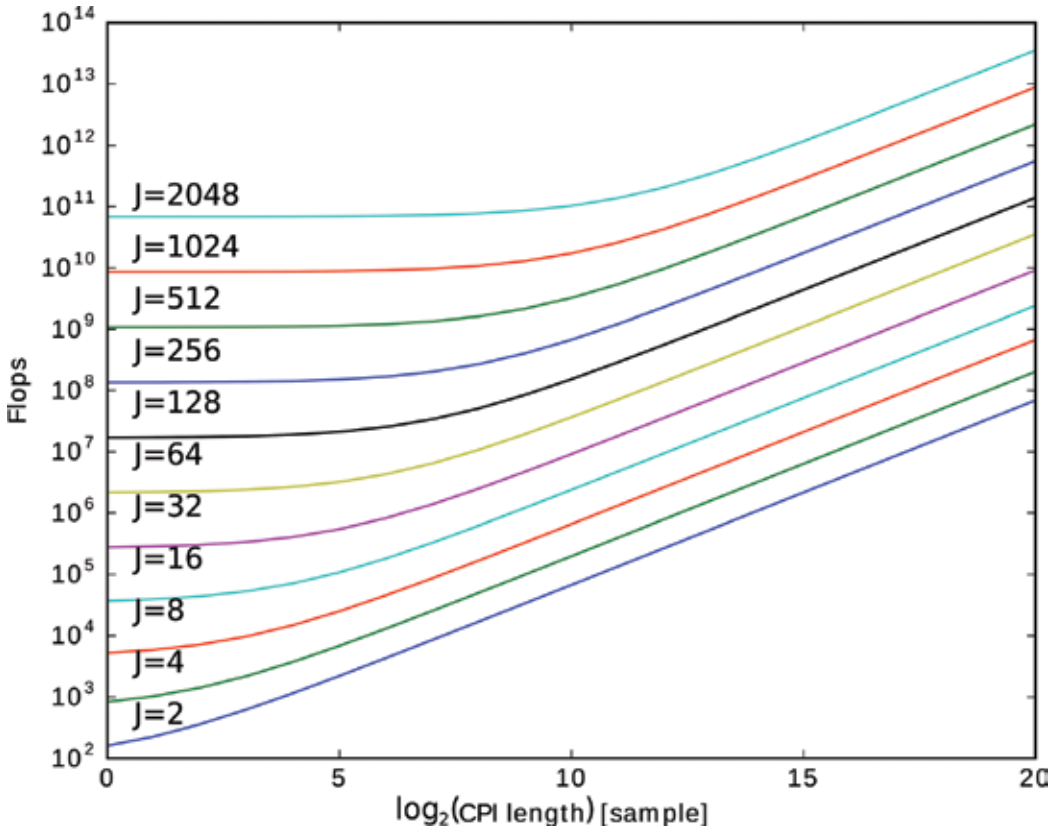

Figure 5. Computation costs of the wiener-SMI algorithm for different filter dimensions.

the zero Doppler line. To cope with this effect, they proposed to extend the reference signal subspace matrix to the Doppler frequencies.

$$\boldsymbol{X}_{ECA} = \left[\boldsymbol{\Lambda}^{-P}\boldsymbol{X}_{SMI} \quad \boldsymbol{\Lambda}^{-P+1}\boldsymbol{X}_{SMI} \quad \dots \quad \boldsymbol{X}_{SMI} \quad \dots \quad \boldsymbol{\Lambda}^{P-1}\boldsymbol{X}_{SMI} \quad \boldsymbol{\Lambda}^{P}\boldsymbol{X}_{SMI} \right] \tag{30}$$

$\boldsymbol{\Lambda} \in \mathbb{C}^{NxN}$ is the transformation matrix of the Doppler shift. In order to perform Doppler shift on the reference signal vector with f_d frequency, the $\boldsymbol{\Lambda}$ matrix should have a diagonal form with the following values:

$$\boldsymbol{\Lambda} = \mathrm{diag}\left(1, e^{j2\pi\frac{f_D}{f_s}}, e^{j2\pi\frac{f_D}{f_s}2}, \dots, e^{j2\pi\frac{f_D}{f_s}(N-1)}\right) \tag{31}$$

The P parameter controls the filter notch width in the Doppler domain. The wider filter notch means more clutter power to cancel and thus it ensures better target detection capabilities. At the same time, the overextended filter notch may prevent the detection of low Doppler frequency targets. The RD map of the ECA filtered surveillance signal can be seen in **Figure 14**. The filter notch for $P=5$ can be inspected in **Figure 15**. The computational burden can be approximated by replacing J with $J(2P+1)$ in Eq. (29). For reasonable P values this can lead to extremely high requirements. For this reason, this algorithm is not applicable in practical cases.

5.3. Batched ECA algorithm (ECA-B)

The Wiener SMI and the ECA algorithm use all the samples in a CPI to estimate and apply the coefficient vector of the filter. In non-stationer environment, the optimal coefficients may change rapidly over the CPI and these algorithms are not able adapt fast enough. This case the calculated coefficient vector may be smoothed between the instantaneous optimal values. To overcome this limitation Colone et al. proposed the batched version of the ECA algorithm [17]. This method divides the CPI into shorter blocks and performs the filtering individually on these consecutive signal portions. This makes the filter more robust against the time-varying characteristic of the environment. Let us partition the N sample of the CPI to T number of batches. We can then describe the t-th signal fraction of surveillance channel as follows:

$$\boldsymbol{x}_s^{(t)} = \left[x_s\left[t\frac{N}{T}\right] \quad x_s\left[t\frac{N}{T}+1\right] \quad \dots \quad x_s\left[(t+1)\frac{N}{T}-1\right] \right] \tag{32}$$

The t-th batch of the reference signal $\boldsymbol{x}_r^{(t)}$ is defined in a similar way. Correspondingly the signal subspace for the t-th batch $\boldsymbol{X}_{ECA-B}^{(t)}$ is constructed from the Doppler shifted and time delayed replicas of the $\boldsymbol{x}_r^{(t)}$ signal vector. Following the same filtering procedure, we have Eq. (33) to calculate the t-th batch of the filtered surveillance signal.

$$\boldsymbol{x}_f^{(t)} = \boldsymbol{P}^{(t)}\boldsymbol{x}_s^{(t)} = \left(\boldsymbol{I}_N - \boldsymbol{X}_{ECA-B}^{(t)}\left(\boldsymbol{X}^{(t)H}_{ECA-B}\boldsymbol{X}_{ECA-B}^{(t)}\right)^{-1}\boldsymbol{X}^{(t)H}_{ECA-B}\right)\boldsymbol{x}_s^{(t)} \tag{33}$$

A direct consequence of the fractioned processing is the widening of the filter notch around zero Doppler. Colone et al. have shown by analytical investigation in [19] that the notch width of the

ECA-B filter is inversely proportional with the batch size and has the shape of $\sin(\pi f N_B/f_s)/\sin(\pi f/f_s)$ where N_B is the number of samples in a batch $N_B = N/T$. According to this result the reduction of the batch size increase the filter notch width and enhance the domain of the canceled clutter components. However, the decreased batch duration may worsen the filter adaptivity. In this case the number of samples used for the coefficient estimation also starts to become insufficiently low that yield inaccurate estimation see **Figure 6**. Another remarkable nature of this filter is the introduction of unwanted sidelobes in the Doppler dimension. These undesired Doppler structures can highly affect the operation of the detection stage and thus resolved in the later development of the algorithm.

Figure 14 illustrates the RD map obtained when the CPI is partitioned to 32 batches. As it is apparent the ECA-B filter can significantly reduce the slowly moving clutter with its extended filter notch. We can also observe the appearing Doppler sidelobes that complicate the identification of true targets. The computation need of the algorithm has the following form.

$$C_{ECA-B} = 8\left(J^3T + J^2T + J^2N + 2NJ\right) + 2N \tag{34}$$

The calculated values for different batch intervals and filter dimensions are illustrated in **Figure 7**. It is clear from the figure that for long CPIs the required FLOPs are practically

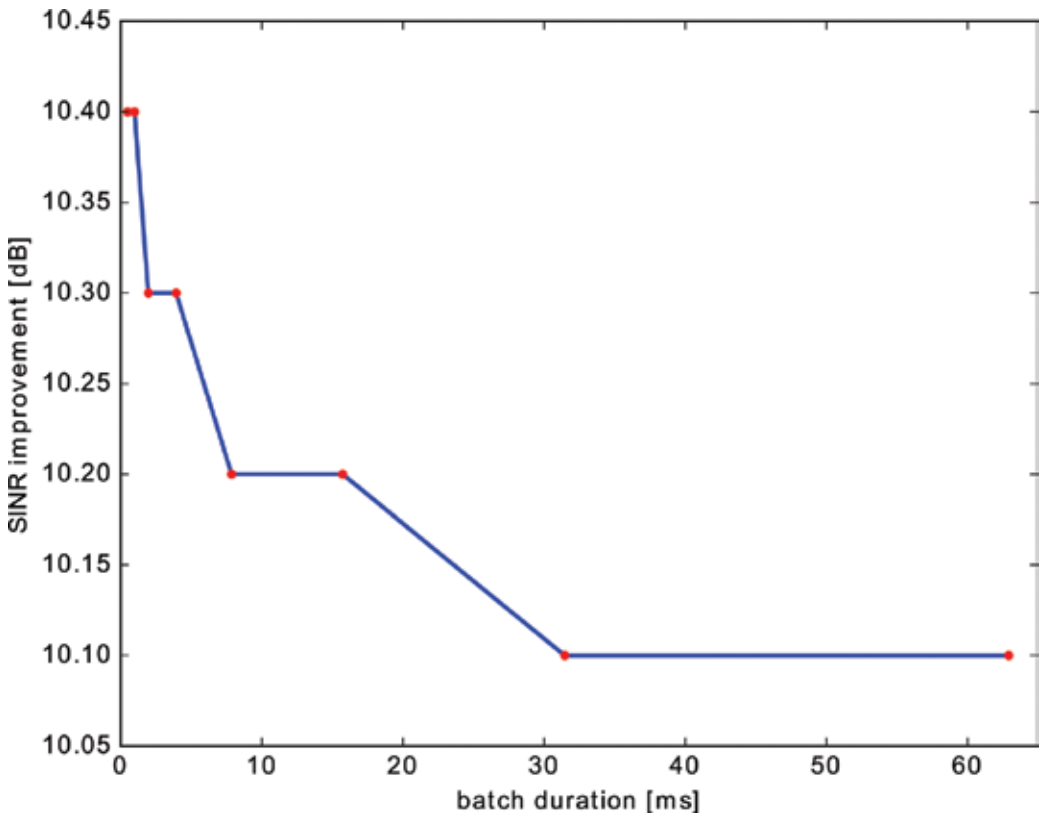

Figure 6. Achieved SINR improvement of the ECA-B algorithm with different batch durations.

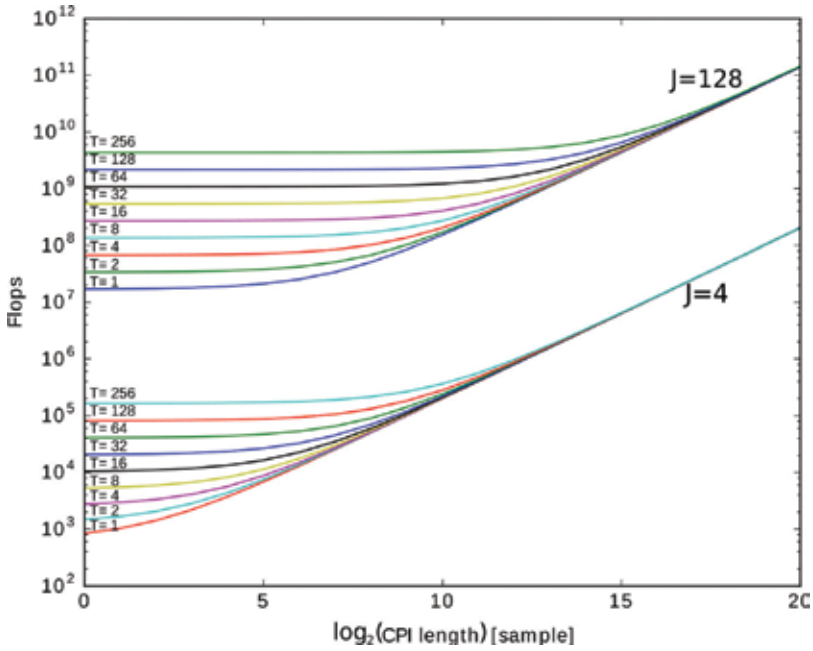

Figure 7. Computational costs of the ECA-B algorithm with different filter dimensions and batch duration.

identical regardless of the batch duration. When $T=1$, the ECA-B algorithm reduces to the Wiener-SMI. This also means that their calculation requirements for long CPIs are practically the same. However, it is worthwhile to mention that the memory requirement of the ECA-B algorithms is less in the direct implementations.

5.4. Sliding window ECA algorithm (ECA-S)

The previously introduced ECA-B algorithm suffers from the effect of parasitic Doppler sidelobes arising from the fractionated filtering. The theoretical investigations in [19] carried out that these Doppler ambiguities are separated by $1/T_B$, where $T_B = N_B f_s$ is the batch duration. One can say that by decreasing the batch size the Doppler ambiguities can be moved out of the interested region of range-Doppler map. However, as described earlier the direct consequence of decreasing the batch duration is the widening of the filter notch around the zero Doppler frequency. To resolve this contradiction Colone et al. [19] suggested to apply different window sizes for the coefficient estimation and the filtering. The coefficient estimation window is selected symmetrically around the filtering window. The batch size used for the filtering is denoted by N_f while we introduce the N_E parameter that describes the number of samples used for the coefficient estimation.

$$\boldsymbol{x}_{s,est}^{(t)} = \left[x_s\left[tN_f - \frac{N_e - N_f}{2}\right] \quad x_s\left[tN_f - \frac{N_e - N_f}{2} + 1\right] \quad \dots \quad x_s\left[(t+1)N_f - \frac{N_e - N_f}{2} - 1\right]\right] \tag{35}$$

$$\boldsymbol{x}_{s,filt}^{(t)} = \left[x_s[tN_f] \quad x_s[tN_f + 1] \quad \dots \quad x_s[(t+1)N_f - 1] \right] \tag{36}$$

After all, the separation between the Doppler ambiguities can be controlled by the N_f parameter while the filter notch can be configured by choosing the proper N_e parameter. This filtering technique also improves the filtering performance of ECA-B as the coefficients are calculated on overlapped signals fractions thus we get a smoothed estimate. **Figure 14** shows the range-Doppler map of the ECA-S algorithm. It is clearly visible that the unwanted Doppler structures are totally disappeared while the width of the filter notch is remained the same. Note that the algorithm reduces to the ECA-B method when $N_f = N_e$. This method utilize more processing power than the ECA-B algorithm as the windows used for the coefficient estimations are inherently wider. The exact requirements can be written as

$$C_{ECA-S} = 8\left(J^3T + J^2T + J^2TN_a + JTN_a + JN\right) + 2N \tag{37}$$

Figure 8 depicts the emerging extra calculation compared to the ECA-B algorithm. The different curves belong to different window sizes used for the coefficient estimation. The tap-size is set to $J = 128$, and the CPI is partitioned to 32 filtering windows. Note that the curve corresponding to $N_e = CPI/32$ is identical with the computational need of the ECA-B algorithm when $T = 32$, see **Figure 7**.

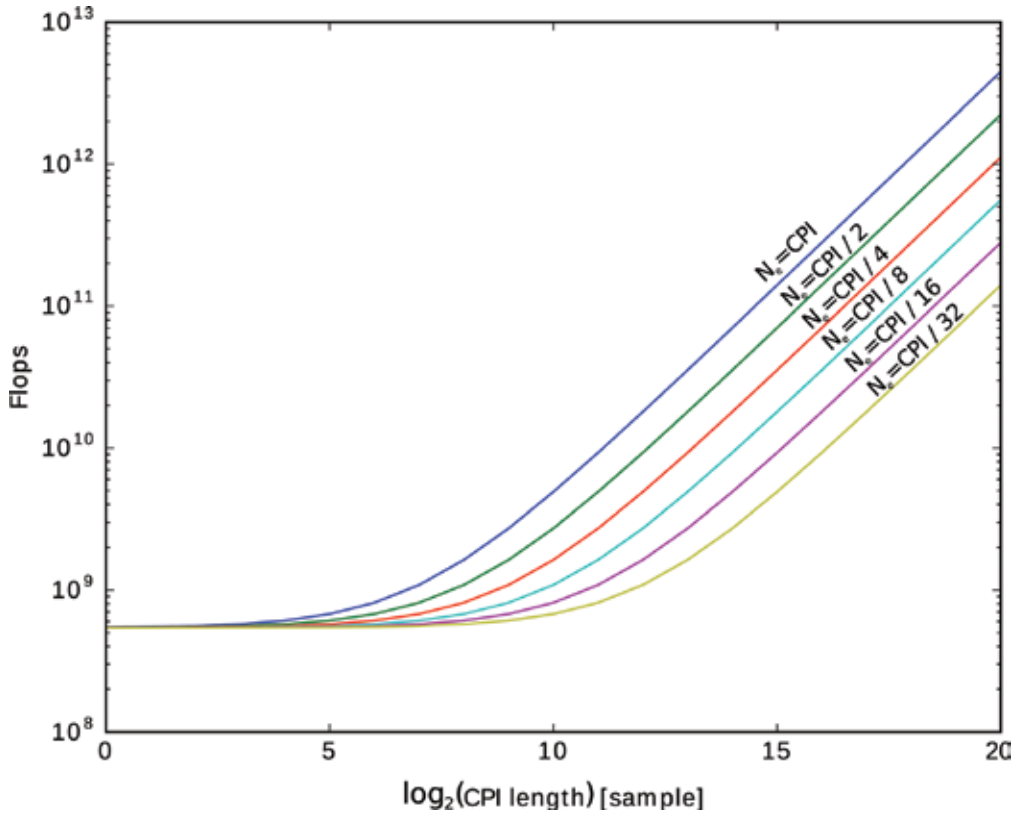

Figure 8. ECA-S algorithm computation cost with different estimation window lengths. ($N_f = N/32$).

5.5. Supplemented autocorrelation matrix technique

As it is well known the autocorrelation matrix of a wide sense stationary (WSS) process has Toeplitz and Hermitian properties. $R_{i,j} = R_{i+1,j+1} = r_{i-j}$ and $\boldsymbol{R} = \boldsymbol{R}^{\boldsymbol{H}}$. This allows us to calculate only J elements from the $J \times J$-sized R autocorrelation matrix and supplement the remaining elements. The obvious advantage of this technique is the fast coefficient calculation. At the same time, the limited information about the random process may lead to inaccuracies that worse the filtering performance. In the current investigations, the calculated J elements are selected as the first column of the autocorrelation matrix. **Figure 9** shows the comparison of the achieved result on the Wiener-SMI and the ECA-B algorithm. As we can observe the difference is negligible when the sample count used for the coefficient estimation is relatively high. However, in case of the ECA-B algorithm, when short batch duration is applied the sample count is very low and the estimated correlation coefficients have still large variance. For this reason, the performance noticeably decreases.

As a conclusion, we can say that for algorithms, which use large signal batches for the coefficient estimation this technique has definitely relevance. The achievable speed up is dependent on the filter depth thus on the dimension of the temporal autocorrelation matrix.

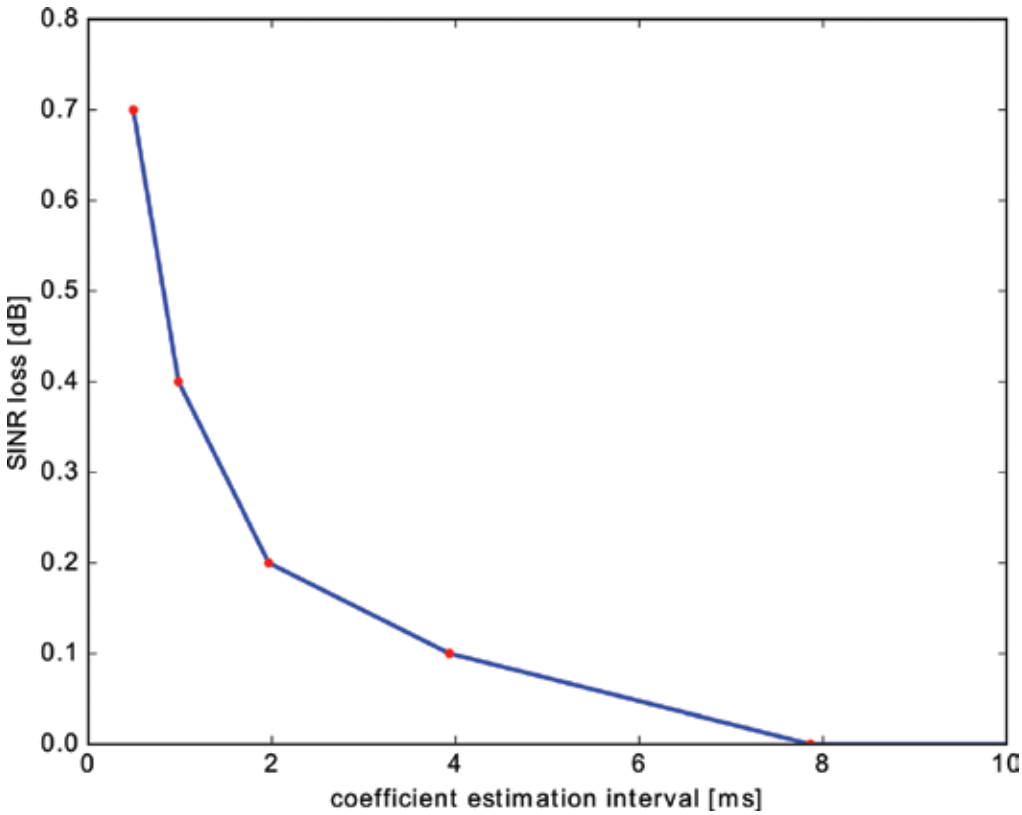

Figure 9. SINR loss arising from the usage of the supplemented autocorrelation matrix in the ECA-B algorithm.

The direct form of the modified computational costs for the Wiener-SMI, ECA-B and ECA-S algorithms are summarized as follows.

$$\begin{aligned} C_{S-Wiener-SMI} &= 8\left(J^3 + J^2 + 3JN\right) + 2N \\ C_{S-ECA-B} &= 8\left(J^3T + J^2T + 3JN\right) + 2N \\ C_{S-ECA-S} &= 8\left(J^3T + J^2T + 2JTN_e + JN\right) + 2N \end{aligned} \tag{38}$$

The achieved speed-ups for different processing batch sizes are illustrated in **Figure 10**. For large CPIs, there is no significant difference in the speed up ratio for different batch durations. For the ECA-S algorithm the speed-up ratio is always greater than the ECA-B method has because, the simplified J^2 term has larger coefficient.

5.6. Least mean square (LMS)

In contrast to the block type algorithms the LMS algorithm updates the $\boldsymbol{w}_{LMS}$ coefficient vector every time when a new signal sample is digitalized. The filter belongs to the family of the stochastic gradient-based algorithms. That means the filter updates the coefficient vector from the current estimation of the error gradient. The update equation for the coefficient vector can be written as

$$\boldsymbol{w}[n+1] = \boldsymbol{w}[n] + \mu \boldsymbol{x_r}[n] e[n]^*, \tag{39}$$

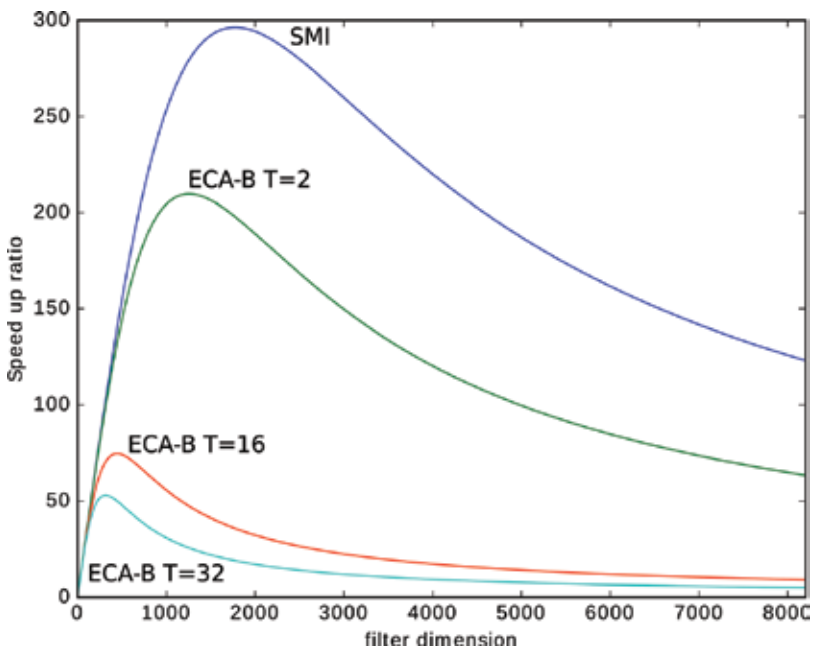

Figure 10. Achievable speed up with the supplemented autocorrelation matrix technique.

where $e[n]$ denotes the filter error at the n th time instant, which is defined as the difference between the n th sample of the filter output and the surveillance signal.

$$e[n] = x_s[n] - \boldsymbol{w}_{LMS}[n]^H \boldsymbol{x}_r[n] \tag{40}$$

The coefficient vector is often initialized with the zero vector at the beginning of the processing interval. The filter uses the μ step size parameter to control the influence of the current modification. Higher step size values offer faster reactions to the changes in the environment, however the filter will suffer from misadjustment and will not able to suppress the ZDI properly. At the same time choosing the step size too small, result in sluggish filter response. In order to ensure stability Eq. (41) must also be satisfied.

$$0 < \mu < \frac{2}{\sum_{j=0}^{J-1} E\left\{|x_s[n-j]|^2\right\}} \tag{41}$$

The optimal choice of the step-size is also dependent on the dimension of the filter and the power of the reference signal. Thus, the proper parametrization of the filter can be a complicated task. This greatly reduces the applicability of the filter. The obvious advantage of the LMS algorithm is that it calculates the filtered output very fast, thus it is capable of the real-time operation. The estimated target SINRs for different step-size values are shown in **Figure 11**.

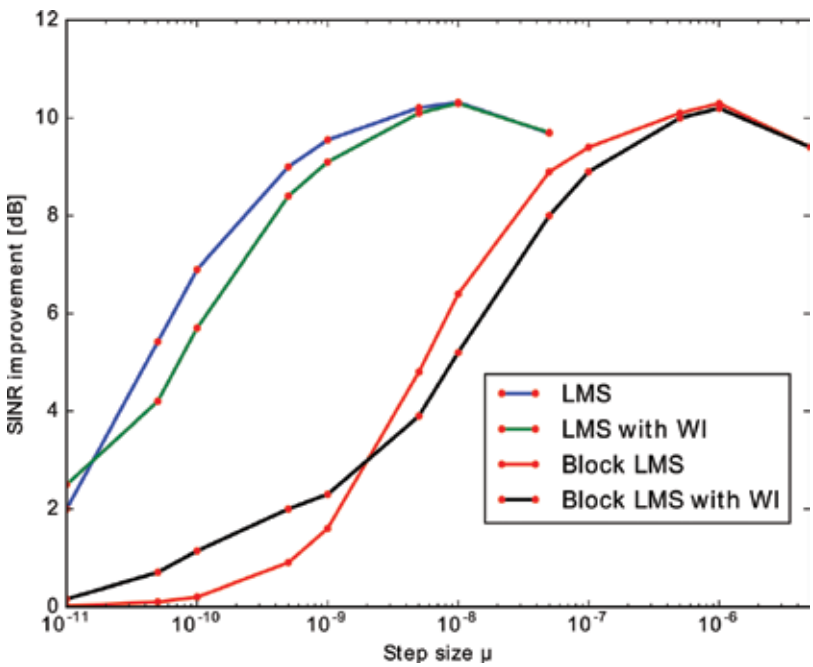

Figure 11. SINR improvements of the LMS algorithm variants for different step-sizes.

5.7. Normalized least mean square (NLMS)

The NLMS algorithm makes the LMS algorithm independent from the scale of the reference signal vector with normalizing the step-size parameter. For the coefficient vector update we have

$$\boldsymbol{w}_{NLMS}[n+1] = \boldsymbol{w}_{NLMS}[n] + \frac{\mu_n}{a + \boldsymbol{x}_r[n]^H \boldsymbol{x}_r[n]} \boldsymbol{x}_r[n] e[n]^*, \tag{42}$$

where a is small number used to prevent instability and μ_n is the step-size of the NLMS algorithm, which must be chosen in the range of $0 < \mu_n < 2$. With normalizing the energy of the reference signal vector the algorithm gains stability and better convergence properties. The price paid for this improvement is the increased computational cost. In every iteration, it is now necessary to determine the instantaneous energy of the reference signal and its time delayed replicas. The convergence behavior of the NLMS algorithm for a variety of step-size values are illustrated in **Figure 12**.The displayed curves represent the evaluation of the L2 norm of the coefficient vector.

5.8. Recursive least squares (RLS)

Beside the instantaneous error the RLS algorithm also takes into consideration the weighted sum of the previous error values.

$$e_{RLS}[n] = \sum_{i=0}^{n} \lambda^{n-i} \left(x_s[i] - \boldsymbol{w}_{RLS}[n]^H \boldsymbol{x}_r[n] \right)^2 \tag{43}$$

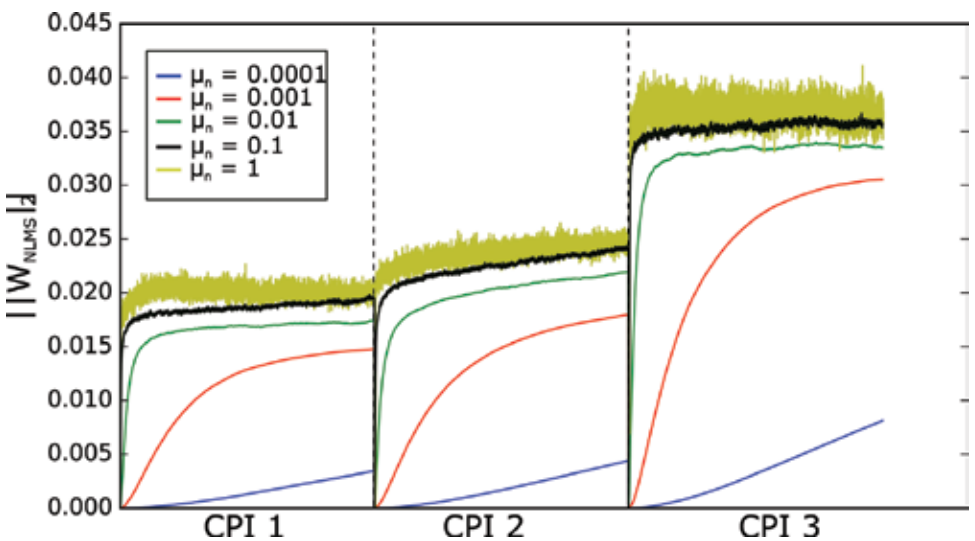

Figure 12. Convergence behavior of the NLMS algorithm for different step-sizes.

where λ is a small number, which is often referred to as the forgetting factor. With choosing the forgetting factor in the range of $0 < \lambda \leq 1$ the algorithm reduces the influence of the previous error values over time. The RLS algorithm recursively finds the optimal coefficient vector that minimizes the weighted sum of the error squares. To accomplish this, the algorithm utilize the Sherman-Morrison formula to the calculate the inverse of the updated autocorrelation matrix. The coefficient update equations of the RLS filter can be written as follows.

$$\begin{aligned} \boldsymbol{k}[n] &= \frac{\lambda^{-1}\,\boldsymbol{P}[n-1]\boldsymbol{x_r}[n]}{1+\lambda^{-1}\boldsymbol{x_r}[n]^H\boldsymbol{P}[n-1]\boldsymbol{x_r}[n]} \\ \alpha[n] &= \boldsymbol{x_s}[n] - \boldsymbol{w}_{\boldsymbol{RLS}}^H[n-1]\boldsymbol{x_r}[n] \\ \boldsymbol{w_{RLS}}[n] &= \boldsymbol{w_{RLS}}[n-1] + \boldsymbol{k}[n]\alpha^H[n] \\ \boldsymbol{P}[n] &= \lambda^{-1}\boldsymbol{P}[n-1] - \lambda^{-1}\boldsymbol{k}[n]\boldsymbol{x_r}[n]^H\boldsymbol{P}[n-1] \end{aligned} \tag{44}$$

The starting values of the inverse of the autocorrelation matrix must be initialized for the RLS algorithm. It is often estimated on a small number of samples.

$$\boldsymbol{P}[0] = \left(\sum_{i=0}^{i_1} \boldsymbol{x_r}[i]\boldsymbol{x_r}[i]^H\right)^{-1} \tag{45}$$

The filter is far more complex than the LMS or the NLMS algorithm, thus the real-time operation is difficult to implement. However, the RLS algorithm has faster convergence than the LMS or NLMS algorithm.

5.9. Weight inheritance technique

The iterative algorithms always have to initialize the coefficient vector to start the iteration. In most applications, the zero vector is an adequate choice. Observing **Figure 12** we can notice that the re-initialization of the coefficient vector at the beginning of the CPI greatly degrades the convergence and lengthens the transient sections. Bárcena-Humanes realized that the large transient sections are responsible for the smoothing effects in range-Doppler map. This effect can be observed in **Figure 14** on the result of the LMS algorithm. To shorten or even eliminate the transient sections he proposed to initialize the coefficient vector of the current CPI with last value of the coefficient vector of the previous CPI.

$$w[0]^{(p)} = w[N-1]^{(p-1)}, \tag{46}$$

where p denotes the index of the currently processed CPI. The success of this modification depends on the stationarity of the environment and the elapsed time between the consecutively processed CPIs. In case the time gap is reasonably large the parameters of the environment may change to a great extent and the filter has to compensate the accumulated error.

Figure 13 shows the result on the LMS filter convergence with and without the weight inheritance technique. On the results obtained from the measured data we can see some improvements,

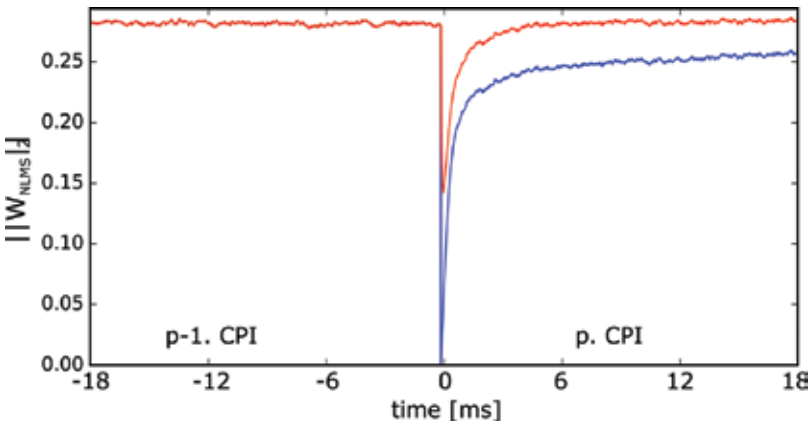

Figure 13. Effect of the weight inheritance technique on the LMS algorithm.

however the time gap between the CPIs was too large. Thus, the necessarily evolving transient sections still greatly affects the range-Doppler map. As a result, no improvement is realized.

5.10. Block least mean square (BLMS)

In the LMS algorithm the fast variation of the instantaneous error signal can lead to the poor estimation of the gradient vector. These disadvantages can be avoided with averaging the gradient vector over a block samples. The block LMS filter only updates the coefficient vector after averaging L gradient estimations. The coefficient vector is then updated at the $t+1$-th block according to Eq. (47).

$$\boldsymbol{w}_{\boldsymbol{BLMS}}[t+1] = \boldsymbol{w}_{\boldsymbol{BLMS}}[t] + \mu_B \frac{1}{N_B} \sum_{i=0}^{N_B-1} e^*[tN_B + i]\, \boldsymbol{x}_{\boldsymbol{r}}[tN_B + i] \tag{47}$$

The coefficient vector is only updated N/N_B times instead of N, where N_B denotes the number of samples in a block. The block size of the filter is often set to be equal to the filter length $N_B = J$. The μ_B parameter gives the step-size of the algorithm. The block LMS filter has a fast implementation in the frequency domain. The fast block LMS (FBLMS) algorithm use the overlap-save method to calculate the linear convolution. The fast block algorithm derived from the NLMS algorithm is first proposed for passive radar application by Zhao et al. [20]. They have shown that the fast block NLMS (FBNLMS) algorithm can realize improvement over the traditional NLMS algorithm both in terms of cancellation and computational cost.

6. Summary

The main objective of this chapter is to provide support on the proper selection of the clutter cancellation algorithms. In the previous sections many of the so far proposed algorithms were investigated, their advantages and weaknesses were analyzed. **Figure 14** shows the calculated range-Doppler maps.

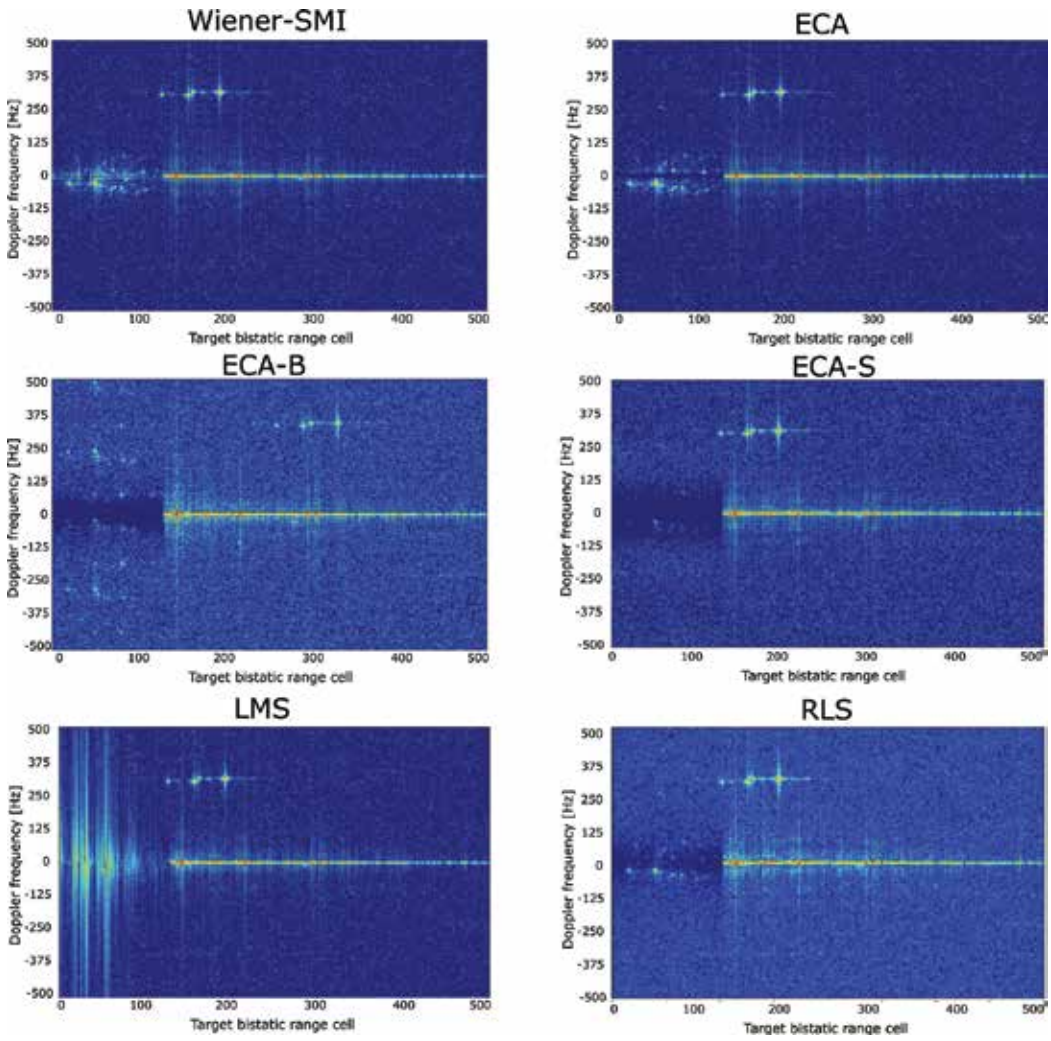

Figure 14. Range-Doppler maps of the differently filtered surveillance channels.

In **Figure 15** filter notch with can be inspected for the different time domain algorithms. The dimension of the applied filters is uniformly set to $J = 128$ expecting the ECA algorithm, where it has been set to $J = 2$.

It can be seen that the ECA-S algorithm has a fairly deep null in contrast to the other algorithms. With applying the supplemented autocorrelation matrix technique (S-ECA-S) this wide and deep null is filled up. Also observe that the RLS algorithm has evolved a relatively wide and shallow notch around the zero Doppler. This can be also seen in **Figure 14**.

Figure 16 shows the location of the investigated algorithms on the map of the filtering performance versus computational cost. The picture provides relevant information on the proper selection of the clutter cancellation algorithm. The variation of the achieved SINR improvements over the different algorithms is relatively small, however the essential features are readable.

http://dx.doi.org/10.5772/intechopen.71289

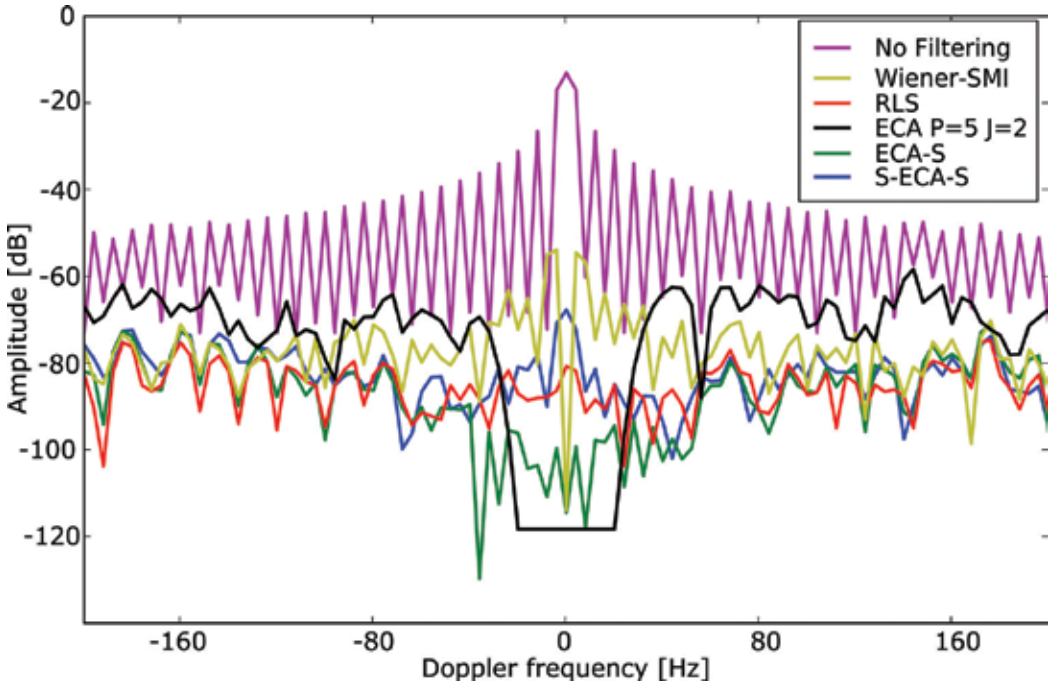

Figure 15. Zero range slice of the range-Doppler map with the different time domain algorithms.

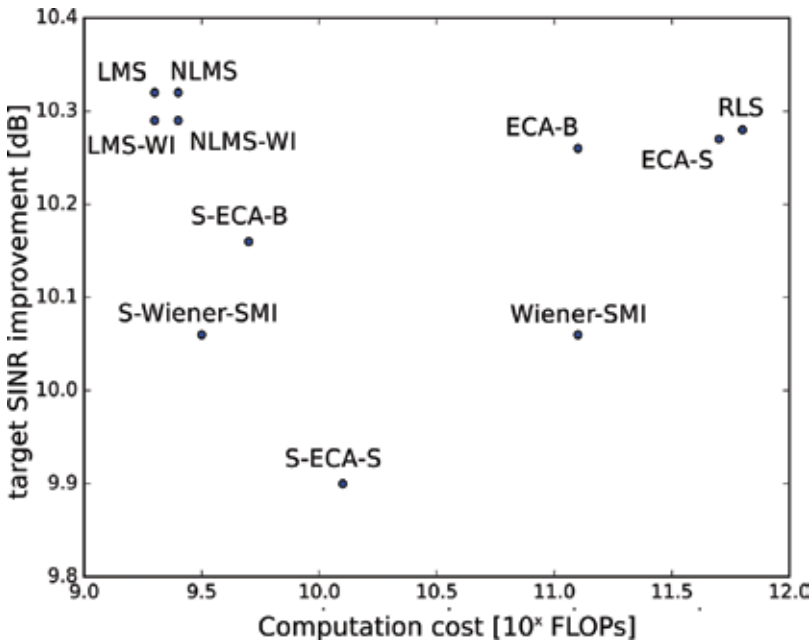

Figure 16. Map of the characterized algorithms, generated according to their filter performance and computation costs ($J = 128$).

Recall that even high clutter cancellation can result in slight improvement, see in **Figure 2**. It must be also strictly emphasized that resultant ambiguities on the calculated range-Doppler map should also be taken into account to the algorithm selection. The following section aims to classify these algorithms based on the application criteria.

Slowly moving targets

For detecting slowly moving targets the information preservation in the low Doppler frequency domain is essential. The Wiener-SMI filter cancels only the zero Doppler contribution while provides great filtering performance. Using the supplemented autocorrelation matrix technique, the rapid coefficient calculation can also be guaranteed. In case the ECA-S algorithm is properly configured it can also be a reasonable choice, however its computation is more complex. The investigated iterative algorithms can only be applied in case the range of interest lies outside the dimension of the filter or the weight inheritance technique can be properly applied.

High filter performance

Among the examined filtering algorithms, the ECA-S method achieved the best filtering performance. The price paid for the superior filtering performance is the high computational burden.

Low computation cost

The iterative algorithms are essentially developed to ensure real-time operation. Several research paper reports about their successful implementations in FPGAs or GPUs [20, 21]. In passive radar application, the block LMS algorithm not only has low computation costs but also grants good filtering performance. The main drawback of these filters is the strong distortion of the range-Doppler map.

Author details

Tamás Pető* and Rudolf Seller

*Address all correspondence to: peto@hvt.bme.hu

Department of Broadband Infocommunication and Electromagnetic Theory, Budapest University of Technology and Economics, Budapest, Hungary

References

[1] Kulpa K. Signal Processing in Noise Waveform Radar. 1st ed. Norwood, MA: Artech House; 2013

[2] Di Lallo A, Fulcoli R, Timmoneri L. Adaptive spatial processing applied to a prototype passive. 2-5 Sept 2008; Adelaide, SA, Australia; IEE; 2008. pp. 1-5. DOI: 10.1109/RADAR.2008.4653906

[3] Peto T, Seller R. Quad channel DVB-T based passive radar. 17th International Radar Symposium (IRS); 10-12 May 2016; Krakow, Poland; IEEE; 2016. pp. 1-4. DOI: 10.1109/IRS.2016.7497383

[4] Tao R, Wu HZ, Shan T. Direct-path suppression by spatial filtering in digital television terrestrial broadcasting-based passive radar. IET Radar Sonar and Navigation. 2010;**4**(6):791-805. DOI: 10.1049/iet-rsn.2009.0138

[5] Villano M, Colone F, Lombardo P. Antenna Array for passive radar: Configuration design and adaptive approaches to disturbance cancellation. International Journal of Antennas and Propagation. 2013;**2013**:16

[6] Moscardini C, Conti M, Berizzi F, Martorella M, Capria A. Spatial adaptive processing for passive Bistatic radar. IEEE Radar Conference 2014; 19-23 May 2014; Cincinnati, OH, USA; IEEE; 2014. p. 6. DOI: 10.1109/RADAR.2014.6875751

[7] Cardinali R, Colone F, Ferretti C, Lombardo P. Comparison of clutter and multipath cancellation techniques for passive radar. IEEE Radar Conference 2007; 17-20 April 2007; Boston, MA, USA; IEEE; 2007. p. 6. DOI: 10.1109/RADAR.2007.374262

[8] Garry JL, Baker CJ, Smith GE. Evaluation of direct signal suppression for passive radar. IEEE Transactions on Geoscience and Remote Sensing. 2017;**5**(7):14. DOI: 10.1109/TGRS.2017.2680321

[9] Baczyk MK, Malanowski M. Reconstruction of the reference signal in DVB-T-based passive radar. International Journal of Electronics and Telecommunication. 2011;**57**(1):43-48. DOI: 10.2478/v10177-011-0006-y

[10] Liu J, Li H, Himed B. Analysis of cross-correlation detector for passive radar application. IEEE Radar Conference, 2015; 10-15 May 2015; Arlington, VA, USA; IEEE; 2015. p. 1-5. DOI: 10.1109/RADAR.2015.713110

[11] Pető T, Seller R. Quad channel software defined receiver for passive radar application. Archives of Electrical Engineering. 2017;**66**(1):5-16. DOI: 10.1515/aeee-2017-0001

[12] Pető T, Seller R. Time domain filter comparison in passive radar systems. 18th International Radar Symposium (IRS) 2017; 28-30 June 2017; Prague, Czech Republic; IEEE; 2017. p. 1-10. DOI: 10.23919/IRS.2017.8008108

[13] Gross FB. Smart Antennas with MATLAB. 2nd ed. New York, Chicago, San Francisco, Athens, London, Madrid, Mexico City, Milan, New Delhi, Singapore, Sydney, Toronto: McGraw-Hill Education; 2015 433 p

[14] Navrátil V, O'Brien A, Garry JL, Smith GE. Demonstration of space-time adaptive processing. International Radar Symposium 2018; 28-30 June 2017; Prague, Czech Republic; IEEE; 2017. p. 10. DOI: 10.23919/IRS.2017.8008146

[15] Simon H. Adaptive Filter Theory. 3rd ed. Upper Saddle River, New Jersey: Prentice Hall Inc.; 1996

[16] Malanowski M, Haugen R, Greco MS. Land and sea clutter from FM-based passive bistatic radars. IET Radar, Sonar and Navigation. 2013;**8**(2):160-166. DOI: 10.1049/iet-rsn.2013.0186

[17] Colone F, O'Hangan DW, Lombardo P, Baker CJ. A multistage processing algorithm for disturbance removal and target detection in passive Bistatic radar. IEEE Transaction on Aerospace and Electronic Systems. 2009;**45**(2):698-722. DOI: 10.1109/TAES.2009.5089551

[18] Colone F, Cardinali R, Lombardo P. Cancellation of clutter and multipath in passive radar using a sequential approach. IEEE Conference on Radar, 2006; 24-27 April, 2006; Verona, NY, USA; IEEE; 2006. p. 393-399. DOI: 10.1109/RADAR.2006.1631830

[19] Colone F, Palmarini C, Martelli T, Tilli E. Sliding extensive cancellation algorithm for disturbance removal in passive radar. IEEE Transactions on Aerospace and Electronic Systems. 2016;**52**(3):1309-1326. DOI: 10.1109/TAES.2016.150477

[20] Zhao YD, Zhao YK, Lu XD, Xiang MS. Block NLMS cancellation algorithm and its real-time implementation for passive radar. 14-16 April 2013; Xi'an, China; IET; 2013. pp. 1-5. DOI: 10.1049/cp.2013.0341

[21] Oba H, Kim M, Arai H. FPGA implementation of LMS and N-LMS processor for adaptive array applications. International Symposium on Intelligent Signal Processing and Communications ISPACS '06; 12-15 Dec 2006; Tottori, Japan; IEEE; 2007. p. 485-488. DOI: 10.1109/ISPACS.2006.364703

Chapter 7

Sense Smart, Not Hard: A Layered Cognitive Radar Architecture

Stefan Brüggenwirth, Marcel Warnke,
Christian Bräu, Simon Wagner, Tobias Müller,
Pascal Marquardt and Fernando Rial

Additional information is available at the end of the chapter

http://dx.doi.org/10.5772/intechopen.71365

Abstract

In this chapter, we present a cognitive radar architecture based on the three-layer model by Rasmussen. The skill-based-layer is characterized by adaptive signal-processing approaches and target matched waveforms. The rule-based-layer comprises reactive execution of optimal illumination policies and resource-management. The knowledge-based layer allows for long term, goal-oriented mission- and trajectory planning. Each layer is illustrated by example algorithms and applications for implementation.

Keywords: adaptive filters, cognitive systems, closed-loop controllers, robotics, signal processing, system architectures

1. Introduction

Modern multifunctional radars with electronic beam-steering (AESA) provide many degrees of freedom to point the antenna beam, usage of the electromagnetic spectrum and waveform selection (**Figure 1**). Complex surveillance and reconnaissance scenarios require increased automation and suited man-machine-interfaces, which is enabled by the cognitive radar approach [1–3].

In this article we explain a cognitive radar architecture developed at the Fraunhofer FHR based on the three-layer-model of Rasmussen [4]. In the following, we will first introduce the concept of cognitive automation and derive our cognitive radar architecture. For each cognitive subfunction several technologies for realization are discussed and illustrated by example applications.

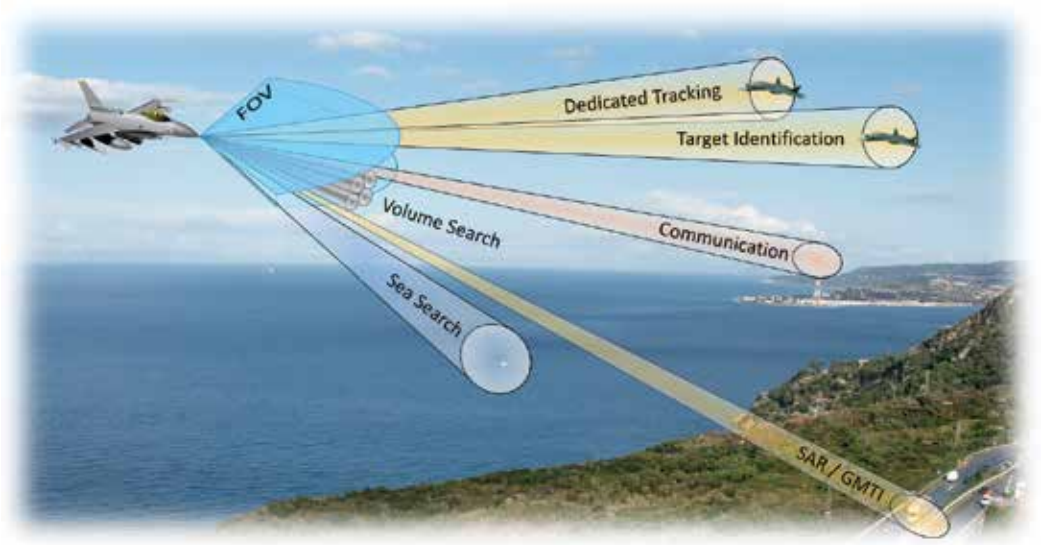

Figure 1. Airborne multifunctional radar.

2. Cognitive automation for radar

The concept of Dual-Mode Cognitive Automation [5] is well suited to deal with the challenges of highly automated radar systems. As shown in **Figure 2**, intelligent software-agents (depicted as robot-heads) can be introduced into the work equipment to increase the level of automation under the supervisory control paradigm [6] .

Alternatively the software-agent can cooperate with the human operator in the sense of an intelligent assistant system [7]. Even though the cognitive radar architecture can be used for both approaches, we will focus on the more traditional supervisory control role in the following.

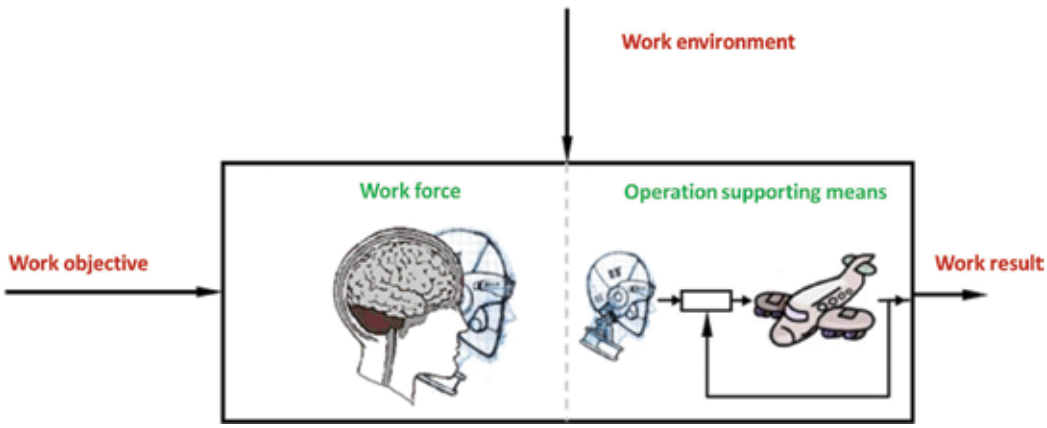

Figure 2. Concept of dual-mode cognitive automation [5].

http://dx.doi.org/10.5772/intechopen.71365

3. Three layer model of a cognitive radar architecture

The three-layer model of human cognitive performance published by Jens Rasmussen in 1983 is widely used in human factors [8], cognitive psychology and robotics [9, 10]. As shown in **Figure 3** the complex process of human cognition is simplified and broken down into cognitive subfunctions (shown as gray boxes) with the indicated flow of information. The Rasmussen-model distinguishes three layers of cognitive performance with increasing level of abstraction.

The *skill-based-layer* comprises subconscious and very efficient perception and control tasks (such as steering along a curvy road). Above it, the *rule-based-layer* describes reactive behavior. Learned procedures are triggered by certain cues in familiar situations (such as stopping the car at a red traffic light). The *knowledge-based-layer* enables deliberate, goal-based behavior. By inferring novel solutions from a-priori knowledge flexible reaction in unknown situations is achieved (e.g. bypassing a traffic jam based on a road-map).

For the development of a cognitive radar architecture in analogy to the Rasmussen-model, each cognitive subfunction had to be mapped into five different radar-technologies as shown in **Figure 3**.

Modern radar system can generate arbitrary waveforms in real-time. This allows for transmit signals to be matched to the target transfer function or the electromagnetic spectrum as explained in Sections 4.1 and 4.2. Perception tasks of a radar comprise signal-processing and classification aspects. We use a machine learning approach that is illustrated in Section 4.3. Rule-based behavior in a radar is emulated by using optimal control policies or resource management approaches as shown in Section 5.1 or Section 5.2. Knowledge-based behavior can be implemented using Bayesian networks or automated planning algorithms. We show an example for robot-trajectory planning in Section 6.1.

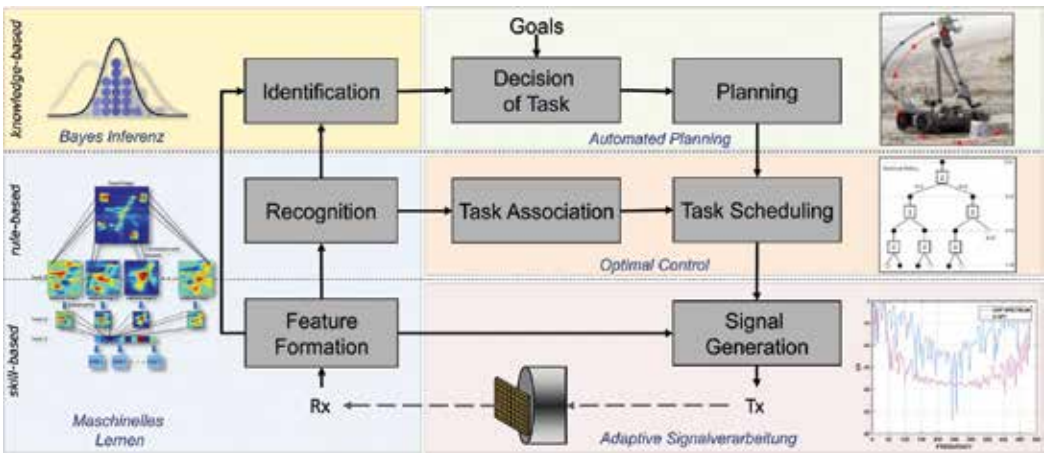

Figure 3. Three-layer-model of a cognitive radar architecture with supporting technologies. Modified from Ref. [4].

4. Skill-based-layer

The skill-based layer represents the basic signal-generation and processing capabilities of the radar system. It operates on the smallest timescale in the architecture in a continuous processing loop. Below, we give an example for adapting the transmit waveform to the target-transfer function using arbitrary waveform generation capabilities. As an extension, the waveform can further be adapted to the electromagnetic spectrum that has to be continuously sensed.

4.1. Matched illumination

If a priori information about a target is available, it is possible to optimize the transmission waveform for this target. Advantages arise for example by discriminating two classes of targets or by reducing resources of the sensor. One example is the reduction of the required bandwidth, if the available a priori information about the target is comprehensive.

In order to resolve the size of the object, two transmission frequencies are sufficient to estimate the extension of two scattering points with a spacing of Δz [11] (see **Figure 4**). The maximal energy at the receiver can be achieved when two frequencies are superposed to a beat frequency where the envelope covers the dimension of the target. If there are more than two scattering points the frequency spacing must be higher to achieve a higher period of the beat. In practice, the assumption of a known target impulse response is often difficult to

realize. In a cognitive radar system, the a priori knowledge of the target can be presupposed by previous measurements and is assumed to be predicted for the next time step. An adapted waveform can be used to update the target track with respect to its extension by a lower allocation of the bandwidth.

Assuming a linear, time invariant channel with additive white Gaussian noise w, the complex received signal y corresponds to a convolution of the transmission signal s and the target transfer function h_i

$$y = y_{s,i} + w = h_i^* s + w = H_i s + w \tag{1}$$

where $y_{s,i}$ represents the undisturbed signal component. The linear convolution can be expressed by a matrix vector multiplication where the Toeplitz structured convolution matrix

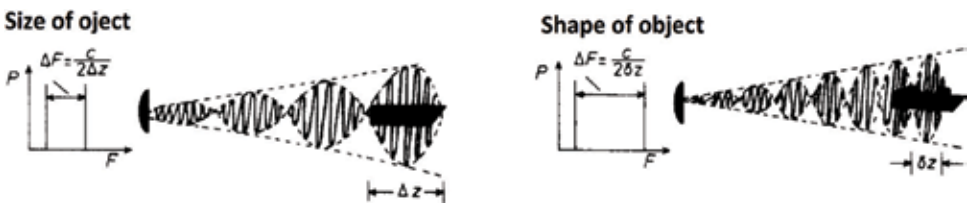

Figure 4. Transmitting two frequencies with a spacing of $\Delta F = c/2\Delta z$, the size of the object can be obtained. The shape of the object requires an even larger frequency separation $\Delta F = c/2\delta z$ (modified from ref. [11]).

H_i for the target index i is created by elements of the impulse response h_i. The detection performance is directly related to the signal to noise ratio (SNR) and depends on the receiver bandwidth and the power of the received signal y_s

$$\mathrm{SNR} = \frac{\|y_s\|_2^2}{\mathbb{E}\left[|w|^2\right]} = \frac{s^H H_i^H H_i s}{\sigma_w^2}. \tag{2}$$

If the target characteristic H_i is known, the signal to noise ratio can be increased by optimizing the waveform s [12]. The optimisation problem can be formulated to

$$\max_s \mathrm{SNR} = s^H A s \qquad \text{subject to} \qquad E_s = s^H s = \|s\|_2^2 = 1 \tag{3}$$

with the constraint of an energy limited transmission signal and the Hermitian correlation matrix $A = \frac{1}{\sigma_w^2} H_i^H H_i$. One possibility to solve this optimisation problem is the Lagrangian multiplier method

$$\begin{aligned} L(s,\lambda) &= s^H A s - \lambda\left(s^H s - 1\right) \\ \frac{\partial}{\partial s} L(s,\lambda) &= 0 = s^H A - \lambda s^H \Rightarrow (A - \lambda I)s = 0 \\ \frac{\partial}{\partial s^*} L(s,\lambda) &= 0 = s^T A^T - \lambda^T s^T \Rightarrow (A - \lambda I)s = 0. \end{aligned} \tag{4}$$

Eq. (4) is obviously an eigenvalue equation where the Lagrange multiplier λ represents the real eigenvalue and the waveform s is the corresponding eigenvector. By choosing the maximal eigenvalue, the signal to noise ratio is maximized. The eigenvector which corresponds to the maximal eigenvalue is directed towards the highest energy (variance).

To gain a better understanding of the solution, the basic example of **Figure 4** is presented for the two dominant scattering points

$$h(t) = a_0\delta(t - t_0) + a_1\delta(t - t_1) \qquad a_0 = |a_0|e^{j\varphi_0}, a_1 = |a_1|e^{j\varphi_1} \in \mathbb{C}. \tag{5}$$

The corresponding frequency spectrum to Eq. (5) is

$$\begin{aligned} H(\omega) &= \frac{1}{2\pi}\left(|a_0|e^{j\omega t_0 + \varphi_0} + |a_1|e^{j\omega t_1 + \varphi_1}\right) \\ |H(\omega)|^2 &= |a_0|^2 + |a_1|^2 + |a_0||a_1|\cos\left(\omega(t_0 - t_1) + \left(\varphi_1 - \varphi_0\right)\right). \end{aligned} \tag{6}$$

The target impulse response fluctuates due to the interference of the scattering centers with a period of $t_1 - t_0 = \frac{2}{c_0}(r_1 - r_0)$ and depends therefore on the target dimension as already visualized in **Figure 4**. The phase shift of the second point target causes a shift of all frequency maxima (see also **Figure 5(a)**). Processing an eigenvalue decomposition according to Eq. (4) to obtain the optimal waveform for this example (see **Figure 5(b)**).

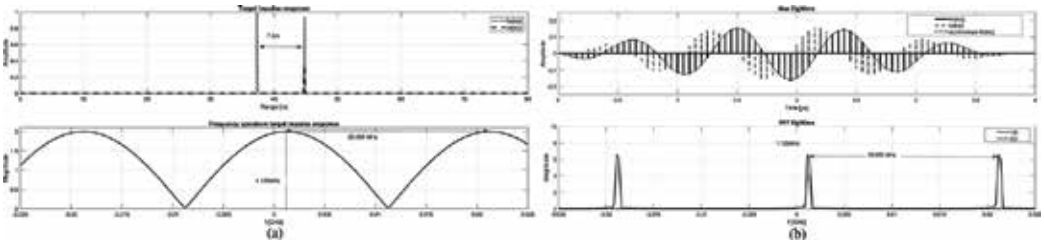

Figure 5. Target impulse response and optimal transmission waveform in time and frequency domain. (a) Target impulse response in time/range (upper) and frequency domain (lower) for two point targets at $r_0 = 37.32$ ($a_0 = 1$) and $r_1 = 44.82$ ($a_1 = 1 \angle 20^\circ$), (b) Optimal transmission waveform (eigenvector corresponding to the maximal eigenvalue) in time (upper) and frequency domain (lower).

Comparing this basic results with the solution of the eigenvalue decomposition, it is obvious that both frequency spectra are related to each other. If all frequency components of the target impulse response have comparable magnitudes, the frequency characteristic of the largest eigenvalue is similar to the target frequency spectrum and the target extension respectively. According to Eq. (6) the period of the target extension corresponds to a frequency of $\Delta F = \frac{c_0}{2(r_1 - r_0)} \approx 20.0$ MHZ. The envelope of the transmission wave is related to the phase difference between r_0 and r_1, and causes a frequency shift in the frequency domain with $f_e = (\phi_1 - \phi_0)\frac{\varphi F}{2\pi} \approx 1.125$ MHZ. Summarizing the characteristic of the optimal transmission signal, the eigenvector corresponds to the main direction of the target variance in the frequency domain and is linked to the physical behavior of the target. If there are more than two scattering points, additional modulation products will occur. In the case where all frequency components of the target spectrum have similar magnitudes, the eigenvector corresponding to the largest eigenvalue will represent all constructive interferences in the resolution bandwidth. But also for small deviations of the spectral magnitudes, the main component (optimal eigenvector) will contain only the dominant frequency while the minor amplitudes are represented by the remaining eigenvectors forming finally the complete signal space.

In order to distinguish between targets an adapted waveform can be used to improve the discrimination between two types of target classes [2]. A binary hypothesis test is one method to discriminate between target classes by evaluating the received signal

$$\begin{aligned} \mathbb{H}_0 &: y = y_{s,0} + w = H_0 s + w \\ \mathbb{H}_1 &: y = y_{s,1} + w = H_1 s + w. \end{aligned} \tag{7}$$

The distance $d = \|y_{s,0} - y_{s,1}\|_2 = \|(H_0 - H_1)s\|_2$ denotes the difference of the received amplitude without taking noise into account. The robustness against incorrect classification increases for higher distances especially in a noise environment. Similar to Eq. (2)–(4), the optimal waveform can be calculated by solving

$$\begin{aligned} 0 &= (A_{01} - \lambda I) s_{opt} \\ A_{01} &= (H_0 - H_1)^H (H_0 - H_1). \end{aligned} \tag{8}$$

The energy is focused in the spectral area where the both target deviations are predominant.

Comparing the performance of a binary hypothesis test for a linear chirp and the optimized waveform, the test statistic of the likelihood ratio for Eq. (7) is calculated [13]

$$L = \log\left(\frac{p_{\mathbb{H}_0}}{p_{\mathbb{H}_1}}\right) = -\frac{1}{\sigma_w^2}\left(y - y_{s,0}\right)^H\left(y - y_{s,0}\right) + \frac{1}{\sigma_w^2}\left(y - y_{s,1}\right)^H\left(y - y_{s,1}\right) \tag{9}$$

with the variance σ_w^2 of the complex noise. The deflection for the likelihood ratio test defines the effective difference of the likelihood centers and represents the output signal to noise ratio

$$d = \frac{\left[\mathbb{E}_{\mathbb{H}_0}(L) - \mathbb{E}_{\mathbb{H}_1}(L)\right]^2}{Var_{\mathbb{H}_1}(L)} = \frac{1}{\sigma_w^2}\left(y_{s,0} - y_{s,1}\right)^H\left(y_{s,0} - y_{s,1}\right). \tag{10}$$

It is possible to achieve the same performance of the receiver operating characteristic (ROC) curve, with a different test statistic of that likelihood ratio but different deflections [14]. That is why a higher deflection is related to a better discrimination and a lower sensitivity with respect to an suboptimal threshold. **Figure 6** shows the results of the binary test for a linear frequency modulation (LFM) and the optimized waveform for two Gaussian targets with the same extension and distance. The deflection between both classes increases for the optimised waveform leading to a lower intersection are of the test statistic for the hypothesis and the alternative. This facilitates a better separability as well as a lower false alarm rate for the same detection probability.

One example of adapting the waveform to the environment is the support of the classification and saving resources like the bandwidth. Applications like interference mitigation can also be executed in the skill-based layer by combining spectrum sensing algorithms with matched illumination.

4.2. Spectrum sensing

Due to the fact that wireless communication technologies are of significant importance in modern times, the available radio frequency spectrum has become a valuable resource for radar. For example the U.S. department of commerce [15] has decided to allocate parts of the S-band (1695–1710 MHZ and 3550–3650 MHZ) to wireless communication. Another example are parts of the C-band (5150–5350 MHZ and 5470–5725 MHZ) which are used by weather

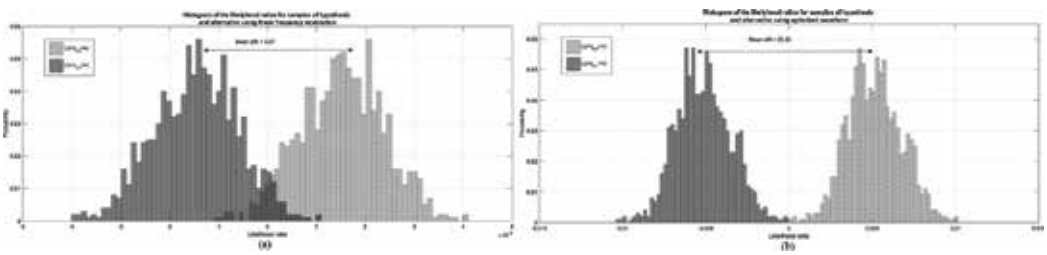

Figure 6. Test statistic of the likelihood ratios with the mean distance of the centers for LFM and optimized waveform. (a) Distribution of the likelihood ratio for noisy samples of the hypothesis and alternative using linear frequency modulation. (b) Distribution of the likelihood ratio for noisy samples of the hypothesis and alternative using the optimized waveform.

radars but are also used by 5GHz-WiFi [16] now. On the other hand these bands, although allocated, are underutilized providing opportunities for secondary (unlicensed) users to share the bands without harming the primary users. The other way round, a similar problem arises when the radar suffers interference from other users or even active jamming. Especially the first is a problem for ultra wideband radars like ground penetrating radars which naturally operate in partially occupied frequency bands. In the future these problems will become even worse and hence future cognitive radar systems must be able to operate in spectrally dense environments. Spectrum sensing techniques from cognitive radio provide algorithms to identify spectrum opportunities, i.e. to decide if a frequency band is occupied or not. With this information a cognitive radar can adapt dynamically its bandwidth, frequency and other transmit parameters to the radio frequency environment.

A significant number of studies dealing with spectrum sensing algorithms exists and hence we only give a brief overview here. For a comprehensive overview the reader is referred, for example, to the surveys [17, 18]. Spectrum sensing algorithms can be split into wideband and narrowband algorithms. Almost all narrowband spectrum sensing methods are statistical hypothesis tests usually written as

$$\mathbb{H}_0 : x(t) = w(t) \quad \text{against} \quad \mathbb{H}_1 : x(t) = s(t) + w(t)$$

where $x(t)$ represents the received complex signal, $s(t)$ the signal of another user and $w(t)$ the noise which is usually assumed white and Gaussian with variance σ_w^2. The most simple spectrum sensing method is the energy detector

$$\frac{2}{\sigma_w^2} \sum_{k=1}^{n} |x_k|^2 \underset{\mathbb{H}_0}{\overset{\mathbb{H}_1}{\gtrless}} F_{\chi^2_{2n}}^{-1}\left(1 - p_{fa}\right) \tag{11}$$

where p_{fa} is the desired probability of false alarm and $F_{\chi^2_{2n}}$ is the χ^2 distribution function with $2n$ degrees of freedom. Although this method is easy and fast, it suffers from bad detection probabilities in low SNR regions and poor robustness, see [19]. More advanced methods exploit certain features like for example cyclostationary properties [20] where a time series x_1, $x_2\ldots$ is said to exhibit cyclic frequency α with delay m if

$$C(\alpha, m) := \lim_{n\to\infty} \frac{1}{n} \sum_{k=1}^{n} \operatorname{red} \mathbb{E}[x_k x_{k+m}] e^{-j\,2\pi\alpha k} \neq 0. \tag{12}$$

Most modern modulations like OFDM or QAM have cyclostationary properties. For details on a test statistic see [21]. These methods offer high detection probabilities even in low SNR regions and are blind in the sense that they do not need information about σ_w^2. The price is a very high computational complexity and prior information about the used modulation. Completely blind methods, i.e. absolutely no prior information is necessary, are based usually on a multi antenna system. The data from the different channels is used to estimate a covariance matrix and from its characteristics e.g. eigenvalues a test statistic is build, see [22].

Because the channel state may change between the sensing and transmitting a prediction step after the sensing is helpful or even needed. For this purpose hidden Markov models are used in Ref. [23] and additionally multilayer perceptrons and recurrent neural networks are considered in Ref. [24]. Especially the neural networks perform well in simulations with a prediction accuracy of about 0.8 to 0.9.

In contrary to the narrowband band spectrum sensing the wideband spectrum sensing methods divide a band into occupied and unoccupied subbands. The most obvious method for classifying a wideband is to split it into fixed subbands (using a FFT or sweep and tune) and perform narrowband sensing in each one. But there are also native wideband spectrum sensing methods like a wavelet based approach, see [25].

If the radar is the primary user and avoiding or reducing interference is the only goal of the spectrum sensing, it is not necessary to decide if a channel is occupied or not. It is sufficient to use the channel with the least interference. But if a lot of interference is present, a compromise between bandwidth (resolution) and interference must be made which leads to an optimisation problem, see Refs. [26, 27].

After each sensing period, a suitable and adaptable waveform must be generated taking the information from the sensing step into account, essentially bandwidth and center frequency. For example, this can be multiple or notched chirps filling the unoccupied bands or a stepped FM waveform which avoids the occupied frequencies, see [27]. A combination with the matched illumination approach presented in Section 4.1 can be considered, too.

Building an experimental radar system with spectrum sensing capabilities is a challenging task. The computational complexity of some algorithms can be a burden and the additional sensing time, i.e. gathering the samples and computation time must be taken into account, causing a reduced duty cycle or pulse repetition frequency. In Ref. [27] a radar system employing spectrum sensing and matched illumination was implemented using an Ettus USRP X310 software defined radio. In a test environment about 10 dB noise floor reduction were achieved using spectrum sensing and a notched chirp.

4.3. Classification with deep learning techniques

The transition from the continuous stream of incoming row-data towards a symbolic representation of objects, which forms the basis for higher-level cognitive processing, is typically achieved using pattern recognition or classification techniques. As shown in **Figure 3**, machine learning approaches comprise subsymbolic feature formation processes that separate characteristic signal features in a higher-dimensional space. In this feature space, it is easier to recognize certain target classes to create an abstracted situational picture within the cognitive radar system.

4.3.1. Convolutional neural networks

Convolutional Neural Networks (CNNs) are inspired by the visual system of the brain and are part of the deep learning research field. For many years, CNNs were the only type of deep neural network that could efficiently be trained due to their structure using the technique of

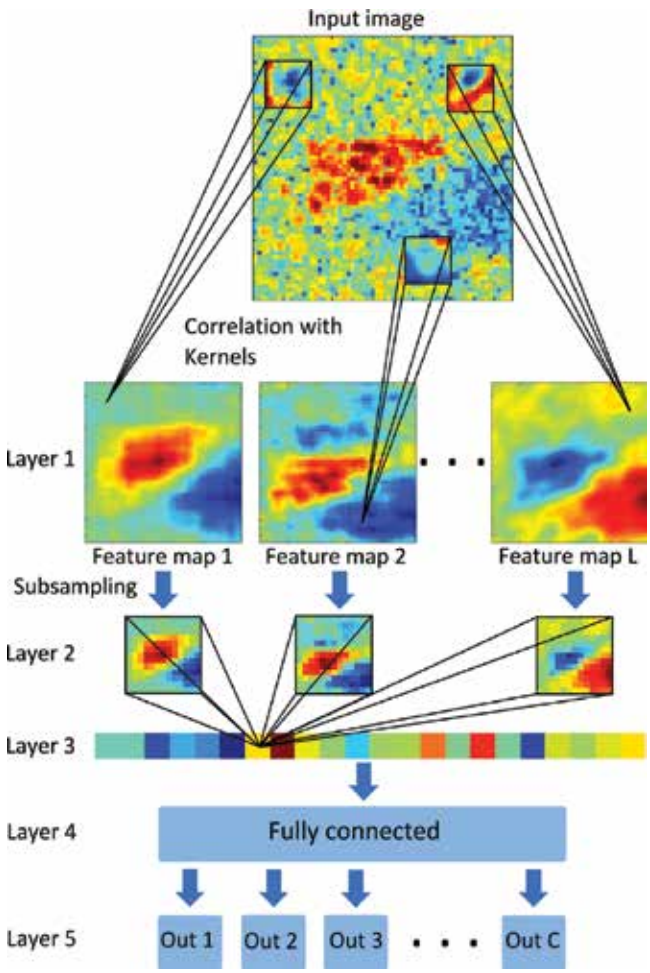

Figure 7. Structure of the used convolutional neural network.

weight sharing [28]. The basic structure of the network used in the presented architecture is shown in **Figure 7**.

CNN's are a special form of multi-layer perceptrons, which are designed specifically to recognize two-dimensional shapes with a high degree of invariance to translation, scaling, skewing, and other forms of distortion [29]. This invariance is achieved by an alternation of convolutional and subsampling layers, in which the neurons are organized in so called feature maps. All neurons in each of these feature maps use the same weights and are connected to a local receptive field in the previous layer. With this weight sharing technique, the number of free parameters is dramatically reduced compared to a fully connected network, what should lead to a better generalization of the network.

In the first convolutional layer, each neuron takes its inputs from a local receptive field in the input image and the output values of each feature map, which are visible in **Figure 7**, represent

the intensity of one specific local spatial feature. The features, i.e. the weights of the neurons, are learned during the training process and since the receptive fields of neighboring neurons in the feature maps are shifted only by one pixel in the corresponding direction in the input image, the output values of each feature map correspond to the result of a two-dimensional correlation of the input image with the learned weights of each particular feature map.

In the input image of **Figure 7** one target is visible in the center of the image. The correlation with the different kernels is visualized for three examples. The learned kernels are depicted inside the black squares on the input image and the result of the correlation can be seen in the feature maps of the first layer.

The second layer of the network is a subsampling layer and performs a reduction of the dimension by a factor of four. With this reduction the exact position of the feature becomes less important and it reduces the sensitivity to other forms of distortion [29]. The subsampling is done by averaging an area of 4×4 pixels, multiplying it with a weight w_j and adding a trainable bias b_j.

The third layer is a convolutional layer again and relates the features found in the image to each other. This layer is trained to find pattern of features, which can be separated by the subsequent layers and discriminate the different classes. The output of this layer is the internal representation and can be considered as feature vector found by the network for the given input image.

The last two layers of the network form the decision part of the system and are fully connected layers, which use the output values of the third layer as features for classification. The last layer consists of as many neurons as classes have to be separated, in our case ten. The classification is done by assigning the corresponding class of the neuron with the highest output value.

One cost function for neural networks trained with the back propagation algorithm is the mean square error (MSE) of the training set. The MSE is the mean value of the quadratic loss function $E(\alpha)$, which is given by

$$E_i(\alpha) = (d_i - f(x_i, \alpha))^2. \tag{13}$$

In (13), α is the set of classifier parameters, d_i is the desired output for the ith element of the training set and $f(x_i, \alpha)$ is the classifier response to input x_i. The MSE of the complete training set with size N is thus

$$MSE(\alpha) = \frac{1}{N}\sum_{i=1}^{N} E_i(\alpha) = \frac{1}{N}\sum_{i=1}^{N} (d_i - f(x_i, \alpha))^2. \tag{14}$$

The MSE is also called the empirical risk with respect to quadratic loss and classifiers using this error as a performance measure are said to implement the empirical risk minimization (ERM) [30].

The training of our network is performed by the stochastic diagonal Levenberg-Marquardt algorithm that is presented in [31, 32]. The core of this algorithm is the stochastic update rule

$$\alpha_l^{(k+1)} = \alpha_l^{(k)} - \gamma_l^{(k)} \frac{\partial E_i(\alpha)}{\partial \alpha_l^{(k)}}, \tag{15}$$

where $\alpha_l^{(k)}$ is the l-th element of the parameter set α at iteration k, E_i is the instantaneous loss function of (13) for image i and $\gamma_l^{(k)}$ is the step size for the particular weight α_l at iteration k. The dependency of the step size on the iteration indicates that the step size is not fixed during the training, but is dynamically updated. The calculation of the step size is done by

$$\gamma_l^{(k)} = \frac{\eta^{(k)}}{\mu + g_l^{(k)}} \tag{16}$$

with the constant μ and a parameter $\eta^{(k)}$ that prevents the step size from becoming too large when the estimate of the second derivative $g_l^{(k)}$ of the loss function $E_i(\alpha)$ with respect to α_l is small. For the calculation of $g_l^{(k)}$ the Gauss-Newton approximation is used that guarantees a nonnegative estimate [32]. The parameter η is marked here as dependent on the iteration, but is fixed over several epochs of the training[1]. The Hessian matrix $g^{(k)}$ is not calculated explicitly in each iteration, instead a running estimate is kept that is updated with

$$g^{(k)} = (1-\beta) g^{(k-1)} + \beta \frac{\partial^2 E_i(\alpha)}{\partial \alpha^2}, \tag{17}$$

where β is between zero and one. Because of the weight sharing, the first and the second partial derivative of the loss function are sums of partial derivatives with respect to the connections that actually share the specific parameter α_l

$$\frac{\partial E_i(\alpha)}{\partial \alpha_l^{(k)}} = \sum_{(m,n) \in V_l} \frac{\partial E_i(\alpha)}{\partial w_{mn}^{(k)}}, \tag{18}$$

$$\frac{\partial^2 E_i(\alpha)}{\partial \alpha_l^{2(k)}} = \sum_{(m,n) \in V_l} \sum_{(j,k) \in V_l} \frac{\partial^2 E_i(\alpha)}{\partial w_{mn}^{(k)} \partial w_{jk}^{(k)}}. \tag{19}$$

In (18) and (19), the w_{mn} is the connection weights from neuron n to m and V_l is the set of unit index pairs (m, n) such that the connection between neuron m and n shares the parameter α_l, i.e.,

$$w_{mn} = \alpha_l \qquad \forall \ (m,n) \in V_l. \tag{20}$$

Further details of the algorithm and the approximations that are done to compute the derivatives can be found in Ref. [32].

[1]The training of neural networks is separated into epochs, in each epoch the complete dataset is presented one time to the classifier [29].

4.3.2. Regularizations and adaptive learning rates

One feature of the presented network is the use of *momentum*, which adds a feedback loop and with this some kind of memory to the algorithm. With this technique a certain amount of the weight change of the last iteration is added to the weight change of the current iteration. This amount is determined by the *momentum constant* ρ and leads to the expression

$$\Delta\alpha^{(k)} = \rho\Delta\alpha^{(k-1)} - \gamma^{(k)}\frac{\partial E_i^{(k)}(\alpha)}{\partial\alpha^{(k)}}, \tag{21}$$

which can also be written as

$$\Delta\alpha^{(k)} = \sum_{n=0}^{k-1}\rho^n\gamma^{(k-n)}\frac{\partial E_i^{(k-n)}(\alpha)}{\partial\alpha^{(k-n)}}. \tag{22}$$

The use of momentum should have a positive effect on the behavior of the training algorithm and may prevent the algorithm from converging to a local minimum of the error function [29]. Another important regularization method used in this network is the max-norm regularization of the weights of the network. For this regularization the Frobenius norm of each kernel in layer one and three is calculated after the weight change at every iteration and if the norm is larger than a certain value c, the kernel is rescaled to a norm of c. With this regularization an improvement of the convergence properties of the training algorithm has been observed.

So far the learning rate in (16) is only determined by the characteristics of the data itself and the error it produces at the output of the network. Another important factor could be meta-information available about the training set. We give here an example of a priority class, which means that we have one target in our database that should always be classified correctly with the additional cost that we might produce more errors in other classes. To incorporate these priority classes into our network, the representation in (22) is used. The general idea is to increase the learning rate $\gamma^{(k)}$ if an image of a priority class is presented at the current iteration. This is done by multiplying a priority weighting p with the learning rate $\gamma^{(k)}$, which is then marked as $\gamma'^{(k)}$

$$\gamma'^{(k)} = p\gamma^{(k)}. \tag{23}$$

If this term is included in the formula for the weight change $\Delta\alpha^{(k)}$, the sum in (22) can be split into two parts. One part that contains all samples of the priority classes and one part with the examples of the remaining classes

$$\Delta\alpha^{(k)} = \sum_{\substack{n\in priority\\ class}}^{k-1}\rho^n\gamma'^{(k-n)}\frac{\partial E_i^{(k-n)}(\alpha)}{\partial\alpha^{(k-n)}} + \sum_{\substack{n\notin priority\\ class}}^{k-1}\rho^n\gamma^{(k-n)}\frac{\partial E_i^{(k-n)}(\alpha)}{\partial\alpha^{(k-n)}}. \tag{24}$$

The need for a different weighting of classes is also discussed in Ref. [33], where it is mentioned that the different costs of misclassification should be part of the classifier design. The

way we used here to include this prior knowledge into our target recognition system was also mentioned in Ref. [34] for Support Vector Machines, where the idea was to penalize the samples of less represented classes higher than others.

To show the benefit of this adaptive learning strategy we show an example of the ten class moving and stationary target acquisition and recognition (MSTAR) data [35] in **Figure 8**. In this example the learning rate of class four is multiplied with different weightings between one, which means no priority, and ten.

Without any weighting, this class has compared to the other classes a rather low correct classification rate calculated with respect to the number of input images Pcc_{in} (curve with round markers). This value gives the amount of input images that belong to class four and are actually classified as class four. The curve with the square markers in the plot gives the probability of correct classification with respect to the number of output images Pcc_{out}, which gives the amount of images that are classified as class four really belong to class four and is thus an indicator on the reliability of the classification. Summarized over all classes, both indicators lead to the same result, the correct classification rate Pcc of the curve with the triangular markers. From the plot can be seen that Pcc_{in} shows a steep increase at small values of p and up to $p=4$ also the overall correct classification rate increases, which is not the purpose here, but shows the positive effect of the additional correct classifications. While Pcc_{in} is increasing, Pcc_{out} shows a steady decreasing behavior. In the extreme case of $p \to \infty$, Pcc_{in} should reach one and both Pcc_{out} and Pcc should reach a value of N_{class4}/N, which means that all images in the dataset are classified as class four. This example and more details about the use of different weightings of different classes can be found in Ref. [36].

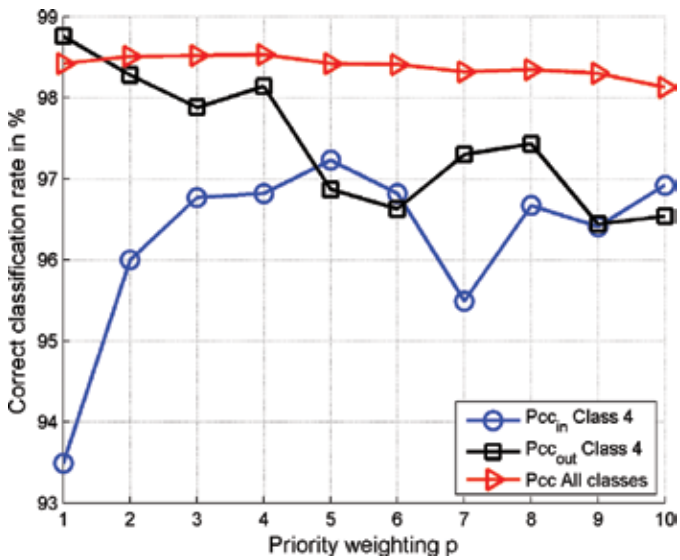

Figure 8. Performance of CNN with priority class.

4.3.3. Combination of convolutional neural networks with support vector machines

An often mentioned benefit of Support Vector Machines (SVMs) is the high generalization capability in comparison to neural networks. The high generalization of SVMs is achieved by a training strategy called *structural risk minimization*, which in comparison to the *empirical risk minimization* of neural networks takes the complexity of the classifier into account. For this reason, the Vapnik-Chervonenkis (VC)-dimension h was introduced to measure the complexity of a classifier. The VC-dimension is defined as the largest training set size N, which can be separated with binary labels in an arbitrary way by the SVM. With a high number of free parameters, the capacity of the classifier increases and thus the VC-dimension increases as well. Due to this relation, single patterns have a higher influence on the classification result for classifiers with a high VC-dimension, which increases the likelihood of overfitting to the training data [37]. To incorporate the VC-dimension into the minimization problem that has to be solved during the training, an additional term $\Phi\left(\frac{N}{h}\right)$ is added to the empirical risk to define the structural risk

$$R_{struc}(\alpha, h) = R_{emp}(\alpha, h) + \Phi\left(\frac{N}{h}\right), \tag{25}$$

where R_{emp} corresponds to the empirical risk. In this problem R_{emp} does not refer to the MSE of (14), which was used for neural networks, but to the specific number of misclassifications in the training set. The VC-dimension has an influence on both terms because a high VC-dimension will increase the complexity of the classifier and thus reduce the empirical risk, but the confidence interval $\Phi\left(\frac{N}{h}\right)$ would increase at the same time, since it only depends on the ratio between the size of the training set and the VC-dimension. SVMs are designed to find the best trade-off between these two terms, decrease the empirical error while keeping the VC-dimension as low as possible. Because of this, SVMs are classifiers with a very high generalization capability.

To use the high generalization of SVMs in our classification framework, we replace the last two layers of the CNN in **Figure 7** with SVMs. In this way we can use the convolutional feature extraction with the invariance to different forms of distortion and a classifier with high generalization. As input for the SVMs, the output values of the third layer are used. The final structure of the classifier is shown in **Figure 9**.

A SVM can only separate between two classes, for this reason the training set must be split for each SVM into two parts, one part containing the class that should give a positive result at the output of the SVM and one part containing the remaining training set that should give a negative result at the output. SVMs trained in that way are working in the one vs. all classification scheme, which means that as many SVMs as classes that need to be separated are necessary. For the actual classification of a SVM, a kernel is used to transform the data to a high dimensional space in which it is more likely that the problem can be linearly separated. Two common kernels are polynomial (including linear and quadratic kernels) and radial basis functions (RBFs). In **Table 1** a small example of the MSTAR database is shown and it can be seen that the already very high correct classification rate of the CNN can be further increased with the use of SVMs as classifier.

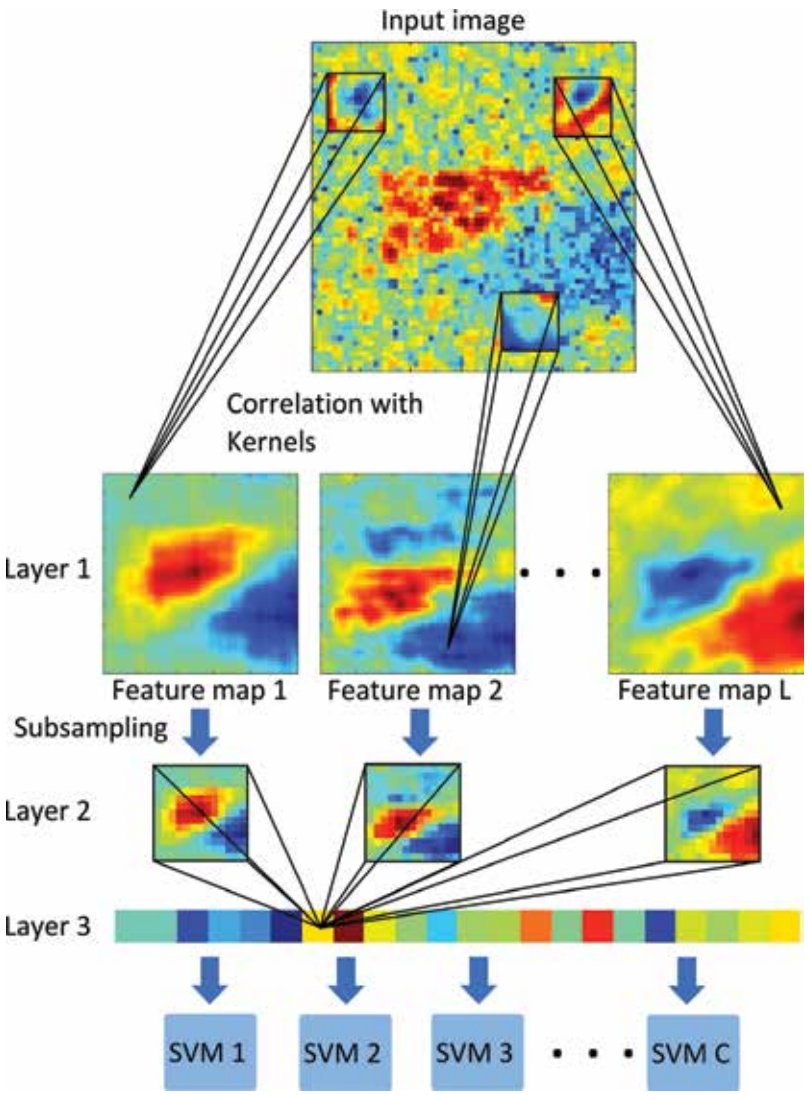

Figure 9. Structure of the used combination of CNN and SVMs.

Classifier	P_{CC}	P_{err}
Original CNN	96.00%	4.00%
CNN feature extraction and polynomial SVM	98.19%	1.81%
CNN feature extraction and RBF SVM	98.28%	1.72%

Table 1. Forced decision results of MSTAR dataset.

The results shown here are so called *forced decision* results, meaning that all images are classified by the highest output value, no rejection criteria like a certain confidence measure that has to be overcome is used. This and more results with the proposed classifier can be found in Ref. [38].

5. Rule-based-layer

Based on the abstracted situational picture derived by signal-processing and machine learning techniques, the cognitive radar system has to react to the perceived scene. Below, we illustrate a MDP based scheme to execute a-priori known, optimal illumination policies. In multifunctional radars, a radar resource manager has to schedule the individual illuminations into a serial radar timeline.

5.1. Optimal illumination policy

Markov-decision-processes (MDPs) are widely used in robotics to derive optimal control policies in stochastic environments. An agent in state s_i can execute different actions a_i, which with probability p_{ij} lead to a follow-up state s_j and a reward of r_{ij}. Different approaches, such as value-iteration or reinforcement-learning are used to determine an optimal policy $\pi = (s_i \mid a_i, s_j \mid a_j, \ldots)$. The policy assigns to each state s_i an optimal action a_i which maximizes the expected reward. MDPs are well suited to model the perception-action-cycle of a radar, e.g. for tracking applications [39]. In the following, we illustrate an example for multi-stage classification from Ref. [40].

Three classes of targets $K = \{1, 2, 3\}$ can appear in a scenario with a priori-probability $\pi_1 = 0.1$, $\pi_2 = 0.2$ and $\pi_3 = 0.7$ (**Figure 10**). A low- and a high-resolution radar-mode ($mode = 1 \mid 2$) are available for up to five consecutive illuminations $t = \{1, 2, 3, 4, 5\}$, which are fused to a final declaration V using the Bayes rule (**Figure 11**). The policy describes the optimal illumination strategy with respect to the highest expectation for correctly classifying targets of class 1 ($V = 1 \Leftrightarrow$ Class 1, $V = 2 \Leftrightarrow \neg$ Class 1). A negative reward (cost) of 1 unit is assigned for a false alarm and 2 units for a missed detection.

The resulting multi-stage illumination policy is shown in **Figure 12**. Initially the target is illuminated with mode 2 and classified. Depending on the result $Y = 1, 2$, the strategy branches and finishes with a final declaration $V = 1, 2$. In a simulation of 100,000 Monte-Carlo runs, the static application of mode 1 resulted in accumulated costs of 20,000 (class 1 never detected, i.e. all missed detections). When randomly switching between mode 1 and 2, costs of 9063 occurred as opposed to the lowest cost of 4797 when using the optimal strategy.

5.2. Radar resource management

The illumination-strategy in **Figure 12** requires up to five consecutive illuminations of a target. As indicated in **Figure 1**, a multifunctional radar must simultaneously carry out additional tasks, in particular search for the new targets and track known targets. Since a shared aperture is used, the radar resource-manager schedules the radar timeline in time-multiplexing mode.

In the following, we simulate an airspace-surveillance radar rotating at 180°/s with electronic beam-steering.

5.2.1. Surveillance

The airspace is discretised depending on the beam width. Let $B_\varphi, B_\theta \in (0, 2\pi)$ be the azimuth and elevation opening angle respectively. The dwell time $\tau = 2\frac{r}{c}$ of an airspace section is

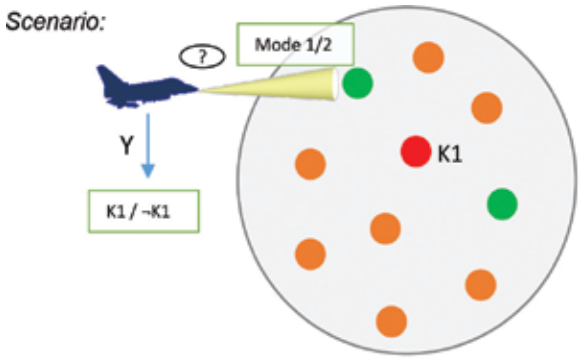

Confusion-matrix: $p(y|x = k, mode)$

Mode 1	K = 1	K = 2	K = 3
Y = K1	0.9	0.9	0.1
Y = ¬ K1	0.1	0.1	0.9

Mode 2	K = 1	K = 2	K = 3
Y = K1	0.75	0.15	0.1
Y = ¬ K1	0.25	0.85	0.9

Cost-matrix: $c(V|x = k)$

Kosten	K = 1	K = 2	K = 3
V = K1	0 (cc)	1 (fa)	1 (fa)
V = ¬ K1	2 (md)	0 (cc)	0 (cc)

Figure 10. Scenario, confusion- and cost matrix for the classification problem according to Ref. [40].

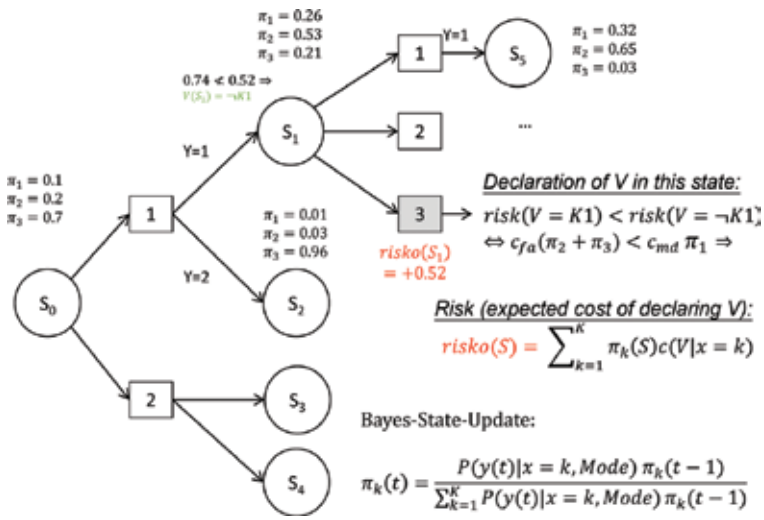

Figure 11. State-space, fusion, and selection of action (further measurement or final declaration V) to minimize the expected costs.

http://dx.doi.org/10.5772/intechopen.71365

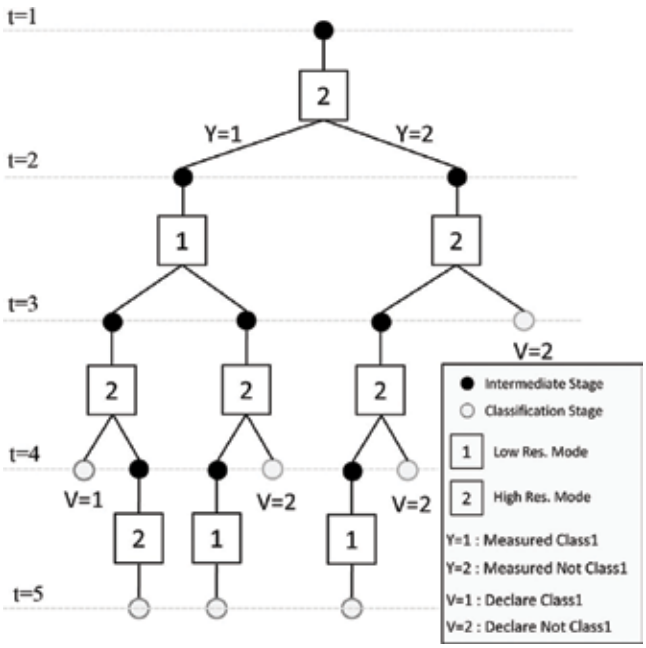

Figure 12. Optimal policy to the MDP.

chosen dependent on the range r of the target to guarantee that the whole range can be scanned within one transmit-receive process. Therefore the discretisation is only made in direction of azimuth and elevation. Since the transmit power decreases with increasing distance to the main lobe the borders are defined overlapping, i.e. a constant $d \in (0,1)$ is selected for the discretisation (typical values are $d = 0.5$ or $d = 0.75$). If the maximum observable range and altitude are limited by R and H respectively, the airspace to be observed can be written as

$$\mathscr{L} = \left\{ x \in \mathbb{R}^3 \middle| \|x\|_2 \leq R \wedge h^{\perp}(x) \leq H \right\}, \qquad R, H \in \mathbb{R}_+ \tag{26}$$

where the sensor is located in center of the coordinate system and $h^{\perp}(x)$ denotes the height of the target perpendicular to earth's surface. Then, after proper transformation the discretisation of $\mathscr{L}$ is given by

$$L_{ij} = \left(\frac{idB_\phi}{\cos\left(jdB_\theta\right)}, jdB_\theta \right) \in [0, 2\pi) \times \left[0, \frac{\pi}{2}\right]. \tag{27}$$

Here the factor $\cos(jdB_\theta)^{-1}$ compensates the circumstance that the same area (in steradians) engages a wider azimuth coverage on higher elevation than it does on lower elevation. When a surveillance task (see Section 5.2.3) is completed it is immediately regenerated with the desired revisit time to guarantee regular observation of the entire airspace.

5.2.2. Tracking

To be able to estimate the position of a target continuously in time all radar detections of a target T_i are put together into a track $\tilde{T}_i$. This is done by bringing them into physical relation using predefined dynamic models. A simple dynamic model assumes for example (statistically zero-mean) constant velocity which is variable through the (process-)noise in acceleration. To be able to determine which measurement belongs to which track the data association is done using scoring and global nearest neighbor approach (GNN) as it is described in Ref. [41]. In this case all unassociated detections generate a new track that applies as verified when the score exceeds a given threshold. In general a track is an estimation of the movement of the target, it contains information about the dynamic model, the covariance matrix P_i and an estimation $\hat{x}_i(t)$ of the real state $x_i(t) = (p_i(t), v_i(t), \ldots)^T$ consisting of position $p_i(t)$, velocity $v_i(t)$ and for example acceleration $a_i(t)$ at time t. All tracks generated by the radar yield an estimation of the airspace situation (see **Figure 13**).

A more complex dynamic model was introduced by Singer [42]. The state $x(t)$ at time t can then shortly be written as $x(t) = (p(t), v(t), a(t))^T = (p(t), \dot{p}(t), \ddot{p}(t))^T$. The acceleration in this model is given by an ordinary differential equation

$$\begin{aligned} & p(t) = -\alpha \ddot{p}(t) + w(t) \\ \Leftrightarrow \quad & \dot{a}(t) = -\alpha a(t) + w(t) \end{aligned} \tag{28}$$

where α is the reciprocal of the maneuver time constant and $w(t)$ is Gaussian white noise. From Eq. (28) a discrete form of the Singer model at the k-th time step can be derived

$$x_k = F_k x_{k-1} + w_k \tag{29}$$

with discrete white noise w_k and process matrix F_k of the following form

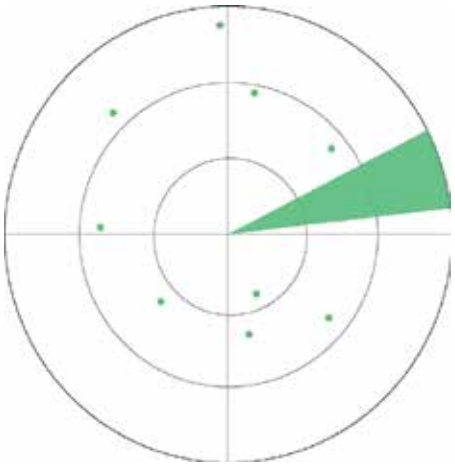

Figure 13. Airspace situation.

$$F_k = \begin{bmatrix} 1 & \Delta t & \frac{1}{\alpha^2}\left(-1 + \alpha\Delta t + e^{-\alpha\Delta t}\right) \\ 0 & 1 & \frac{1}{\alpha}\left(1 - e^{-\alpha\Delta t}\right) \\ 0 & 0 & e^{-\alpha\Delta t} \end{bmatrix} \tag{30}$$

where Δt denotes the time elapsed between time steps $k-1$ and k.

Recursive Bayesian estimators can be used to calculate the state x and the covariance matrix P (for a better readability the index i will be dropped from now on). One commonly used estimator is, for example, the (Extended) Kalman Filter (EKF) [41, 43]. In general the Kalman filter assumes a state transition model and an observation model

$$x_k = f(x_{k-1}) + w_k \tag{31}$$

$$z_k = h(x_k) + v_k \tag{32}$$

where z_k denotes the measurement, f and h are (not necessarily linear) functions, and w_k and v_k are additive, zero mean, white noises with process noise covariance Q_k and measurement noise covariance R_k respectively. In our case it is for example

$$h : \mathscr{L} \to [0, 2\pi)^2 \times \mathbb{R}, \begin{pmatrix} x \\ y \\ z \end{pmatrix} \mapsto \begin{pmatrix} \varphi \\ \theta \\ r \end{pmatrix} = \begin{pmatrix} \text{atan2}(y, x) \\ \arcsin\left(\frac{z}{r}\right) \\ \sqrt{x^2 + y^2 + z^2} \end{pmatrix} \tag{33}$$

the mapping between the state space $\mathscr{L}$ and the measurement in azimuth ϕ, elevation θ and range r. For the Singer model the state transition is a linear function with

$$f(x_{k-1}) = F_k x_{k-1}. \tag{34}$$

The EKF consists of two steps. First the state $x_{k\,|\,k-1}$ and the covariance $P_{k\,|\,k-1}$ are *predicted* using the previous information $x_{k-1\,|\,k-1}$ and $P_{k-1\,|\,k-1}$ (the index $k\,|\,k-1$ depicts the dependency of the estimates at time steps k and $k-1$):

$$\widehat{x}_{k|k-1} = f\left(x_{k-1|k-1}\right) \tag{35}$$

$$P_{k|k-1} = F_{k-1} P_{k-1|k-1} F_{k-1}^T + Q_{k-1} \tag{36}$$

In the general case the matrix F_{k-1} is defined by

$$F_{k-1} = \frac{\partial}{\partial x} f\left(\widehat{x}_{k-1|k-1}\right). \tag{37}$$

Second the prediction will be *corrected* using the (erroneous) measurement z_k:

$$\widehat{x}_{k|k} = \widehat{x}_{k|k-1} + K_k\left[z_k - h\left(\widehat{x}_{k|k-1}\right)\right] \tag{38}$$

$$P_{k|k} = [I - K_k H_k] P_{k|k-1} \tag{39}$$

with observation matrix

$$H_k = \frac{\partial}{\partial x} h\left(\hat{x}_{k|k-1}\right) \tag{40}$$

and Kalman gain

$$K_k = P_{k|k-1} {H_k}^T \left[H_k P_{k|k-1} {H_k}^T + R_k\right]^{-1}. \tag{41}$$

Process noise and measurement error accumulate over time until a new measurement is executed. This leads to a probability density of the track $\tilde{T}_i$ with state x_i.

The probability density is used to calculate the maximum time difference Δt that allows the track to stay in a predefined range relative accuracy:

$$\max \Delta t \tag{42}$$

subject to

$$\left\| \overline{P}^T P_i(t+\Delta t) \overline{P} \right\|_2 \leq \nu \sin\left(\min\left(B_\phi, B_\theta\right)\right) \left\| \tilde{p}_i(t) \right\|_2 \tag{43}$$

where $\overline{P}$ denotes a projection into the plane orthogonal to the beam direction and $\nu \in (0,1)$ is the track sharpness. The time difference Δt is added to the tracking task of the track T_i and it is updated at every measurement.

5.2.3. Scheduler

In the simulation presented here a task is generated for each L_{ij} and placed into a sorted waiting queue (see **Figure 14**). The scheduler executes those tasks, whose time stamp do not lie in the past, in the given order. If tasks are delayed, they will be prioritized following the hierarchy of the waiting queue. The tasks inside the waiting queue are sorted according to their time stamps **Figure 15**.

5.2.4. Performance metrics

In this section three metrics are introduced to validate the performance of the resource manager.

One key element is the tracking accuracy. For the validation the distance between the estimated position $\tilde{p}_i(t)$ and the real position $p_i(t)$ of a target is calculated. The track does not contain any information about to which target it is related to, since the radar system does not know the ground truth. Therefore the track with the closest approach to the target is chosen as reference. The track sharpness is given as % of the beam width:

$$d_{TS} : \mathbb{R} \to \mathbb{R}, t \mapsto \max_i \min_j \frac{\left\| p_i(t) - \tilde{p}_j(t) \right\|_2}{\sin(\psi) \left\| p_i(t) \right\|_2}, \qquad \psi = \min\left(B_\phi, B_\theta\right) \tag{44}$$

The metric d_{TS} does not take into account whether the number of tracks matches the number of targets. Therefore the number of tracked targets $\#\tilde{T}$ is compared to the number of actually existing targets $\#T$ by the following metric:

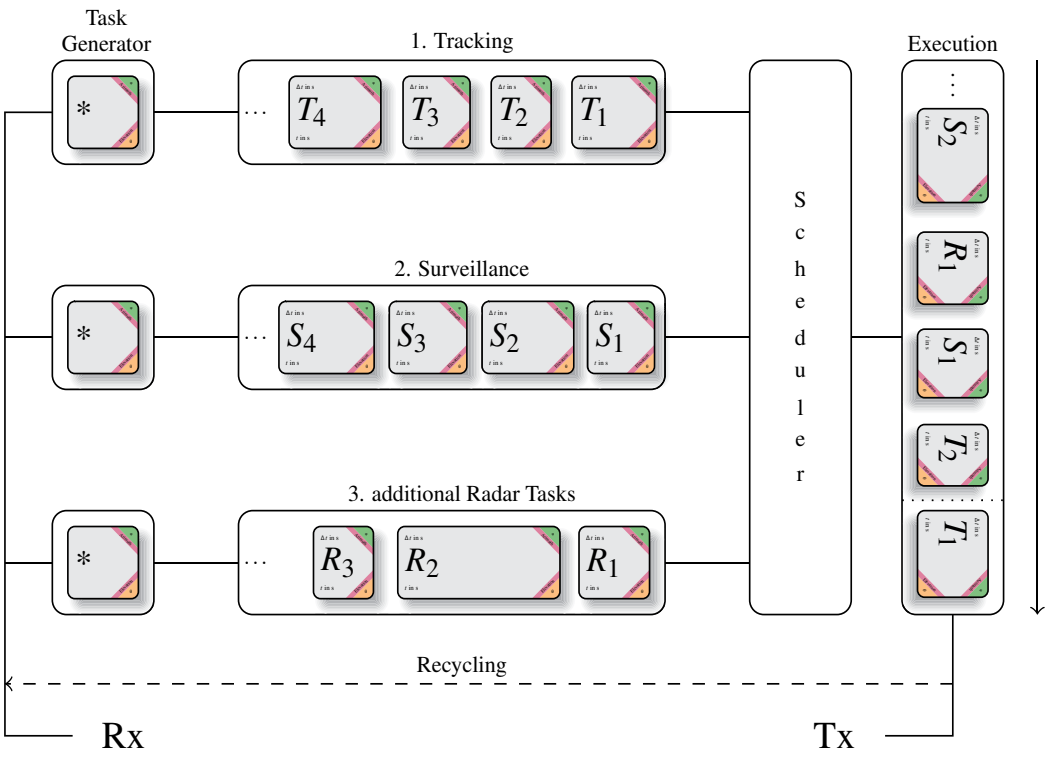

Figure 14. Schematic illustration of the scheduler.

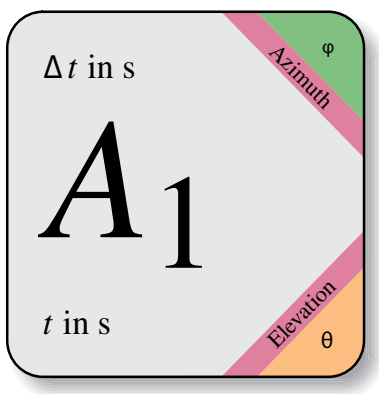

Figure 15. Detailed illustration of the task A_1. Containing a time stamp, the duration of the task, azimuth and elevation.

$$d_{\#} : \mathbb{R} \to \mathbb{R}, t \mapsto |\#T(t) - \#\tilde{T}(t)| \tag{45}$$

To evaluate the surveillance performance, the revisit time is considered. Let therefore be $t_{L_{ij}}$ the time of the last update of direction L_{ij} and let $\overline{L}(t)$ be the direction the radar is facing at time t. Then the metric is given by

$$d_{RT} : \mathbb{R} \to \mathbb{R}, t \mapsto |t - t_{\overline{L(t)}}|. \tag{46}$$

5.2.5. Results

In this section the validation results of the simulation are presented. The actual airspace situation is depicted in **Figure 13**. **Figures 16** and **17** show the evaluations of the metrics defined in Section 5.2.4.

The simulation starts with an occupied airspace. This can be a difficult situation for the radar since pop-up targets significantly decrease the reaction time as the distance to the radar is shortened.

Figure 16(a) shows that the revisit time for the surveillance settles around a constant value after 4 seconds. The stepped line in **Figure 16(b)** shows that all targets are tracked in less than 3 seconds. The second line in (b) shows that the tracking accuracy is poor at the beginning of the simulation since the filters need several measurements to initialize correctly. **Figure 17** shows that the revisit time oscillates around 4 seconds and that the tracks are stable during routine operation.

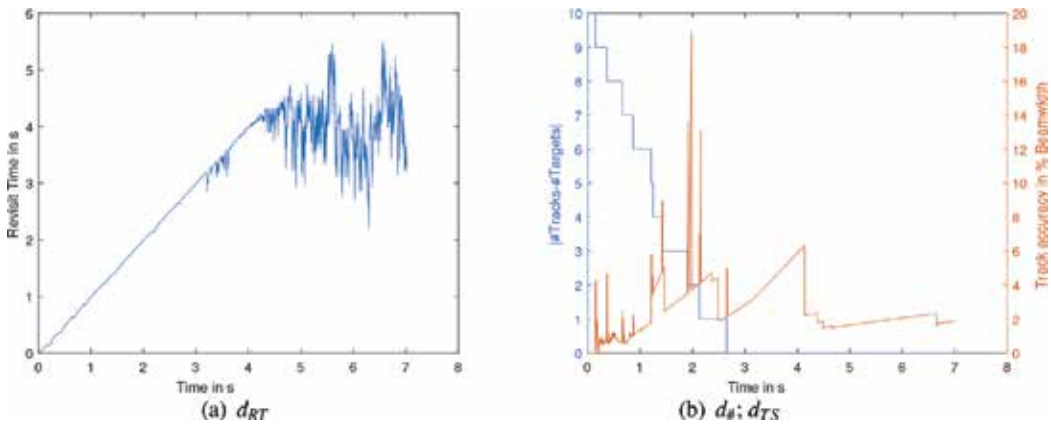

Figure 16. Results during initialization.

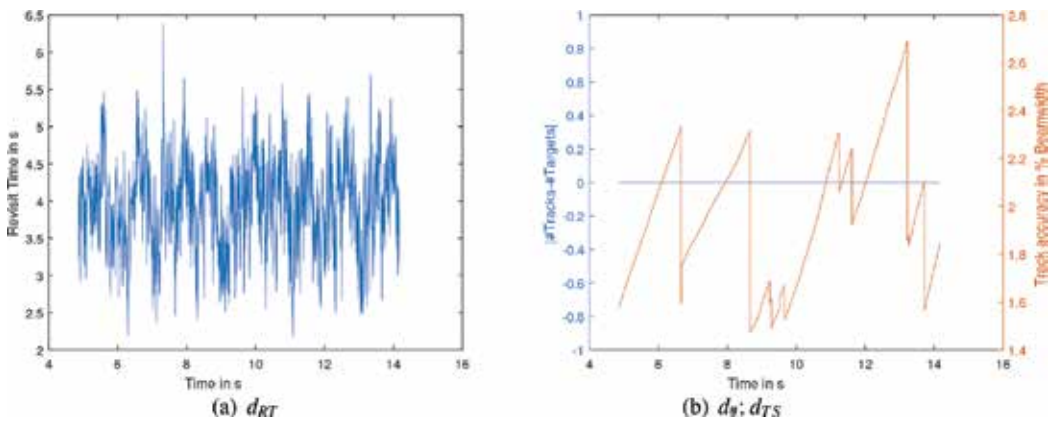

Figure 17. Results during routine operation.

http://dx.doi.org/10.5772/intechopen.71365

6. Knowledge-based-layer

In this section, we discuss knowledge-based behavior of a cognitive radar. As discussed in Section 3, the knowledge-based layer works on structured a-priori knowledge about the application domain and its goals and constraints. Automated planning or optimisation tools can be applied to generate mission-level commands that, for example, control the trajectory of the sensor-carrying platform.

Below, we discuss an illustrative trajectory planning problem for a 6-DOF robotic manipulator arm that carries a UWB sensor able to work in synthetic aperture radar (SAR) mode. Results from a real measurement setup using a ST Robotics R17 robot arm are also shown. The sensor has one transmitter and one receiver in a typical common-offset arrangement (**Figure 18**).

6.1. Robot trajectory planning

The spatial resolution and processing gain that the system can achieve ultimately depend on the trajectory and velocity profile of the sensor head. The constraints can be modeled as an optimisation problem to obtain a feasible, collision-free trajectory of the end-effector of the manipulator arm in Cartesian coordinates that minimizes observation time.

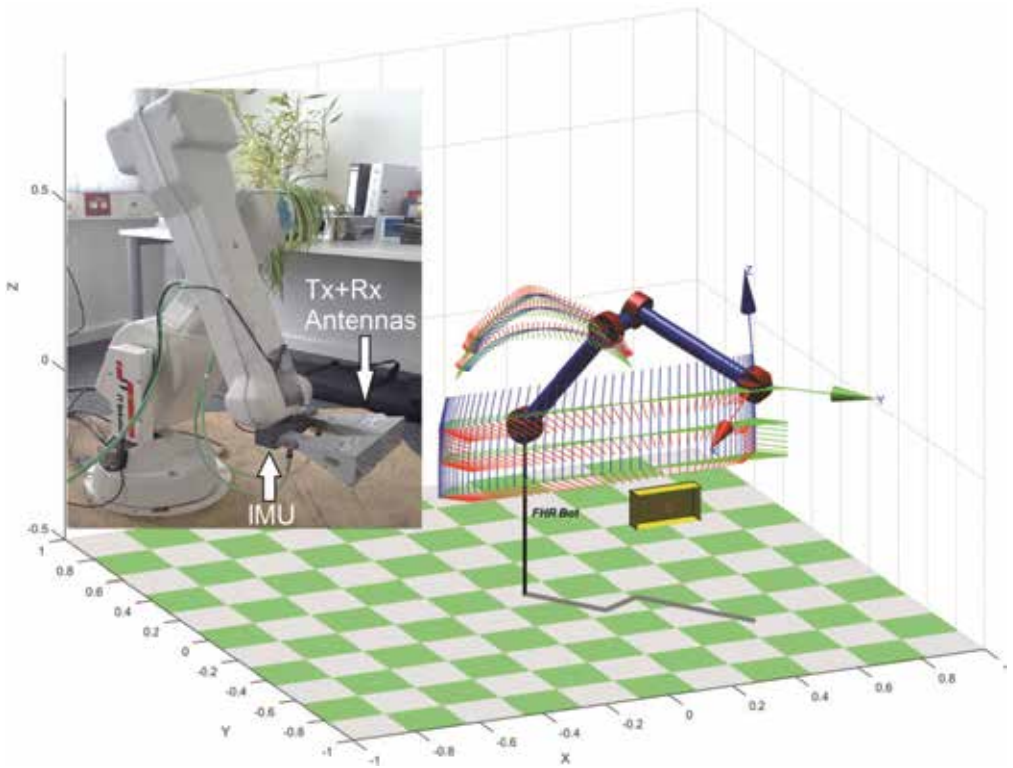

Figure 18. Trajectory planning for IED inspection with R17HS robot arm.

6.1.1. Sensor characteristics and trajectory constraints

The radar sensor under consideration uses a selectable center-frequency from 3 to 8 GHz and 4 GHz of bandwidth, resulting in 3.75 cm of range resolution. The center frequency can be tuned according to a particular target or propagation environment (ground penetration, through-the-wall imaging, IED inspection…). The horn-type antennas can be rotated to exploit polarization diversity. The sensor is able to operate in stripmap or spotlight SAR modes using linear trajectories. Several parallel trajectories can be combined for 3D imaging. The mobility of the arm could be further exploited to generate non-linear trajectories around a target to obtain a more accurate 3D reconstruction.

In order to obtain a similar resolution in cross-range than in range the trajectory planning must (aim to create at least an aperture of 0.5 to 1.3 times the distance to the target in both dimensions (azimuth and elevation) depending on the center frequency used by the system 3 to 8 GHz respectively).

High resolution imaging can only be achieved with an even higher precision positioning. The 3D-trajectory of the sensor needs to be measured and synchronized with the sensor data. For that purpose, accelerometers and gyroscopes from an attached inertial measurement unit (IMU) are used. The IMU drift is additionally stabilized using the hardware readout of optical encoders of the robot arm joints controlled by step-motors.

Two other important parameters to be considered for the trajectory planning are the optimal size of the scanning area and the sampling requirements. Considering the case of planar acquisition geometries working in stripmap mode, to obtain full resolution imaging of the total area of interest, an additional half beam aperture must be extended in both dimensions.

Another important parameter is related with the sampling requirements of a particular acquisition. The measurement positions in the synthetic radar aperture require a minimum spacing

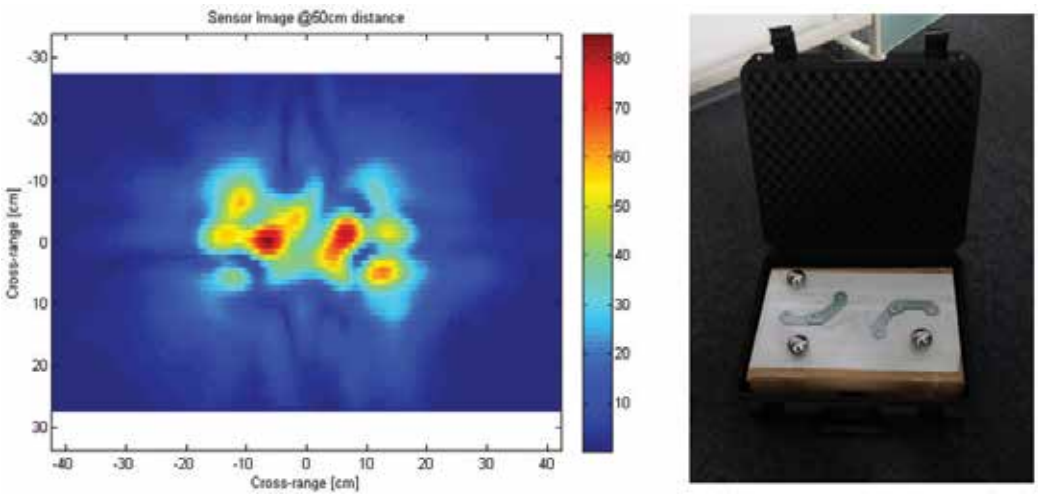

Figure 19. Image of objects inside a suitcase using the robot arm.

in order to sample adequately the phase history associated with all the scatterers. If the distance between measurements is too large the Nyquist criterion is not fulfilled and artifacts may appear in the reconstructed image.

It must be considered also that signal propagation in dielectric materials (ground, wall) will shrink the wavelengths, and sampling requirements become then even more stringent [44]. A previous estimation of the dielectric permittivity of the propagation media may further optimize the acquisition geometry and the imaging process. **Figure 19** shows an example of an image obtained with the robot arm using some reference objects inside a plastic suitcase. The trajectory followed by the sensor has been planned considering the constraints previously mentioned to obtain unaliased high-resolution images of the total area of interest.

7. Conclusions

In this article, a three-layered cognitive radar-architecture based on the Rasmussen model was presented. Several examples illustrated technologies to implement the cognitive subfunctions in a radar system.

For the skill-based layer, an approach for matching a waveform to the target transfer function was shown. In addition, spectrum sensing methods can be used to adapt the transmit signal to the electromagnetic environment. Rule-based behavior can be implemented using Markov-decision processes (MDPs) to compute optimal illumination policies. For a shared-aperture multifunctional radar, radar-resource management approaches are required to schedule the radar timeline. For knowledge-based behavior, an example for sensor-controlled trajectory generation of a robotic-arm were presented.

The different layers of the architecture encompass a broad range of time-scales and levels of abstraction. The full potential is achieved, if all layers interact consistently. This and further experimental validation of the approach are currently investigated at FHR.

Author details

Stefan Brüggenwirth*, Marcel Warnke, Christian Bräu, Simon Wagner, Tobias Müller, Pascal Marquardt and Fernando Rial

*Address all correspondence to: stefan.brueggenwirth@fhr.fraunhofer.de

Fraunhofer-Institut für Hochfrequenzphysik und Radartechnik FHR, Wachtberg, Deutschland

References

[1] Haykin S. Cognitive radar: A way of the future. Signal Processing Magazine. USA: IEEE. Jan. 2006;**23**(1):30-40

[2] Guerci JR. Cognitive Radar: The Knowledge-Aided Fully Adaptive Approach. Artech House, Incorporated, 2010. ISBN: 9781596933651

[3] Ender J, Brüggenwirth S. Cognitive radar-enabling techniques for next generation radar systems. In: 2015 16th International Radar Symposium (IRS). IEEE. 2015. pp. 3-12

[4] Rasmussen J. Skills, rules, and knowledge; signals, signs, and symbols, and other distinctions in human performance models. Systems, Man and Cybernetics, IEEE Transactions on SMC. May 1983;**13**(3):257-266

[5] Schulte A. Kognitive und kooperative Automation zur Führung unbemannter Luftfahrzeuge. Online Journal Kognitive Systeme. 2013;**1**

[6] Sheridan TB. Telerobotics, Automation, and Human Supervisory Control. Cambridge MA: MIT Press; 1992

[7] Wohler M, Schulte A. On board assistant system for UAS integration into civil airspace. In: AIAA Infotech@ Aerospace (I@ A) Conference. 2013. p. 5047

[8] Onken R, Schulte A. System-Ergonomic Design of Cognitive Automation. Heidelberg: Springer; 2010

[9] Putzer H, Onken R. COSA–A generic cognitive system architecture based on a cognitive model of human behavior. Cognition, Technology & Work. 2003;**5**(2):140-151

[10] Brüggenwirth S, Schulte A. COSA2 cognitive system architecture with centralized ontology and specific algorithms. In: 2012 International Conference on Systems, Man, and Cybernetics (IEEE SMC 2012). IEEE. 2012

[11] Gjessing DT. Environmental remote sensing, part 1: Methods based on scattering and diffraction of radio waves. Physics in Technology. 1979;**10**:266-271

[12] Bell MR. Information theory and radar waveform design. Proceedings. IEEE International Symposium on Information Theory. Jan 1993:428-428. DOI: 10.1109/ISIT.1993. 748744

[13] Schreier PJ, Scharf LL. Statistical Signal Processing of Complex-Valued Data: The Theory of Improper and Noncircular Signals. Cambridge: Cambridge University Press; 2010

[14] Wysocki T, Razavi H, Honary B. Digital Signal Processing for Communication Systems. New York: Springer US; 1997 9780792399322

[15] An Assessment of the Near Term Viability of Accommodating Wireless Broadband Systems in the 1675–1710 MHz, 1755, 1780 MHz, 3500–3650 MHz, and 4200–4220 MHz, 4380–4400 MHz Bands. Tech. rep. U.S. Department of Commerce; 2010

[16] Use of the Bands 5150–5250 MHz, 5250–5350 MHz and 5470–5725 MHz by the Mobile Service for the Implementation of Wireless Access Systems Including Radio Local Area Networks. Tech. rep. ITU-R Resolution 229; 2012

[17] Axell E, et al. Spectrum sensing for cognitive radio. IEEE Signal Processing Magazine. 2012;**29**(3):101-116

[18] Yucek T, Arslan H. A survey of spectrum sensing algorithms for cognitive radio applications. IEEE Communications Surveys & Tutorials. 2009;**11**(1):116-130

[19] Tandra R, Sahai A. SNR walls for signal detection. IEEE Journal of Selected Topics in Signal Processing. 2008;**2**(1):4-17. DOI: 10.1109/JSTSP.2007.914879

[20] Gardner W. Measurement of spectral correlation. IEEE Transactions on Acoustics, Speech, and Signal Processing. 1986;**34**(5):1111-1123

[21] Dandawate AV, Giannakis GB. Statistical tests for presence of cyclostationarity. IEEE Transactions on Signal Processing. 1994;**42**(9):2355-2369

[22] Zeng Y, Liang Y-c. Eigenvalue-based Spectrum sensing algorithms for cognitive radio. IEEE Transactions on Communications. 2009;**57**(6):1784-1793

[23] Stinco P, Greco MS, Gini F. Spectrum sensing and sharing for cognitive radars. IET Radar, Sonar & Navigation. 2016;**10**(3):595-602

[24] Kovarskiy JA, et al. Comparison of RF spectrum prediction methods for dynamic spectrum access. In: KI Ranney and A Doerry, ed. Proc. SPIE 10188. May 2017, p. 1018819. DOI: 10.1117/12.2262306

[25] Tian Z, Giannakis GB. A wavelet approach to wideband spectrum sensing for cognitive radios. In: 2006 1st International Conference on Cognitive Radio Oriented Wireless Networks and Communications. June 2006. pp. 1-5. DOI: 10.1109/CROWNCOM.2006.363459

[26] Martone A, et al. Passive sensing for adaptable radar bandwidth. In: 2015 IEEE Radar Conference (RadarCon). May 2015. pp. 0280-0285. DOI: 10.1109/RADAR.2015.7131010

[27] Kirk BH, et al. Cognitive software defined radar: Waveform design for clutter and interference suppression. In: Ranney KI, Doerry A, editors. SPIE Defense + Security. SPIE Proceedings. SPIE. 2017. p. 1018818

[28] Bengio Y. Learning deep architectures for AI. Foundations and Trends in Machine Learning. 2009;**2**(1):1-127. ISSN: 1935-8237. DOI: 10.1561/2200000006

[29] Haykin S. Neural Networks and Learning Machines. 3rd ed. Upper Saddle River, New Jersey: Pearson Education Inc.; 2009

[30] Zhao Q, et al. Synthetic aperture radar automatic target recognition with three strategies of learning and representation. Optical Engineering. 2000;**39**(5):1230-1244. DOI: 10.1117/1.602495

[31] leCun Y. Generalization and Network Design Strategies. Technical Report CRG-TR-89-4. Department of Computer Science. Toronto, Canada: University of Toronto; June 1989

[32] LeCun Y, et al. Gradient-based learning applied to document recognition. Proceedings of the IEEE. Nov. 1998;**86**(11):2278-2324. ISSN: 0018-9219. DOI: 10.1109/5.726791

[33] Schachter BJ. Target classification strategies. Proceedings of SPIE. 2015;**9476**:947602-947602. DOI: 10.1117/12.2176193

[34] Lauer F, Bloch G. Incorporating prior knowledge in support vector machines for classification: A review. Neurocomputing. 2008;**71**(7–9):1578-1594 ISSN: 0925-2312

[35] Diemunsch JR, Wissinger J. Moving and stationary target acquisition and recognition (MSTAR) model-based automatic target recognition: Search technology for a robust ATR. Proceedings of SPIE. 1998;**3370**:481-492. DOI: 10.1117/12.321851

[36] Wagner S, Barth K, Brüggenwirth S. A deep learning SAR ATR system using regularization and prioritized classes. In: 2017 IEEE Radar Conference (RadarConf). May 2017. pp. 0772-0777. DOI: 10.1109/RADAR.2017.7944307

[37] Vapnik VN. The Nature of Statistical Learning Theory. Second. Statistics for Engineering and Information Science. New York: Springer-Verlag; 2000

[38] Wagner SA. SAR ATR by a combination of convolutional neural network and support vector machines. IEEE Transactions on Aerospace and Electronic Systems. Dec. 2016;**52** (6):2861-2872. DOI: 10.1109/TAES.2016.160061

[39] Haykin S. Cognitive Dynamic Systems: Perception-Action Cycle, Radar and Radio. Cambridge: Cambridge University Press; 2012. 9780521114363

[40] Castanon DA. Approximate dynamic programming for sensor management. In: Decision and Control, 1997. Proceedings of the 36th IEEE Conference on. Vol. 2. IEEE. 1997. pp. 1202-1207

[41] Blackman S, Popoli R. Design and Analysis of Modern Tracking Systems. Norwood, MA: Artech House; 1999

[42] Singer RA. Estimating optimal tracking filter performance for manned maneuvering targets. IEEE Transactions on Aerospace and Electronic Systems. 1970;**4**:473-483

[43] Van Trees HL. Detection, Estimation, and Modulation Theory. New York, NY: John Wiley & Sons; 2004

[44] Grasmueck M, Weger R, Horstmeye H. Full resolution 3-D GPR imaging. Geophysics. 2005;**70**(1):12-19

Chapter 8

Representation of Radar Micro-Dopplers Using Customized Dictionaries

Shobha Sundar Ram

Additional information is available at the end of the chapter

http://dx.doi.org/10.5772/intechopen.71675

Abstract

Human motions give rise to frequency modulations, known as micro-Dopplers, to continuous wave radar signals. Micro-Doppler signals have been extensively researched for the classification of different types of human motions as well as to distinguish humans from other moving targets. However, there are two main scenarios where the performance of existing algorithms deteriorates significantly—one, when the channel consists of multiple moving targets resulting in distorted signatures, and two, when the systems conditions during the training stage deviate significantly from the conditions during the test stage. In this chapter, it is demonstrated that both of these limitations can be overcome by representing the radar data through customized dictionaries, fine-tuned to provide sparser representations of the data, than traditional data-independent dictionaries such as Fourier or wavelets. The performances of the algorithms are evaluated with both simulated and measured radar data gathered from moving humans in indoor line-of-sight conditions.

Keywords: micro-Doppler, dictionary learning, classification, detection

1. Introduction

Radar detection of humans has emerged as a topic of considerable research interest in the last two decades for varied applications such as security and law enforcement, through-wall surveillance, search and rescue operations, biomedical applications, and automobile radars. Two types of radars have been studied for these applications. The first type is the broadband impulse radars with high range resolution. These radars map the surroundings and moving targets (such as humans) are detected with the assistance of moving target detection algorithms [1, 2]. The second type of radars is the phase coherent continuous wave radars. These could be either broadband frequency-modulated continuous wave radars [3], such as those

used in automobile radar applications. Alternately, narrowband (single tone) radars have been used for through-wall surveillance applications [4]. The latter are cheap to build with off-the-shelf components. In this chapter, human detection and classification by a monostatic continuous wave Doppler radar that transmits a sinusoidal signal of carrier frequency f_c is discussed. The human body can be considered as an extended target with multiple point scatterers on different body parts. When the radar signal impinges on a non-rigid moving human body, the micro-motions of the arms, legs and torso introduce micro-Doppler shifts (f_D) on the scattered radar signal at the radar receiver. Each of these shifts is proportional to the carrier frequency and the radial relative velocity (v) between the body part and radar—$f_D = \frac{2vf_c}{c}$. Each of these body parts follows a unique trajectory giving rise to multiple micro-Doppler components that superpose. The scattered radar signal at the receiver is amplified and demodulated. There are several methods for representing the time-domain micro-Doppler returns, $x(t)$, of which, the most popular technique is to use joint time-frequency transforms such as the short-time Fourier transform (STFT) as shown below:

$$\chi(t,f) = \int x(\tau)h(t-\tau)\,e^{-j2\pi f\tau}\,d\tau \tag{1}$$

In the above equation, the short time window is given by $h(t)$. The STFT showcases the time-varying nature of the individual Doppler tracks from multiple body parts [5, 6]. For example, **Figure 1** shows the micro-Doppler signature of a human walking toward a monostatic continuous wave radar at 7.5 GHz. The micro-Dopplers are mostly positive since the human is moving towards the radar. Dopplers from the right and left arms and legs alternate with each other due to the swinging motion of the limbs.

The highest Dopplers arise from the feet followed by the arms and then the torso. The torso, though, gives rise to the strongest signal due to the high radar cross-section.

Different periodic motions—such as running, crawling, and boxing—each give rise to unique micro-Doppler spectrograms. Hence, these STFT-based signatures have been extensively studied for classification of different human activities as well as to differentiate humans from

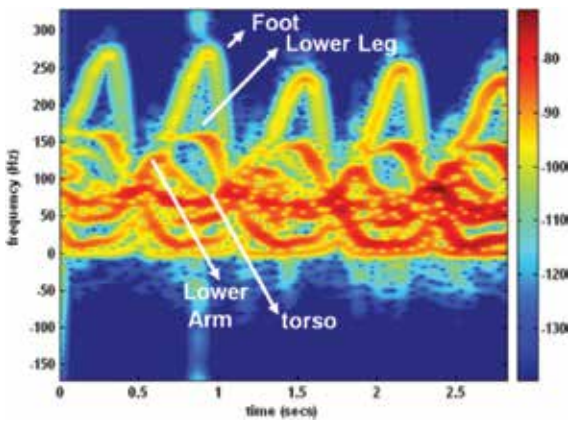

Figure 1. Spectrogram of walking human at 7.5 GHz.

other movers [7–23]. The main limitation of the STFT, however, is that the resolution along both the time and frequency domains are controlled by the choice of the dwell time or short time window used in the transform. Depending on the type of target, the dwell time parameters are often chosen heuristically, to realize the most informative signatures. Other representations include the use of signal processing techniques such as independent component analysis [24], Hilbert-Huang transforms [25, 26], etc. In all of these cases, the dictionaries or bases for representation of the radar data are independent of the data. While data-independent dictionaries are usually computationally simple to derive, they are not specifically fine-tuned to the underlying features of the data and are dependent on heuristic parameter selection. Hence, while they have had success in simple scenarios—such as target classification when the channel consists of only a single target or when the test and training conditions are identical—they are not suited for more complex realistic scenarios.

Over the last decade, dictionary learning has emerged under the aegis of machine learning. Here, customized dictionaries are derived directly from the data and hence are capable of abstracting the fundamental characteristics of the data. Dictionary learning has been used successfully in a variety of domains such as image processing and face recognition [27, 28] and energy disaggregation [29]. Due to the abstraction of the data bases, the hypothesis is that they will be useful for addressing detection and classification challenges under more complex scenarios. This chapter specifically addresses two such scenarios discussed in [30, 31].

In the first scenario in [30], the problem when the propagation channel consists of multiple simultaneously moving targets is considered. Whether the radar is deployed in indoor or outdoor environments, the presence of multiple simultaneous movers is highly likely. For instance, in indoor environments, multiple human movers are encountered along with dynamic clutter from moving fans, loud speakers, etc. Similarly, in outdoor environments, moving vehicles and animals along with pedestrians are encountered. When multiple targets move simultaneously in the propagation channel, their radar scattered returns superpose giving rise to distorted spectrograms. Therefore, the radar returns from these targets must be disaggregated before they can be fed into classifiers. In other words, the research problem focuses on *single channel source separation* or *multiple target detection* rather than *single target classification*. Specifically, unique dictionaries are learned directly from the raw time domain radar data from each of the single target categories. This means that no type of parameter selection operation is carried out. Then, these unique dictionaries are used to detect the presence of multiple targets in test data.

Next in [31], the scenario when the training and test conditions of radar data measurement deviate considerably is considered. Usually training data are gathered in tightly controlled laboratory conditions. But the test data are gathered in real world scenarios where the radar system deployment may encounter some challenges. For instance, presence of wireless interference sources or dispersion in the propagation channel (say through-wall scenario) may render some change in the carrier frequency inevitable. In such instances, a degree of reconfigurability in the radar hardware parameters and flexibility in the radar software is desirable. While the hardware reconfigurability can be realized by implementing the radar on software defined radio platforms, the flexibility in the software can only be realized if the processing

algorithms can handle diversity in the training and test data. When data-driven dictionaries are derived from diverse radar data, collected across multiple carrier frequencies, the algorithms derive fundamental characteristics of the data that are common to specific motions across different carrier frequencies. In this manner, they are capable of recognizing that specific motion category even when the radar data are gathered at a new carrier frequency that is distinct from those used previously while training.

The chapter is organized as follows. Section 2 details the analytical framework for learning dictionaries from raw time domain data along with description of how these dictionaries can be utilized for both single channel source separation (or disaggregation) and for classification (when training and test data are gathered in different conditions). Sections 3 and 4 provide the experimental validation and results for both of these scenarios. Section 5 concludes with a discussion on the advantages and limitations of the dictionary learning algorithm in the context of radar.

2. Theory

Throughout the chapter, vectors are indicated with small bold letters, matrices with capital bold letters, and constants or variables with small letters. In this section, the concept of representing time-domain micro-Doppler data with uniquely customized dictionaries is introduced. These dictionaries are learnt from training data. In this chapter, we discuss the synthesis learning dictionary framework which is based on the idea that radar data, $\boldsymbol{x}$, can be synthesized with unique data dependent bases functions, $\boldsymbol{D}$, and their corresponding coefficients, $\boldsymbol{z}$. In other words, $\boldsymbol{x} = \boldsymbol{D}\boldsymbol{z}$. An alternate framework that has also been investigated is called the analysis dictionary learning framework. Here, the data is analyzed by dictionaries to create sparse coefficient representations. This can be shown as $\boldsymbol{D}\boldsymbol{x} = \boldsymbol{z}$. The analysis dictionary framework is quicker to execute than the synthesis dictionary learning in the test stages, since it involves a multiplicative operation rather than matrix inversion. Interested readers may refer to [32] for further details on the analysis dictionary learning framework and its experimental validation.

2.1. Dictionary learning

Consider the case of I targets. Each target is assumed to be moving in isolation in the propagation environment. The radar data from the target, i, is represented as a vector $\boldsymbol{x}_i$ which consist of N samples. The training data corresponding to target i consist of M such measurements and hence $\boldsymbol{X}_i \epsilon [N \times M]$. The objective is to represent $\boldsymbol{X}_i$ as shown in Eq. (2):

$$\boldsymbol{X}_i = \boldsymbol{D}_i \boldsymbol{Z}_i \tag{2}$$

Here, $\boldsymbol{D}_i \epsilon [N \times P]$ and $\boldsymbol{Z}_i \epsilon [P \times M]$ are the dictionary and coefficient matrices corresponding to the target i. The distinction of this dictionary learning process from other data-independent transforms such as Fourier or DCT is that $\boldsymbol{Z}_i$ must be a row-wise sparse coefficient matrix with a sparsity value of τ. Therefore, the objective of the dictionary learning algorithm is given as Eq. (3)

$$min_{D_i Z_i} \left\| X_i - D_i Z_i \right\|_F^2 s.t \left\| Z_i \right\|_0 < \tau \tag{3}$$

It is well known that the l_0—minimization problem stated above is NP-hard [33]. There are therefore, two approaches for solving Eq. (2). One is to implement the l_0—minimization using computationally expensive greedy techniques. Alternately, the l_0—minimization can be reduced to a l_1—minimization technique as shown in Eq. (4)

$$min_{D_i Z_i} \left\| X_i - D_i Z_i \right\|_F^2 + \lambda \left\| Z_i \right\|_1 \tag{4}$$

Here, λ is the regularization parameter that trades off between the representational accuracy and the sparsity in the l_1—minimization operation. An iterative alternative minimization approach is used to solve Eq. (4). First, D_i is initialized using random columns selected from the training data X_i. Then Z_i is determined using Eq. (5) by implementing the iterative soft thresholding algorithm (ISTA) discussed in [34]

$$min_{Z_i} \left\| X_i - D_i Z_i \right\|_F^2 + \lambda \left\| Z_i \right\|_1 \tag{5}$$

Once Z_i is determined, D_i is estimated using the simple least squares minimization shown in Eq. (6). Each of the P columns of the dictionary has to be normalized to less than unity in order to prevent scale ambiguities

$$min_{D_i} \left\| X_i - D_i Z_i \right\|_F^2 \; s.t \; \left\| d_p \right\|_2^2 \leq 1 \tag{6}$$

Equations (5) and (6) are iterated until the representation error falls below a pre-defined threshold or when it converges. The process is repeated to learn unique dictionaries for every target. Then, all the dictionaries are concatenated to form an aggregate over-complete dictionary $D = [D_1 \; D_2 \; \cdots \; D_I]$. The aggregate dictionary, $D \in [N \times IP]$, is used for both single channel source separation and for classification of test micro-Dopplers. Both of these are discussed in the succeeding sections.

The dictionaries of multiple targets are learned individually in Eq. (4). An alternate mechanism would be to learn the multiple dictionaries together as suggested by [35]. Here, besides the sparsity penalty in Eq. (3), an additional penalty is introduced to increase the discrimination across multiple target categories. This step increases the computational complexity during the training stages. But since there was no discernible improvement in the performance of the disaggregation and classification algorithms, this scheme is not discussed in this chapter.

2.2. Single channel source separation of multiple radar micro-Dopplers

Now each single test measurement—a vector consisting of N samples, $\tilde{x} \in [N \times 1]$ is considered. In the test scenario, there may be single or multiple targets moving simultaneously in the propagation channel. Therefore, the test signal may be the aggregate of time-domain micro-Dopplers from multiple targets. Using the aggregate dictionary, the test coefficient vector $\tilde{z}_{1:I} \in [IP \times 1]$ is derived using Eq. (7)

$$min_{\tilde{z}_{1:I}} \left\| \boldsymbol{x}_i - \boldsymbol{D}\ \tilde{\boldsymbol{z}}_{1:I} \right\|_{\mathrm{F}}^2 + \lambda_1\ \tilde{\boldsymbol{z}}_{1:I} \tag{7}$$

Note that the test coefficient vector, $\tilde{z}_{1:I}$, is distinct from the columns of the coefficient matrix, $\boldsymbol{Z}_i$, derived earlier from Eq. (5). In $\tilde{z}_{1:I}$, the coefficients ($\tilde{z}_i$) corresponding to *each* of the I categories of targets are obtained at once as opposed to Eq. (5), where the coefficients corresponding to just the training target category are realized. If one or more targets are present, then the hypothesis is that their corresponding coefficients ($\tilde{z}_i \in [P \times 1]$) extracted from the composite test coefficient vector ($\tilde{z}_{1:I}$) will be non-sparse, while the coefficients belonging to the absent targets will be close to zeros. The intuition here is that if the dictionaries are sufficiently discriminative, then they will be able to extract the corresponding target coefficients even when the radar data consists of superposition of returns from multiple targets. Therefore, a target i is determined to be present if the corresponding $\boldsymbol{D}_i \tilde{z}_i$ is above a predefined threshold.

2.3. Classification of radar micro-Dopplers

In the previous section, single channel source separation of test data that comprises of radar returns from multiple targets was discussed. Now, the focus is on classification of radar data from an unknown test target category. It is important to note that while the previous problem focused on *multiple target detection*, the problem in this section focuses on *single target classification*. In both cases, the aggregate dictionary matrix, $\boldsymbol{D}$, obtained from concatenation of the individual dictionaries learned from each of the target categories is utilized. For classification purposes, the training features for each target i are derived from the coefficient vector, $\ddot{\boldsymbol{Z}}^i_{1:I}$, obtained using the training data, $\boldsymbol{X}_i$, and the aggregate dictionary using Eq. (8)

$$min_{\ddot{\boldsymbol{Z}}^i_{1:I}} \left\| \boldsymbol{X}_i - \boldsymbol{D}\, \ddot{\boldsymbol{Z}}^i_{1:I} \right\|_{\mathrm{F}}^2 + \lambda_2\, \ddot{\boldsymbol{Z}}^i_{1:I} \tag{8}$$

Though the training data matrix is identical, the training feature, $\ddot{\boldsymbol{Z}}^i_{1:I}$, is distinct from the previously derived $\boldsymbol{Z}_i$ from Eq. (5) since $\ddot{\boldsymbol{Z}}^i_{1:I}$ is a composite matrix derived from the aggregate $\boldsymbol{D}$ rather than an individual dictionary $\boldsymbol{D}_i$. The the training feature shows the sparsity pattern corresponding to an i^{th} target *within the cluster of coefficients from multiple targets*. Any well-established classifier, such as support vector machine or K-Nearest neighbor, etc., can now be trained with multiple columns of the training feature matrix. Each of the columns of $\ddot{\boldsymbol{Z}}^i_{1:I}$ is treated as a single training instance for the i^{th} target and the classifier is similarly trained for all the target classes.

During the test stage, test features, $\ddot{z}_{1:I}$, are extracted from each test measurement, $\ddot{x}_i$ (from a single target category) using Eq. (9)

$$min_{\ddot{z}_{1:I}} \left\| \ddot{\boldsymbol{x}}_i - \boldsymbol{D}\, \ddot{\boldsymbol{z}}_{1:I} \right\|_{\mathrm{F}}^2 + \lambda_2\, \ddot{\boldsymbol{z}}_{1:I} \tag{9}$$

The test data are subsequently classified based on the similarity between $\ddot{z}_{1:I}$ and the columns of $\ddot{\boldsymbol{Z}}^i_{1:I}$ across all the I target categories. In this chapter, the support vector machine classifier is used. The data were tested on other popular classifiers such as KNN but did not result in any significant difference in the results.

http://dx.doi.org/10.5772/intechopen.71675

3. Experimental data collection

The proposed dictionary learning methods are validated on experimental radar data gathered from moving humans. Both simulated radar data and measured data are considered. Both types of data offer some advantages and some limitations. The simulated radar data offer an opportunity to test the performance of the algorithms quickly and under a variety of radar operating conditions. In other words, the simulations offer a flexible mechanism to change radar parameters. The data are also highly sanitized due to the absence of noise and limitations of radar hardware. The measurement data collection is limited by radar system parameters such as the dynamic range of the radar receiver, the carrier frequency, sampling frequency, and antenna characteristics. On the other hand, current state-of-the-art simulation methodologies for human radar data do not capture the entire physics of the human scattering phenomena. The measurement data, therefore, are crucial for validating the proposed algorithms in real world scenarios. The second important limitation of the simulation data (unlike the measurement data) is that with the current techniques, the channel can consist of only a single target. Therefore, the simulation data are only used for the single target classification problem and not for the multiple target detection or disaggregation problem.

In the following two subsections, both the simulation and measurement methodologies are detailed.

3.1. Simulation data

Simulation of radar scatterings of *still* humans has been investigated with full wave electromagnetic techniques as well as the computationally cheaper ray tracing technique at frequencies below X band [36]. The results from the simulations of a uniformly dielectric human body showed that the ray tracing results were comparable to the results from full wave methods. However, both of these methods are computationally not feasible for simulating radar returns from *dynamic* humans since this requires modeling of multiple human poses. Alternately, the simple primitive-based modeling has proven to be reasonably accurate for modeling human motions [37, 38]. Here, the different body parts on the human are modeled as simple primitives such as the head as a sphere, the torso as a cylinder or ellipsoid, and so forth. The radar cross-sections of these simple shapes (σ_b) are well characterized for different carrier frequencies (f_c) and aspect angles. One or more point scatterers ($\vec{r}_b$) are identified for each body part. When the human moves, the time-varying positions of the point scatterers give rise to micro-Dopplers. Then, the radar returns of the human are obtained by the complex sum of the returns from each of the body parts as shown in Eq. (10)

$$x = \sum_{b=1}^{B} \sqrt{\sigma_b}\, \frac{1}{r_b^2}\, e^{-j\frac{2\pi f_c}{c} 2r_b(t)} \tag{10}$$

This simplistic model is easy to execute in real time. However, it does not capture the entire physics of the human scatterings. For instance, it does not capture the multiple scatterings of waves between the different body parts or their shadowing effects.

There are three methods that are currently used to describe human motions. The simplest method is to model the swinging motion of the two legs as a double pendulum. A more complete analytical model, known as the Boulic-Thalmann model, was proposed in [37]. This model provides analytical equations to describe different human body parts (arms, legs, hands, and feet) as a function of the human height and relative velocity with respect to height. However, the model is restricted only to a simple human walking motion. More complex and realistic motions, such as crawling, hopping, and running, can be obtained using computer animation data. The radar scattered returns from complex human motions can be therefore obtained by combining animation data with the primitive-based electromagnetic modeling [38]. However, the animation data are obtained through motion capture technologies of a live actor. Therefore, the model cannot be parameterized to obtain varied data for different humans (of different heights or gait patterns) through a single measurement.

In this study, the Thalmann model was used to model human walking motions for multiple human heights (1.5–1.8 m) and velocities (1.5–3.6 m/s). Due to the limitations of the model, a variety of human motions could not be simulated. Instead, just two types of motions were considered—when a human is walking towards the radar and when the human is walking away from the radar. The human moves in the line-of-sight of a monostatic continuous wave radar anywhere from a distance of 2–8 m. The duration of the human motion is 1 s and the sampling frequency of the simulation is 1 kHz. We imparted frequency diversity to the simulation data by varying the carrier frequency across five values—{2.5, 3, 3.5, 4, and 4.5 GHz}. Three hundred and sixty distinct walking motions are simulated both toward and away from radar at each of the carriers. Of these, 80% of the 1800 total simulations—corresponding to four of the five carrier frequencies—were used for training the classification algorithm; and the remaining 20%—from the fifth remaining carrier frequency—were used for testing purposes. The objective here is to test the capability of the dictionary learning algorithm to learn fundamental features from the human micro-Doppler data pertaining to a specific motion despite the variations of the carrier frequency. The dictionaries are learned directly from the raw data without any additional post processing. Therefore, at no stage were any parameters heuristically chosen.

A third category of indoor mover may give rise to significant dynamic clutter—a fan. Hence, a fan was modeled with three blades and multiple point scatterers on each blade. A lot of variety in the experimental data from the fan was generated by changing its speed of rotation (200–400 rpm), the length of the blades (0.2–0.4 m), width of the blades (0.14–0.17 m) and the orientation of the fan with respect to the monostatic radar. The fan micro-Dopplers at five carrier frequencies (1800 distinct simulations) were simulated of which data from four carriers were used for training and the data from the fifth carrier for testing purposes. The results and analyses for dictionary-based classification of simulated human radar data are presented in the following section.

3.2. Measurement data

Next, experimental data were collected in indoor line-of-sight conditions. A monostatic continuous wave radar was set up using a N9926A FieldFox vector network analyzer (VNA) and

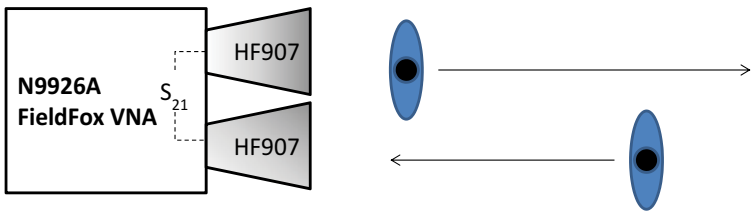

Figure 2. Measurement data collection in indoor line-of-sight conditions using a VNA and two horn antennas.

two linearly polarized broad band horn antennas (HF907). The VNA was configured to make narrowband measurements around a center carrier frequency (**Figure 2**).

The transmitted power of the VNA was set at +3 dBm. The instrument is highly sensitive with a dynamic range of over 100 dB. The received signal is amplified, in-phase quadrature (IQ) demodulated and digitized inside the instrument and then directly processed in a 2.4GHz Intel Pentium processor. Two sets of experiments were carried out.

The first experiment was carried out to validate the multiple target detection algorithm based on dictionary learning. The center frequency of the VNA was set to 7.5 GHz. Then, human radar data were collected for two types of motions—when a human is walking towards the radar (FH) and when a human is walking away from the radar (BH). Each measurement trace is 2.7 s long with 1000 samples. The low sampling frequency is due to the system constraints of the VNA when it is configured in the narrowband mode. Measurement data were gathered for 40 humans of both genders and of varying heights and gait patterns. The humans move between 1 and 9 m away from the radar in line-of-sight conditions. The third motion class that was considered was of a table fan (TF) with three blades. The table fan was operated at three different rotation rates and was placed at different distances and orientations from the radar. Then, measurement data were gathered with multiple targets moving simultaneously. The cases are: FH + BH, FH + TF, BH + TF, and FH + BH + TF. The objective is to learn dictionaries using training data in the single-target scenario. Then these dictionaries are combined and used to detect targets in multiple target scenarios.

The next experiment that was conducted was again based on the same set up. However, this time only single-target scenarios were considered. Instead, the carrier frequency of the measurement data was varied across five values—{2.5, 3, 3.5, 4, and 4.5} GHz. A variety of human motions were considered—two humans walking simultaneously before the radar (TH), human standing still but boxing with his arms (HB) and a human walking while holding a stick (HHS). The last case that was considered was of the rotating table fan (TF). The challenge in this experiment is to learn dictionaries and training features from measurement data corresponding to four carrier frequencies, while testing the classifier with data from a fifth distinct carrier frequency. This experiment was specifically chosen since the human micro-Doppler shows a lot of variations due to the carrier frequency and the Dopplers are directly proportional to the frequency. The table fan was selected for both types of experiments, since it is one of the key contributors of dynamic clutter in indoor environment.

4. Results and analysis

In this section, the results of using the customized micro-Doppler dictionaries of the different types of motions for both multiple target detection as well as single target classification are discussed.

4.1. Results from multiple target detection using disaggregation of radar data

First, the measured data that are gathered for multiple target detection are considered. As mentioned in Section 3.2, three target classes—human walking toward the radar (FH), away from the radar (BH), and table fan (TF) are considered. The dictionaries are learned from single target data and use them to detect the presence of multiple simultaneous movers in three scenarios—single-target scenario, two-target scenario, and three-target scenario. The true detection and false alarm percentage for each of these cases is summarized in **Table 1**. The results show that for a single-target scenario, the true detection is very high (above 93%) in all the three cases. The true detection of the fan is slightly poorer than that of the humans because of greater probability of aliasing arising with the fan micro-Dopplers due to the limited sampling frequency of the radar measurements. This also gives rise to the slightly higher false alarm rate of the fan when compared to the humans. Next, three two-target scenarios are considered. In each of the scenarios, the algorithm correctly detects the presence of two targets in more than 80% of the cases by disaggregating their micro-Dopplers. The false alarm rate though is high especially from the table fan due to the aliasing. In the three-target scenario, the algorithm correctly detects the presence of all three targets in more than 90% of the cases. This sort of multiple target detection cannot be carried out using basic data independent transforms and this result demonstrates the usefulness of representing micro-Dopplers with unique data-dependent dictionaries.

Scenarios	**True detections**			**False alarms**		
	FH	**BH**	**TF**	**FH**	**BH**	**TF**
Single target (FH)	100	NA	NA	NA	4	14
Single target (BH)	NA	100	NA	12	NA	8
Single target (TF)	NA	NA	94	2	0	NA
Two targets (FH + BH)	87.5	80	NA	NA	NA	52.5
Two targets (FH + TF)	88	NA	94	NA	12	NA
Two targets (BH + TF)	NA	94	96	28	NA	NA
Three targets (FH + BH + TF)	95	90	90	NA	NA	NA
Mean	94			11		

Table 1. Disaggregation and detection results from measured human micro-Dopplers in multiple target scenario at 7.5 GHz from [29].

4.2. Results of single target classification using frequency diverse radar micro-Dopplers

Now the objective is to correctly classify that target class when the propagation channel consists of only one type of target class. The challenge here is to classify test data where system conditions (carrier frequency) during test deviate significantly from the training conditions. Therefore, during the training stage, the dictionaries for each target class are learned from diverse frequency data (from four carrier frequencies) and the test data consists of micro-Dopplers from a fifth carrier frequency that was previously not used for training.

The following five carrier frequencies—{2.5, 3, 3.5, 4, and 4.5} GHz are considered. In fold 1 through fold 5, the test frequencies are 2.5, 3,…,4.5 GHz, respectively, and the training data for each fold are obtained from the corresponding complimentary set from the total set of carrier frequencies. The performance of the algorithm for both simulation and measurement data are studied. In the simulation set up, three target classes are considered—a human walking towards the radar (FH), a human walking away from the radar (BH), and a fan (TF). The classification results obtained from the fivefold classification are presented in **Table 2**. The results show very high classification accuracy (close to 100%) for all the cases. This shows that the algorithm is capable of learning unique dictionaries corresponding to each human motion from frequency diverse training data. Again, this type of classification would not be possible with other data-independent transforms which rely on heuristic parameter selection.

The simulation data are highly sanitized, since they are not affected by real world conditions such as noise, interference, and radar system limitations. Therefore, in the next study, the performance of the algorithm on real world data is studied. Four types of motions—two humans walking simultaneously in the propagation channel (forming a single class of motion—TH), a single human standing still and boxing his arms (HB), a human walking with a stick (HHS), and a table fan are considered. Five-fold classification is performed on the target data and the results are presented in the following two tables. **Table 3** shows the confusion matrix obtained for a single fold (fold 4). The column headers show the class labels that the classification algorithm assigns to the test data. The true class labels are shown as row headers. The results show that TH, HB, and TF are classified with 100% accuracy, while the HHS is confused with TH and HB. There are two reasons for this confusion. When two humans are walking together,

Cases	Fold 1	Fold 2	Fold 3	Fold 4	Fold 5	Mean
Human walking away from radar	100	100	100	100	100	100
Human walking towards radar	100	100	100	100	100	100
Ceiling Fan	100	98	100	100	97	99

Data from four carriers are used for training while data from the fifth carrier are used for testing.

Table 2. Fivefold cross-validation of classification based on dictionary learning of simulated human micro-Dopplers at {2.5, 3, 3.5, 4.0, 4.5} GHz from [30].

Cases	TH	HB	HHS	TF
Two humans (TH)	100	0	0	0
Human boxing (HB)	0	100	0	0
Human holding stick (HHS)	15	10	75	0
Table fan (TF)	0	0	0	100

The classifier was trained using measured data at {2.5, 3, 3.5, and 5} GHz from [30].

Table 3. Confusion matrix obtained while classifying human measured micro-Dopplers at 4 GHz.

Cases	Fold 1	Fold 2	Fold 3	Fold 4	Fold 5	Average
TH	95	100	75	85	80	87
HB	85	100	85	100	100	94
HHS	85	75	85	80	100	85
TF	90	100	90	85	90	91

Data from four carriers are used for training while data from the fifth carrier are used for testing.

Table 4. Fivefold cross-validation of classification based on dictionary learning of measured human micro-Dopplers at {2.5, 3, 3.5, 4.0, 4.5} GHz from [30].

there are times when the scattered signal from one human may be weaker than the other human (due to shadowing or due to different distances of the two humans from the radar). As a result, there are similarities at times between TH and HHS. Second, when the human is boxing, the micro-Dopplers occur at both positive and negative frequencies due to motions of the arms toward and away from the radar. This can be confused with the HHS, especially from the back swing of the legs, stick, and arms. The micro-Dopplers of both these motions could resemble each other especially across different carrier frequencies.

Table 4 shows the classification results across all the fivefolds. The results show a fairly good classification performance (above 85%) for all of the cases. The confusion of the table fan with the human motions can again be attributed to the limited sampling frequency of the measurement data.

5. Conclusion

In conclusion, the usefulness of representing human micro-Dopplers with unique data dependent dictionaries is investigated. These dictionaries are applied subsequently to two applications. The first application is for detecting multiple simultaneously moving targets in the propagation channel. Results demonstrated that weak targets are detected in the presence of stronger targets and strong targets are correctly identified even when their signatures are distorted by returns from the weaker targets. The second application that was discussed was classification when there is significant variation between the training and test conditions. Specifically,

the carrier frequency—the fundamental parameter that controls the resolution, extent, and quality of micro-Doppler data—was varied. The algorithm learned dictionaries from diverse training data and was capable of correctly classifying completely different test data. While the dictionary learning techniques were examined in the context of micro-Doppler data, the encouraging results suggest that these techniques may be successfully extended to other radar scenarios especially the range-Doppler images of ISAR.

Author details

Shobha Sundar Ram

Address all correspondence to: shobha.sundarram@gmail.com

Indraprastha Institute of Information Technology, Delhi, India

References

[1] Nag S, Barnes MA, Payment T, Holladay G. Ultrawideband through-wall radar for detecting the motion of people in real time. In: AeroSense 2002. International Society for Optics and Photonics; 2002. pp. 48-57

[2] Yarovoy A, Ligthart L, Matuzas J, Levitas B. UWB radar for human being detection. IEEE Aerospace and Electronic Systems Magazine. 2006;**21**(3):10-14

[3] Maaref N, Millot P, Pichot C, Picon O. A study of UWB FM-CW radar for the detection of human beings in motion inside a building. IEEE Transactions on Geoscience and Remote Sensing. 2009;**47**(5):1297-1300

[4] Ram SS, Li Y, Lin A, Ling H. Doppler-based detection and tracking of humans in indoor environments. Journal of The Franklin Institute. 2008;**345**(6):679-699

[5] Ram SS, Ling H. Through-wall tracking of human movers using joint Doppler and array processing. IEEE Geoscience and Remote Sensing Letters. 2008;**5**(3):537-541

[6] Chen VC, Li F, Ho S-S, Wechsler H. Analysis of micro-Doppler signatures. IEEE Proceedings - Radar, Sonar and Navigation. 2003;**150**(4):271-276

[7] Chen VC, Li F, Ho SS, Wechsler H. Micro-Doppler effect in radar: Phenomenon, model, and simulation study. IEEE Transactions on Aerospace and Electronic Systems. 2006;**42**(1):2-21

[8] Nicolas GLVJM. Micro-Doppler analysis of wheels and pedestrians in ISAR imaging. IET Signal Processing. 2008;**1**(1):29-34

[9] Nanzer JA, Rogers RL. Bayesian classification of humans and vehicles using micro-Doppler signals from a scanning-beam radar. IEEE Microwave and Wireless Components Letters. 2009;**19**(5):338-340

[10] Li Y, Du L, Liu H. Hierarchical classification of moving vehicles based on empirical mode decomposition of micro-Doppler signatures. IEEE Transactions on Geoscience and Remote Sensing. 2013;**51**(5):3001-3013

[11] Du L, Li L, Wang B, Xiao J. Micro-Doppler feature extraction based on time-frequency spectrogram for ground moving targets classification with low-resolution radar. IEEE Sensors Journal. 2016;**16**(10):3756-3763

[12] Nepal R, Cai J, Yan Z. Micro-Doppler radar signature identification within wind turbine clutter based on short-CPI airborne radar observations. IET Radar, Sonar and Navigation. 2015;**9**(9):1268-1275

[13] Thayaparan T, Abrol S, Riseborough E, Stankovic L, Lamothe D, Duff G. Analysis of radar micro-Doppler signatures from experimental helicopter and human data. IET Radar, Sonar and Navigation. 2007;**1**(4):289-299

[14] Bączyk MK, Samczyński P, Kulpa K, Misiurewicz J. Micro-Doppler signatures of helicopters in multistatic passive radars. IET Radar, Sonar and Navigation. 2015;**9**(9):1276-1283

[15] Molchanov P, Egiazarian K, Astola J, Totsky A, Leshchenko S, Jarabo-Amores MP. Classification of aircraft using micro-Doppler bicoherence-based features. IEEE Transactions on Aerospace and Electronic Systems. 2014;**50**(2):1455-1467

[16] Kim Y, Ling H. Human activity classification based on micro-Doppler signatures using a support vector machine. IEEE Transactions on Geoscience and Remote Sensing. 2009; **47**(5):1328-1337

[17] Orović I, Stanković S, Amin MG. A new approach for classification of human gait based on time frequency feature representations. Signal Processing. 2011;**91**(6):1448-1456

[18] Park J, Johnson JT, Majurec N, Frankford M, Stewart K, Smith GE, Westbrook L. Simulation and analysis of polarimetric radar signatures of human gaits. IEEE Transactions on Aerospace and Electronic Systems. 2014;**50**(3):2164-2175

[19] Amin MG, Ahmad F, Zhang YD, Boashash B. Human gait recognition with cane assistive device using quadratic time–frequency distributions. IET Radar, Sonar and Navigation. 2015;**9**(9):1224-1230

[20] Narayanan RM, Fairchild DP. Classification of human motions using empirical mode decomposition of human micro-Doppler signatures. IET Radar, Sonar and Navigation. 2014;**8**(5):425-434

[21] Fioranelli F, Ritchie M, Griffiths H. Classification of unarmed/armed personnel using the NetRAD multistatic radar for micro-Doppler and singular value decomposition features. IEEE Geoscience and Remote Sensing Letters. 2015;**12**(9):1933-1937

[22] Fioranelli F, Ritchie M, Griffiths H. Aspect angle dependence and multistatic data fusion for micro-Doppler classification of armed/unarmed personnel. IET Radar, Sonar and Navigation. 2015;**9**(9):1231-1239

[23] Zabalza J, Clemente C, Di Caterina G, Ren J, Soraghan JJ, Marshall S. Robust PCA micro-Doppler classification using SVM on embedded systems. IEEE Transactions on Aerospace and Electronic Systems. 2014;**50**(3):2304-2312

[24] Chen VC. Spatial and temporal independent component analysis of micro-Doppler features. In: IEEE Radar Conference; 2005. pp. 348-353

[25] Lai C-P, Narayanan RM, Ruan Q, Davydov A. Hilbert-Huang transform analysis of human activities using through-wall noise and noise-like radar. IET Radar, Sonar and Navigation. 2008;**2**(4):244-255

[26] Cai C, Liu W, Fu JS, Lu Y. Radar micro-Doppler signature analysis with HHT. IEEE Transactions on Aerospace and Electronic Systems. 2010;**46**(2):929-938

[27] Wright J, Yang A, Ganesh A, Sastry S, Ma Y. Robust face recognition via sparse representation. IEEE Transactions on Pattern Analysis and Machine Intelligence. 2009;**31**(2):210-227

[28] Ramirez I, Sprechmann P, Sapiro G. Classification and clustering via dictionary learning with structured incoherence and shared features. In: IEEE Conference of Computer Vision and Pattern Recognition; 2010. pp. 3501-3508

[29] Kolter JZ, Batra S, Andrew YN. Energy disaggregation via discriminative sparse coding. In: Advances in Neural Information Processing Systems. Vancouver Canada: ACM; 2010. pp. 1153-1161

[30] Vishwakarma S, Ram SS. Detection of multiple movers based on single channel source separation of their micro-Dopplers. IEEE Transactions on Aerospace and Electronic Systems. 2017

[31] Vishwakarma S, Ram SS. Dictionary learning for classification of indoor micro-Doppler signatures across multiple carriers. In: Radar Conference (RadarConf), 2017, IEEE. IEEE; 2017

[32] Vishwakarma S, Ram SS. Dictionary learning for real time classification of human micro-Dopplers across multiple carrier frequencies. Signal Processing. 2017

[33] Natarajan BK. Sparse approximate solutions to linear systems. SIAM Journal on Computing. 1995;**24**(2):227-234

[34] Selesnick IW. Sparse Signal Restoration. 2010. Proceedings Available Online: http://cnx.Org/content/m32168/latest

[35] Jiang Z, Lin Z, Davis LS. Label consistent k-svd: Learning a discriminative dictionary for recognition. IEEE Transactions on Pattern Analysis and Machine Intelligence. 2013;**35**(11):2651-2664

[36] Dogaru T, Calvin L. Validation of Xpatch computer models for human body radar signature. Army Research Lab Adelphi MD Sensors and Electron Devices Directorate, 2008. No. ARL-TR-4403

[37] Boulic R, Thalmann NM, Thalmann D. A global human walking model with real-time kinematic personification. The Visual Computer. 1990;**6**(6):344-358

[38] Ram SS, Christianson C, Kim Y, Ling H. Simulation and analysis of human micro-dopplers in through-wall environments. IEEE Transactions on Geoscience and Remote Sensing. 2010;**48**(4):2015-2023

Chapter 9

Adaptive Coding, Modulation and Filtering of Radar Signals

Moutaman Mirghani Daffalla and
Ahmed Awad Babiker

Additional information is available at the end of the chapter

http://dx.doi.org/10.5772/intechopen.71542

Abstract

In this chapter, some of the issues associated with radar signal processing are highlighted, with an emphasis on adaptability. Signal processing operations are carried by systems in order to enhance the received signal or to clarify its content of information. Received radar signal should be subjected to processing prior to the extraction of useful target information out of it so as to emphasize desired signal among other accompanying signals. Processing of the radio frequency (RF) signal is generally done in an analogue manner, while digital signal processing (DSP) became dominant in the intermediate-frequency (IF) and low-frequency portions of the system. Since the detectability and immunity against interference and clutter strongly depend on the waveform used, it will be more efficient to apply a diverse waveform instead of confinement to an invariable waveform of a fixed code and pattern. Adaptive coding, modulation and filtering of radar signals provide high degree of diversity as well as flexibility and agility for signal processors versus changing sources of interference and environmentally dependent reflectors. Constant false alarm rate (CFAR) is an adaptive processing technique that reduces noise and clutter. Different methods are applied in CFAR technique to adaptively cope with varying clutter density and distribution.

Keywords: filtering, coding, waveform, modulation, adaptive, CFAR

1. Introduction

Radar signal processing is essential in a radar receiver as it is required to enhance and detect received echo signals that are immersed in noise and clutter. The waveform of the transmitted signal plays a distinctive role in the performance of the radar receiver to distinguish valid echo signals from interfering random or hostile received signals. In addition to enhancing the signal-to-noise ratio (SNR) of received signals, receiver needs to enhance the signal-to-clutter ratio (SCR) so as to increase the radar detectability of targets inside the sever clutter. The performance of the radar is highly affected by the level of the interfering signals that share

with the radar signal the same channel. It is affected by the unintentional interference from adjacent channels, environmental and industrial noise sources and the system noise that is generated within the elements of radar system itself.

In military applications, radar is affected as well as by intentional interference or jamming caused by others to deteriorate the ability of the radar to detect hostile targets. Increase in noise and interference lowers the signal-to-noise ratio and thus allows the false alarms rate (FAR) at the receiver output to increase. Wideband jamming signals which have already enough power may find the chance to totally saturate the receiver channel to the extent that the radar might become useless. One of the drawbacks of pulse radar is its relatively large receiver bandwidth, which adds more noise and interference. Such a large bandwidth is required to pass the narrow radar pulses with satisfactory distortion. However, filtering that reduces receiver bandwidth broadens the pulse and causes distortion, which, as well as noise and interference, deteriorate the range resolution and accuracy of the radar. This disadvantage of pulse signals makes continuous wave (CW) radar signals, which require a smaller bandwidth, more preferable within heavy jammed environments. A narrowband interfering signal affects both CW and pulse radars and does not need a large bandwidth to penetrate through the receiver; however, it needs higher power to contest with the desired radar signal.

In addition to noise and interference, the radar suffers from other types of signals which are known as clutter signals. Clutter is any unwanted object that reflects radar signals and will be shown on the radar display, together with the real targets. In air traffic control radar, both fixed and very slow moving objects are considered as clutter and need to be filtered out, so as to not reach the receiver output. There are many radar signal processing techniques that are used to reduce the clutter, such as constant false alarm rate techniques that serve in the reduction of both interference and clutter problems. Doppler processing techniques, such as the long-established moving target indication (MTI) and moving target detection (MTD), are also used to process cluttered radar signals.

2. Filtering of radar signals

Signal filtering means the processing of signals by altering their behaviour in the frequency domain, mostly to reject lower and higher frequency interfering signals. In general, in order to use filters to enhance SNR, bandpass filters (BPFs) process passband signals, while low-pass filters (LPFs) are used to process baseband signals, namely video signals. On the other hand, high-pass filters are used in Doppler processing to enhance demodulated video signals due to reflections that come back from moving objects. **Figure 1** demonstrates the frequency response of a typical BPF.

From the spectral analysis of pulse radar signal, it could be noticed that most of the pulse energy is concentrated on the main lobe centred about the carrier frequency. North [1] suggests the reciprocal of the pulse width as the optimum value for the bandwidth of the LPF used to process radar signals in the presence of white noise. The signal-to-noise ratio at the input of the filter can be expressed as the signal power to the average thermal noise power:

$$\mathrm{SNR} = \frac{\mathrm{S}}{\mathrm{N}} = \frac{\mathrm{S}}{\mathrm{kTB}} \tag{1}$$

where k is the Boltzmann's constant that equals 1.38×10^{-23} JK^{-1}, T the temperature in Kelvin and B the bandwidth of the system in Hz. By substituting B with the optimum bandwidth suggested by North, we get

$$\mathrm{SNR} = \frac{\mathrm{S}\,\tau}{\mathrm{k}\,\mathrm{T}} = \frac{\mathrm{E}}{\mathrm{N_o}} \tag{2}$$

where E is the pulse energy and $\mathrm{N_o}$ is the single-sided noise density in W/Hz. This signal-to-noise ratio which is directly proportional to the energy of the signal is sometimes known as the detectability factor [2], which is defined as the minimum SNR at the output of a filter that is matched to the signal. Generally, microwave circuits and transmission lines are still being used to realize filters in the radio frequency (RF) stages, while passive LC and crystal filters were used within the intermediate-frequency (IF) stages. Other passive elements, such as surface acoustic wave (SAW) devices, have been employed in many radar receivers as bandpass filters and for other purposes [3]. However, digital signal processing (DSP) is often applied in IF and baseband stages of the radar in order to accomplish the processing of IF and video signals. Nevertheless, DSP is gradually moving towards RF.

Due to the rapid growth in the fabrication of digital processors and analogue-to-digital converters (ADCs), digital filters today are widely utilized in the IF stages for bandpass filtering

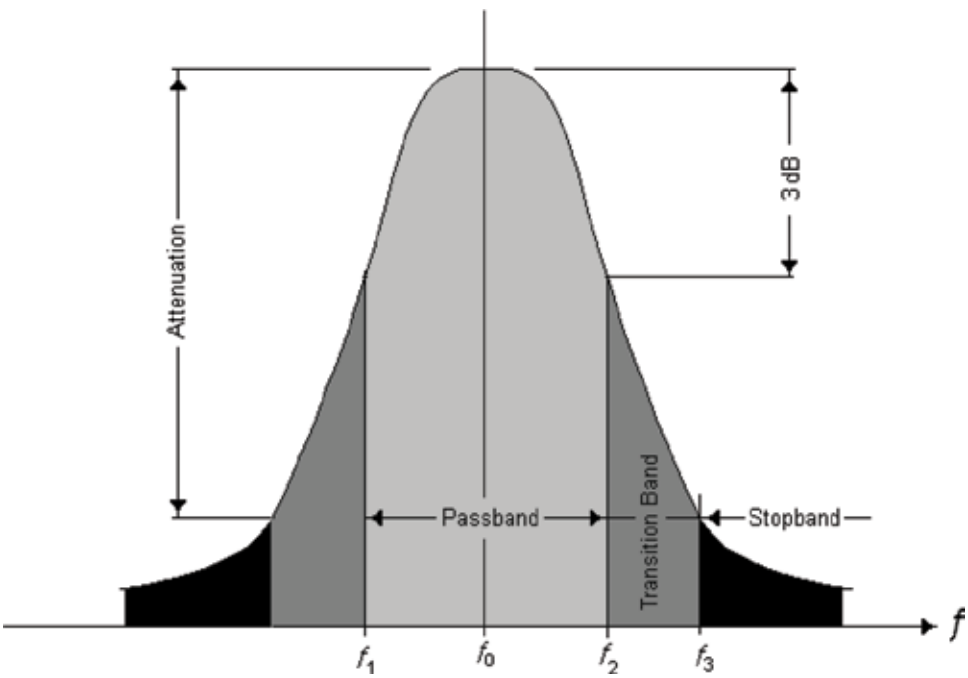

Figure 1. Frequency response of a BPF.

and other radar signal processing schemes. Both finite impulse response (FIR) and infinite impulse response (IIR) filters are used to filter IF and video radar signals [4]. For the FIR filter shown in **Figure 2**, the current sample of the output signal *y(n)* can be computed as the sum of the present sample of the input signal *x(n)* and the samples prior to it, multiplied by the coefficients of the filter b_k as

$$y(n) = \sum_{k=0}^{N-1} b_k x(n-k) \tag{3}$$

where N is the number of taps or filter coefficients. $N-1$ is the filter order, which equals the number of delays marked as Z^{-1}. FIR filters are stable for all values of coefficients, which makes them more suitable to be adaptive. Also, they can be designed to have a linear phase response, unlike IIR filters that have a nonlinear phase response and might be instable.

The design of an FIR filter involves finding the coefficients b_k which are the samples of the filter impulse response *h(n)*, which results in the frequency response that suits the required filter behaviour. An ideal LPF has an impulse response (kernel) that is proportional to the *Sinc* function, which extends to infinity. The convolution of any input signal with that impulse response shall produce perfect low-pass filtering. Nevertheless, the *Sinc* function has to be truncated in order to have an impulse response of a finite length. Because of truncation, the frequency response of the real filter will involve ripples as well as slower transition band, that occur because of the discontinuity that arises at the end of the truncated *Sinc* function. An increase of samples of *h(n)* will not eliminate these deficiencies because discontinuity is of a key effect. A number of windows are formulated in order to reduce the side lobes that occur because of rectangular windowing [5]. For instance, for a filter kernel of length N, the Hamming window is

$$win(n) = 0.54 - 0.46\cos\left(\frac{2\pi.n}{N}\right) \quad for \quad 0 \le n \le N-1 \tag{4}$$

The design of a windowed FIR filter is based on two parameters: the bandwidth, or cut-off frequency, and the length of the kernel, N. The bandwidth is set as a fraction of the sampling frequency f_s and has a value from 0 to 0.5 (i.e. the folding frequency). Kernel length N sets the roll-off using the estimate $N = 4/BW$, where BW is the transition bandwidth, measured from where the curve just departs from 1 to where it is about 0. The transition bandwidth is also set as a fraction of the sampling frequency, in the range 0–0.5.

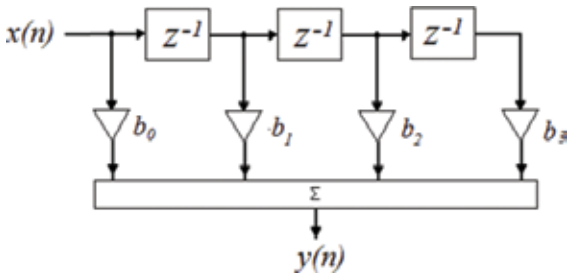

Figure 2. Structure of the FIR filter.

http://dx.doi.org/10.5772/intechopen.71542

3. Matched filtering

We discussed the role of filters in shaping the frequency response of the receiver channel and the reflection of that on the reduction of the white noise signals. Such filtering is less effective with interfering signals that share the same band with the radar signal, that is, the passband of the filter. A filter that is matched to a signal is the one whose impulse response is a time-inverted delayed replica of that signal [6]. Thus, for a transmitted signal *s(t)*, the impulse response of the filter matched to the transmitted signal will be a delayed time-inverted replica of *s(t)*, that is,

$$h(t) = s(t_o - t) \tag{5}$$

where t_o is the optimum sampling moment. In its discrete form, for a matched FIR digital filter, its impulse response for a discrete signal of length N is expressed as

$$h(n) = s(N - n) \tag{6}$$

If we consider the response of the matched filter (MF) in the frequency domain, we will find that the transfer function of that filter is the complex conjugate of a delayed replica of the signal or a scaled value as

$$H(f) = K\, S^*(f)\, e^{-j2\pi fto} \tag{7}$$

The abovementioned equation indicates that the filter will be matched to waveform of the signal represented by its spectrum $S(f)$ rather than its amplitude or time of its arrival. When we decide on using matched filtering for the processing of signals, we must carry with us that the signal will be distorted. The idea is to maximize the signal-to-noise ratio at the output of the filter prior to detection rather than preserving the original waveform of the signal. In most of the cases, it will be difficult or impossible to realize the filter of a specific transfer function that is proportional to the signal spectrum conjugate. Thus, special waveforms are to be designed to accomplish certain functions, such that the corresponding matched filters are realizable and practical. For further reading, the subject of radar signal waveform design is explained in detail in [7].

From [1, 4], it is derived that a matched filter can be realized with the aid of a correlator. This is because the output signal of a filter matched to the transmitted signal is proportional to the autocorrelation function (ACF) of the transmitted signal or a delayed replica of it, as follows:

$$y(t) = R_{ss}(t - t_o) \tag{8}$$

This conclusion states that if the received signal was free of noise, the signal at the MF output would be the autocorrelation function of the transmitted signal. If the received signal was affected by the presence of any form of noise, the output signal will be the cross-correlation function of both signals. Due to the lack of correlation between the transmitted signal and noise, the effect of noise will be dramatically reduced in the output. **Figure 3** demonstrates the use of a correlator in the processing of radar signals. The output signal at the output of a digital

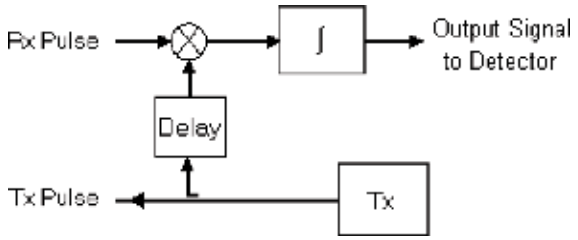

Figure 3. Correlator as MF.

MF could be either expressed as convolution between the received signal and the impulse response of the MF given in Eq. (6) or as correlation between the received signal and a delayed version of the transmitted signal like that shown in **Figure 3**, according to:

$$y(n) = h(n) * x(n) = \sum_{k=-\infty}^{\infty} h(k)x(n-k) \tag{9}$$

$$y(n) = R_{sx}(n) = \sum_{k=-\infty}^{\infty} s^*(k)x(n+k) \tag{10}$$

4. Doppler filtering

Doppler filters are applied in the processing of radar signals in order to remove fixed targets and raise the signal-to-clutter ratio. There are several processing techniques to enhance the SCR in pulse radar, such as moving target indication used in the short pulse radar and moving target detection that is used in the pulse Doppler radar [2]. CFAR that will be discussed in detail is another signal processing technique that improves detection of targets inside clutter. If the wavelength of radar signal is λ, the Doppler frequency shift in the signal received from a target moving with a relative velocity v_r (to or from the radar) is given as

$$f_d = \frac{2v_r}{\lambda} \tag{11}$$

MTI filters are easier to be implemented and cost less compared to MTD processors. For a video signal, the MTI filter is a high-pass filter used to filter out signals of fixed targets, which is of zero Doppler frequency, and weakens signals reflected by slow targets. The MTI filter is a discrete analogue or digital filter. Therefore, it has a periodic frequency response that repeats each multiple of the sampling frequency, that is, the pulse repetition frequency (PRF) of the pulse radar. Hence as seen in **Figure 4**, an MTI filter will reject more than one moving target of the Doppler frequency that is not actually zero. Those rejected targets are of frequencies that are multiples of the PRF, which are due to targets having blind speeds that are not sensed by the radar, that is, it will be blind and will not detect those targets. Substituting PRF in Eq. (11), the first of those blind speeds is related to the PRF and the wavelength as

$$v_B = \frac{PRF\lambda}{2} \tag{12}$$

http://dx.doi.org/10.5772/intechopen.71542

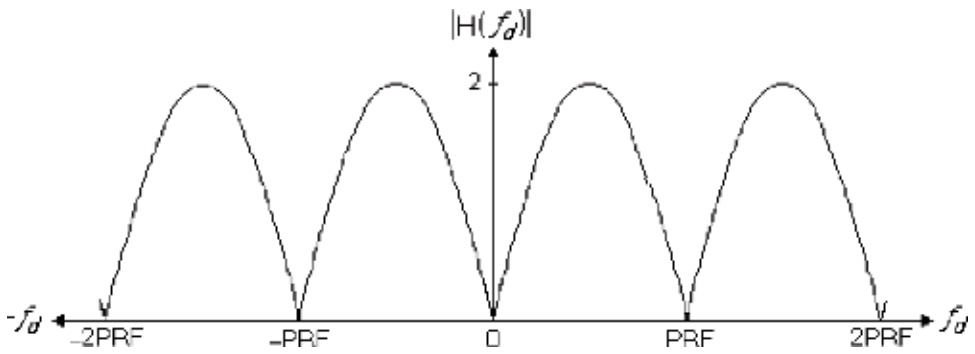

Figure 4. Frequency response of the MTI filter.

The MTI filter will act as a proper HPF only within the Doppler frequency range $-PRF/2 \le f_d \le PRF/2$, as illustrated in **Figure 4**, where f_d is the Doppler frequency of the echo signal, as defined in Eq. (11). That complies with the Nyquist rate that restricts $f_s \ge 2\, f_d$, where f_s is the sampling frequency. For targets of higher Doppler shifts, velocity ambiguity occurs. A solution to avoid blind speeds difficulty is to use a staggered PRF instead of a fixed PRF. Accordingly, the probability that a target is in motion with one of the blind speeds is significantly reduced [6]. For the pulse Doppler radar that applies MTD processing, a bank of Doppler (i.e. MTI) filters is used to realize a more dynamic range in the Doppler domain. The use of this technique avoids rejection of moving targets that have blind speeds and will minimize the ambiguity in the measurement of target velocity.

MTI filters are frequently designed as FIR filters. Two-pulse canceller is a first-order FIR filter of filter coefficients b = {1, −1}, which is the simplest MTI filter. Higher order filters, such as the three-pulse canceller of b = {1, −2, 1} and four-pulse canceller of b = {1, −3, 3, −1}, are mostly used since they provide more flat amplitude frequency response, both in the pass-band and stopband.

5. Adaptive filtering

FIR filter shown in **Figure 2** is stable by definition, and hence it can easily become adaptive whatever its coefficients are. Its kernel could be modified to adapt, either to the required radar signal or to the unwanted signal due to noise or clutter [8]. For all FIR filters, the coefficients b_k are the elements of its kernel, that is, samples of its impulse response. For example, an LPF may be modified in order to reshape its frequency response according to variations of the received signal. A matched filter can be adapted to diverse waveforms that are transmitted by the radar to enhance the diversity of detection and/or to avoid some jamming signals. The MTI filter may alter the location of its notch so as to compensate for a moving radar platform, for example, an airborne MTI (AMTI) radar [2].

Figure 5 illustrates the basic concept of the adaptive filter. The idea is to filter the input signal *x(n)* using an adaptive filter, such that it excels to match that signal to a desired signal *d(n)*. The

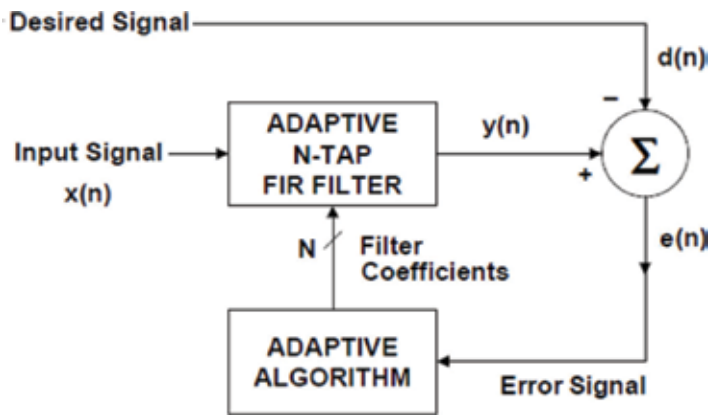

Figure 5. Adaptive FIR filter.

filtered signal *y(n)* is subtracted from the desired signal in order to generate an error signal. That error signal *e(n)* drives some adaptive algorithm, which in order generates the filter coefficients b_k in a manner that minimizes the error signal according to that adaptive algorithm. Filter coefficients are known also as tap weights *w(k)* of the FIR filter. Mean square error (MSE) algorithm is one of the most popular known algorithms, which in turn includes the least mean square (LMS) and the recursive least squares (RLS) algorithms [9].

In **Figure 5**, the estimation error signal at the time index n is *e(n)*. It is fed back to the adaptive algorithm to minimize some function of the error, known in the literature as the cost function [10]. In case of the radar, the optimal output signal of the applied adaptive filter is identical to the desired echo signal, that is, it looks like the transmitted signal. If the output signal of the filter is identical to the desired signal, the error signal becomes zero.

All MSE algorithms intend to minimize the cost function, which is equal to the expectation of the square of the difference between the current output signal of the adaptive filter *y(n)* and the desired signal, as follows:

$$\xi(n) = E\{e^2(n)\} = E\left\{[y(n) - d(n)]^2\right\} \tag{13}$$

LMS algorithm is generally used in adaptive filtering because of the simplicity of the required computations. It is also known as stochastic gradient-based algorithm, which makes use of the gradient vector of the filter tap weights in order to converge on the optimal Wiener solution [9]. That relative simplicity made it the benchmark versus which all other adaptive filtering algorithms would be judged. At each of the iterations of the LMS algorithm, the filter tap weights of the filter will be updated in accordance to:

$$w(n+1) = w(n) + 2\mu e(n)x(n) \tag{14}$$

In Eq. (14), the parameter μ is the step size, which will be a small positive constant. The step size manages the influence of the updating factor. The selection of a suitable value for μ is crucial to the performance of the LMS algorithm. If that value is so small, the time taken by the

adaptive filter to converge on the optimal solution is going to be very long. In contrast, if μ is so large, then the adaptive filter might become unstable and thus its output signal would diverge away from the desired signal [9].

6. Coding of radar signal

A short pulse waveform of a single pulse is modulated only in amplitude. For the small pulse width, the range resolution is excellent and is directly proportional to that width, namely $\delta R = c\ \tau/2$. However, it will not be enough to resolve scattering targets in Doppler because Doppler resolution is proportional to the bandwidth. Bandwidth is equal approximately to the reciprocal of the pulse width and thus the time bandwidth product is about unity. Such waveforms are used in the MTI radar that uses Doppler processing just to filter out non-moving targets from its output, which does not require much better Doppler resolution.

Long pulse waveforms consist of a single pulse that is modulated only in amplitude, but now the duration will be long enough for the scattering targets to be resolved in Doppler. CW radar signals belong to this class of waveforms, with very long pulse duration. On the other hand, in a practical situation, it will not be suitable for resolving targets in range, of course unless we modulate the angle of the signal. Noise-type waveforms consist of pulses that are modulated with amplitude or phase modulation function that is irregular or noise like and has a relatively larger time-bandwidth product. This class of waveforms includes those used in pulse compression of radar signals like biphase codes (such as Barker and pseudorandom codes), polyphase codes (such as Frank codes), nonlinear frequency modulation (NLFM) pulses, pulse trains with staggered PRF pulses, trains with frequency shift coding and long pulses with irregular amplitude modulation [7].

The radar signal is frequently coded with the purpose of pulse compression. Nevertheless, the frequency and phase coding of the radar signal are employed to accomplish other requirements rather than the compression of echo signals. Thus, the conventional pulse or CW radar signals with fixed frequencies and phase angles are not always the favourable waveforms. Nevertheless, the environment in the region of the radar includes ground clutter, multipath, refraction, weather and interference. The optimum radar signal waveform for this application must contain sufficient energy to achieve detection on the smallest aircraft at the longest range. It must also have sufficient bandwidth to provide the necessary range accuracy and resolution and must have a duration long enough to permit velocity discrimination of targets relative to ground clutter.

Pulse compression [2], also known as pulse coding, is a signal processing practice that is intended to maximize the sensitivity and resolution of radar systems. In a pulse radar system, there are several factors that affect each of the radar functional parameters. One of these factors is the effect of the pulse width in the determination of the range resolution and accuracy. The radar range equation [1] indicates that the range is affected by the energy of the transmitted pulse, that is, its power and pulse width. Generally speaking, the ability of any radar to detect far objects depends primarily on the transmitted signal energy.

For pulse radar, energy is indicated by the average transmitted signal power, which is expressed as the peak power multiplied by the duty cycle of the transmitter. Even though the peak transmitter power could be as high as hundreds of kilowatts or even some megawatts, as pulse radars transmit very short pulses (typically in order of microseconds), the average transmitted signal power perhaps is much less than 1% of that value. Obviously, this would not be the efficient use of the available transmitter power.

Transmission of longer pulses improves the detectability of the radar as it increases the average transmitted signal power. On the other hand, just lengthening the radar pulse has the result of degrading its range resolution, because the RF pulse would be spread over a larger distance. Thus, some technique is needed to increase the average power without degradation in the range resolution and accuracy of measurement. In order to solve this dilemma, we have to understand that the range resolution of the pulse radar does not essentially depend on transmitted pulse duration but in fact it depends on the bandwidth of the transmitted pulse. In old radars, a simple rectangular RF pulse is transmitted in each repetition interval. Its bandwidth is just $1/\tau$, where τ is the duration. If the carrier signal within the pulse is altered using frequency or phase modulation, the bandwidth will be increased. Accordingly, the radar resolution is changed independent of the average transmitted signal power. This kind of modulation of the transmitted radar pulse is generally known as radar signal coding.

In radar signal processing, pulse compression is one of the techniques that makes use of coding to increase the bandwidth of the radar signal. At the radar receiver, reflected coded pulses are compressed in the time domain, which produces a pulse of a finer range resolution than that of an uncoded pulse. Decoding or compression involves correlating the received signal with a replica of the transmitted signal. Several methods were developed to realize that, such as binary phase and polyphase coding, frequency modulation and frequency hopping. Applying linear frequency modulation (LFM) to the transmitted pulse is often referred to as chirp coding. The main drawback of pulse compression is the appearance of range side lobes around the main signal peak after decoding. It may produce echoes that spread out from neighbouring targets and bring in range ambiguities.

A common signal coding method used in the pulse radar is binary phase shift keying (BPSK), which involves repeatedly flipping the phase of the RF signal within the duration of the pulse, according to a code known as the spreading code, which should yield minimum side-lobe levels after decoding. Barker codes are efficient binary codes, which have lengths of up to 13 bits [2] only. Side lobes can be minimized by the use of complementary codes, which are carefully selected pairs of codes whose range side lobes cancel out under ideal conditions. Generally, the efficiency of a particular code is judged by the time-bandwidth product, BT, where B is the pulse bandwidth and T is the entire transmitted pulse width. To realize a higher compression ratio, more subpulses of τ width are used per one long pulse of T duration. For an uncoded pulse, $BT = 1$, as $B = 1/T$ only.

For example, a 13-bit Barker code has a time-bandwidth product of 13, which means that each radar pulse contains 13 times the energy of an uncoded pulse of the same resolution. Range resolution becomes 13 times finer than that for an uncoded pulse of the same width. A pulse Doppler radar compromises between range and velocity resolution by applying relatively

longer pulses, while some radar systems focus on the issue of range resolution more than other parameters. Precise target tracking, range finders, target recognition and radar imagery applications are examples of those areas of interest. Synthetic aperture radar (SAR) is widely used for radar imagery and mapping and for space and aerial reconnaissance, which requires superior range resolution [3].

Pulse compression is the solution that solves almost all those problems mentioned. It makes use of specific radar signal processing techniques to provide most of the advantages of very narrow pulses yet retaining long range with less power. Matched filters, similar to those discussed in Section 3, are used to perform pulse compression of the received signals. Compression is needed because radar signals are usually expanded in time before transmission and must be compressed to obtain the desired resolution or sharp focusing. This will enhance extensively the received signal SNR and thus improve the radar detectability of far and small targets immersed inside noise and clutter. We can briefly state the merits of the pulse compression mentioned above in addition to others as follows [7]:

1. Large compression ratio offers higher resolution and accuracy in range and reduction in the radar minimum range.
2. The reduction of the required receiver bandwidth and thus reduction of interference.
3. The improvement of the SNR of the received signal due to matched filtering or correlation of signals.
4. Better anti-jamming capabilities, low probability of intercept (LPI), low probability of exploitation (LPE) and low power that makes the radar system difficult to be detected or positioned.
5. Long transmitted pulses cause low interference to other radar and communication equipment and thus provide better electromagnetic compatibility (EMC).
6. Ease of using solid-state transmitters and small power supplies like batteries that leads to small and light systems.
7. The Doppler information in the long pulse received back from a target will be richer than what is gained from a short pulse.
8. Pulse compression realizes radar imagery and mapping in addition to the possibility for target recognition and classification, using a high-range resolution (HRR) radar.

There are many techniques used in pulse compression that are generally divided into passive and active techniques, which include frequency modulation and phase modulation techniques.

7. Phase coding of signals

In this technique of pulse compression, the phase angle of the transmitted radar pulse is switched between two or more values, while the long pulse is modulated with the radar PRF

as usual. The relatively long transmitted pulse is divided into an integer number of subpulses, of equal widths and amplitudes but with different phase angles.

A digital signal or a code sequence is used to determine the phase of each subpulse. It is more common to use binary or biphase coding [11] to provide the modulated pulse rather than the ternary, quaternary or higher coding of signal. A signal multiplier may be used to obtain the binary phase shift keying signal that has a phase angle that swings between 0 and 180°, according to the modulating digital signal. In **Figure 6**, such a BPSK modulated pulse is illustrated. Due to the modulation of the carrier of the transmitted signal with the digital signal, the bandwidth of the transmitted signal is increased. The spreading of the digital signal in most cases is a pseudorandom signal that has special desirable correlation features. Such signals look like white noise, which has an infinite bandwidth and an infinitesimal autocorrelation function centred about the zero axis. Those pseudo-noise (PN) binary codes are used in spread spectrum communication systems, in a similar manner, in order to spread data signals along the frequency domain. They can be easily generated with the aid of shift registers (D-type flip flops) and logic circuits.

After the phase-coded signal is amplified and emitted into the radar zone of operation, the echo signal will be reflected by targets inside that zone. The received echo pulse is compressed by a matched filter or a correlator. The peak value of the compressed signal, for any code, is equal to the number of subpulses N times the pulse amplitude. The pulse width of the pulse is equal to that of the subpulse used, τ. The pulse compression ratio (PCR) is equal to the code length, that is,

$$PCR = BT = \frac{T}{\tau} = \mathrm{N} \tag{15}$$

Side lobes are generated within the output of the matched filter, before and after the main lobe. Those side lobes may be reduced by the selection of the proper code for the modulating signal.

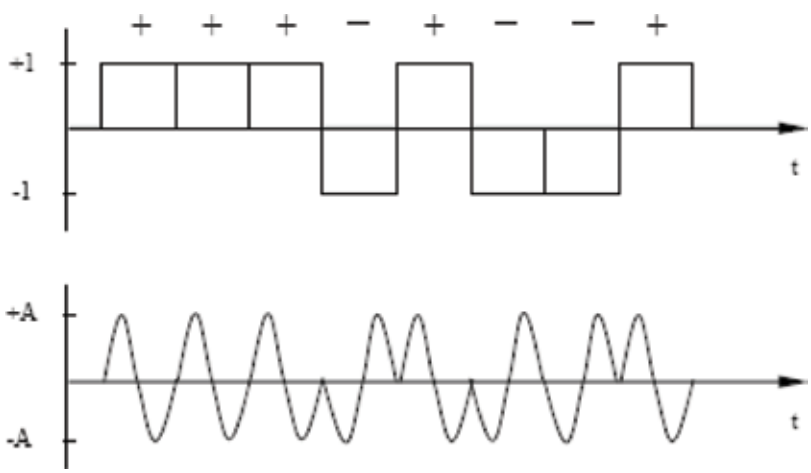

Figure 6. Phase-coded BPSK signal.

Many measures exist to differentiate between the available codes and decide which code is more desirable for a certain application. The features of a specific code are extracted from the ACF of the sequence that represents that code. The relations between the peak and the side lobes are of big importance. The peak-to-side-lobe level (PSL) is defined as the ratio of the largest square of side-lobe levels x_i to the square of the peak of the compressed pulse x_o, which is computed in decibels by [11].

$$PSL = 10\log\left[\frac{\mathrm{Max}\left(x_i^2\right)}{x_o^2}\right] \tag{16}$$

Barker codes are one class of the famous classes of codes used in the biphase coding of the radar signal with the purpose of pulse compression. Those codes are characterized with very small PSL values and particular autocorrelation functions that have side lobes with equal amplitudes and unity absolute value, similar to that shown in **Figure 7**.

Barker codes exist for only certain code lengths that are limited to a maximum code length of 13 bits. **Table 1** shows all the available Barker codes, where a plus sign represents +1 and the minus represents −1 bit. We notice that for any of these codes, there exist four allomorphic codes that are formed by the inversion of the bits and/or the reversal of their order. All these allomorphic codes will have the same autocorrelation function, and thus we consider only one of them. The autocorrelation function of a discrete bipolar signal, that is, of '+1' or '−1' values, is approximated using the discrete temporal aperiodic ACF given as

$$\Phi(m) = \sum_{k=1}^{N} x_k x_{k+m} \tag{17}$$

where the integer index m steps over the domain $-(N-1) \le m \le (N-1)$ and x = 0 for all indices k < 0 and k > N + 1.

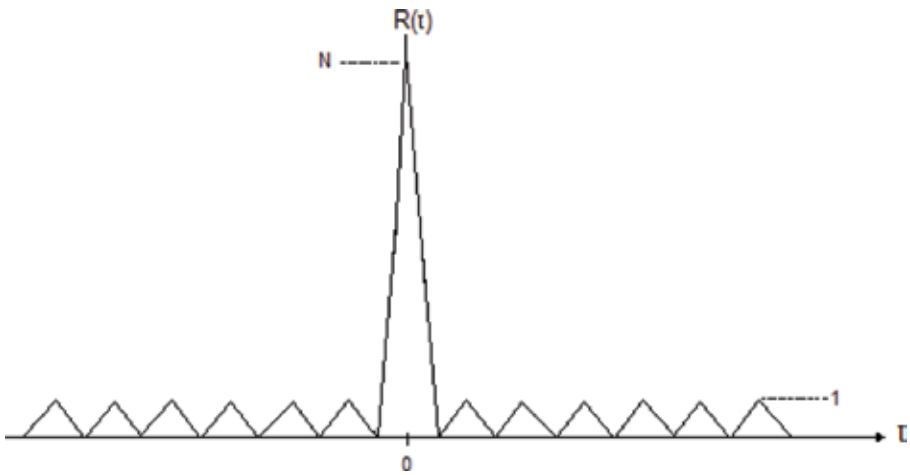

Figure 7. ACF of 13-bit Barker code.

Code length	Code sequence	PSL, dB
1	+	-
2	+ −, + +	−6
3	+ + −	−9.5
4	+ + − +, + + + −	−12
5	+ + + − +	−14
7	+ + + − − + −	−16.9
11	+ + + − − − + − − + −	−20.8
13	+ + + + + − − + + − + − +	−22.3

Table 1. List of Barker codes.

Barker codes are a subset of other binary codes known as the minimum peak side lobe (MPS) codes that attain the lowest PSL for a given code length. Thus, we find that many approaches to finding binary sequences with good side lobes have been undertaken. By means of an extensive computer search, binary codes of long lengths can be found. According to [11], Delong has discovered a considerable number of these codes as long as 99 bits with a peak side lobe amplitude of 7. And according to [7], Kerdock later has built a dedicated computer and has applied it successively to search for good codes. However, neither of them has made any attempt to ascertain that the discovered codes are MPS nor have they compiled a list of all codes of a given length with a given PSL, although long codes with excellent PSL values have been discovered this way.

There exist other approaches to achieve longer codes providing higher pulse compression ratios but look different somewhat from Delong and Kerdock approaches. One of these is the process of code concatenation or combination, in which available codes are utilized to code the transmitted pulse at more than one level; thus, each segment of the code is coded again with another phase code. When utilized with Barker codes it has been called Barker-squared or combined Barker coding. Referring to [11], Hollis combined a Barker code of length 4 with the code of length 13 in two ways, each of different ACFs.

8. Pseudorandom codes

A random code is to be obtained when the binary bipolar sequence is determined by a random process, with an equal probability of 0.5 for both positive and negative values. A pseudorandom, or pseudo-noise code, is obtained when the binary sequence has approximately the same number of positive and negative values with a probability ≈0.5.

An important class of pseudorandom codes is the maximal-length sequences or shortly the m-sequences. These sequences are known also in the literature as Galois and PN codes [7]. While Barker codes are finite, the m-sequences are not finite and can realize higher compression ratios. Periodic m-sequences are easily generated with the aid of linear shift registers and XOR gates. The register is fed back with a number of its different stages of outputs, after they

are XORed or modulo-2 summed. However, certain feedback connections of the register stages outputs to the input and not all of them will produce codes of maximal length, that is, m-sequences. The maximal length of the sequence is the longest possible period for an n-stage register, which is given in terms of the number of register stages (flip-flops) as

$$N = 2^n - 1 \tag{18}$$

A cycle of the periodic autocorrelation function of an m-sequence can be computed by Eq. (17). It is shown in **Figure 8** where it looks somehow different from the ACF of a Barker code. The ACF function might be preferred to be normalized to N, which is the peak value at $m = 0$. As the code length N tends to infinity and the subpulse width τ tends to zero, the ACF of the m-sequence tends to that of white noise, which is an impulse that is centred at a zero time shift. Hence, the name PN is significant. It may be worth to remember that the power spectrum density of white noise is constant with frequency. A well-known example of white noise is the thermal noise that has a power density of kT_o, where k is the Boltzman's constant and T_o is the absolute temperature. In the absence of Doppler shift, the circular autocorrelation function has two levels. Its amplitude at the origin (i.e. for $m = 0$) is equal to the length of period N. For all offsets other than multiples of one period, the magnitude of the function is unity. This may be written as

$$x_m = \sum_{k=1}^{N} a_k a_{k+m} = \begin{cases} \mathrm{N} & \mathrm{m} = 0, \pm \mathrm{N}, \ldots, \pm \mathrm{kN} \\ -1 & \text{otherwise} \end{cases} \tag{19}$$

There are $2N-1$ samples in the autocorrelation function and this function is symmetrical about the origin. PN codes are often chosen over randomly coded words for application because their generation and decoding can be easily mechanized, their side lobe levels easily predicted and they provide a rich source for good codes of arbitrary length. Pseudorandom sequences have some properties that they share with random sequences and other properties that are unique for them. The number of segments of *ones* in each period of the sequence is within one, that is, ± 1, of the number of *zeros* (minuses), which is known as the balance property. In every period, half the runs have length 1, one-fourth have length 2, one-eighth have length 3 and so on (the run property).

PN codes can be generated deterministically through the implementation of shift registers with feedback connections. The initial condition in the shift register determines the starting point of the code. The condition of all zeros is forbidden. The last stage in the shift register must be connected to the feedback circuit and there must be an even number of feedback taps [4]. For maximal-length PN codes, each period has a length of $2^{\mathrm{n}}-1$ pulses. There are $2^{\mathrm{n}}-1$ different maximal-length codes that can be generated from each n-bit shift register, which are simply shifts of each other derived by changing the seed utilized. The number of different n-bit shift registers that yield maximal-length codes, that is, the number of codes (including mirror images), is given by

$$\mathrm{M} = \frac{\Phi(2^{\mathrm{n}} - 1)}{\mathrm{n}} \tag{20}$$

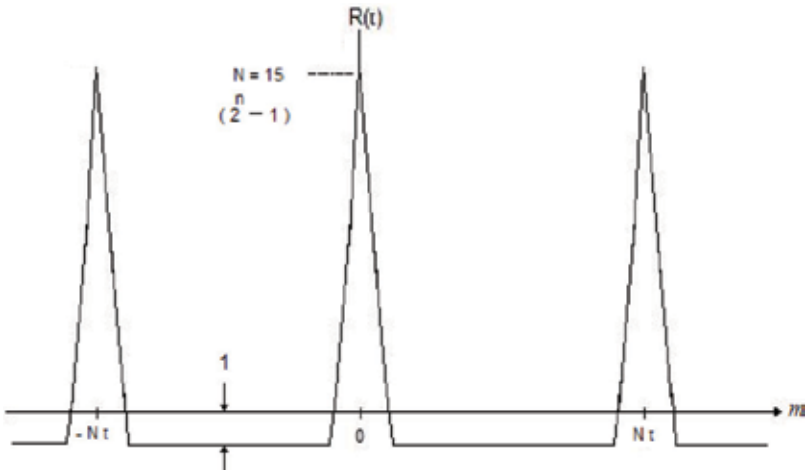

Figure 8. ACF of a 15-bit M-sequence.

where $\Phi(x)$ here is the Euler phi function [11]. If 2^n-1 is a prime number, the number of codes will be $(2^n-2)/n$, whereas if 2^n-1 is factorable into prime numbers denoted as P_i then

$$M = \frac{(2^n - 1)}{n} \prod \frac{(P_i - 1)}{P_i} \tag{21}$$

Each prime P_i is used in the foregoing computation only once even if it appears in the factorization more often. Algebraic sum of all the ACFs for all the starting points of a given code is $(2^n-1)^2$ at the origin and $[(N-k)/N]\ (2^n-1)$ for each segment, k, away from the origin, in either direction. The ACFs of this waveform is symmetrical about the time delay axis, as shown in **Figure 8**.

9. Adaptive coding

Diversity is a key solution for many radar and telecommunications problems. Using diverse radar elements of different parameters rather than depending on a single element enhances the radar capability and functionality. For instance, frequency diversity increases the detectability of the radar to detect different targets of different resonant sizes. Similarly, using diverse PRF reduces the problem of blind speeds in the Doppler processing of signals [7]. Earlier, most radar pulse coding was done for the sole purpose of achieving the benefits provided by pulse compression. Exceptions included the use of frequency modulation for ranging applications, for example, continuous wave and high PRF radar and the use of coded pulse trains to increase Doppler resolution. Nowadays, radar signal coding is used for other purposes such as security and waveform diversity. Waveform diversity takes many forms, including PRI diversity, frequency diversity, amplitude diversity and phase diversity.

Optimal coding is based on a certain criterion such as measurement errors, detection performance and false alarm probability. These criteria have traditionally placed certain restrictions

on code selection. For instance, the repeated use of a single pulse code meets most optimality requirements for traditional applications, and identically coded pulse trains can be used to demonstrate greatly enhanced Doppler processing [12]. On the other hand, diverse pulse coding techniques are required to ensure that target responses from individual pulses are distinguishable from one another. This inherently requires the generation of code families that possess good autocorrelation properties and cross-correlation properties as well, which are often mutually exclusive properties.

Phase-coded radar signals offer a remarkable flavour of diversity that simply depends on the change of the code of the modulation sequence. Such signals are easily generated compared to other diverse radar signals that require changing the carrier frequency. Frequency hopping signals may be considered as diverse code signals, in which its pattern of changing codes is optimized for diversity to avoid jamming, rather than to enhance the range resolution of radar. For a radar that uses a pseudorandom waveform, a comprehensive search of possible waveforms could be attempted. The choice of waveform may be reduced upon many rules, such as search of maximal-length sequences that do not include binary codes of all '1s or all '0s, which definitely do not accomplish the required resolution. Several codes are satisfactorily close that only one of a set might need to be tried. However, the number of combinations is still big, and extensive search of high time-bandwidth codes could not be practical using available computers. Nevertheless, regarding the current improvement in computer speeds, the power to do this seems to be achievable.

For example, if a correlator can correlate a waveform with 1 ms integration length in real time, it could search 10,000 waveforms in only 10 s. Therefore, if all the possible low probabilities of exploitation techniques were employed as efficiently as possible, it becomes so difficult to exploit the transmitted signal within tactical timescales. A great deal of research is being carried on to investigate waveform that designed and the related signal processing for the high-resolution pulse Doppler imaging, both in radar and in sonar.

The uncertainty association of Fourier transformation states the primary limitation on the ability of any individual waveform to simultaneously resolve two or more targets closely spaced in both time delay and Doppler shift [13]. Transmitting successive signals of adequately diverse waveforms and processing them properly could make it possible to resolve those targets and generate a high-resolution delay-Doppler image. It is somehow similar to the situation of generating a high-resolution optical image from several low-resolution optical images with somehow different imaging apertures. A selection of optimal sets of coded waveforms and designing associated processing algorithms has already been considered [13], for example, in order to generate pulse-echo delay-Doppler images of a substantially higher resolution than that is possible using a single waveform with comparable time-bandwidth product. In an adaptive diverse system, the instantaneous waveform is selected to improve the performance according to changes in clutter and noise variations [8].

The importance of this technique is based on the fact that it realizes the higher discrimination of radar or sonar targets compared to those that are possible using only one waveform. It results in higher resolution images in pulse-echo imaging systems, in addition to improved capability in resolving targets in tracking systems. There are many applications that can benefit from this superior delay-Doppler resolution, such as SAR, planetary and ground-based

astronomy radar, ionospheric radio sounding, meteorological radar, aircraft surveillance and tracking radar and in active sonar systems.

For better reduction of interference of several radar signals, one may use sort of orthogonal codes, such as Walsh codes, in same manner as in the code division multiple access (CDMA) technique used in mobile networks. However, though those codes have good cross-correlation properties that make them exceptional in multiuser environments, and they have poor PSL due to their undesirable ACF properties. On the other hand, MPS and PN codes are not orthogonal but they have very considerable PSL that realize high SNR at the output of matched filter and high-pulse compression ratio, with the minimum range ambiguity [7].

10. Constant false alarm rate

A major problem that encountered the performance of radar is clutter, which is defined as the unwanted targets that may compete with the desired targets in the radar receiver. There are many efforts exerted to model, analyse and mitigate clutter in radar systems. Many techniques appeared in the literature deal with modelling and filtering of clutter. Clutter is a random phenomenon and it is well described in the context of a probabilistic framework.

In this section, analysis of well-known CFAR detectors is going to be accomplished. It also includes a brief overview of topics related to clutter modelling and mitigation in the monostatic radar. Finally, the schemes of CFAR detectors under different clutter scenarios will be covered.

10.1. CFAR in monostatic configuration

Sometimes the clutter residue, after the moving target indicator, is enough to saturate the radar display. To overcome such shortcomings, a clutter estimation circuitry is provided after MTI to reduce the effect of false alarms. There are many schemes devised in the literature to keep the level of false alarms constant. Here in this section, an analysis of some well-matured schemes will be given. It is well known that when the radar returns come from a background with homogeneous clutter, the cell average (CA) CFAR is adequate to control the false alarms. In some cases, there will be strong returns from some targets that may mask other weaker targets. In these cases, it is better to use a clutter estimation scheme based on choosing the Smallest-Of (SO) sample of returned clutter power to represent estimation to the background clutter, which is known as SO-CFAR. In cases of clutter power transition, it is better to use a scheme based on choosing the Greatest-Of (GO) sample in the reference window as an estimation to clutter background. This scheme is known as GO-CFAR sample, as a representative to clutter.

In other situations, there may be spiky samples of the clutter in one side of the reference window, which is known as a clutter edge. Order statistic is another clutter estimation scheme that may be used to alleviate both the problem of multiple targets and clutter power transition in the reference window. In some situations, a radar receiver is encountered by a fixed position clutter during several scans. Such types of clutter can be stored and subtracted in the course of the following scans. Such clutter is called a clutter map or area clutter. In the following

paragraphs, we will give a short review to the concept of each of these schemes that is used to reduce the effect of false alarms. All these schemes are capable of setting adaptively a threshold to represent the local clutter background in the chosen reference window. The threshold in these schemes of CFAR is set on a cell-by-cell basis by processing a group of cells of a reference window sited on either side of a cell under test (CUT). **Figure 9** gives a general structure of the CA-, SO- and GO-CFAR.

10.2. CA-CFAR clutter estimation scheme

In this scheme, a reference window of length N cells is chosen to represent the local clutter power background. The CA-CFAR will maximize the probability of detection if the clutter background is homogeneous and of independent and identically distributed (IDD) observations. As the size of the window increases, the detection probability approaches that of the optimum detector based on a fixed threshold.

The CA-CFAR makes its estimate of clutter power by summing samples of background before and after a CUT, then taking the average of them, assuming that the underlying noise distribution is homogeneous (i.e. exponentially and independent and identically distributed samples). Of course the processor will encounter severe performance degradation if the above assumption is violated. These violations may occur in terms of interfering targets or a clutter power transition (clutter edge), and in both cases a result is the unnecessary increase in the threshold and reduction in probability of detection.

In order to analyse the detection performance of a CA-CFAR scheme with the assumption that the clutter background is homogeneous, assume that the square-law detected output for any range cell is exponentially distributed with the probability density function (PDF) [14]

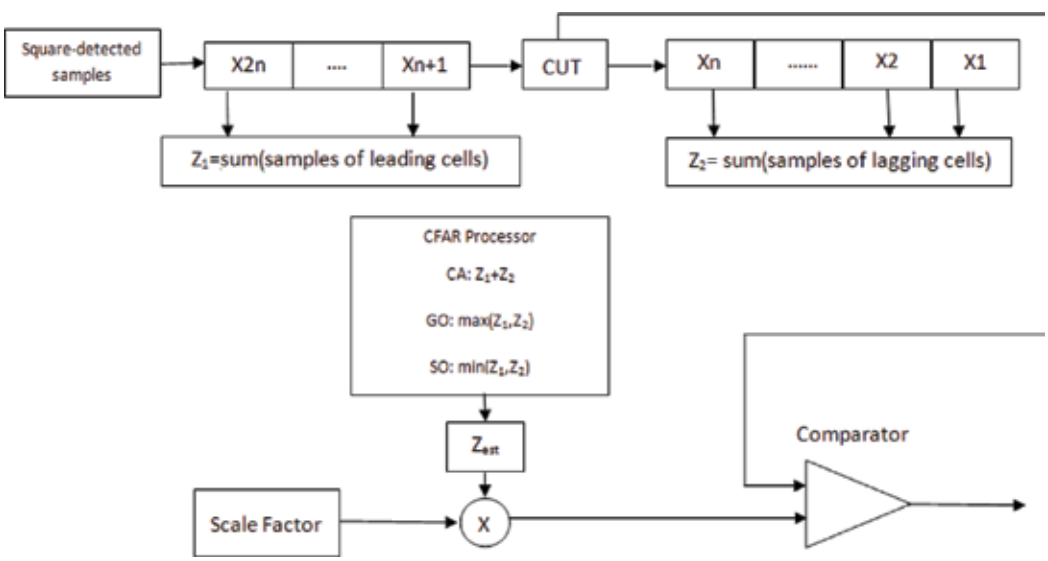

Figure 9. Mean level CFAR processors.

$$f(x) = \frac{1}{2\lambda'}\exp\left(-\frac{x}{\lambda'}\right) \tag{22}$$

Under the null hypothesis (H_0) of no target in a range cell and homogeneous background, μ' is denoted as the total background clutter plus thermal noise power, which is denoted as λ'. under the alternative hypothesis (presence of target H1); λ' is equivalent to $\mu'(S+1)$, where S is SNR of a target. This means that we are assuming the Swerling I model for a target. Therefore, the CUT will be given as

$$\lambda' = \left\{ \begin{array}{c} \mu' \rightarrow H_0 \\ \mu'(S+1) \rightarrow H_1 \end{array} \right\} \tag{23}$$

The cells surrounding CUT is always given by μ'. The optimum detector sets a fixed threshold to determine the presence of a target under the assumption that the total homogeneous noise power μ' is known a priori. In this case the probability of false alarm P_{fa} is given by [15]

$$P_{fa} = P\left[y \succ y_b | H_0\right] = \exp\left(-\frac{y_b}{2\mu'}\right) \tag{24}$$

where y_b denotes the optimum fixed threshold. Similarly, the probability of detection in the case of optimum detector is given as [15]

$$P_{dopt} = P\left[y > y_b | H_1\right] = \exp\left(-\frac{y_b}{2\mu'(S+1)}\right) \tag{25}$$

Eqs (24) and (25) can be combined to give

$$P_{dopt} = \left[P_{fa}\right]^{\frac{1}{S+1}} \tag{26}$$

A code written in Matlab is used to present the performance of the optimum receiver in terms of SNR versus P_d with fixed P_{fa} and varying reference window length, using Eq. (26), as shown in **Figure 10**.

In the problem of setting adaptive threshold for the radar receiver to cope with the varying clutter power levels, the CFAR scheme has to follow the clutter localities. The estimate of clutter power, $\widehat{Z}$, in this case is a random variable which is dependent on the specific CFAR scheme. It can be stated that P_{fa} is determined by the following expression [15]:

$$P_{fa} = E\left[P(y) > \hat{Z}\check{T}\middle|H_0\right] = E\left[\int_{\hat{Z}\check{T}}^{\infty}\left(\frac{1}{2\lambda'}\exp\left(-\frac{y}{\mu'}\right)\right)\right] = E\left[\left(\exp\left(\frac{-\hat{Z}\check{T}}{2\mu'}\right)\right)\right] = M\left(\frac{-\check{T}}{2\mu'}\right) \tag{27}$$

http://dx.doi.org/10.5772/intechopen.71542

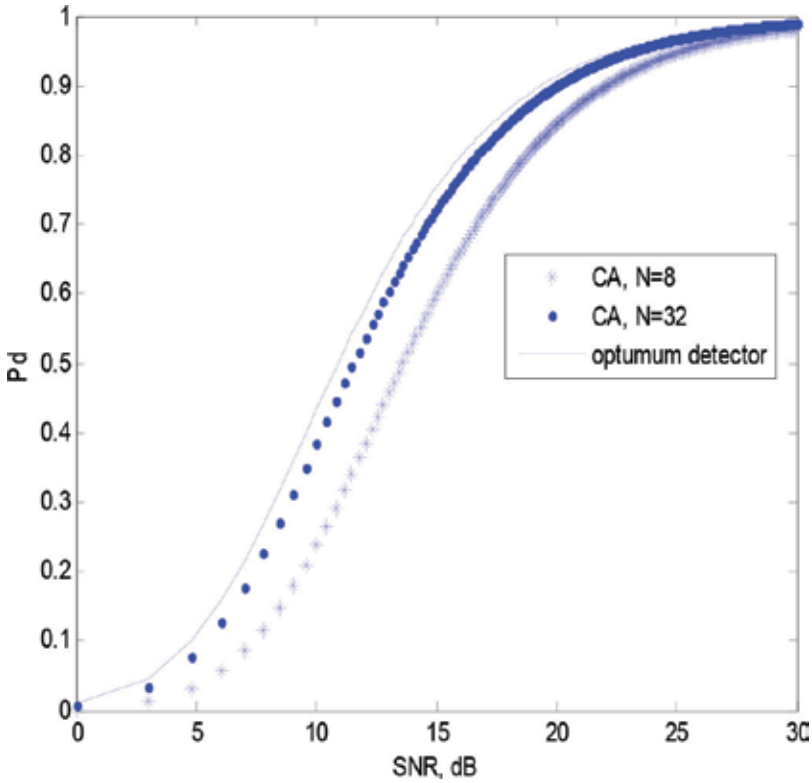

Figure 10. Performance of CA-CFAR with varying window length and fixed P_{fa} = 1e-4 detector.

where M(.) is the moment generating function (MGF). Similarly, the probability of detection can be given by [14]

$$P_d = M\left(-\frac{\check{T}}{2\mu'(S+1)}\right) \tag{28}$$

For CFAR action to hold, M(.) must be independent of μ'.

In the CA-CFAR scheme, the noise estimate is obtained by summing the power content in the reference cells before and after the CUT. This may be the adequate estimate when the background noise is exponentially distributed. Therefore, the noise estimate for this scheme can be written as

$$\widehat{Z} = \sum_{i=1}^{N} X_i \tag{29}$$

where X_{is} are range cells surrounding CUT. The exponential density is a special case of the gamma density with $\alpha = 1$ in the PDF given by [16]

$$f(y) = \frac{\beta^{-\alpha} y^{\alpha-1} \exp\left(-\frac{y}{\beta}\right)}{\Gamma(\alpha)} \qquad y \geq 0, \beta \geq 0, \alpha \geq 0 \tag{30}$$

The cumulative distribution function (CDF) corresponding to this PDF is denoted by G(α,β). The moment generating function to G(α, β) is [16]

$$M_y(u) = (1 + \beta u)^{-\alpha} \tag{31}$$

The probability detection P_d for the CA-CFAR processor is obtained by substituting Eq. (31) into Eq. (27) with $\beta = 2\mu'$, and α is number of samples in the reference window; the following expression for P_d will result in

$$P_d = \left[1 + \frac{\check{T}}{1+S}\right]^{-N} \tag{32}$$

When setting S = 0 in Eq. (32), the scale factor $\widehat{Z}$ is obtained as

$$\check{T} = \left[P_{fa}\right]^{-\frac{1}{N}} \tag{33}$$

It is clear that from Eqs. (32) and (33), that both the P_d and P_{fa} expressions are independent of μ', proving the action of CFAR. The performance of CA-CFAR is shown in **Figure 11** in terms of SNR versus P_d with P_{fa} as a parameter. Also, it is shown in **Figure 12** the performance of

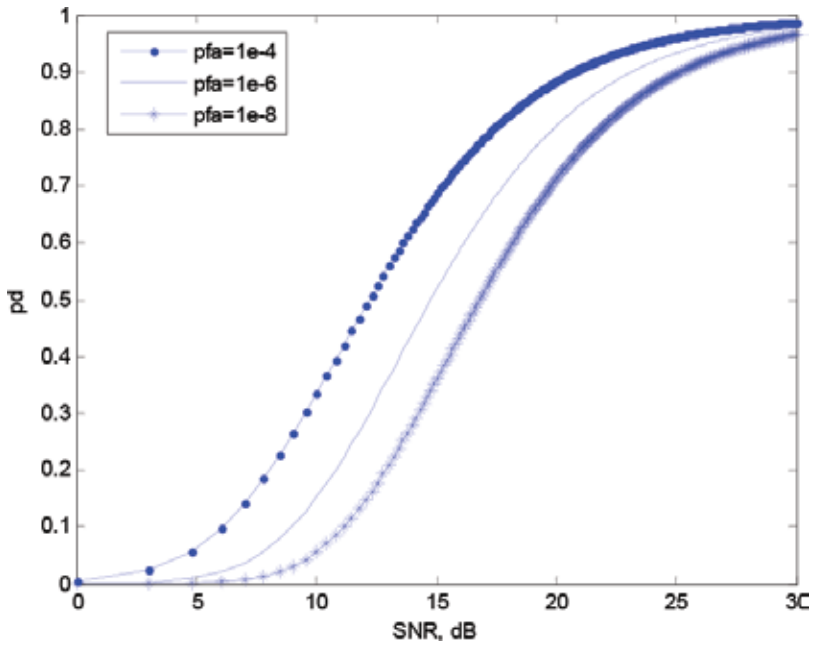

Figure 11. Performance of CA-CFAR.

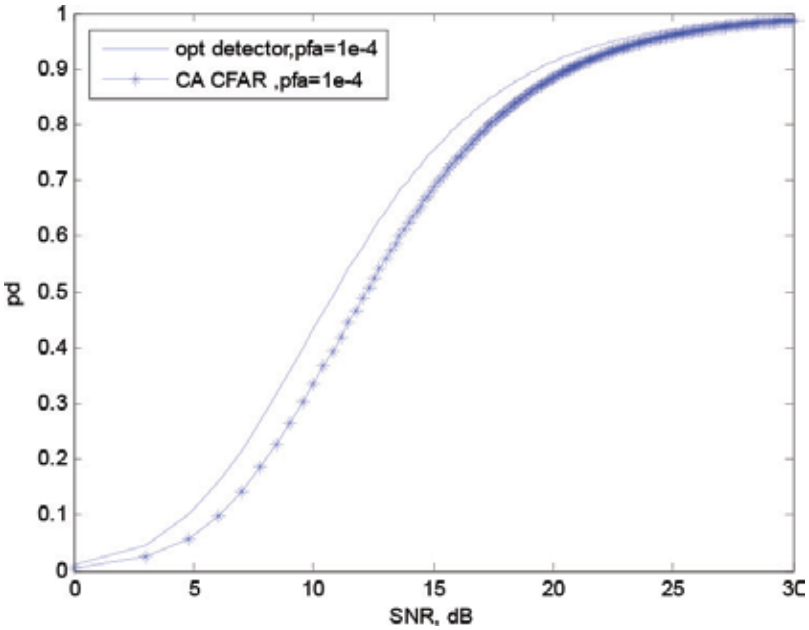

Figure 12. Performance of CA-CFAR compared to that of optimum detector.

CA-CFAR compared to the performance of the optimum detector when the designed probability of false alarm is $P_{fa} = 10^{-4}$.

The performance of CA-CFAR in a non-homogeneous background taken from a reference window can be analysed in similar way to the above discussion. The probability of detection obtained under CA-CFAR for this case is given as

$$P_d = \left[1 + (1+I)\check{T}\right]^r \left[1 + \frac{\check{T}}{1+S}\right]^{r-N} \tag{34}$$

where r is the number of interfering targets. **Figure 13** shows the performance of CA-CFAR in a non-homogeneous environment compared to that in a homogeneous one. Also from **Figure 14**, it illustrates the performance of this processor when the number of interfering targets is two and probability of false alarm is 10^{-4} with the reference window length as a varying parameter.

10.3. SO-and GO-CFAR clutter estimation schemes

Excessive number of false alarms in the CA-CFAR processor at clutter edges and degradation of detection probability in multiple target environments are prime motivations for exploring other CFAR schemes that discriminate between interference and primary targets. Candidate schemes are SO- and GO-CFAR to deal with the two problems, respectively. Here in this section, analysis of the two schemes will be given. The two schemes are modifications to the CA-CFAR scheme, and each of them overcomes one of the two mentioned problems, with the

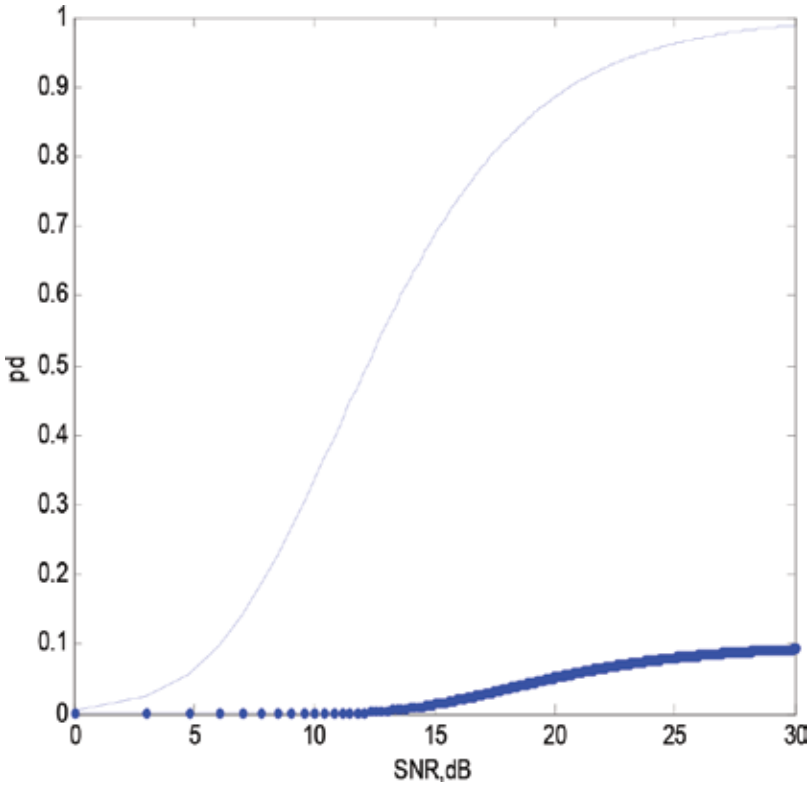

Figure 13. Performance of CA-CFAR processor in a homogeneous environment versus performance in a non-homogeneous environment (two interfering targets).

addition of loss of power when operating in a homogeneous background. As abovementioned, the GO-CFAR maintains the false alarms constant when the clutter edge is encountered in the reference window, while the SO-CFAR resolves the interfering targets.

A modified scheme proposed in [16] known as GO-CFAR is specifically aimed at reducing false alarms at clutter edges. The estimated total noise power is obtained from the larger of two separate sums calculated for leading and lagging reference cells to the CUT. For this scheme, we have (see **Figure 9**)

$$Z = \max(Y_1, Y_2) \tag{35}$$

where

$$Y_1 = \sum_{i=1}^{n} X_i$$

with n=N/2, where N is the number of tested cells. In general, the PDF of Z in (35) is given in [15] as

$$f(Z) = f_1(Z)F_2(Z) + F_1(Z)f_2(Z) \tag{36}$$

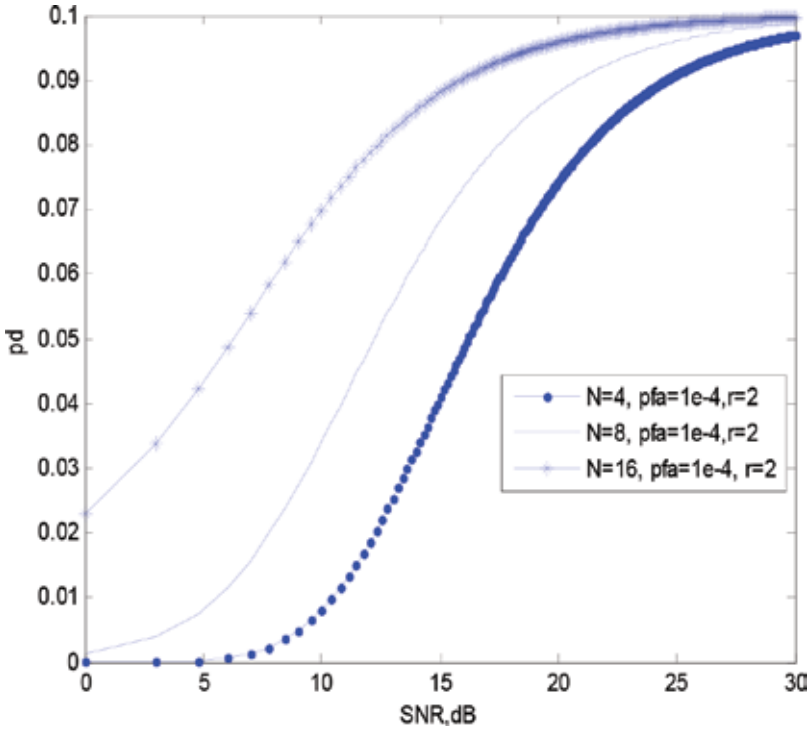

Figure 14. Performance of CA-CFAR at a non-homogeneous background (two interfering targets) with varying reference window and fixed P_{fa}.

where *f*(Z) and F(Z) are the PDF and CDF, respectively. For a homogeneous background, $F_i = G(n,2\mu')$. The false alarm probability in this case is found by computing the moment generating function (MGF) of Z as follows:

$$M_z(T) = \int_0^\infty f_1(y)F_2(y)\exp(-Ty)dy + \int_0^\infty f_2(y)F_1(y)\exp(-Ty)dy = \mathrm{M1} + \mathrm{M2} \tag{37}$$

where

$$f_1(y) = \frac{{\gamma_1}^{-n} y^{n-1} \exp\left(-\frac{y}{\gamma_1}\right)}{(n-1)!} \tag{38}$$

$$f_2(y) = \frac{{\gamma_2}^{-n} y^{n-1} \exp\left(-\frac{y}{\gamma_2}\right)}{(n-1)!} \tag{39}$$

$$F_1(y) = 1 - \exp\left(-\frac{y}{\gamma_1}\right) \sum_{j=0}^{n-1} \left(\frac{y}{\gamma_1}\right)^j / j! \tag{40}$$

$$F_2(y) = 1 - \exp\left(-\frac{y}{\gamma_2}\right) \sum_{j=0}^{n-1} \left(\frac{y}{\gamma_2}\right)^j / j! \tag{41}$$

Substituting Eqs. (38)–(41) into Eq. (37) and after some algebraic manipulations, the following expression is obtained:

$$M_1 = \left(1+\gamma_1\check{T}\right)^{-n} - \sum_{j=0}^{n-1}\binom{n+j-1}{j}{\gamma_1}^{-n}{\gamma_2}^{-j}\left\{\frac{1}{\gamma_1}+\frac{1}{\gamma_2}+\check{T}\right\}^{-(n+j)} \tag{42}$$

$$M_2 = \left(1+\gamma_2\check{T}\right)^{-n} - \sum_{j=0}^{n-1}\binom{n+j-1}{j}{\gamma_2}^{-n}{\gamma_1}^{-j}\left\{\frac{1}{\gamma_1}+\frac{1}{\gamma_2}+\check{T}\right\}^{-(n+j)} \tag{43}$$

Exploiting the assumption that both sides of the window are of homogeneous clutter, we can see in Eqs. (42) and (43) $\gamma_1 = \gamma_2$ therefore

$$P_{fa} = M_1 + M_2 = 2\left(1+\check{T}\right)^{-n} - 2\sum_{j=0}^{n-1}\binom{n+j-1}{j}\left(2+\check{T}\right)^{-(n+j)} \tag{44}$$

The probability of detection for GO-CFAR is simply obtained by setting $\check{T} = \frac{\check{T}}{S+1}$ in Eq. (44), that is,

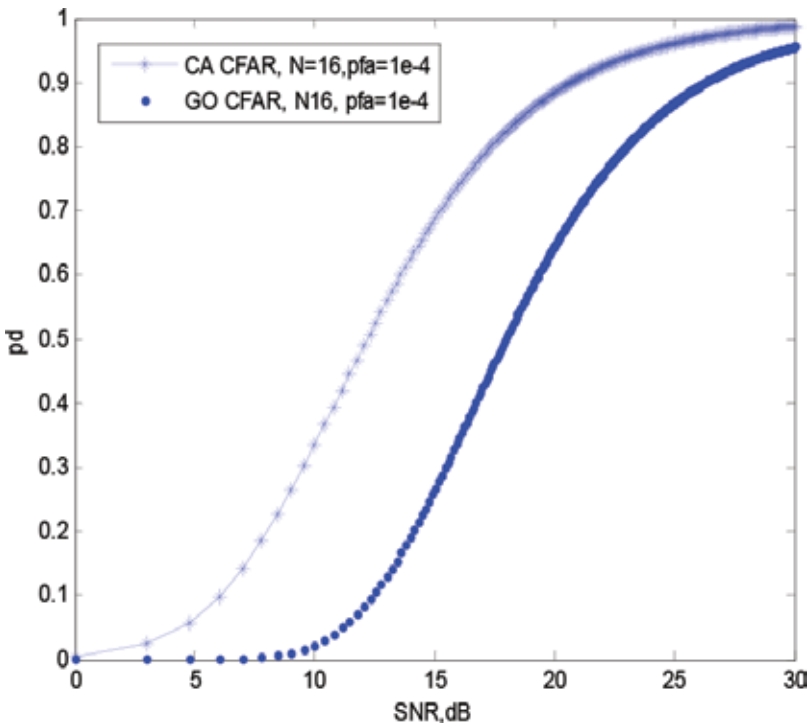

Figure 15. Performance of GO-CFAR compared to CA-CFAR when clutter background is homogeneous.

$$P_d = 2\left(1+\frac{\check{T}}{S+1}\right)^{-n} - 2\sum_{j=0}^{n-1}\binom{n+j-1}{j}\left(2+\frac{\check{T}}{S+1}\right)^{-(n+j)} \tag{45}$$

where $\check{T}$ is the scale factor.

Figure 15 shows the performance of GO-CFAR compared to that of CA-CFAR when the clutter background is homogeneous. It is clear that CA-CFAR outperforms GO-CFAR when both algorithms operate in homogeneous background.

The SO-CFAR is a modification of the CA-CFAR scheme so as to alleviate the problem of the presence of close spaced targets in the reference window. In the SO-CFAR scheme, the estimated power noise represents the smaller value of two sums Y_1 and Y_2. That is [16]

$$Z = \min(Y_1, Y_2) \tag{46}$$

In this case, the PDF of Z is given as [Weiss]

$$f_z = f_1(Z)[1-F_2(Z)] + f_2(Z)[1-F_1(Z)] = f_1(Z) + f_2(Z) - \left[f_1(Z)F_2(Z) + f_2(Z)F_1(Z)\right] \tag{47}$$

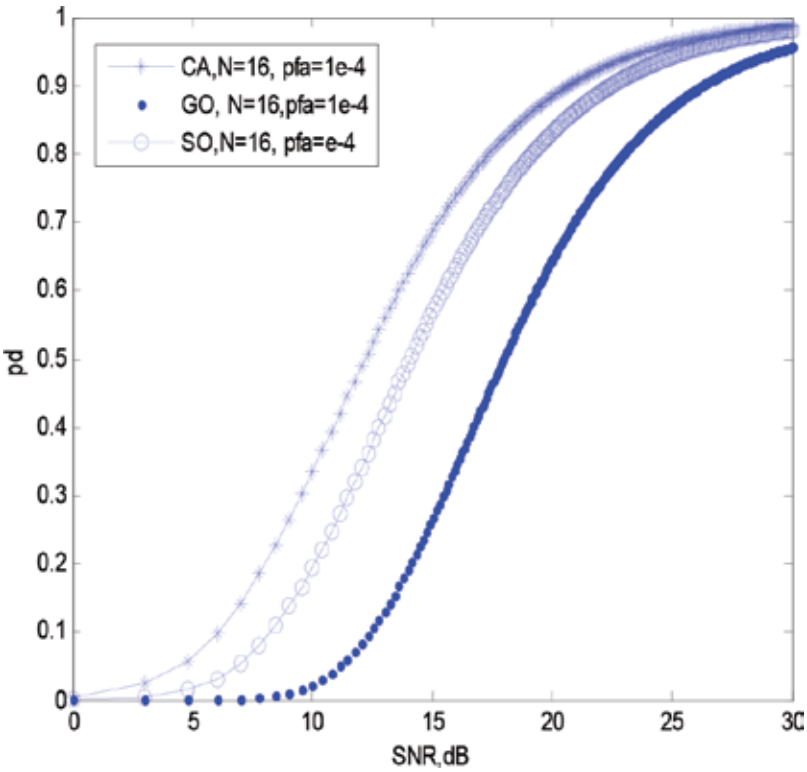

Figure 16. Performance comparison of the three processors (CA-, GO- and SO-CFARs) in the homogeneous background (Pfa = 1e-4).

The probability of SO-CFAR can be obtained by the MGF or

$$P_{fa-SO} = M_{Y1}\left(\frac{\check{T}}{2\mu'}\right) + M_{Y2}\left(\frac{\check{T}}{\mu'}\right) - P_{fa-GO} = 2\sum_{j=0}^{n-1}\binom{n+j-1}{j}\left(2+\check{T}\right)^{-(n+j)} \tag{48}$$

The probability of detection for this scheme can be given by the setting $\check{T} = \frac{\tilde{T}}{S+1}$, that is,

$$P_{d-SO} = 2\sum_{j=0}^{n-1}\binom{n+j-1}{j}\left(2+\frac{\check{T}}{S+1}\right)^{-(n+j)} \tag{49}$$

Figure 16 shows a performance comparison between CA-, GO- and SO-CFARs when the background is homogeneous. When the background of clutter is not homogeneous, that is, the reference window contains clutter edges or more than one target found in the reference window, this situation increases the false alarms when the processor is CFAR.

Author details

Moutaman Mirghani Daffalla[1]* and Ahmed Awad Babiker[2]

*Address all correspondence to: mtnmir@gmail.com

1 Institute of Space Research and Aerospace (ISRA), Khartoum, Sudan

2 Engineering College, Karary University, Omdurman, Sudan

References

[1] Skolnik MI. Introduction to Radar Systems. 3rd ed. Boston: McGraw-Hill; 2001

[2] Skolnik MI. Radar Handbook. New York: McGraw-Hill; 2008

[3] Brookner E. Radar Technology. Dedham: Artech House Inc.; 1977

[4] Mirghani M. Signal Analysis and Processing. Sudan: Communication and Navigation Research Center (CNRC), Karary University; 2012

[5] Smith SW. The Scientist and Engineer's Guide to DSP. San Diego: California Technical Publishing; 1997

[6] Mirghani M. Radar Principles. Sudan: Karary Academy of Technology; 2006

[7] Mirghani M. Radar Signal Coding and Waveform Design. Lambert Academic Publishing. ISBN: 978-3-659-94632-5 2016

[8] Mirghani M. Adaptive multifunction filter for radar signal processing. In: ICCEEE 2013, IEEE Conference, Khartoum; 2013

[9] Haykin S. Adaptive Filter Theory. 4th ed. Upper Saddle: Prentice Hall; 2002

[10] Haykin S, Widrow B. Least-Mean-Square Adaptive Filters. Hoboken: Wiley; 2003

[11] Nathanson FE. Radar Design Principles, Signal Processing and the Environment. 2nd ed. New York: McGraw-Hill Inc.; 1991

[12] Anderson JM. Nonlinear suppression of range ambiguity in pulse Doppler radar. PhD dissertation, Air Force Institute of Technology, Air University; 2001

[13] Bell MR. Diversity and Adaptive Waveform Techniques for Pulse-Doppler Radar and SAR. Indiana: Purdue University; 2006

[14] Rohling H. Radar CFAR thresholding in clutter and multiple target situations. IEEE Transaction on Aerospace and Electronic Systems. 1983;**AES-19**(4):608-618

[15] Weis M. Analysis of some modified cell-averaging CFAR processors in multiple target situations. IEEE Transaction on Aerospace and Electronic Systems. 1982;**AES-18**(1):102-113

[16] Gandhi PP, Kassam SA. Analysis of CFAR processors in non-homogeneous background. IEEE Transaction on Aerospace and Electronic Systems. 1988;**24**(4):427-444

Chapter 10

Bispectrum- and Bicoherence-Based Discriminative Features Used for Classification of Radar Targets and Atmospheric Formations

Alexander Totsky and Karen Egiazarian

Additional information is available at the end of the chapter

http://dx.doi.org/10.5772/intechopen.71034

Abstract

This chapter is dedicated to bispectrum-based signal processing in the surveillance radar applications. Detection, recognition, and classification of the targets by surveillance radars have various applications including security, military intelligence, battlefield purposes, boundary protection, as well as weather forecast. One of the particular and effective discriminative features commonly exploited in modern radar automatic target recognition (ATR) systems is the micro-Doppler (m-D) contributions extracted from joint time-frequency (TF) distribution. However, a common drawback of the energy-based strategy lies in the impossibility to retrieve additional particular information related to frequency-coupling and phase-coupling contributions containing in the radar backscattering. Phase coupling contains additional discriminative features related to individual target properties. Bispectrum-based strategy allows retrieving a phase-coupled data containing unique discriminative features related to individual target properties. Bispectrum tends to zero for a stationary zero-mean additive white Gaussian noise (AWGN), providing smoothing of AWGN in TF distributions. Hence, bispectrum-based approach allows improving extraction of robust discriminative features for ATR radar systems.

Keywords: surveillance radar, micro-Doppler frequency, instantaneous frequency time-frequency distribution, vegetation clutter, radar target detection and classification, bispectrum, bicoherence, phase coupling, high-resolution radar range profile, weather radar, "angel echo"

1. Introduction

Bispectral density or third-order cumulant spectrum, in opposite to the common energy spectrum, allows not only describing the statistical properties of an observed process more

correctly and profoundly but also extracting novel information features such as the contributions caused by spectral component correlation relationships. Moreover, bispectrum estimate allows to extract the phase relationships existing between the spectral components contained in the observed process. Therefore, the main benefit of bispectrum in comparison with energy spectrum is in the preservation of phase information contained in a process under study and possibility to recover this important information.

Triple autocorrelation function (TAF) $R_x(k, l)$ of a discrete process $\{x^{(m)}(i)\}$, m = 1, 2,…, M is related to the class of third-order statistics [1]. TAF is a function of two-shift variables, and it can be written in the discrete form as

$$R_x(k,l) = \left\langle \sum_{i=0}^{I-1} \left[x^{(m)}(i) - E\right]\left[x^{(m)}(i+k) - E\right]\left[x^{(m)}(i+l) - E\right] \right\rangle_{M\to\infty}, \tag{1}$$

where E is the mean value; $k = -I + 1,\ldots, I - 1$ and $l = -I + 1,\ldots, I - 1$ are the shift indices.

According to the definitions given in [1], bispectrum is the 2-D direct Fourier transform (DFT) of TAF. Unlike common real-valued spectral density, bispectrum is the complex-valued function $\dot{B}_x(p,q)$ of two independent frequency variables p and q defined as

$$\dot{B}_x(p,q) = \sum_{k=-I+1}^{I-1} \sum_{l=-I+1}^{I-1} R_x(k,l) \exp\left[-j2\pi(kp + lq)\right], \tag{2}$$

or given in the form of

$$\dot{B}_x(p,q) = \left\langle \dot{X}^{(m)}(p)\dot{X}^{(m)}(q)\dot{X}^{*(m)}(p+q) \right\rangle_{\infty}, \tag{3}$$

where $\dot{X}^{(m)}(p)$ is the DFT of mth realization $\{x^{(m)}(i)\}$, m = 1, 2,…, M; * denotes complex conjugation; $\dot{B}_x(p,q) = \left|\dot{B}_x(p,q)\right| \exp\left[j\gamma_x(p,q)\right]$; $\left|\dot{B}_x(p,q)\right|$ and $\gamma_x(p, q)$ are the magnitude bispectrum (*bimagnitude*) and phase bispectrum (*biphase*), respectively; $p = -I + 1, \ldots, I - 1$ and $q = -I + 1, \ldots, I - 1$ are the frequency indices.

According to (3), bispectral density $\dot{B}_x(p,q)$ is the ensemble averaging of triple product of three complex-valued functions related to three different frequencies: p, q, and $p + q$. It means that bispectrum can be defined as the correlation measure between the frequencies p, q, and $p + q$ contained in the process. The main properties of bispectrum [1] are listed below.

1. Bispectrum tends to be zero for stationary zero-mean Gaussian process. Note, however, that for a process with non-symmetrical probability density function (PDF), its bispectrum differs from zero. This property allows to extract non-Gaussian contributions against the background of Gaussian noise.

2. TAF and bispectrum are equal to zero for deterministic signals having zero asymmetry. For example, TAF and bispectrum are of zero values for a simple signal x(i) = A0 cos(2πfi). However, when some little non-linear distortions appear or when a constant component is

added to a harmonic signal, TAF and bispectrum become non-zero valued functions. The latter property can serve as a very sensitive tool to detect and evaluate non-linear distortions contained in the observed signal.

3. Bispectrum is the periodical function with period equal to 2π

$$\dot{B}_x(p,q) = \dot{B}(p+2\pi, q+2\pi). \tag{4}$$

4. Bispectral density has the following symmetry property

$$\begin{aligned}\dot{B}(p,q) &= \dot{B}(q,p) = \dot{B}^*(-p,-q) = \dot{B}^*(-q,-p)\\ &= \dot{B}(-p-q,q) = \dot{B}(p,-p-q) = \dot{B}(-p-q,p) = \dot{B}(q,-p-q).\end{aligned} \tag{5}$$

By using (5), bispectrum can be defined by a hexagon given in the bifrequency plane. It follows from (5) that bispectrum of a real-valued process can be defined completely just only within the area of the main triangular domain given by the inequalities

$$q \geq 0, p \geq q, p+q \leq I\text{–}1. \tag{6}$$

It is sufficient to use the symmetry relationships (5) taking into account (6) to compute bispectrum function within all other parts of hexagonal domain. Note that the conditions (6) limiting the total number of bispectrum samples allow to decrease essentially the memory requirements and, hence, to reduce the computational time of bispectrum.

5. In many practical cases, it is necessary to detect and estimate the phase coupling contributions. Since the phase relationships are lost in power spectral density estimator, it is impossible to extract information about phase coupling from common power spectral density. Meanwhile, it is possible to do that by using bispectrum

This property can be explained by considering the following two processes

$$x_1(i) = \cos\left(2\pi f_1 i + \varphi_1\right) + \cos\left(2\pi f_2 i + \varphi_2\right) + \cos\left(2\pi f_3 i + \varphi_3\right), \tag{7a}$$

$$x_2(i) = \cos\left(2\pi f_1 i + \varphi_1\right) + \cos\left(2\pi f_2 i + \varphi_2\right) + \cos\left[2\pi f_3 i + \left(\varphi_1 + \varphi_2\right)\right], \tag{7b}$$

where $f_3 = f_1 + f_2$ are the frequencies: φ_1, φ_2, φ_3 are the initial phases that are supposed to be independent random values varying within the limits of [0, 2π] and having uniform distribution law.

Assume that the frequency f_3 in (7a) is an independent component, and an initial phase ϕ_3 corresponding to this frequency is an independent random value. Assume also that the frequency f_3 in (7b) is the result of phase coupling. It is evident that the power spectrum densities computed for the processes (7a) and (7b) are of the same shape because each considered process contains the contributions of the same frequencies f_1, f_2, and f_3, i.e., $P_{x1}(p) = P_{x2}(p)$. At the same time, magnitude bispectrum of the process (7a) tends to be zero, i.e., $\dot{B}_{x1}(p,q) = 0$, and the magnitude bispectrum of the process (7b) is of non-zero value, i.e., $\dot{B}_{x2}(p,q) \neq 0$.

6. Invariance property of bispectrum to a signal time delay or signal spatial shift: this property can be demonstrated by the following simple expression

$$\begin{aligned}\dot{B}_{x\,\tau}(p,q) &= \dot{X}_{\tau}(p)\dot{X}_{\tau}(q)\dot{X}_{\tau}(-p-q) = \\ &= \dot{X}(p)\dot{X}(q)\dot{X}(-p-q)\exp j2\pi\{-\tau p-\tau q-\tau[(-p-q)]\} = \dot{B}_{x}(p,q),\end{aligned} \tag{8}$$

where $\dot{X}_{\tau}(p) = \dot{X}(p)\exp(-j2\pi\tau)$ is the Fourier transform of a process shifted by a τ value in the temporal domain. It follows from (8) that both for the original process $x^{(m)}(i)$ and for its replica $x^{(m)}(i\text{-}\tau)$ shifted by τ, the bispectra are congruent.

2. Extracting bispectral discriminative features from radar backscattering provoked by walking pedestrian

One of the most important problems arising in radar automatic target recognition (ATR) systems is the extraction of robust discriminative features contained in raw radar backscattering contaminated by clutter contribution. The Doppler velocity spectrum commonly serves for ground moving radar target detection, recognition, and classification. Often, the processed radar echo signals are of non-stationary behavior, whence the common notion of frequency becomes meaningless and a new parameter *instantaneous frequency* (IF) must be exploited in order to analyze how the Doppler spectral content varies with time. IF is defined as the frequency value existing within a short-time interval, and a given parameter allows one to estimate the distribution of spectral peaks varying with dwell time.

Note that the most frequently used tool for spectral analysis of non-stationary signals is an estimation of *energy* per unit time per unit frequency. Spectrogram is a typical representative of such energy-based estimators. Since the possible existing phase relationships between harmonics are lost in energy spectra, it is impossible to extract *phase-coupled frequencies* by means of time-varying energy spectrum. In other words, energy spectrum is unable to extract phase-coupled instantaneous frequencies (PCIFs) contained in time sequences processed. This peculiarity is the most serious shortcoming of energetic versions of evolutionary spectral estimators.

A walking person can be considered in the form of a complex physical phenomenon with simultaneous motion of different body parts: the torso, the legs, and the arms. Hence, for an extended human body, the backscattered field is a sum of multiple contributions.

Time-varying phase contributions are of paramount importance. Doppler frequencies provoked by swinging body parts may be *phase coupled*. In addition, radar returns obtained by applying vertical or horizontal polarizations differ one from another just by different spatial phase distribution of the reflection coefficients for corresponding vertical or horizontal polarizations.

The observed discrete-time received multicomponent and non-linearly FM radar returns corresponding to the vertical $y^{V}(i)$ and horizontal $y^{H}(i)$ polarizations can be written, respectively, as

$$y^{V}(i) = \sum_{m=1}^{M} A_m^V(i)\cos\left[\Phi_m^V(i)\right] = \sum_{m=1}^{M} a_m^V(i)\cos\left[\varphi_m^V(i)\right]F^2(\theta_m)\cos\left\{\frac{4\pi}{\lambda_0}[r_m(i)-r_0(i)]\right\}, \tag{9a}$$

$$y^{H}(i) = \sum_{m=1}^{M} A_m^H(i)\cos\left[\Phi_m^H(i)\right] = \sum_{m=1}^{M} a_m^H(i)\cos\left[\varphi_m^H(i)\right]F^2(\theta_m)\cos\left\{\frac{4\pi}{\lambda_0}[r_m(i)-r_0(i)]\right\}, \tag{9b}$$

where $a_m^V(i)$ and $a_m^H(i)$ are the time-varying magnitudes of the local reflection coefficients corresponding to an arbitrary mth object scattering center for vertical and horizontal polarizations, respectively; $\varphi_m^V(i)$ and $\varphi_m^H(i)$ are the local time-varying phases for vertical and horizontal polarizations, respectively; $i = 1, 2, \ldots, I$ is the sample index; $F(\theta)$ is the radar antenna pattern; θ_m is the angle location of the m-th object scattering center; $r_m(i)$ and $r_0(i)$ are the time-varying distances from antenna phase center to the arbitrary m-th moving object scattering center and object phase center, respectively; λ_0 is the radiated wavelength; $A_m(i)$ and $\Phi_m(i)$ are the total radar echo signal magnitude and phase corresponding to the m-th object scattering center, respectively.

Two motion contributions are involved in the model (9a) and (9b): first, the *translation motion* of the human torso provoking approximately constant low Doppler frequency shift due to the relatively constant and low speed of the human body and, second, the *swinging motion* of the legs and arms provoking time-varying micro-Doppler frequency shifts caused by different non-uniform time-varying velocities of swinging body parts. These IFs may be related due to *phase coupling*.

Suggested approach takes into account the fact that the swinging torso, legs, and arms are not independent sources of Doppler frequency shifts but are related via the same "carrier" (the human torso) that can be considered as the "common basis" for the swinging legs and arms. Therefore, one can expect the presence of phase coupling contributions in radar returns (9a) and (9b).

Let us define the short-time bispectrum estimate of a transient signal $y(i, n)$, whose time duration is significantly shorter than the total time observation interval of I samples contained in (9a) and (9b). Transient signal $y(i, n)$ can be separated from the total observation (9a) and (9b) by a sliding window that moves step by step along the recorded process and takes $n = 1, 2, \ldots, N$ non-overlapping locations.

Time-varying bispectrum estimate can be computed according to (3) as follows

$$B(p,q;n) = Y(p,n)Y(q,n)Y^*(p+q,n) = |B(p,q;n)| \exp\left[j\beta(p,q;n)\right], \tag{10}$$

where $Y(p, n) = |Y(p, n)| \exp[j\varphi(p, n)]$ is the short-time Fourier transform of the transient signal $y(i, n)$; $|B(p, q; n)|$ and $\beta(p, q; n)$ are the time-varying bimagnitude and biphase, respectively; $p = 1, 2, \ldots, P$ and $q = 1, 2, \ldots, P$ ($P \ll I$) are the frequency indices.

Coherent, homodyne, and surveillance radar operating in continuous-wave mode at the wavelengths of $\lambda_0 = 2$ cm, 3 cm, and 8 mm with the vertical polarization and polarimetric radar operating at the wavelength of $\lambda_0 = 8.8$ mm with the vertical and horizontal polarizations have been exploited for experimental study. The output of the 10 bits' ADC allows collecting frequency radar returns containing Doppler frequency shifts. Experimental investigations have been carried out during the spring and summer periods. It is evidently seen from the histogram in **Figure 1** the presence of a large number of the PCIFs contained in the radar return.

First, we consider the case of vertical polarization. The radar returns were recorded during total data collection time of 63 s that corresponds to 200,000 digitized signal samples. The window width of 256 samples sliding along the signal provides frequency resolution of

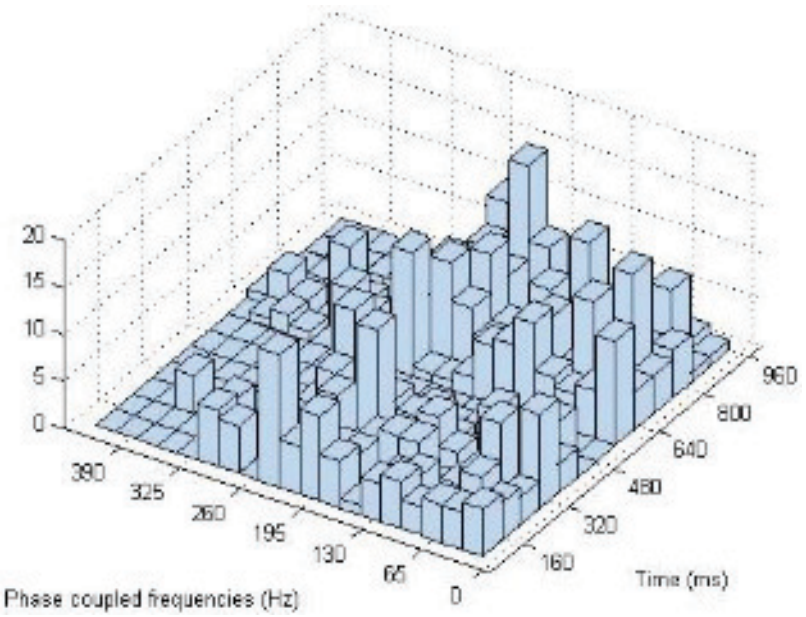

Figure 1. The histogram of the PCIF distribution computed for a walking human.

approximately 12.4 Hz. The sequence of time-varying bispectrum estimates contained 256 × 256 samples has been computed according to (10). Phase coupling contributions corresponding to the bimagnitude peaks were mapped from bifrequency plane onto the TF plane as two separate values on the frequency axis in the coordinates of p and q.

TF distribution of the PCIFs and bimagnitude estimates are demonstrated in **Figure 2**.

The analysis of the PCIF evolutionary behavior in **Figure 2a** indicates the contributions provoked by both the swinging pedestrian torso in the low-frequency range (30 Hz) and the legs and arms in the high-frequency range (from 120 through 240 Hz).

The following question arises: is there a difference between the radar Doppler TF signatures obtained with the vertical and horizontal polarizations and how much they differ one from another? In fact, according to the signal model (9a) and (9b), the last terms (electrical distances) in the quadruple products in the sums are the same for the vertical and horizontal polarizations. The distinction is due to the different behavior of the local time-varying phases $\varphi_m^V(i)$ and $\varphi_m^H(i)$. It can be explained by the distinction *in-phase spatial distributions* in a human body for the vertical and horizontal polarizations. In order to confirm this hypothesis experimentally, we pay attention to the difference between the bimagnitude estimates computed for the vertical and horizontal polarizations for a pedestrian walking toward the radar.

The plots of the bimagnitudes are shown in **Figure 2b** and **c** for vertical and horizontal polarization, respectively. The difference between these bimagnitude estimates is clearly seen.

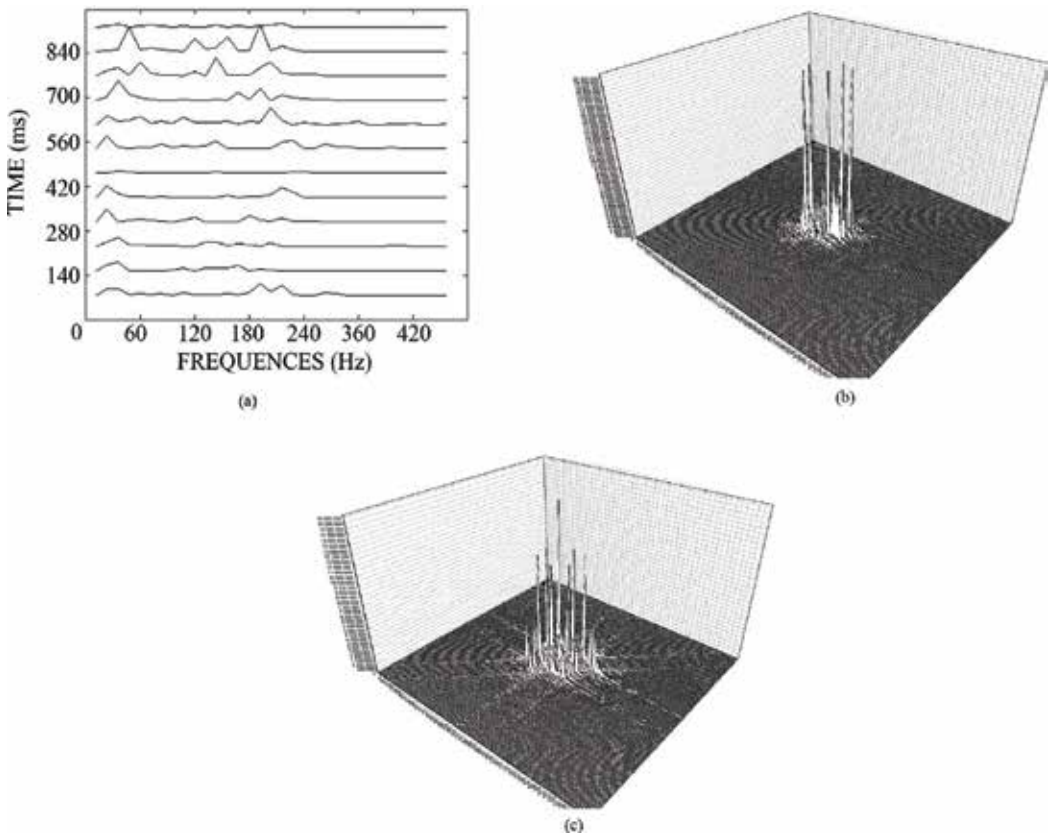

Figure 2. TF distribution of the PCIFs for a walking human, vertical polarization, λ_0 = 2 cm. (a) Bimagnitude: vertical (b) and horizontal (c) polarization.

TF distributions computed by common energy-based strategy do not provide discriminating contributions provoked by the vertical and horizontal polarizations. Using proposed bispectrum-based approach permits recognizing the difference between PCIF TF distributions computed for the vertical and horizontal polarizations. This important peculiarity of the suggested approach can serve as a new perspective classification feature for solving classification problems in radar ATR systems.

Let us define the short-time *cross-bispectrum* estimate $B_{VH}(p, q; n)$ in the form of

$$B_{VH}(p,q;n) = S_V(p,n)S_V(q,n)S_H^*(p+q,n) = |B_{VH}(p,q;n)| \exp\left[j\beta_{VH}(p,q;n)\right], \tag{11}$$

where S_V $(p,\ n)$ and S_H $(q,\ n)$ are discrete time-varying Fourier transforms of the transient signals $y^V(i,\ n)$ and $y^H(i,\ n)$, respectively; $|B_{VH}\ (p,\ q;\ n)|$ and $\beta_{VH}\ (p,\ q;\ n)$ are the time-varying cross-bimagnitude and cross-biphase, respectively.

Note that if there exists a phase coupling between two certain frequencies contained in the signals (9a) and (9b), a peak in the cross-bimagnitude distribution $|B_{VH}\ (p,q;n)|$ will appear at

the intersection of two frequency samples p and q in the bifrequency plane. Otherwise, for the Gaussian process provoked by a backscattering from vegetation, the cross-bimagnitude tends to be zero. Therefore, cross-bispectrum estimates (11) will contain the peaks caused by phase coupling. This important characteristic can serve for retrieving novel detection and recognition features for radar objects moving in a growing vegetation clutter.

The radar returns corresponding to the V and H polarizations both for a walking pedestrian and vegetation stirred by a light breeze were measured and recorded in the PC memory with the time interval of approximately 1 min. The sequence of N cross-bispectrum estimates (11) contained 256 × 256 samples each has been computed. The peaks of cross-bimagnitude $|B_{VH}(p,q;n)|$ have been analyzed, and their values were projected into the TF domain. The plots of TF distributions computed for a human walking in the vegetation clutter and the vegetation clutter itself are shown in **Figures 3** and **4**, respectively.

The number of pronounced cross-bimagnitude peaks is observed in **Figure 3**: the torso provokes the peaks in the low-frequency range, and the responses of swinging arms and legs are observed in a high-frequency range. The TF distribution computed for the vegetation clutter

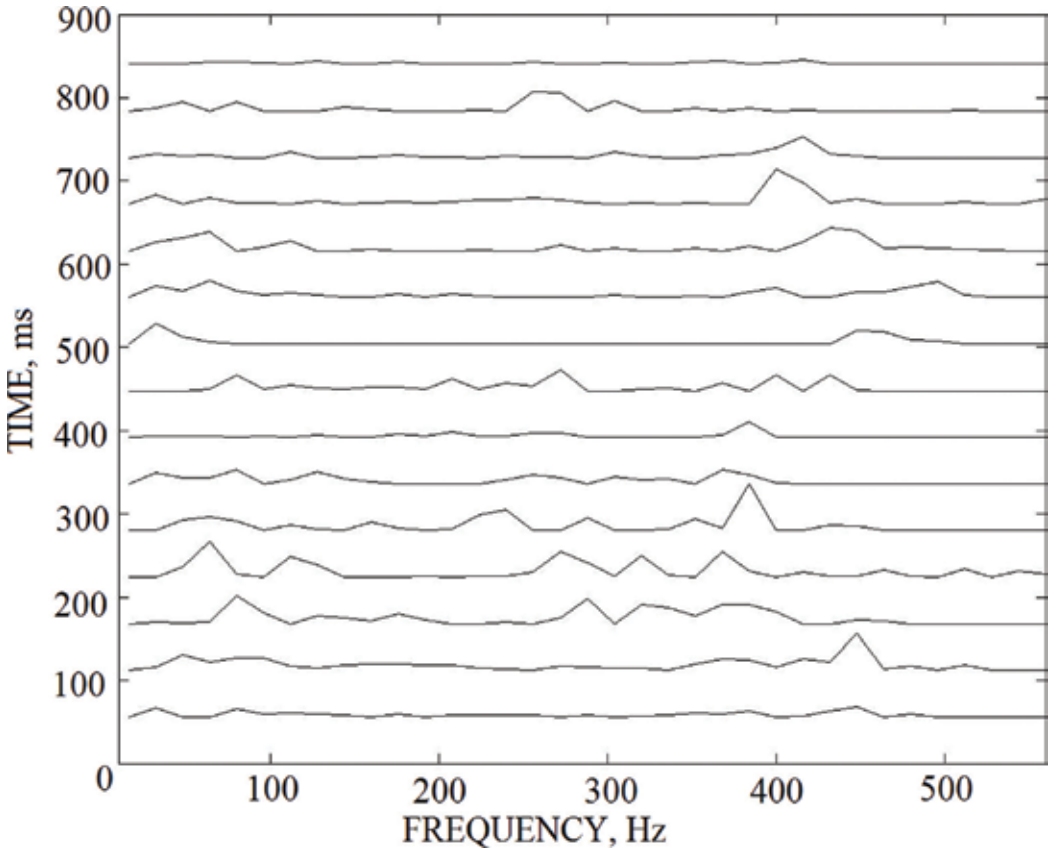

Figure 3. TF distribution for a human walking in vegetation clutter.

http://dx.doi.org/10.5772/intechopen.71034

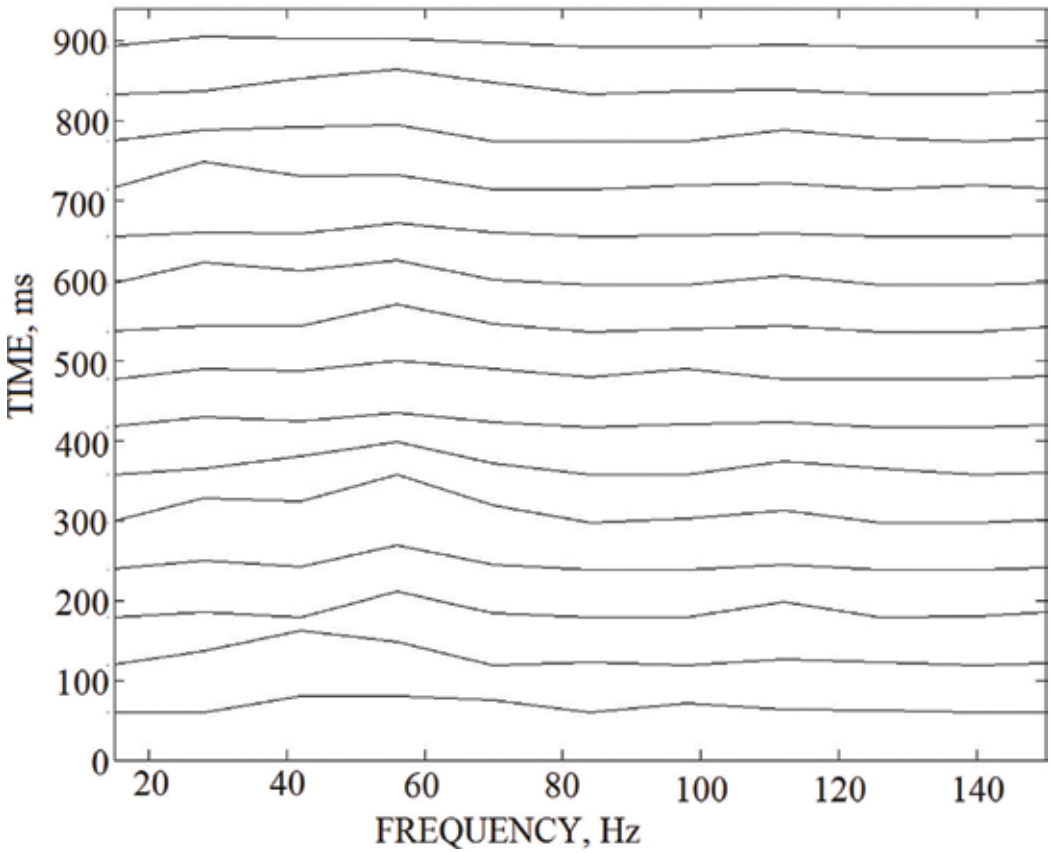

Figure 4. TF distribution for vegetation clutter.

differs from that of a walking human substantially: the cross-bimagnitude peaks are observed only in the low-frequency range, and their values are considerably smaller in comparison to those of a walking human. It permits one to single out and identify a human walking in a vegetation clutter by the TF signature proposed.

Note that detection and classification of moving objects in through-foliage environment is one of the most important problems arising in surveillance radar systems serving for state border protection in the forest environment.

3. Classification of aerial radar targets by using bicoherence-based features extracted from micro-Doppler content

The problem of classification of various types of aerial targets by extraction of the information features contained in radar returns is of particular interest for ATR systems [2]. High-resolution radar range profile (HRRP) can be considered as a projection of a target spatial intensity distribution of the backscattered electromagnetic field onto the radar line of sight. Therefore,

HRRP contains certain information about geometry of aircraft. Contributions caused by rotating turbine or propeller blades and contained in radar backscattering in the form of micro-Doppler data [3] also can contain supplementary classification information about aircraft's particular characteristics. Both HRRPs and jet engine modulation (JEM) allow extracting classification features conforming to the aircraft geometry and particular engine characteristics.

As a result of aerial target travel over a large azimuth angle, its HRRPs measured and recorded during this travel considerably suffer by three main reasons: speckle, rotational range migration, and translational range migration. Due to the speckle effect, HRRP can fluctuate essentially even for slight aspect variations (about tenths of one angle degree), i.e., only a slight rotation of aerial target in elevation or aspect azimuth is enough to provoke considerable variations in the HRRPs. A typical example demonstrating considerable variability of HRRPs for the aircrafts AH-64, An-26, and B-52 under consideration is shown in **Figure 5** for three fixed aspect angles of 185°, 190°, and 195°. These HRRPs have been computed by using radar backscattering models described in [2].

It is well-known that performance achieved in ATR systems largely depends both on robustness of information features and dimensionality of classification feature vector. Consequently, the most serious limitation for using HRRPs for ATR is in their extreme variability. In addition, when the signal-to-noise ratio (SNR) is of rather low value, classification probability rate considerably degrades due to the contamination of radar signature by the noise. Therefore, search for both noise-robust and aspect-angle robust classification features is of paramount interest in ATR radar systems.

Phase information contained in radar returns can provide additional knowledge about the target. Unfortunately, phase information contained in radar returns in the form of *phase coupling* of micro-Doppler harmonics is irretrievably lost in common HRRP. In addition, micro-Doppler content is less sensitive to aspect angle variations compared to the HRRPs. This peculiarity can give certain advantages over HRRP-based approaches for ATR.

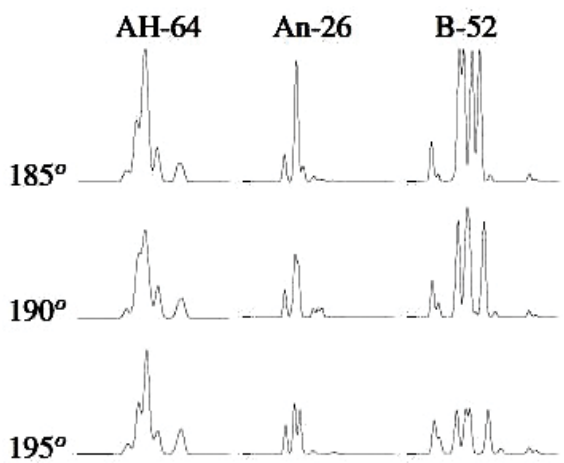

Figure 5. Examples of dependence of HRRP on aspect angle.

The approach which is most frequently cited for comparison of the performances of aircraft classification has been proposed by Zyweck and Bogner in [4]. We will refer to it as "Zyweck and Bogner technique" (ZBT). ZBT contains the following data processing steps.

- Computation of the following sequence of N HRRPs as

$$Y_n(m) = |K_n(m)|^2, n = 1, 2, \ldots, N; \quad m = 1, 2, \ldots, M, \tag{12}$$

where $K_n = S(:, n) \in \mathbf{C}^n$ is the matrix representation related to the sequence of N radar returns accumulated in the form of M in-phase (I) and M quadrature-phase (Q) digital samples, respectively.

- Each HRRP must be normalized to provide level invariance property. Aligning consecutive HRRPs (12) by using correlation procedure and following averaging of normalized HRRPs $\widehat{Y}_n(m)$ as

$$R(m) = \sum_{n=1}^{P} \widehat{Y}_n(m), \tag{13}$$

where P is the number of HRRPs selected for extraction of classification features.

- Direct Fourier transform is computed for averaged HRRP (13). In order to achieve translation invariance property, magnitude Fourier spectrum is used for extraction of classification features.

In practice, HRRPs consecutively accumulated according to the chain of received pulses have variable spatial shifts observed within fixed range strobe. These shifts are caused by translation of aircraft, and hence, migration of intensity contributions from one range cell to another is observed. ZBT exploits aligning procedure based on correlation analysis to provide *translation invariance*.

One more approach using classification feature extraction from HRRP is proposed in [5] by Kim et al. Below it will be referred as "Kim technique" (KT). The main idea behind KT is to use the first 20 central moments as the features. KT contains the following data processing steps:

- computation of range profiles according to (12) and their normalization;

- aligning consecutive HRRPs by using correlation procedure and averaging of aligned range profiles according to (13); and

- using the first 20 central moments related to averaged HRRP as classification features.

Micro-Doppler content can be extracted from the following accumulation of radar returns by the procedure represented in [3] as:

$$D(n) = \sum_{m=1}^{M} K_n(m). \tag{14}$$

Joint TF distribution of radar echo-signal can be defined by the following short-time Fourier transform:

$$TF(f,t) = \sum_{l=1}^{L} D\left(l + (t-1)(L-Q)e^{\frac{j2\pi ft}{L}} w(l)\right), \tag{15}$$

where L is the length of suitable smoothing window $w(l)$; Q is the number of overlapping samples; f and t are the IF and time indices, respectively. The dimensionality of TF distribution (15) can be defined as $\mathbf{C}^{\mathrm{LxG}}$, where G = (P−Q)/ (L−Q).

Examples of spectrograms computed for three types of aerial targets are shown in **Figure 6**.

Each of these radar signatures contains micro-Doppler contributions inherent in particular aerial target. These radar signatures are of periodical behavior, and a period depends on the radial velocity of corresponding rotating parts. The contributions caused by front and back helicopter blades can be recognized in the spectrogram shown in **Figure 6a**. The front blade provokes larger radar cross-section (RCS) value and, in the position perpendicular to the radar line of sight, excites harmonics in the whole spectrum. The back helicopter blade provokes smaller RCS value and excites harmonics with smaller frequency bandwidth. The patterns referred to the aircrafts An-26 and B-52 and shown in **Figure 6b** and **c**, respectively, demonstrate higher periodicity frequency, and they look like more intricate radar signatures.

An approach proposed in [4] provides a translation invariance property for moving radar target classification dealing with cepstrum-based features. Rather low-dimensional and shift-invariant classification features can be extracted by using the cepstrum coefficients $C(.)$. They are computed by using TF distribution (15) by the following transform

$$C(.) = \left| IDTF\left(\log_{10}\left(\frac{1}{T}\sum_{t=1}^{T} |TF(:,t)|^2 \right) \right) \right|^2, \tag{16}$$

where IDFT denotes the indirect discrete Fourier transform.

Note that a dimensionality of the cepstrum-based classification features extracted by using transform (16) depends on required frequency resolution. It is relevant to note here that frequency resolution depends on the window length equal to L samples (see (15)).

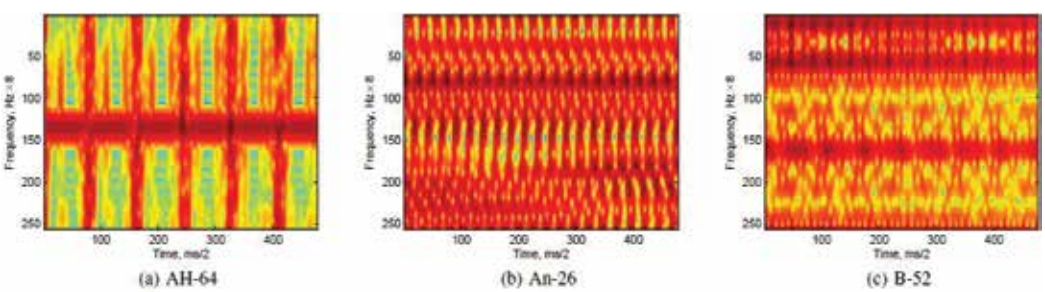

Figure 6. Spectrograms of aerial targets computed for aspect angle equal to 185°: (a) helicopter AH-64 Apache; (b) military transport aircraft An-26; and (c) B-52 Stratofortress.

Suggested feature extraction strategy is based on *bicoherence estimation* of radar data [6]. In order to compute bicoherence estimates from finite data records, first, the following evolutionary sequence of short-time bispectrum estimates $B_t(f_1, f_2)$ corresponding to TF distributions (15) are computed as:

$$B_t(f_1,f_2) = TF(f_1, t)TF(f_2, t) \quad TF^*(f_1 + f_2 \quad t). \tag{17}$$

Estimation of the bimagnitude of radar returns allows extracting information about presence of *phase coupling* in micro-Doppler content. It makes it possible to extract the features related to novel particular properties of target under classification.

Squared bicoherence version defined in [1] can serve as a quantitative measure of phase coupling. Squared bicoherence $\widehat{b}^2(f_1,f_2)$ can be interpreted as the proportion of signal energy corresponding to the frequency $(f_1 + f_2)$ which is *coupled* with the frequencies f_1 and f_2 as follows:

$$\widehat{b}^2(f_1,f_2) = \left(\left|\frac{1}{T}\sum_{t=1}^{T} B_t\ (f_1,f_2)\right|^2\right) / \left[\left(\widehat{X}(f_1,f_2)\ \widehat{P}(f_1,f_2)\right)\right], \tag{18}$$

where $\widehat{P}(f_1 + f_2) = \frac{1}{T}\sum_{t=1}^{T} \left|TF(f_1 + f_2)\right|^2$ is the power spectrum estimate averaged over T finite data samples; $\widehat{X}(f_1,f_2) = \frac{1}{T}\sum_{t=1}^{T} \left|TF(f_1 + f_2)\right|^2$.

The bicoherence (18) values vary within the limits of [0, 1]. If bicoherence tends to $\widehat{b}^2(f_1,f_2) \neq 0$, it means that there exists a phase coupling at some pairs of frequencies, and if $\widehat{b}^2(f_1,f_2) = 0$, it means that there is no phase coupling in the signal under study.

Note that, unfortunately, the value of bicoherence estimate (18) depends on variations of target velocity. In order to provide target velocity invariance property, the following bicoherence-based feature (referred below as Bic) is introduced as

$$Bic = \left|F_{2D}\left(\widehat{b}^2(f_1,f_2)\right)\right|, \tag{19}$$

where F_{2D} denotes the 2-D Fourier transform.

Examples of bicoherence estimates (19) are illustrated in **Figure 7**. The bicoherence signature computed for helicopter AH-64 corresponds to the contribution of numerous phase-coupled harmonics, and $\widehat{b}^2(f_1,f_2)$ tends to the unity for a multiple number of points distributed in bifrequency plane. In contrast, bicoherence estimate computed for aircraft An-26 has the small number of phase-coupled harmonics. Moreover, only two points can be found with contribution larger than value of 0.1. The bicoherence estimate computed for aerial target B-52 has a number of frequency coupled responses with phase coupling coefficient larger than 0.6.

Two different types of classifiers are studied in simulations [7–9]. The first classifier is the support vector machine (SVM) belonging to the *non-probabilistic linear* classifiers, and the second

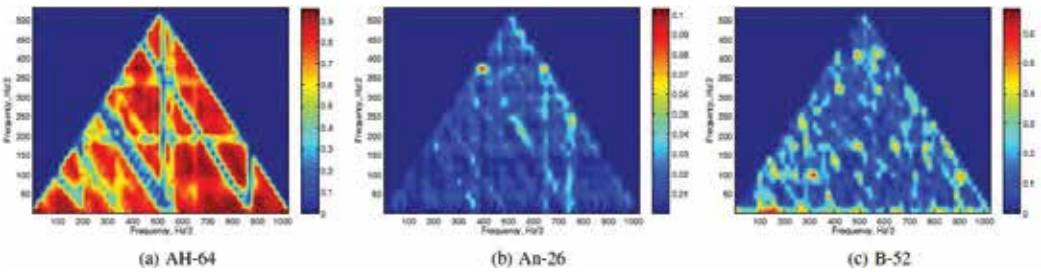

Figure 7. Bicoherence estimates.

type is the Naive Bayes Classifier (NBC) belonging to the *probabilistic linear* classifiers. Linear discriminant analysis (LDA) [5] is applied for reduction of feature vector dimensionality.

Modeled radar echo-signals backscattered by different flying aircrafts are computed in the sequences of I and Q samples by using the software described in [2]. Bandwidth of chirp radar signal equal to $\Delta f = 150$ MHz provides range resolution of $\Delta R = c/2\Delta f = 1$ m. Pulse repetition frequency and central wavelength are equal to 2 KHz and 3 cm, respectively. The coherent chain of $N = 2000$ chirp pulses is received within observation time interval equal to 1 s.

Aerial targets of three different types are studied: helicopter AH-64 (the speed is of 160 km/h and height is of 200 m) and airplanes An-26 (the speed is of 400 km/h and height is of 2000 m) and B-52 (the speed is of 800 km/h, height is of 2000 m). For each target, data are available in the form of $N = 2000$ realizations related to the radar returns recorded within 1 s. Each radar return corresponding to reception of one pulse contains $M = 1200$ I and Q digital samples. Three fixed values of aspect angles equal to A = {185°, 190°, or 195°} are considered in computer simulations. The aspect angle equal to $\alpha = 180°$ corresponds to the situation, when the aircraft is flying toward the radar.

Classification probability rates are examined depending on the following three different scenarios. Under *Scenario #1*, a half of received signal samples related to each of three abovementioned aspect angles are used for training, and the remainder half is used as testing data. For extraction the TF-based classification features, the parameters used in TF distribution (19) are selected to be equal to $L = 56$ and $Q = 46$, and Hamming window is exploited in computer simulations.

According to *Scenario* #2, radar data conforming to one of three aspect angles equal to A = {185°, 190°, or 195°} are used for training database, and the records related to other two aspect angles are used for testing procedure. Step by step, each radar record from three available aspect angles is used one time for training and other two times for testing procedure. Under *Scenario #3*, data accumulated for two aspect angles are used for training procedure, and the remainder is used for testing. In the latter case, three sets of radar data corresponding to different aspect angles are examined, and three combinations of testing and training sets are possible for study. For each of them, classification probability rate is estimated, and final result is evaluated by averaging.

Table 1 shows the results obtained for three types of aerial targets under abovementioned three scenarios. It can be seen from *Scenario* #1 that both SVM and NBC classifiers provide

	Classifier	Feature extraction technique			
		ZBT	KT	Cepstrum	Bic
Scenario #1	SVM	99.99	99.98	95.51	98.98
	NBC	99.97	93.06	98.67	100
Scenario #2	SVM	63.65	76.5	76.89	83.9
	NBC	71.8	79.32	77.38	–
Scenario #3	SVM	78.52	85.63	90.97	87.14
	NBC	75.92	79.46	88.15	82.78

Table 1. Classification probability rate computed in percent.

approximately similar classification probability rates. The best performance is achieved by ZBT and Bic technique. HRRP-based schemes, i.e., ZBT and KT outperform the performances of TF-based techniques (Bic and Cepstrum) approximately by 1–4% for SVM classifier. This can be explained by a fact that the *optimal* values of parameters L, G, and Q given in (15) are not estimated. The best performance between the features related to the TF-based techniques is achieved by bicoherence-based (Bic) feature with NBC.

Within *Scenario* #2, the best classification probability rate is achieved by using Bic technique. It allows to note that bicoherence-based classification feature demonstrates better robustness regarding the aspect of angle variations than other features. The Bic technique outperforms KT approximately by 4–8% and ZBT approximately by 12–20%.

Feature spaces of highest rank related to *Scenario* #2 are illustrated in **Figure 8**.

At the same time, the highest probability of correct classification is achieved by cepstrum-based features and SVM classifier for *Scenario* #3. Within *Scenario* #3, Bic technique takes the second place having the lags equal approximately to 4 or 6% depending on SVM or NBC classifier, respectively.

Summarizing the results presented in **Table 1**, the best robustness referred to aspect angle variations is demonstrated by TF-based schemes and extraction of cepstrum-based and

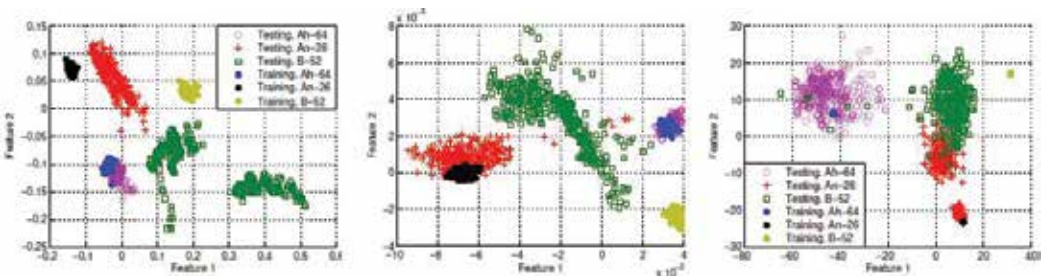

Figure 8. Feature space after LDA, *Scenario* #2. Aspect angle of 185° is given for training data set, and aspect angles of 190° and 195° are selected for testing data set: (a) KT, (b) Cepstrum, and (c) Bic.

bicoherence-based discriminative features. Taking into account the results obtained for *Scenario* #2, the information about phase coupling provides the best immunity regarding the aspect angle variations.

It can be seen from **Figure 8c** that variance of training samples is rather small compared to the distances observed between classes. Consequently, a problem occurs for computing the classification conditional probabilities for testing data. It follows from **Figure 8a** and **b** that testing sequences of samples are good when separated between each other. However, a variation of aspect angle leads to shifting of the features and misclassification in the final analysis. In contrast, the Bic-based features (see **Figure 8c**) belonging to testing sequence are overlapped for classes related to An-26 and B-52. As a result, classification errors can appear.

In order to study the influence of atmosphere turbulence, the same strategy is used as approach described for *Scenario* #1 with small difference. The training set is constructed in the same way by using clean, i.e., computed with less turbulence range profiles. At the same time, the testing set is constructed from the range profiles corrupted by a turbulence effect.

Classification probability rates computed under atmospheric turbulence influence are represented in **Table 2**. The following peculiarities should be emphasized by the comparison of the results demonstrated in **Tables 1** and **2**. Classification probability rates computed for ZBT, Bic-, and cepstrum-based approaches tend to decreasing approximately by 1–2% in a turbulence environment. Classifier using KT- and SVM-based decision making demonstrates the best robustness regarding influence of atmosphere turbulence.

Classification performance evaluated for various SNRs is demonstrated in **Figure 9**. As can be seen from **Figure 9a**, the best performance is achieved by KT technique. Bicoherence-based classification feature becomes comparable to KT starting from SNR = 1 dB. The cepstrum-based approach outperforms Bic method only for SNR smaller than 2 dB. The worst performance is achieved by ZBT, and the loss is rather high comparing to other techniques. Concluding analysis of the results represented in **Figure 9a**, the best performance of 72% is achieved by KT even for SNR = −10 dB, whereas other techniques provide the probability of random guess of 33%.

Bayes classifier demonstrates quite different results shown in **Figure 9b**. The Kim and Cepstrum techniques provide the same result as the results obtained with SVM classifier. The main difference is achieved by Bic method. For SNR ≥ −1 dB, the Bic method outperforms all other considered techniques. Errorless classification can be achieved starting from SNR = 2 dB for bicoherence-based features.

Classifier	**Feature extraction technique**			
	ZBT	**KT**	**Cepstrum**	**Bic**
SVM	98.22	99.99	97.09	97.82
Bayes	99.47	91.79	97.55	98.08

Table 2. Classification probability rate computed for turbulence environment.

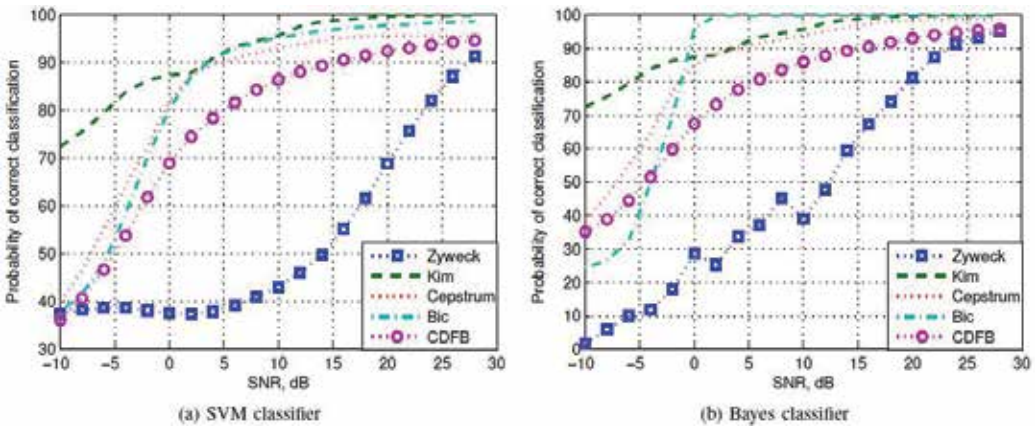

Figure 9. Classification probability rates depending on SNR value.

Thus, the best robustness to the aspect angel variability is provided by bicoherence- and cepstrum-based classifiers. These classifiers can be recommended for ATR radar systems.

4. Bispectrum-based radar range profile evaluation for the naval targets embedded in sea clutter environment

First, let us focus on the peculiarities characteristic for spatial-temporal model of surveillance radar signals received in sea clutter environment. Such signal model includes data contribution related to backscattering of naval surface target and interference contribution caused by a sea clutter. Assume that radar antenna irradiates the chain of M RF pulses of rectangular shapes and without any carrier modulation. Radar echo signal $\dot{s}_{ik}(t)$ can be written in the form of

$$\dot{s}_{ik}(t) = \dot{S}_{ik}(t)\exp\left(j2\pi f_0 t\right), \tag{20}$$

where $t \in [-T/2, T/2]$; $i, k = \{H, V\}$ are the indices corresponding to horizontal H and vertical V polarization, respectively; $\dot{S}_{ik}(t)$ is the complex-valued envelope; τ_p is the pulse length; $T = T_r M$ is the total radar signal processing time, T_r is the pulse repetition period; $m = 1, 2, 3,\ldots, M$ defines the pulse number index; f_0 is the central frequency given in radar signal, $f \in [f_0 - \Delta F/2, f_0 - \Delta F/2]$, and the frequency bandwidth ΔF is assumed to be of $\Delta F << f_0$; $j = \sqrt{-1}$.

During the time interval T, the naval target location on the sea surface can vary, and both its orientation and visibility can also be changed due to the wind's influence. In order to obtain a smooth estimation of the radar range profile (RP) contaminated by contribution of the unpredictable variability of maritime environment, the common strategy presumes dividing time interval T into N separate short-time segments and performing the averaging for N observed realizations [2].

Assuming that contribution of additive noise is negligible, the nth (n = 1, 2, …, N) arbitrary echo signal realization (further, the nth scan) observed at the amplitude detector output can be written as

$$S_{ik}^{(n)}(l\Delta t) = \mathrm{Re}\left\{ \int_{\Omega} \dot{F}(\theta)\dot{\varepsilon}_{ik}^{(n)}(\theta, l\Delta t)S[l(\Delta t + T_r) - \tau(\theta)]d\theta \right. \tag{21}$$

where $\dot{F}(\theta)$ is the complex-valued antenna pattern; $\dot{\varepsilon}_{ik}^{(n)}(\theta)$ is the nth relative (normalized for surface unit equal to 1 m^2) complex backscattering coefficient; $\tau(\theta)$=$2R(\boldsymbol{\theta})/c$ denotes the time signal delay; $R(\boldsymbol{\theta})$ and c are the slant range and speed of light, respectively; l = 1, 2, …, L is the index of current temporal digital sample; $L = M/N$ is the total sample number related to one scan; Δt is the pulse repetition period related to the range bin $\Delta R = c\Delta t$. Eq. (21) is valid under spatial-temporal and band-limitedness condition, i.e., for $2\Delta F/f_0 < \lambda_0/D$, where D is the size of radar antenna aperture.

The complex-valued coefficients $\dot{\varepsilon}_{ik}^{(n)}(\theta, l\Delta t)$ in (21) contain the sum of two contributions. First of them is random backscattering signal components $\dot{\varepsilon}_{Tik}^{(n)}(\theta, l\Delta t)$ corresponding to the contributions of the echoes caused by small surfaces $\Delta\boldsymbol{\theta}$ of the randomly moving target and second is the random component $\dot{\varepsilon}_{Sik}^{(n)}(\theta, l\Delta t)$ caused by a sea clutter. These two contributions are statistically independent. Hence, $\dot{\varepsilon}_{ik}^{(n)}(\theta, l\Delta t)$ can be expressed as

$$\dot{\varepsilon}_{ik}^{(n)}(\theta, l\Delta t) = \dot{\varepsilon}_{Tik}^{(n)}(\theta, l\Delta t) + \dot{\varepsilon}_{Sik}^{(n)}(\theta, l\Delta t), \tag{22}$$

where the first term is given by signal polarization matrix contained the coefficients $\dot{\varepsilon}_{T\,ik}^{(n)}(\theta, \Delta t) = \left|\dot{\varepsilon}_{T\,ik}^{(n)}(\theta, \Delta t)\right| \exp\left[j\xi_{T\,ik}^{(n)}(\theta, \Delta t)\right]$, and the second term is provoked by interference that can be represented by a polarization matrix containing the random coefficients $\dot{\varepsilon}_{S\,ik}^{(n)}(\theta, \Delta t) = \left|\dot{\varepsilon}_{S\,ik}^{(n)}(\theta, \Delta t)\right| \exp\left[j\xi_{S\,ik}^{(n)}(\theta, \Delta t)\right]$.

Commonly, the RP estimates are obtained by using the averaging strategy performed over N observed realizations. The mixture of signal and interference can be written as

$$\widehat{S}_{ik}(l\Delta t) = < \tilde{S}_{ik}^{(n)}(l\Delta t) > = < \tilde{S}_{T}^{(n)}\left(l\Delta t - \tau_{T}^{(n)}\right) > + < \tilde{S}_{S}^{(n)}\left(l\Delta t - \tau_{S}^{(n)}\right) >, \tag{23}$$

where $\tilde{S}_{T}^{(n)}\left(l\Delta t - \tau_{T}^{(n)}\right)$ and $\tilde{S}_{S}^{(n)}\left(l\Delta t - \tau_{T}^{(n)}\right)$ are the nth echo envelopes smoothed by antenna pattern and corresponding to both target and sea clutter backscattering, respectively; $\tau_{T}^{(n)}$ is the time lag integrated for all object backscattering centers during the nth scan; $\tau_{S}^{(n)}$ is the time lag integrated for all sea backscattering elements during the nth scan; <… > denotes the averaging for N observed scans. Both $\tau_{T}^{(n)}$ and $\tau_{S}^{(n)}$ are the random values that vary from one realization to another.

Due to random motions of target on the sea waves, the backscattering signal is a fluctuation process. Different wave propagation paths lead to different time lags $\tau_T^{(n)}$ and $\tau_S^{(n)}$ contained in (23), and these lags vary randomly. The target and sea radar responses are independent processes for which the corresponding PDF and correlation intervals differ from each other. The correlation intervals for processes that correspond to backscattering from sea surface are comparable to one scan processing time. Therefore, the contribution caused by sea clutter is an unpredictable fluctuating process that rapidly varies from one scan to another. Therefore, the time-varying sea echo radar responses that usually overlap with the signal target response can destroy the estimate (23).

Let us consider bispectrum-based data processing approach aimed for smoothing maritime interference contribution. Bispectrum estimate $\widehat{\dot{B}}(p,q)$ of the process (20) can be written as

$$\widehat{\dot{B}}(p,q) = \left|\widehat{B}(p,q)\right| \exp\left[j\widehat{\gamma}(p,q)\right] = < X^{(n)}(p)X^{(n)}(q)X^{(n)*}(p+q) > , \tag{24}$$

where $\left|\widehat{B}(p,q)\right|$ and $\widehat{\gamma}(p,q)$ are the bimagnitude and biphase estimates, respectively; $p = 1, 2, \ldots, L$ and $q = 1, 2, \ldots, L$ are the frequency indices; $\dot{X}^{(n)}(\ldots)$ is the direct Fourier transform of (20) equal to $\dot{X}^{(n)}(p) = \dot{S}_T^{(n)}(p)\exp\left(j2\pi\tau_T^{(n)}p\right) + \dot{S}_S^{(n)}(p)\exp\left(j2\pi\tau_S^{(n)}p\right)$; $\dot{S}_T^{(n)}(p)$ and $\dot{S}_S^{(n)}(p)$ are the Fourier transforms of the object $\tilde{S}_T^{(n)}(\ldots)$ and sea $\tilde{S}_S^{(n)}(\ldots)$ contributions given in (23), respectively.

Bispectrum estimate $\widehat{\dot{B}}(p,q)$ (24) contains eight terms. The first term in the form of $\widehat{\dot{B}}_T(p,q) = < \dot{S}_T^{(n)}(p)\dot{S}_T^{(n)}(q)\dot{S}_T^{(n)*}(p+q) >$ corresponds to the contribution of original target bispectral estimate. The other seven terms represent the interference contribution. Theoretically, considerably good accuracy of signal contribution $\widehat{\dot{B}}_T(p,q)$ can be obtained under traditional assumptions that interference is of zero mean, and its PDF is close to a symmetric law. However, in number of real-life situations, interference does not obey the latter symmetric law. Therefore, the real-life case of sea clutter with non-zero mean value and with long-tail PDFs needs to be studied, and this problem is one of the subjects of our consideration and discussion in this chapter.

Final step of the bispectrum-based forming of RP estimate can be represented as the following inverse Fourier transform (IFT)

$$\widehat{S}_{range}(l) = \left| IFT\left\{ \left|\hat{\dot{S}}_{bisp}(r)\right| e^{j\hat{\Phi}_{bisp}(r)} \right\} \right| \quad r = 1, 2, \ldots, L, \tag{25}$$

where $\left|\hat{\dot{S}}_{bisp}(r)\right|$ and $\hat{\phi}_{bisp}(r)$ are the magnitude and phase target RP Fourier spectrum estimates, respectively. They can be recovered from (24) by recursive algorithms described in details in [10].

The main difference between traditional signal processing (23) and suggested bispectrum-based approaches can be explained by the difference in averaging procedures necessary to

smooth the sea clutter contribution. Traditional signal processing (23) using direct ensemble averaging is performed in the signal space, i.e., in time domain. Due to the random signal lags $\tau_T^{(n)}$ contained in (23), averaged received response estimate (23) becomes considerable spread shape. It provokes decreasing the performance in ATR system by using common RP evaluation. At the same time, suggested bispectrum-based technique exploits *coherent averaging* of non-translated bispectrum estimates in bifrequency domain. As a result, due to the invariance property of bispectrum to a signal lags $\tau_T^{(n)}$, suggested strategy provides *coherent ensemble averaging* of bispectrum estimates. Therefore, the shape of RP transformed considerably less as compared to the common signal averaging procedure (23). Hence, better performance of bispectrum-based ATR system can be achieved.

Experimental study was performed during summer period using X-band polarimetric surveillance radar operating at the central frequency equal to f_0 = 9.370 MHz. The fixed transmitting/receiving radar antenna was located on the sea shore at the height of y_0 = 8 m over sea level.

After passing through analog IF amplifier and amplitude detector, the received radar echo signals were digitized and accumulated in the processor memory. The sampled experimental data were accumulated and recorded in the form of the sets of scans (realizations) contained L = 32 samples in each scan for each HH, HV, VH, and VV polarization, respectively. The scan duration for each polarization was set to 320 ms.

The anchored metallic buoy was served as the naval surface target. Its size was considerably smaller than the radar range bin. The radar echoes were recorded under grazing angles of about 0.4°.

We compare the bispectrum-based RP recovery with RP estimations evaluated by the common direct averaging procedure. The number of N scans accumulated for each separate polarization mode was equal to N = 256.

Consecutive two arbitrary scans experimentally measured for HH polarization mode are demonstrated in **Figure 10**.

The plots of normalized range profile (NRP) are represented in the form of function of range sample index l. *A priory* known slant range from antenna to buoy was equal to R = 1500 m. Therefore, the buoy location corresponds approximately to the range sample index l = 26. Note that random buoy translation on sea waves can be expected to become apparent during considerably long observation time interval. Hence, the target $\dot{\varepsilon}_{Tik}^{(n)}(\theta, l\Delta t)$ and sea clutter $\dot{\varepsilon}_{Sik}^{(n)}(\theta, l\Delta t)$ contributions given in (22) are the values that are randomly varying during time interval related to each separate observed scan.

As can be seen from **Figure 10**, both radar backscattering response corresponding to buoy RP and to sea clutter have random nature, and their appearance and shapes considerably vary from scan to scan. Particularly, the buoy is not visible for some scans at all, e.g., for scan in **Figure 10b**. Though the target RP should appear itself as single peak because its size is much smaller than the radar range bin, the target response shape is considerably distorted. Due to sea clutter contribution, several peaks are observed in the neighborhood of the range index

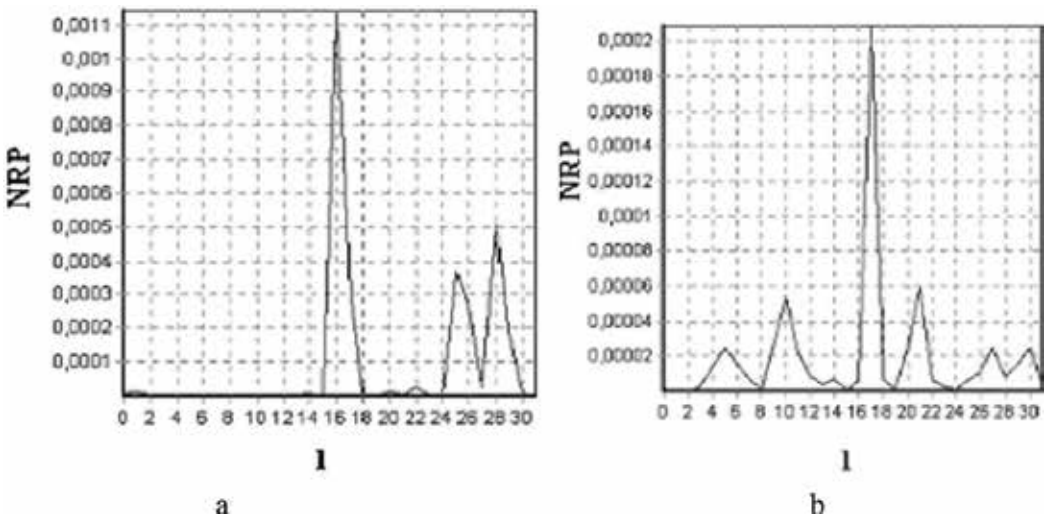

Figure 10. Consecutive scans.

number $l = 26$ related to the buoy location. Such distortions in the NRP prevent target classification in ATR system.

In order to improve estimator accuracy, the average procedure performed over N scans is commonly used according to (23). Example of averaged NRP is demonstrated in **Figure 11a**. The bispectrum-based NRP signature is shown in **Figure 11b**. Note that due to bispectrum shift invariance property, the latter NRP is centered with respect to the center of gravity.

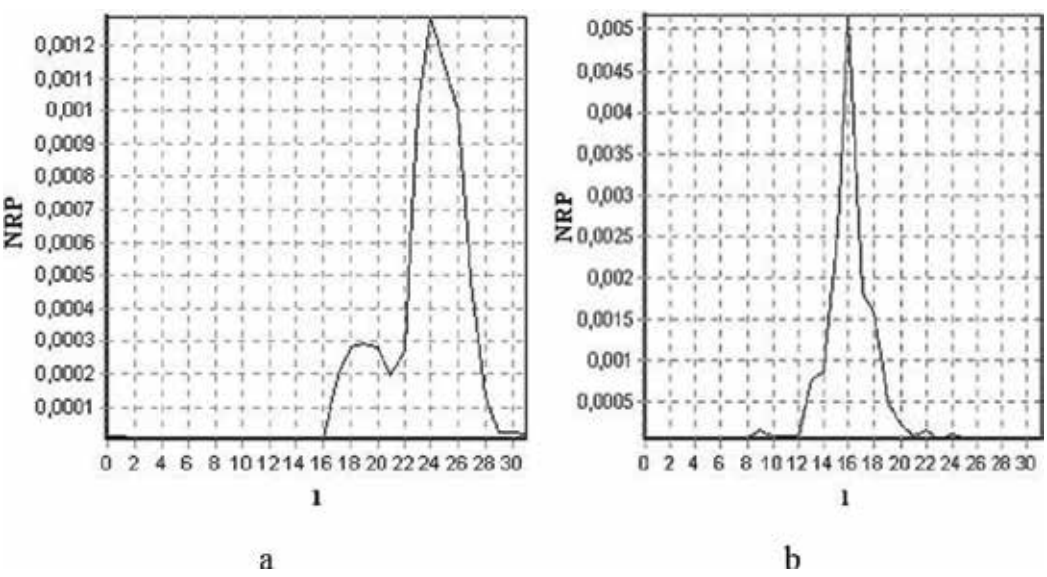

Figure 11. Averaged RP, VV polarization, wind speed 7–10 m/s; sea state 2–2.5 (a). Bispectral NRP, VV polarization, wind speed 7–10 m/s; sea state 2–2.5 (b).

As clearly seen from the **Figure 11a**, the NRP ensemble averaged according to (23) is considerably distorted. The shape of averaged NRP is spread considerably. This value is essentially larger than the radar range bin equal to 75 m that can be expected as the target response width. This spreading results in decreasing of radar range resolution caused by sea clutter influence. It is clearly seen that range resolution obtained with bispectral NRP (see **Figure 11b**) is considerably better as compared with averaged RP (see **Figure 11a**).

In **Tables 3** and **4**, the summary of the key parameters of the NRP estimation, namely the range resolution data under sea clutter level, is represented for two considered techniques.

As can be seen from **Table 3**, the range resolution is worsen from 2 to 12 times as compared to the theoretical radar range bin equal to 75 m.

The results represented in **Table 4** demonstrate the stability of the range resolution that is worsen only by 2 times in comparison to the above mentioned theoretical radar range bin except the case of wind speed of 7–10 m/s, as well as for HH polarization.

The values of the sea clutter levels given in **Tables 3** and **4** depend both on polarization mode and sea state. As clearly seen from comparison, the data contained in the **Tables 3** and **4**, bispectrum-based technique provides suppression of sea clutter level from 11 dB (HH polarization mode) to 20 dB (VV polarization mode) in the case of absence of wind and from 4 dB (HH polarization mode) to 20 dB (HV polarization mode) in the case of wind speed equal to 7–10 m/s. Hence, the bispectrum-based technique provides considerable improvement of range resolution in sea clutter environment.

Consequently, conventional RP estimation technique based on the averaging of the received signal envelopes has low-range resolution and low robustness to sea clutter.

Absence of wind			**Wind speed of 7–10 m/s**		
HH	HV	VV	HH	HV	VV
NRP width at the half-amplitude level, m					
450	300	300	900	300	300
Sea clutter level, dB					
−13	−6	−6	−13	−8	−13

Table 3. Experimental results obtained for common averaging procedure according (23).

Absence of wind			**Wind speed of 7–10 m/s**		
HH	HV	VV	HH	HV	VV
NRP width at the half-amplitude level, m					
150	150	150	450	150	150
Sea clutter level, dB					
−24	−20	−26	−17	−28	−26

Table 4. Experimental results obtained for suggested bispectrum-based data processing.

http://dx.doi.org/10.5772/intechopen.71034

5. Classification of the atmospheric formations by using bicoherence-based features

Recently, weather radars play an important role in the world for atmosphere surveillance and weather forecasts. Radar techniques dedicated to study the meteorological formations are based on extraction of the data from backscattering of electromagnetic waves by the particles concentrated in the clouds and precipitations. Spatial distribution of the numerous backscattering centers contained in a cloud creates the contribution into total radar echo signal. Parameters of this backscattering signal contain meteorological information about atmosphere formations [11, 12].

Reliable meteorological data serve as one of the main and important component necessary for securing flight safety in modern aviation. According to statistical data, dangerous phenomena like thunderstorm frontal passages, squalls, and wind fluctuations cause approximately 70% of the aviation crashes. Turbulent movement of atmospheric flows as opposed to laminar air movement is specified with random variability of wind-rate field, presence of fluctuation of air heterogeneity, or so-called turbulent atmospheric vortexes that cause mixing of the airflows. Atmospheric turbulence causes abrupt movement of aircraft called as bumpy flight. As the bumpy flight piloting becomes a difficult and dangerous procedure, additional mechanical loads related to the elements of aircraft construction appear and even destruction of aircraft construction may happen. Consequently, reliable recognition of dangerous turbulent formations and areas is an important problem in modern aviation radar meteorology and aviation safety of the flights.

Power spectral density of radar backscattering signals is one of commonly used and widespread information features extracted from "angel echo." Usually, the severity of turbulence is accessed from the measurements of the radial velocity variance observed in the air flows. The power spectral density describes the dissipation of turbulence energy caused by decay of large atmospheric vortexes into smaller fractions. In order to recognize the type of cloud formation, it is commonly accepted that it is enough to estimate the power spectral width of radar backscattering signal. In order to make a decision about atmospheric turbulence state and, hence, about dangerous areas located at the course of aircraft, the value referred to the power spectrum spreading must be estimated. After that, the pilot must make a decision in order to avoid a weather hazard area. However, the spreading of power spectrum can be related to sufficiently rough classification feature serving for estimation of the scale of turbulence contained in the atmosphere formations. Solving the problems of discrimination of turbulent and laminar atmosphere flows by using spectral density width can lead to ambiguous interpretation of measured data and, consequently, to provoke the errors related to the correction of the aircraft course in order to round the dangerous atmospheric turbulent formations and areas.

In order to improve reliability of recognition and discrimination of laminar and turbulent meteorological formations, it is necessary to seek novel information features contained in radar backscattering signals. Spatial-temporal, frequency-phase relationships, as well as phase-coupling phenomena may serve as novel discrimination and classification features. These frequency-phase relationships can be caused by physical nature of radar signal scattering with laminar aerial flow contained within a pulse volume.

In order to extract phase coupling contained and prevail in laminar atmospheric formation, we suggest exploiting bispectrum-based strategy to the weather radar signal processing.

The approach suggested in this section is based on the hypothesis that radar signal backscattered by atmospheric formation can contain phase-coupled spectral contributions carrying useful data for extraction of the classification features. This phase coupling contains novel classification features used for discrimination and classification of turbulent and laminar atmospheric flows and, hence, information about dangerous areas located in the atmosphere. As novel information feature and measure, we suggest exploiting bicoherence in the form defined in [13].

Bicoherence $b^2(p, q)$ [13] can be computed in the form of statistical averaging of the bispectral estimate and further normalization procedure as

$$b^2(p,q) = |< B(p,q) >|^2 / \left\{ < |X(p+q)|^2 < |X(p)X(q)|^2 > \right\} \tag{26}$$

Bicoherence $b^2(p, q)$ given in the form of (26) can be interpreted as squared version related to the normalized bispectrum. The dimensionless value (26) varies within the limits from zero to unity, i.e. $b^2(p,q) \in [0, 1]$. So, bicoherence is the value serving as *a quantitative measure of phase relationships* between spectral components contained in a signal under study.

If the electromagnetic waves are backscattered by volume-distributed turbulent meteorological formation, all the phases in backscattering signals are of random and independent values. In such case, bicoherence estimate (26) tends to be of zero value. Phase-coupled spectral components are contained in the radar backscattering caused by volume-distributed laminar formation. In latter case, bicoherence estimate (26) tends to be a non-zero value.

Experimental study was performed by upgraded weather radar of the type of MRL-1 equipped by additional facilities necessary for control of orientation of maximum of antenna main lobe pattern, calibration of radar energy potential, expansion of dynamic range in receiving device, and digital signal processing. Weather radar operates at the wavelengths of 8 mm and 3.2 cm.

The power spectral density and bicoherence of the echo signal measured for the case of antenna elevation angle equal to 10° and the downrange of 3750 m are plotted in the **Figure 12**. These demonstrative examples correspond to the stratocumulus "non-translucent" clouds #122.

Due to stochastic behavior of the echo-signals, their power spectral density function is of pronounced irregular shape. Because of this, in order to smooth power spectral density estimate, statistical averaging has been performed over each four realizations. After digitalization procedure and averaging performed over four realizations, 512 digital samples corresponding to each range bin were accumulated in PC memory. These data are used to compute both power spectral density and bicoherence estimate.

Computation of smoothed bicoherence estimate has been accomplished by averaging over eight segments contained 64 received signal samples with 50% overlap in each segment. Additional

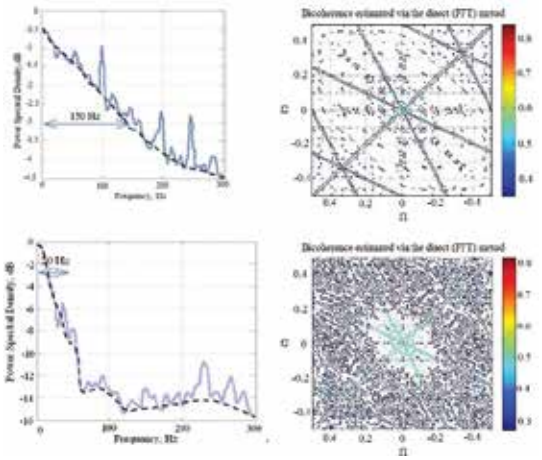

Figure 12. Power spectrum (a) and bicoherence estimate (b) for "non-translucent" clouds #122.

smoothing of the bicoherence estimate has been carried out under fixed antenna elevation angle equal to 10°. Ensemble averaging has been performed over 100 observed realizations and with time interval equal to 0.85 s. Therefore, total time interval exploited for computation of bicoherence estimate was equal to 100×0.85 s = 85 s.

Decision about belonging of meteorological formation to laminar or turbulent kind is made by comparison the bicoherence value with threshold given *a priory*. In the case, when the bicoherence samples do not take the values belonging to the given threshold, decision is made in favor of turbulent formation. In opposite case, one made decision in favor of laminar formation.

Two different threshold values equal to 0.7 and 0.5 were examined (see **Table 5**).

Data represented in **Table 5** indicate the following results. For the stratocumulus "non-translucent" clouds #122, the percentage of the bicoherence values exceeding both threshold

Type of cloudiness	Slant range (m)	Index of excess	
		Threshold 0.7 (%)	Threshold 0.5 (%)
Clouds #122	3750	0.02	0.76
White cumulus clouds	3150	0.77	11.2
Flocculent clouds T-36	5100	16.19	95.0
	3300	18.4	96.7
	1500	0.6	3.7
"White flaky"	2400	0.1	4.07

Table 5. The indexes of exceeding of the threshold computed in percent.

values of 0.7 and 0.5 are equal to 0.02 and 0.76%, respectively. For the flocculent altocumulus clouds T-36, the percentage of the bicoherence values acceding the thresholds of 0.7 and 0.5 are equal to 16.19 and 95%, respectively. It is also seen from the data contained in **Table 5** that for the clouds #122, the turbulent contributions are predominated at the slant range of 3750 m. At the same time, the laminar content is predominated for the T-36 clouds at the slant range equal to 5100 m.

Thus, using common classification features evaluated in the form of width of power spectral density leads to certain ambiguity. At the same time, suggested bicoherence-based approach proposed in this chapter eliminates this ambiguity.

6. Conclusions

Bispectrum density estimator in opposite to the common energy spectrum estimator allows not only describing statistical characteristics of a process more correctly and more profoundly but also to detect and extract a new class of dependences contained in the data under study. These dependences can exist in the form of spectral component correlation relationships and phase coupling between the spectral component pairs. Therefore, the main difference between bispectral and energy spectral strategies is in the preservation of phase information and possibility of extracting this phase contributions. Bispectrum-based signal processing allows extracting novel information features providing signal detection and discrimination, as well as object recognition and classification. The benefits of the suggested bispectrum-based data processing techniques were demonstrated by experimental study of radar target detection, classification and identification for naval, aerial, and ground moving objects. Experimental results represented in this chapter demonstrate sea clutter suppression and improving of naval object range resolution provided by polarimetric X-band radar. Essential reduction of speckle distortions in aerial high resolution range profiles obtained by using suggested bicoherence-based classification features was shown. Experimental results of time-frequency analysis of backscattered signals recorded by ground surveillance Doppler radar were represented and discussed. Suggested bispectrum-based approach can serve for improving the detection and recognition performances in radar ATR systems operating in vegetation clutter. Bicoherence estimates were proposed for detection and discrimination of the atmospheric turbulence formations performed by weather surveillance radar. Results of experimental study indicate discrimination of the turbulent and laminar air flows by exploiting bicoherence classification features.

Author details

Alexander Totsky[1]* and Karen Egiazarian[2]

*Address all correspondence to: totskiyalexander@gmail.com

1 Department of Transmitters, Receivers and Signal Processing, National Aerospace University, Kharkov, Ukraine

2 Signal Processing Laboratory, Tampere University of Technology, Tampere, Finland

References

[1] Nikias CL, Raghuveer MR. Bispectral estimation: A digital signal processing framework. Proceedings of IEEE. 1987;**75**(7):869-891

[2] Shirman YD, Gorshkov SA, Leshchenko SP, Orlenko VM, Sedyshev SY, Sukharevskiy OI. Computer Simulation of Aerial Targets, Radar Scattering, Recognition, Detection, and Tracking. Artech House: Boston-London; 2002

[3] Chen V. The Micro-Doppler Effect in Radar. London: Artech House; 2011

[4] Zyweck A, Bogner RE. Radar target classification of commercial aircraft. IEEE Transactions on Aerospace and Electronic Systems. April 1996;**32**(2):598-606

[5] Kim K-T, Seo D-K, Kim H-T. Efficient radar target recognition using the MUSIC algorithm and invariant features. IEEE Transactions on Antennas and Propagation. Mar. 2002;**50**(3):325-337

[6] Molchanov Pavlo O, Astola Jaakko T, Egiazarian Karen O, Totsky Alexander V. Moving target classification in ground surveillance radar ATR system by using novel bicepstral-based information features, European Radar Conference (EuRAD), 2011, p. 194-197, 12-14 Oct. 2011

[7] Duda RO, Hart PE, Stork DG. Pattern Classification. New York: John Wiley & Sons Inc.; 2000. p. 680

[8] Thayaparan T, Abrol S, Riseborough E, Stankovic L, Lamothe D, Duff G. Analysis of radar micro-Doppler signatures from experimental helicopter and human data. IET Radar, Sonar & Navigation. Aug. 2007;**1**(4):289-299

[9] Ahdesmäki M, Strimmer K. Feature selection in omics prediction problems using cat scores and false nondiscovery rate control. Annals of Applied Statistics. 2010;**4**(1):503-519

[10] Bartelt H, Lohmann AW, Wirnitzer B. Phase and amplitude recovery from bispectra. Applied Optics. 1984;**23**:3121-3129

[11] Doviak RJ, Zrnic DS. Doppler Radar and Weather Observations. 2nd ed. San Diego, CA: Academic Press; 1993. p. 562

[12] Bringi VN, Chandrasekar V. Polarimetric Doppler Weather Radar. Principles and Applications. UK: Cambrige University Press; 2004. p. 636

[13] Fackrell J. Bispectral analysis of speech signals [PhD thesis]. Edinburg: The University of Edinburg; 1996. p. 216

Edited by Graham Weinberg

Radar has been an important topic since its introduction, in a military context, during World War II. Due to advances in technology, it has been necessary to refine the algorithms employed within the signal processing architecture. Hence, this book provides a series of chapters examining some topics in modern radar signal processing. These include synthetic aperture radar, multiple-input multiple-output radar, as well as a series of chapters examining other key issues relevant to the central theme of the book.

Published in London, UK

IntechOpen

ISBN 978-1-83881-419-9